IN-46-CR
19914
P.226

SEMI-ANNUAL STATUS REPORT #9

TO THE NATIONAL AERONAUTICS AND SPACE ADMINISTRATION

CRUSTAL DYNAMICS PROJECT

NASA GRANT NAG 5-814

"The Interpretation of Crustal Dynamics Data in Terms of Plate Motions and Regional Deformation Near Plate Boundaries"

for the period

22 September 1990 - 21 March 1991

Principal Investigator:

Prof. Sean C. Solomon
Department of Earth, Atmospheric, and Planetary Sciences
Massachusetts Institute of Technology
Cambridge, MA 02139

24 June 1991

TABLE OF CONTENTS

This is a Semi-Annual Status Report on research conducted between 22 September 1990 and 21 March 1991 under NASA Grant NAG 5-814, entitled "The Interpretation of Crustal Dynamics Data in Terms of Plate Motions and Regional Deformation near Plate Boundaries." This grant supports the research of one Investigator (S. C. Solomon), one Research Staff (R. Reilinger), and two Ph. D. students (A. F. Sheehan and C. J. Wolfe) on behalf of the NASA Geodynamics and Crustal Dynamics Programs.

The focus of the research has been in two broad areas during the most recent 6-month period: (1) the nature and dynamics of time-dependent deformation and stress along major seismic zones, and (2) the nature of long-wavelength oceanic geoid anomalies in terms of lateral variations in upper mantle temperature and composition. The principal findings of our research to date are described in the accompanying appendices. The first two and the fourth are preprints of papers recently submitted for publication, and the third is the abstract of a recently completed Ph.D. thesis supported by this project.

APPENDIX 1

GPS measurements of strain accumulation across the Imperial Valley, California: 1986-1989

by S. Larsen and R. Reilinger

Submitted to *Journal of Geophysical Research*, 1991

GPS Measurements of Strain Accumulation Across the Imperial Valley, California: 1986-1989

Abstract

GPS data collected in southern California from 1986 to 1989 indicate considerable strain accumulation across the Imperial Valley. Displacements are computed at 29 stations in and near the valley from 1986 to 1988, and at 11 sites from 1988 to 1989. The earlier measurements indicate 5.9 $\pm$ 1.0 cm/yr right-lateral differential velocity across the valley, although the data are heavily influenced by the 1987 Superstition Hills earthquake sequence. Some measurements, especially the east-west trending displacements, are suspect for large errors. The 1988-1989 GPS displacements are best modeled by 5.2 $\pm$ 0.9 cm/yr of plate-boundary deformation, but rates calculated from conventional geodetic measurements (3.4-4.3 cm/yr) fit the data nearly as well. There is evidence from GPS and VLBI observations that the present slip rate along the southern San Andreas fault is smaller than the long-term geologic estimate, suggesting a lower earthquake potential than is currently assumed. The Imperial Valley GPS sites form part of a larger network of 183 stations spanning an entire cross-section of southern California and northern Mexico. Once data from a recent 1990 campaign are fully analyzed and integrated with the previous measurements, the strain distribution across the San Andreas, San Jacinto, and Elsinore faults will be well established.

5.1 Introduction

The Global Positioning System (GPS) is rapidly becoming one of the most important tools to study tectonic deformation. Signals from earth-orbiting NAVSTAR satellites (NAVigation Satellite Time And Ranging) are inverted to obtain 3-dimensional coordinates of geodetic monuments with high precision. For crustal deformation studies, the relative position (or baseline) between stations is often measured. Under optimal conditions, the typical accuracy for a 50 km baseline is about 1 cm in the horizontal and 3 cm in the vertical [e.g., *Davis et al.*, 1989]. The accuracy is significantly degraded from poor observing conditions. GPS measurements are used to monitor secular deformation such as that associated with plate motion, or to record rapid strain fluctuations such as those due to seismic and volcanic activity.

A prime location for GPS studies is the Imperial Valley of southern-most California (Figure 5.1). The valley is one of the most tectonically active regions in the state and has been the site of several large earthquakes. In fact, GPS monitoring was initiated in 1986 with resurveys in 1988 and 1989. GPS station displacements from 1986 to 1988 have been discussed by *Larsen et al.* [1990]. These measurements illustrate the effect of the 1987 Superstition Hills earthquake sequence, as well as nonseismic displacement components attributed to interplate deformation. In the present study we incorporate the 1989 GPS observations. Station displacements from 1986-1988 and 1988-1989 are computed and these movements are related to the relative motion between the North American and Pacific plates.

5.2 Seismicity and Tectonics

Figure 5.1: Major faults and seismicity from 1932 to 1990 (Caltech Catalog) in the Imperial Valley. Large earthquakes are shown as stars. The Brawley Seismic Zone is the region of anomalously high activity between the Imperial and San Andreas faults. Major earthquakes include the 1940 and 1979 events along the Imperial fault, the 1954 and 1968 events along the San Jacinto fault, and the 1987 Superstition Hills earthquake sequence along the Superstition Hills and Elmore Ranch faults.

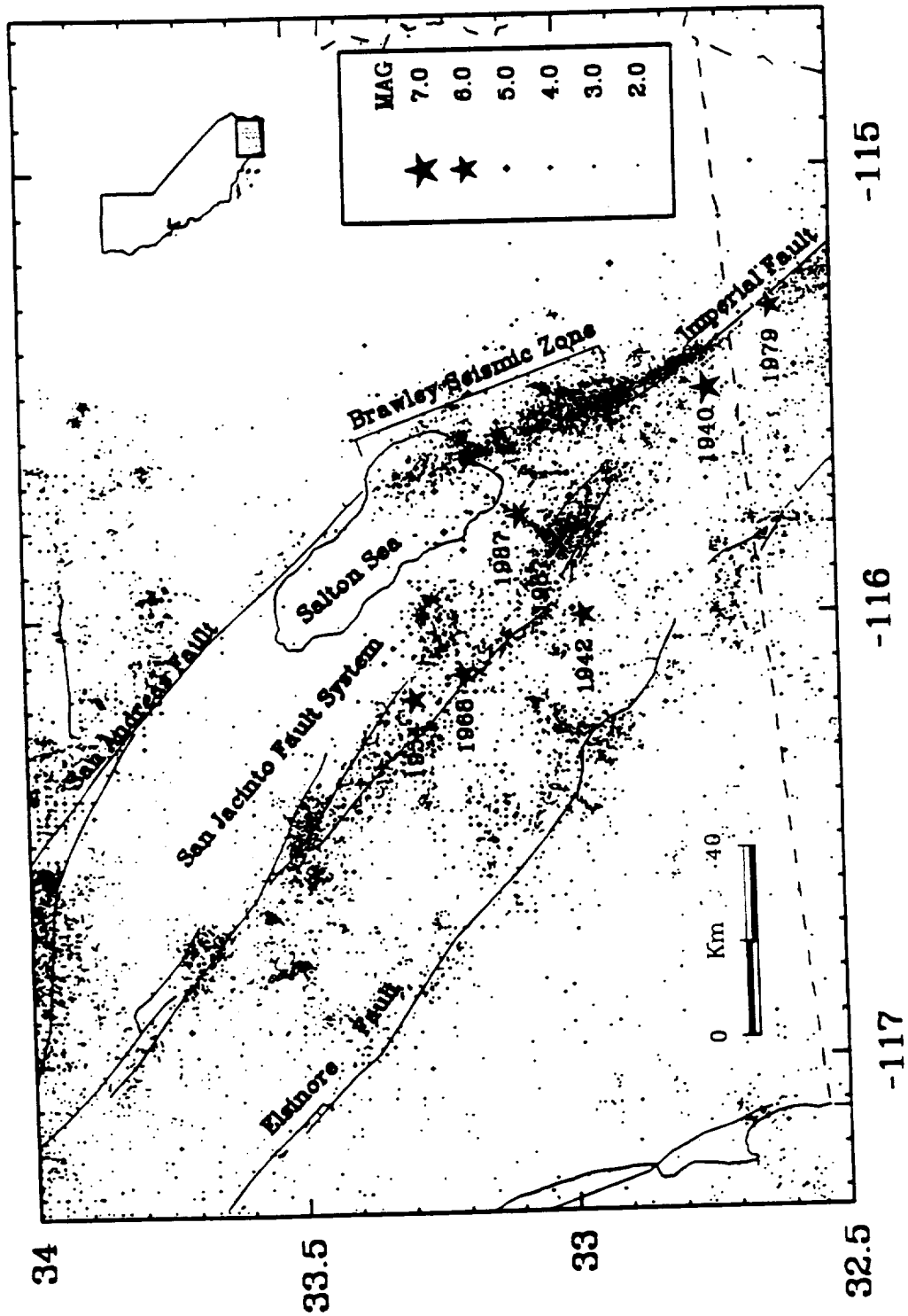
MAG
7.0
6.0
5.0
4.0
3.0
2.0
Brawley Seismic Zone
Imperial Fault
1940
1979
Salton Sea
1987
San Andreas Fault
San Jacinto Fault System
1968
1942
Elsinore Fault
0
40
Km
34
33.5
33
32.5
-115
-116
-117

The Imperial Valley (Figure 5.1) is a complex transition zone between crustal spreading in the Gulf of California and right-lateral transform motion along the San Andreas fault [*Lomnitz et al.*, 1970; *Elders et al.*, 1972]. The valley is 4-5 million years old and has been filled by up to 5 km of late Cenozoic sediments [*Fuis et al.*, 1982]. The structural axis of the valley and its major fault systems trend to the northwest, roughly parallel to the Pacific-North American plate motion. A significant fraction of the relative plate displacement may be accommodated across the valley.

The Imperial Valley is one of the most seismically active regions of California with much of the activity occurring along the Imperial fault and in the Brawley Seismic Zone [*Johnson and Hill*, 1982]. Several large earthquakes have occurred in and near the Imperial Valley since 1940. The Imperial fault ruptured with a M_S 7.1 event in 1940 and a M_L 6.6 event in 1979 [*U. S. G. S.*, 1982]. Segments of the San Jacinto fault system broke with a M_L 6.2 earthquake in 1954 (Clark segment) and the 1968 M_L 6.5 Borrego Mountain event (Coyote Creek segment). The most GPS relevant episode of seismic activity occurred recently along the Superstition Hills segment of the San Jacinto fault system [e.g., *Magistrale et al.*, 1989]. On November 24, 1987, a large (M_S 6.2) earthquake occurred along a northeast trending seismic lineament, and was followed 12 hours by a larger event (M_S 6.6) along the Superstition Hills fault.

Conventional geodetic measurements indicate significant displacements across the Imperial Valley, inferred to represent interplate deformation. Triangulation data averaged from 1941 to 1986 suggest 4.3 cm/yr plate-boundary movement oriented N40°W [*Snay and Drew*, 1988]. The observed

deformation is time dependent, with rates of 6.1, 2.1, and 4.5 cm/yr for the intervals 1941-1954, 1954-1967, and 1967-1979, respectively. The high velocity for the earliest period supports the hypothesis of northwestward strain migration following the 1940 earthquake [*Thatcher*, 1979; *Reilinger*, 1984]. Furthermore, the computed station displacements indicate that north of the Imperial fault interplate deformation is distributed over a zone at least 50 km wide whereas to the south interplate deformation is concentrated within a 20 km wide band centered along the Imperial fault. Trilateration measurements made by the U.S. Geological Survey from 1972 to 1987 [*Prescott et al.*, 1987a; *Prescott et al.*, 1987b] indicate 3.45 cm/yr differential displacement oriented roughly N40°W between stations on opposite sides of the valley. Unlike the increased rate following the 1940 earthquake, these measurements reveal no significant change in station velocity after the 1979 event [*Savage et al.*, 1986].

New global plate models (NUVEL-1) [*DeMets et al.*, 1987; *DeMets et al.*, 1990] predict the Pacific-North American relative velocity at Imperial Valley coordinates (longitude 115.5°W, latitude 33.0°N) averaged over the last several million years to be 4.7 cm/yr oriented N39.6°W. VLBI observations during the 1980's suggest a similar present-day rate [e.g., *Clark et al.*, 1987; *Kroger et al.*, 1987]. A significant fraction of this motion may be distributed along faults in and near the Imperial Valley.

5.3 GPS Observations

The data presented here were obtained in a series of GPS field campaigns in 1986, 1988, and 1989. Here we provide summaries regarding the collection

and processing of the 1986 and 1988 surveys, discussed in more detail by *Larsen et al.* [1990], and present a more detailed account of the most recent campaign. In all, a total of 32 Imperial Valley stations have been occupied more than once between 1986 and 1989 (Table 5.1).

The National Geodetic Survey (NGS) began GPS observations in southern California with a 54 station network in 1986; 42 stations are located in or near the Imperial Valley (Figure 5.2). TI-4100 GPS receivers were used for all data collection. Each of the 20 days of observation are processed independently utilizing the GPS22 software developed at the NGS, with satellite orbit parameters provided by the NSWC (Naval Surface Weapons Center). The day to day solutions are integrated into one set of station coordinates with the geodetic adjustment program DYNAP (DYNamic Adjustment Program) [*Drew and Snay*, 1989]. Due to insufficient coverage and poor data quality during the 1986 survey, uncertainties are suggested to be approximately 1 ppm (parts per million) [*Neugebauer*, 1988].

During late February and early March, 1988, university GPS crews (UNAVCO) occupied 19 sites in the Imperial Valley, including 15 marks observed in 1986 (Figure 5.2). The following month, the NGS returned to the Imperial Valley and reoccupied 21 previously established monuments. TI-4100 receivers were used for all measurements. Data from both surveys are processed independently with the Bernese GPS software package from the University of Bern in Switzerland. For each campaign, the data are combined into one multiday solution. Satellite orbits are improved with the aid of fiducial observations from Mojave (California), Westford (Massachusetts), and Richmond (Florida), made as part of the Cooperative International GPS

Table 5.1 Reoccupied Stations (1986-1989)

Station Name	Abbr.	Occupation 1986	1988	1989	Longitude °	Latitude °	Elevation (m)
Acute 1934	ACUT	•	•		-115.6093	33.0300	-80.91
Alamo	ALAM	•	•	•	-115.6111	33.1964	-72.91
Black Butte NCMN 1982	BLAC	•	•	•	-115.7198	33.6638	490.01
Brawley 2 rm 5	BRAW	•	•		-115.5434	32.9773	-66.78
Calexico 1954	CALE	•	•		-115.5064	32.6645	-34.07
Calipatria 2	CALI	•		•	-115.5088	33.1690	-89.03
Coach	COAC	•	•		-115.4070	33.1962	-8.40
College 1967	COLL	•	•	•	-115.5024	32.8269	-54.63
El Centro 2 1959	ELEC	•	•		-115.5622	32.7846	-45.76
Frink 1934	FRIN	•	•	•	-115.6470	33.3603	-85.39
GLO Cornew 1934	GLOC	•	•		-115.2465	32.8396	-15.46
Hamar 2 1967	HAMA	•	•		-115.5007	33.0375	-79.80
Holt 1924	HOLT	•	•		-115.3963	32.7814	-36.79
Holtville (Alt) 1934	HLTV	•	•		-115.3821	32.8084	-38.77
Imp 1934	IMPI	•	•		-115.5698	32.8982	-59.27
Imperial 1934	IMPE	•	•		-115.5788	32.8439	-51.85
Junction	JUNC	•	•	•	-115.0619	32.7092	8.35
Kane 1939	KANE	•	•	•	-115.8237	33.0614	10.05
L 589 1967	L589	•	•	•	-115.7611	32.9506	13.62
Mack 2 1967 bm reset	MACK	•	•		-115.1441	32.7288	1.20
Mello 3 1967	MELL	•	•		-115.4653	32.7961	-47.00
Monument Peak NCMN 1983	MONU	•		•	-116.4228	32.8918	1839.41
Ocotillo NCMN 1982	OCOT	•	•	•	-115.7962	32.7901	-36.43
Ocotillo 1935	OCTI	•	•	•	-116.0017	32.7338	111.33
Offset 217	O217	•	•		-115.3131	32.6782	-17.16
Offset 224	O224	•	•		-115.7055	32.6493	50.00
Offset 227	O227	•	•		-115.8173	32.6414	70.64
Orient 1939	ORIE	•	•	•	-115.4064	32.9168	-61.36
Pinyon Flat	PINY	•	•		-116.4588	33.6093	1235.88
Sandy Beach	SAN1		•	•	-115.8344	33.1929	-99.92
T 1226	T122	•	•		-114.8050	32.8583	141.19
Tamarisk 3 1967	TAMA	•	•		-115.4783	32.8829	-68.19

Figure 5.2: GPS stations surveyed in 1986 and 1988. The 1986 campaign was conducted by the National Geodetic Survey and included 42 stations in and near the Imperial Valley. The 1988 observations consisted of two campaigns, the first by university groups in February/March and the second by the National Geodetic Survey in March/April. A total of 32 stations were occupied in 1988, of which 29 were repeat measurements from 1986. Stations mentioned in text are indicated.

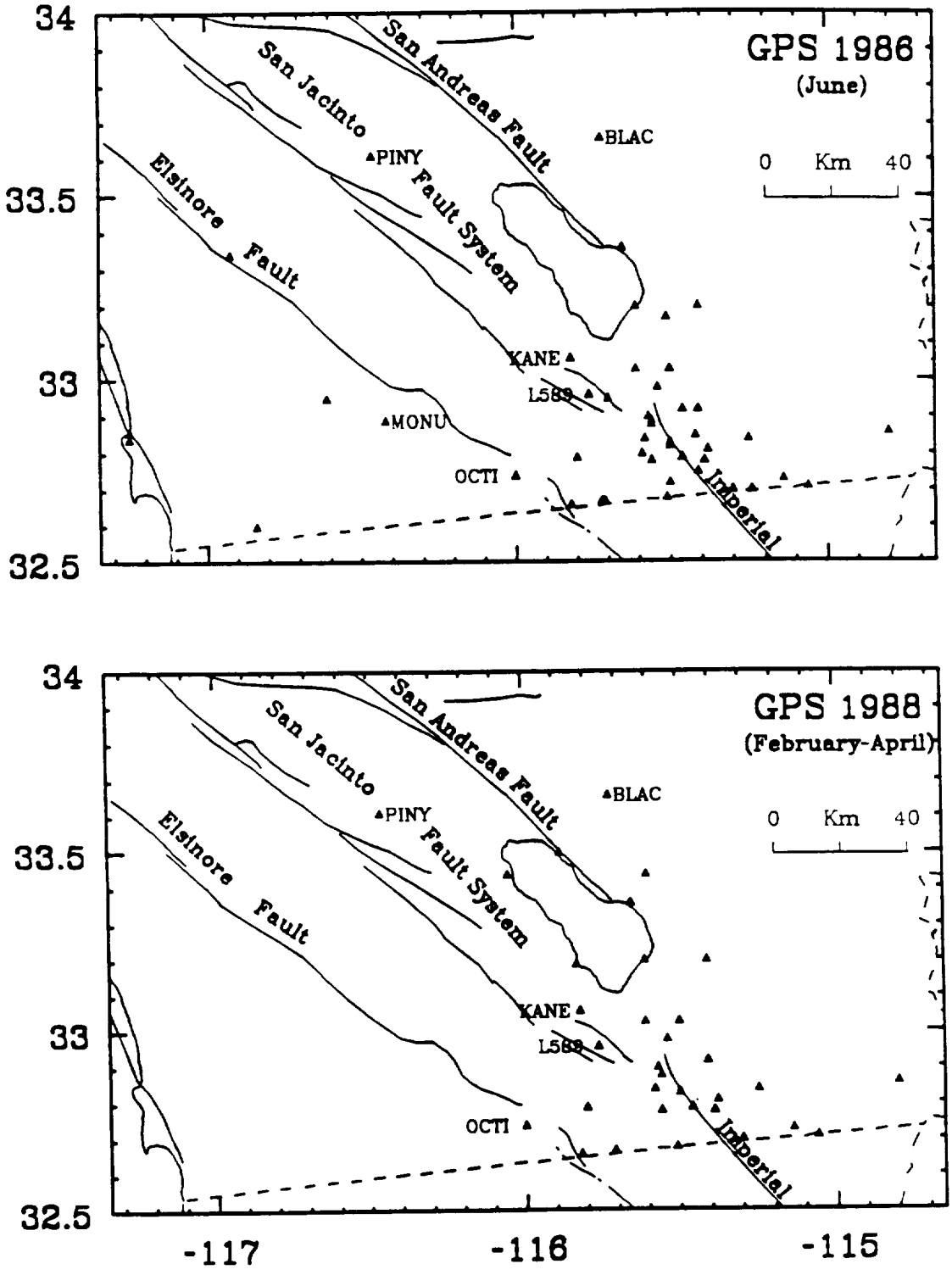
GPS 1986
(June)
0 Km 40
San Andreas Fault
San Jacinto
Fault System
Elsinore
Fault
BLAC
PINY
KANE
L588
MONU
OCTI
Imperial
34
33.5
33
32.5
GPS 1988
(February-April)
0 Km 40
San Andreas Fault
San Jacinto
Fault System
Elsinore
Fault
BLAC
PINY
KANE
L588
OCTI
Imperial
34
33.5
33
32.5
-117
-116
-115

Network (CIGNET) [*Chin*, 1987]. Since orbit improvement techniques are used, the (horizontal) precision for each survey is about $\sim$ 0.03 ppm (sub-centimeter) [e.g., *Davis et al.*, 1989; *Dong and Bock*, 1989]. The Cartesian coordinate differences from the university and NGS surveys are adjusted by least squares to obtain station positions for 1988.

During March, 1989, university groups occupied 28 geodetic marks in the vicinity of the Imperial Valley, 19 of which were previously surveyed in 1986 or 1988 (Table 5.2, Figure 5.3). Several new marks were established north of the Salton Sea in the Coachella Valley. While most data were collected with TI-4100 GPS instruments, this campaign differed from previous surveys in that Trimble-4000SD receivers were used at some sites. The field experiment was conducted at a time of anomalously high solar flare activity which created large ionospheric disturbances [*Jackson et al.*, 1989]. The ionosphere creates a frequency dependent delay for the GPS multi-signal structure, composed of two carrier phase transmissions at 1575.42 MHz (L1) and 1227.60 MHz (L2) [e.g., *King et al.*, 1985]. For dual frequency observations (L1 and L2) the ionospheric contribution (error) is removed by an appropriate combination of the two phase observables. However, if only single frequency measurements are available (either intentionally or due to poor observing conditions), the positioning accuracy on all but the shortest baselines will be seriously degraded. The 1989 phase observations contain a disproportionate number of cycle slips and data gaps, presumably due to the poor ionospheric conditions. The TI-4100 instruments generally collected both the L1 and L2 phase signals, so the ionospheric effect could be eliminated. The Trimble 4000SD receivers, however, experienced significant difficulty maintaining

Table 5.2 Imperial Valley GPS Occupation History (1989)

Day	Stations						
65	OCOT	PINY[1]	MONU	BLAC	ROBO	EXTR[1]	COAC[1]
66	OCOT	PINY[1]	MONU	BLAC	ROBO	EXTR[1]	COAC[1]
67	OCOT	PINY[1]	MONU	BLAC		VARN	SAN1[1]
68	OCOT	TRAN[1]	FRIN		COCH	VARN	SAN1[1]
69	OCOT	TRAN[1]	FRIN	DUNP	COCH	GLOC[1]	VORO[1]
70	OCOT	TRAN[1]	ALAM	DUNP	ROBO	GLOC[1]	VORO[1]
72	OCOT	KANE	ALAM	L589	TAMA[1]	GLOC[1]	
73	OCOT	KANE	O217[1]	L589	TAMA[1]		ACUT[1]
74	OCOT	BORD	O217[1]	ORIE		SIPH	ACUT[1]
75	OCOT	BORD[1]	CALI	ORIE	TAMA[1]	SIPH	
76	OCOT	JUNC	COLL[1]	HAMA[1]	TAMA[1]	SIPH	SAN1
77		JUNC	COLL	ORIE[1]	TAMA[1]	GLOC[1]	SAN1

Day is Julian day of year
[1] Trimble 4000SD

Figure 5.3: Imperial Valley GPS stations surveyed in 1989. TI-4100 GPS receivers (triangles) were used at most sites. Trimble 4000sd receivers (open circles) were also used. Thirty sites were occupied; 10 for the first time. Due to very poor ionospheric conditions, data collected with the Trimble 4000SD receivers are not discussed here.

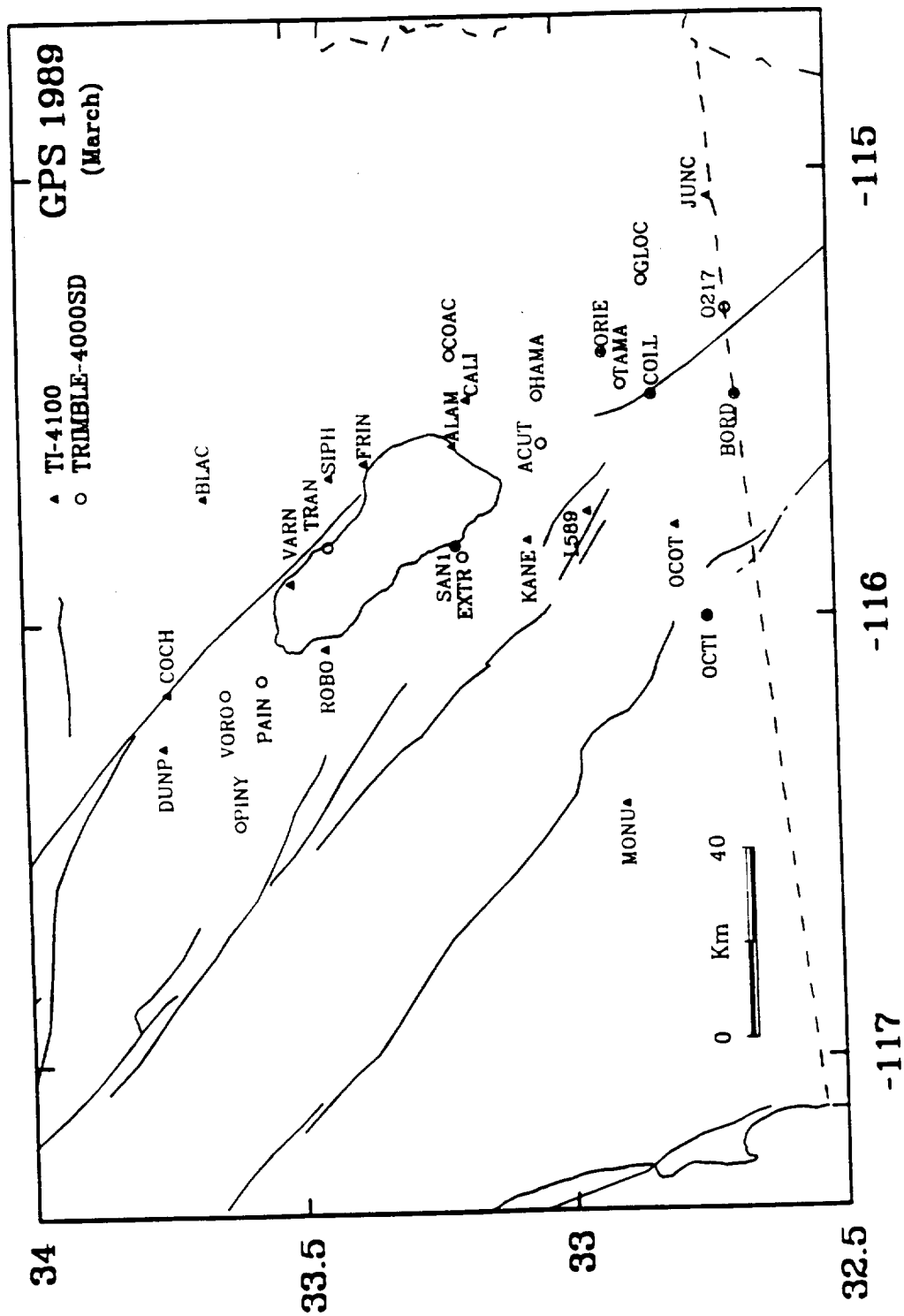
GPS 1989
(March)
TI-4100
TRIMBLE-4000SD
BLAC
COCH
DUNP
VORO
OPIN
PAIN
ROBO
VARN
TRAN
SIPH
FRIN
ALAM
COAC
CALI
SAN1
EXTR
ACUT
OHAM
KANE
1589
OCOT
OCTI
MONU
BORD
COLL
ORIE
OTAM
GLOC
0217
JUNC
0
Km
40
34
33.5
33
32.5
-115
-116
-117

phase-lock on the L2 frequency (it is found that newer Trimble models, specifically the 4000SDT, are not as susceptible to solar activity). In fact, between 30-60 percent of the L2 data (Trimble 4000SD) was lost. It is unlikely that the centimeter level accuracy required for this study could be achieved solely with the L1 frequency. Therefore, data collected with Trimble 4000SD instruments are not considered, although we are currently working on schemes to utilize these measurements through ionospheric modeling constrained by the dual frequency TI-4100 data. Continental fiducial phase observations from the CIGNET tracking sites were either nonexistent or of extremely poor quality, presumably due to the unfortunate ionospheric conditions. We were therefore not able to apply orbit improvement techniques so a multiday solution is obtained with the Bernese software utilizing the broadcast orbits. Positioning errors from the broadcast ephemerides are believed to be 0.1-1.0 ppm.

5.4 GPS Displacements

GPS vector displacements for the intervals 1986-1988 and 1988-1989 are shown in Figures 5.4 and 5.5, respectively. All measurements are made relative to station OCTI. Formal estimates of GPS uncertainty almost always underestimate variances derived from repeatability studies. We attempt to define more realistic errors by multiplying the structure of the formal covariance matrix calculated with the GPS solution by an estimated variance factor, which scales as the average baseline length. For the 1986-1988 displacements, we assume a variance factor so that the average baseline error is 5 cm, or 1 ppm for a 50 km baseline. The large uncertainty is due to

the poor quality of the 1986 data. For the 1988-1989 displacements, the average baseline error is assumed 2 cm, or 0.4 ppm for a 50 km baseline. The largest component of uncertainty is attributed to the broadcast orbits used for the 1989 solution. *Larsen et al.* [1990] found 1-3 cm discrepancies between broadcast and improved-orbit solutions in a similar sized network spanning the Santa Barbara channel. This approach, albeit somewhat ad hoc, allows for self consistent relative errors and it illustrates the much larger uncertainties in the east-west direction ($\sim$ 4 times larger than the north-south uncertainties). This distortion is primarily due to the north-south ground track of the satellite orbits, which significantly improves solution constraint along this orientation.

Displacements for the 1986-1988 interval (Figure 5.4) are complicated by the 1987 Superstition Hills earthquake sequence, as well as large measurement uncertainties. Effects of the earthquake sequence are clearly demonstrated in the GPS vectors; displacements at KANE and L589 approach 0.5 meters. Estimates of fault rupture suggest 10 stations near the seismic rupture zone moved at least 5 cm [*Larsen et al.*, 1990]. The displacements are consistent with right-lateral slip along the Superstition Hills fault and left-lateral slip along the Elmore Ranch fault. Still, there is a considerable component of southeast trending movement which can not be explained as seismic deformation or measurement uncertainty. The relative displacement between stations on opposite sides of the valley averages 5-6 cm/yr. We take this motion to represent continuous strain accumulation due to plate motion.

The 1988-1989 station displacements clearly demonstrate the right-lateral southeast trending movement across the GPS network. Stations furthest to

Figure 5.4: GPS station displacements for the interval 1986-1988 (1.8 years). All measurements are made relative to station OCTI. Errors are determined by multiplying the formal uncertainties from the GPS solution by a variance factor so that the average baseline error scales as 1 ppm. The east-west uncertainties are about 4 times larger then the north-south. Seismically induced displacements from the 1987 Superstition Hills earthquake sequence are most apparent at stations KANE and L589. The large non-seismic displacements are assumed to represent relative motion between the Pacific and North American plates, which is concentrated across the valley.

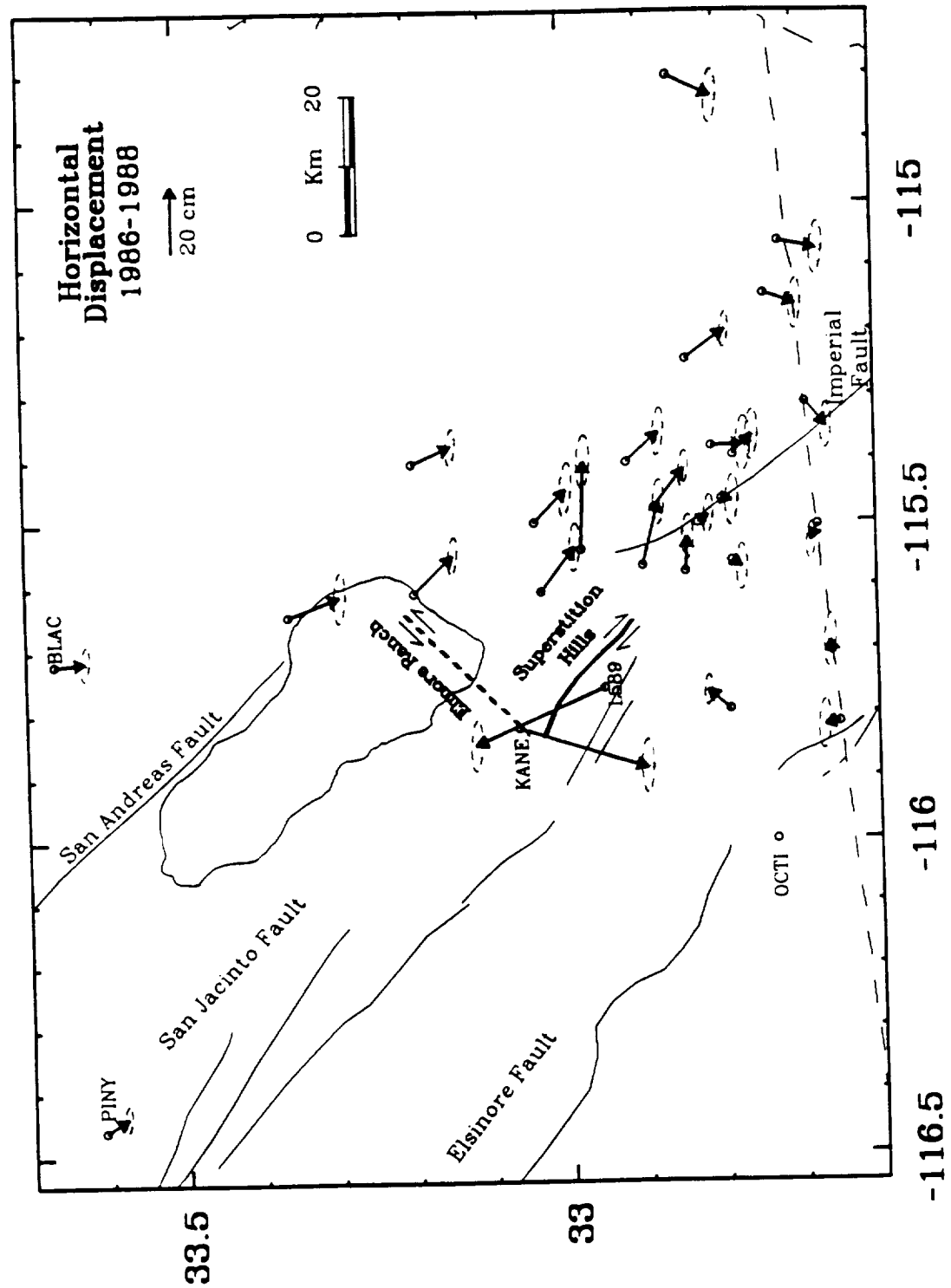
Horizontal
Displacement
1986-1988
20 cm
0 Km 20
PBLAC
PINY
OCTI
KANE
San Andreas Fault
San Jacinto Fault
Elsinore Fault
Superstition
Hills
Imperial
Fault
33.5
33
-116.5
-116
-115.5
-115

Figure 5.5: GPS station displacements for the interval 1988-1989 (1.0 years). All measurements are made relative to station OCTI. Errors are determined by multiplying the formal uncertainties from the GPS solution by a variance factor so that the average baseline error scales as 0.5 ppm. Stations to the northeast moved about 5 cm southwest relative to stations on the other side of the valley.

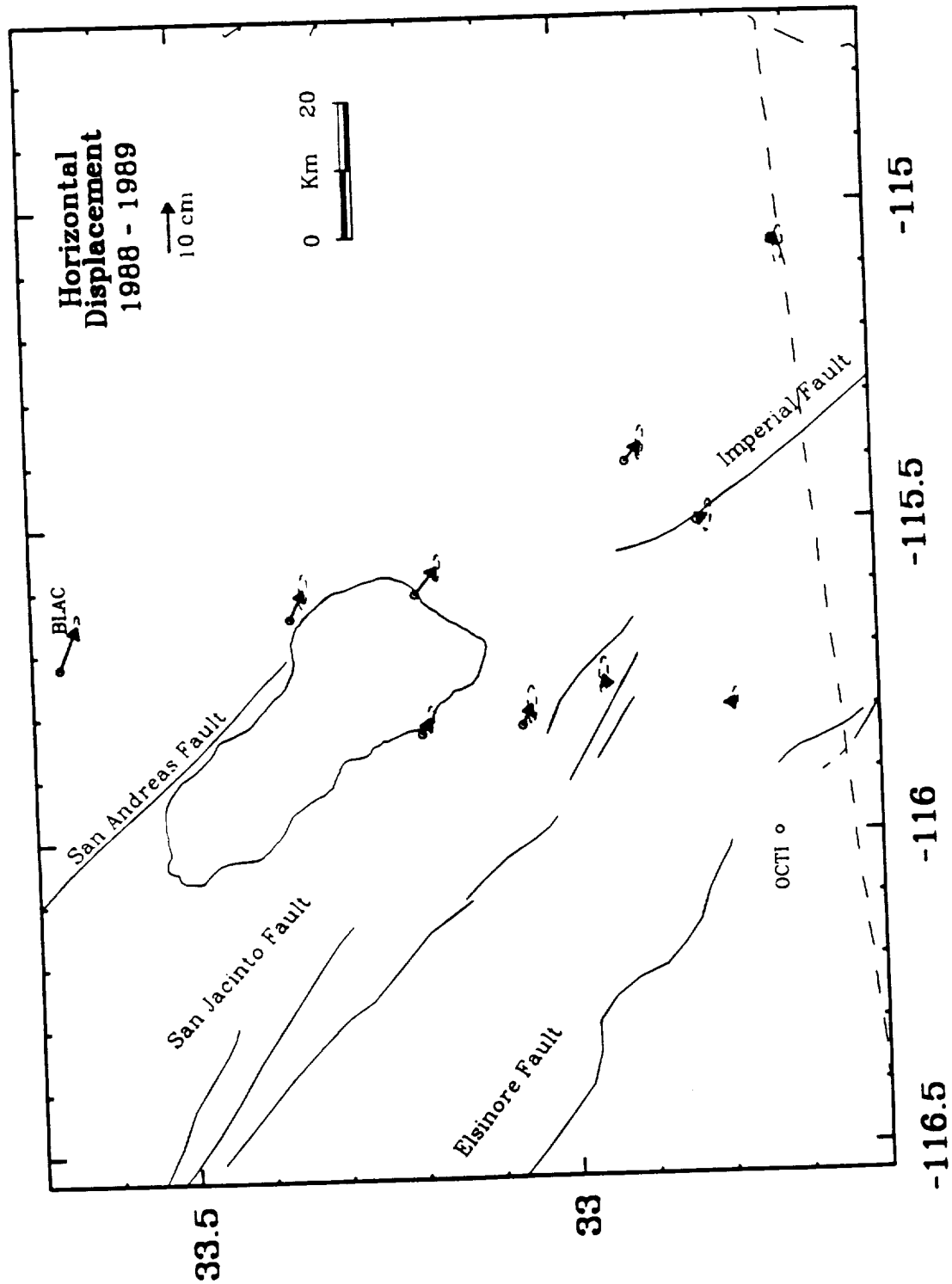
Horizontal
Displacement
1988 - 1989
10 cm
0 Km 20
BLAC
San Andreas Fault
San Jacinto Fault
Elsinore Fault
Imperial Fault
OCTI
33.5
33
-116.5
-116
-115.5
-115

the northeast are displaced approximately 5 cm to the southeast relative to sites on the other side of the valley, although some of the observed motion (e.g., BLAC) may be distortion from the larger east-west uncertainties. In addition, Figure 5.5 demonstrates how easily GPS can monitor tectonic deformation even over time scales as short as 1 year.

The 1986-1988 and 1988-1989 displacements are decomposed into their north-south and east-west components, corresponding to the directions of minimum and maximum error, respectively (Figure 5.6 and 5.7). Each component is plotted as the distance from OCTI on a cross section trending N50°E, perpendicular to the predicted plate motion orientation (N40°W) (Figure 5.8). Simple dislocation theory [e.g., *Mansinha and Smylie*, 1971] is used to remove the effect of the 1987 Superstition Hills earthquake sequence from the observed 1986-1988 displacement field, following fault models suggested by *Larsen et al.* [1990] (approximately 109 cm right-lateral slip on the Superstition Hills fault and 45 cm left-lateral slip on the Elmore Ranch fault).

Decomposing the vector displacements into geographic components tends to separate the uncertainties which are magnified along the longitudinal direction. The north-south movements clearly exhibit right-lateral displacement for both intervals; stations to the northeast display southerly offsets relative to sites on the other side of the valley. The magnitude of the displacement is roughly proportional to the time interval spanned by the measurements, suggesting continuous strain accumulation. Stations which display the largest scatter in Figure 5.6 are for the most part those sites where the applied seismic correction is greater than 4 cm (open circles). This may

indicate additional fault complexity not accounted for by the dislocation model used to remove the effects of the 1987 earthquake.

The east-west movements for the 1986-1988 interval exhibit large scatter with no discernible trend across the valley. This is invariant of the seismic correction, so the scatter is not explained simply as unmodeled effects from the Superstition Hills earthquakes. Presumably, the large deviations are due to fairly significant east-west oriented errors from the 1986 survey. This may explain the anomalous vector displacements observed in Figure 5.4, especially noticeable for those sites near the border east of the Imperial fault. On the other hand, the 1988-1989 displacements clearly show large east directed movements for stations furthest to the northeast, consistent with southeast trending deformation across the valley.

5.5 Discussion

Deformation across valley

The 1986-1988 measurements are concentrated along the Imperial fault (Figure 5.4). The nonseismic displacements reveal a sharp boundary 15-20 km wide between deformation on either side of the valley (Figure 5.6). This suggests that in the southern half of the Imperial Valley strain is being accommodated exclusively along the Imperial fault. The 1988-1989 measurements are distributed more uniformly throughout the region (Figure 5.5), and indicate a broader strain-transition zone (Figure 5.7). This implies that deformation may be occurring along several structures to the north, including the San Andreas, San Jacinto, and Elsinore faults. The same

Figure 5.6: The north-south and east-west displacement components for the 1986-1988 interval. All distances are relative to OCTI on a cross section trending N50°E, perpendicular to the plate motion (see Figure 5.8). The effect of the 1987 Superstition Hills earthquake sequence is removed. Open circles indicate stations where the seismic correction is greater than 4 cm. The north-south offset between stations on opposite sides of the valley is 8.1 cm. The large scatter for the east-west components are presumably due to errors in the 1986 survey. The average uncertainty for each displacement component is shown.

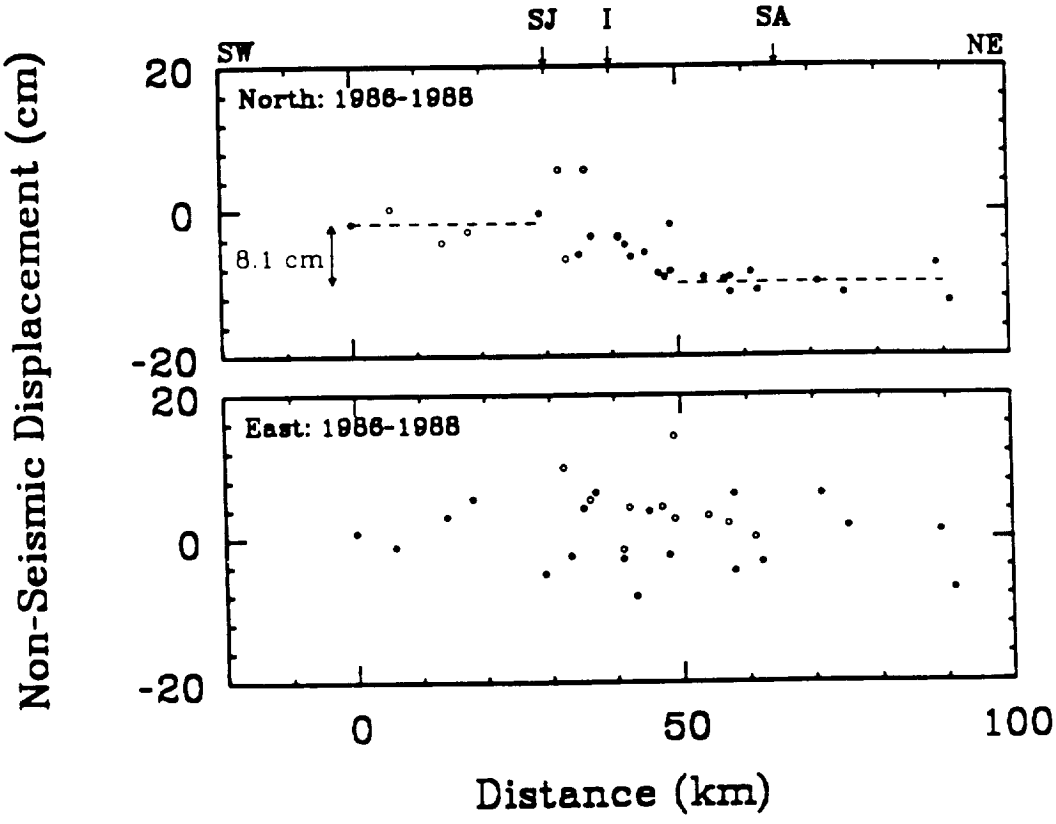
SJ
I
SA
SW
NE
North: 1986-1988
8.1 cm
East: 1986-1988
20
0
-20
20
0
-20
0
50
100
Non-Seismic Displacement (cm)
Distance (km)

Figure 5.7: The north-south and east-west displacement components for the 1988-1989 interval. All distances are relative to OCTI on a cross section trending N50°E, perpendicular to the plate motion direction. The data are best-fit by 5.2 cm/yr displacement across the valley (solid line), although a rate of 3.4 cm/yr fit the data nearly as well (dashed line). The average uncertainty for each displacement component is shown.

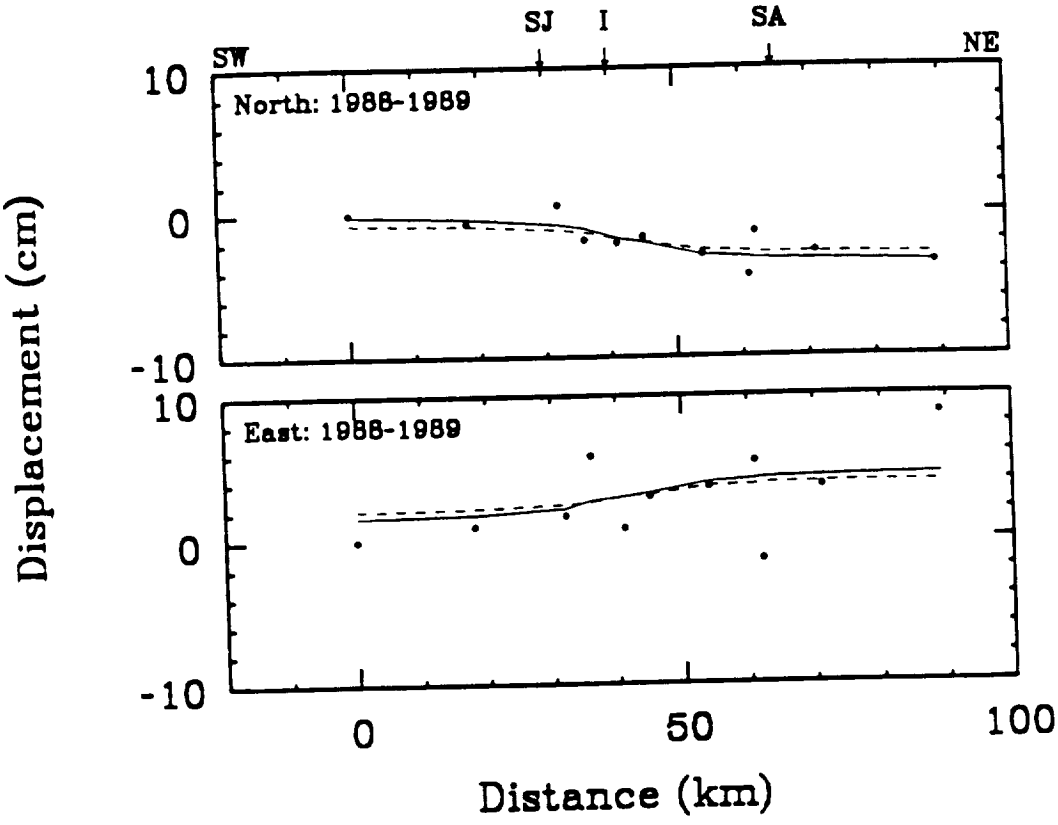
SJ
I
SA
SW
NE
10
North: 1988-1989
0
-10
10
East: 1988-1989
0
-10
0
50
100
Displacement (cm)
Distance (km)

Figure 5.8: Shear plane (10 km depth) used to model the 1988-1989 displacements (shaded band); cross section used in Figures 5.6 and 5.7; and stations surveyed at least twice between 1986 and 1989. Considerable strain is observed across the GPS network, which is attributed to plate-boundary deformation between the North American and Pacific plates.

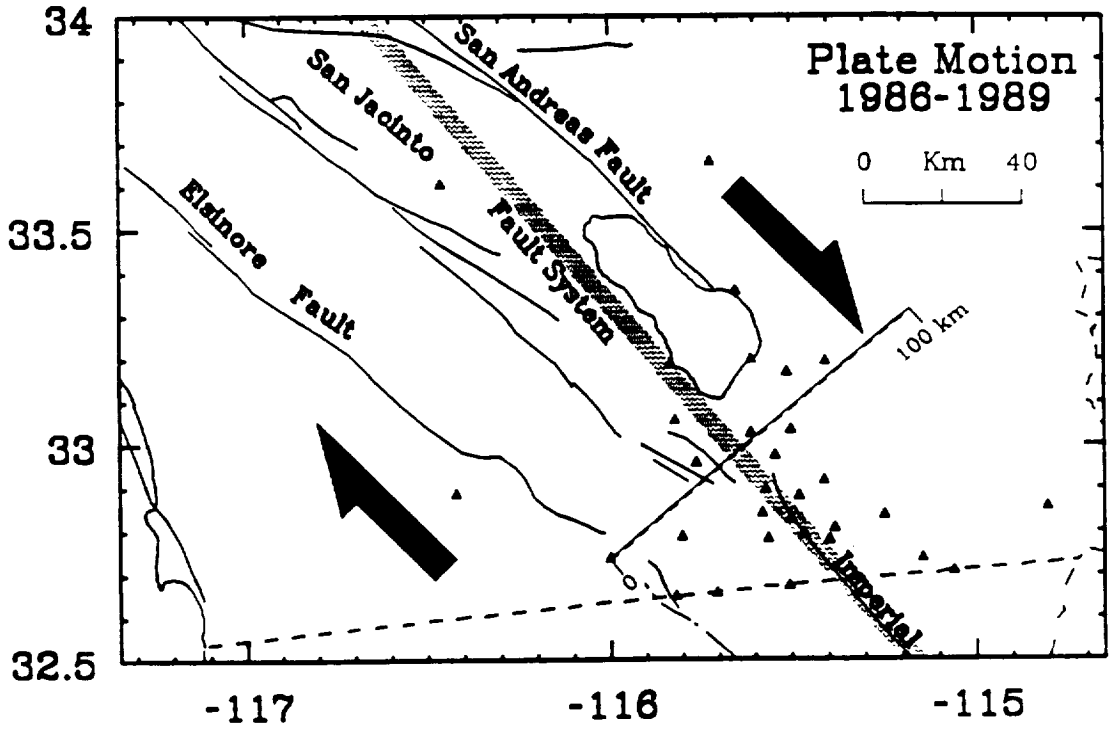
Plate Motion
1986-1989
0 Km 40
San Andreas Fault
San Jacinto
Fault System
Elsinore
Fault
100 km
Imperial
34
33.5
33
32.5
-117
-116
-115

pattern is observed in the conventional geodetic measurements, which indicate concentrated strain in a narrow 20 km wide zone about the Imperial fault, and diffuse deformation of at least 50 km wide to the north [*Snay and Drew*, 1988; *Prescott et al.*, 1987b].

The 1986-1988 displacements (Figure 5.4) have been modeled by *Larsen et al.* [1990]. The station movements are consistent with right-lateral slip along the Superstition Hills fault and left-lateral offset along the Elmore ranch fault. The nonseismic residuals indicate remaining deformation across the valley, evidenced by the 8.1 $\pm$ 1.3 cm offset in the north-south displacement component (Figure 5.6). The differential movement is calculated by linearly fitting those data furthest to the southwest and northeast. The data errors are increased by 0.33 times the estimated seismic displacements, giving less weight to those stations most affected by the 1987 earthquakes. The east-west components are not used due of the large data scatter. The observed movement is taken to represent plate-boundary deformation due to the relative motion between the North American and Pacific plates. The calculated north-south differential displacement averaged over the 1.8 year observation interval, is equivalent to 5.9 $\pm$ 1.0 cm/yr right-lateral movement oriented N40°W, assuming a uniform velocity field parallel to the direction of plate motion. Conventional geodetic data are consistent with the assumed orientation [*Prescott et al.*, 1987a; *Snay et al.*, 1988].

The differential movement across the Imperial Valley is clearly visible in the 1988-1989 displacements (Figure 5.5 and 5.7), and is observed in both the north-south *and* east-west components. The movement is smaller than the earlier interval because of the shorter observation period (1.0 years).

However, the most recent measurements are not influenced by seismic activity and contain smaller experimental error. Since the 1988-1989 station displacements are more uniformly distributed across the valley, it is difficult to constrain an absolute differential offset. Instead, the measurements are modeled assuming a semi-infinite right-lateral shear plane at depth representing the Pacific-North American plate margin (Figure 5.8). The plane is oriented N40°W about coordinates 32.796°N, 115.454°W, almost congruent with the Imperial fault and the axis of the valley. The upper depth is constrained at 10 km and uniform slip is assumed over the entire shear boundary. *Snay and Drew* [1988] incorporate a similar model to explain triangulation observations from 1941 to 1986, but allow additional slip along the Imperial fault necessitated by the detailed station coverage in this region. More complex models assuming distributed offset along the Imperial, San Andreas, San Jacinto, and Elsinore faults, and within the Brawley Seismic Zone have been used to explain other geodetic measurements in the valley [e.g., *Savage et al.*, 1979]. The measurements presented here are not of sufficient resolution or accuracy (due to the short time coverage) to warrant such detail. The 1988-1989 GPS displacement vectors are best constrained by 5.2 $\pm$ 0.9 cm/yr plate-boundary deformation. The best-fit solution to the observed GPS movements is shown in Figure 5.7. Additional solutions are obtained by varying the depth to the upper boundary of the shear plane from 5 to 15 km. The calculated displacement rates range from 4.4 (5 km) to 6.0 cm/yr (15 km), while the minimum residual solution is obtained at 10 km depth (5.2 cm/yr).

Because the 1988-1989 displacements are not affected by seismic

deformation, we speculate this interval yields a more reliable GPS estimate of strain across the Imperial Valley. The GPS rates, as well as those derived through conventional geodetic techniques, are listed in Table 5.3. These are compared with the predicted relative velocity between the Pacific and North American plates (NUVEL-1), and rates derived from VLBI measurements between stations along the western coast of California and the stable North American continent. The 1988-1989 GPS rate is comparable to the plate velocity estimates, while the earlier GPS interval is somewhat higher. This suggests that all plate motion is concentrated across the valley, with little or no deformation west of the Elsinore fault. Conventional measurements taken over the last 50 years indicate significantly smaller rates (3.4-4.3 cm/yr), and thus require additional slip on faults not spanned by the networks to satisfy the plate velocity. GPS and trilateration (EDM) provide comparable accuracies, and both are considerably more precise than triangulation (although GPS yields 3-dimensional positions whereas the conventional methods do not). Since the EDM observations span a 15 year period compared to the 3 year GPS coverage, the trilateration rate should more accurately reflect the deformation across the valley, which suggests the GPS measurements over-estimate the true displacement. In fact, a 3.4 cm/yr deformation rate fits the 1988-1989 observations nearly as well (Figure 5.7). An alternate explanation is accelerated deformation between 1986 and 1989. The triangulation data indicate highly time-dependent displacements. Between 1941 and 1954 the calculated rate is significantly greater than the average between 1941 and 1986, although this is attributed to post-seismic effects following the 1940 Imperial Valley earthquake. No increased rate is observed following the 1979 earthquake [*Savage et al.*, 1986]. There is

Table 5.3 Displacement Rates

Method	Region	Interval	Rate (cm/yr)	Reference
GPS	Imperial Valley	1986-1988	4.8	This Study
		1988-1989	5.2	
Triangulation	Imperial Valley	1941-1986	4.3	*Snay and Drew* [1988]
		1941-1954	6.1	
		1954-1967	2.1	
		1967-1986	4.5	
Trilateration	Imperial Valley	1972-1987	3.4	*Prescott et al.* [1987b]
Plate Model	Plate boundary	$\sim$ 3 m.y.	4.7	*DeMets et al.* [1990]
VLBI	Continental	1979-1987	4.8-5.1	*Clark et al.* [1987]
				Kroger et al. [1987]

marginal evidence for a regional strain fluctuation (increase) during 1978 and 1979 throughout southern California, but the nature of this apparent deformation is uncertain [*Savage et al.*, 1981; *Savage et al.*, 1986]. Given the large uncertainties for the GPS estimates ($\sim$ 1 cm), it is not possible with the available data to distinguish if there has been increased deformation over the last several years.

Imperial and southern San Andreas fault earthquake potential

The earthquake recurrence interval along the Imperial fault is estimated using the geodetically determined strain rates. The 1940 Imperial Valley earthquake ruptured the entire length of the Imperial fault. Approximately 3.0 and 4.5 m slip (coseismic plus postseismic) are estimated for the northern and southern segments of the fault, respectively [*Reilinger*, 1984]. Surface offsets were as great as 6 m south of the border with displacements tapering off rapidly to the north [*Trifunac and Brune*, 1970; *Sharp*, 1982]. Surface rupture was confined to the fault north of the border during the 1979 earthquake. Geodetic and strong ground motion modeling suggest an average slip of about 1 m along the 1979 rupture plane, with patches of higher displacement (asperities) [e.g., *Hartzell and Heaton*, 1983; *Archuleta*, 1984; *Reilinger and Larsen*, 1986]

Triangulation measurements along the Imperial fault and north of the U.S.-Mexico border indicate concentrated deformation in a narrow 20 km wide zone. At an observed strain rate of 4-5 cm/yr and per event ruptures between 1 and 3 m, a 20-75 year earthquake recurrence interval is calculated for the northern Imperial fault. This assumes total strain release during seismic

episodes. The estimated recurrence rate is comparable to the 32 year earthquake repeat time suggested by *Sykes and Nishenko* [1984] and the $\sim$ 50 year interval predicted by *Anderson and Bodin* [1987].

Conventional geodetic data north of the Imperial fault indicate distributed deformation over a fairly wide region ($\geq$ 50 km wide) [*Snay and Drew*, 1988]. Presumably the strain that occurs almost exclusively along the Imperial fault in the south is transferred by some mechanism to the San Andreas, San Jacinto, and Elsinore faults. The slip distribution across each fault segment is important from an earthquake hazard standpoint.

Three Imperial Valley GPS sites have well determined VLBI solutions (Very Long Baseline Interferometry) from observations since 1979 [*Clark et al.*, 1987; *Sauber et al.*, 1989; *Ma et al.*, 1989]. Relative velocities of BLAC-PINY and BLAC-MONU for the GPS and VLBI analyses are listed in Table 5.4 and illustrated in Figure 5.9. The VLBI velocities vary depending on the continental or global nature of each solution and the extent of data availability. Only the north-south GPS displacements are considered because of the large east-west errors inherent in the 1986 survey. The fault parallel velocities are right-lateral assuming relative motions are oriented N40°W. The calculated effect from the 1987 Superstition Hills earthquake sequence is removed from the GPS data. The VLBI measurements indicate 1.5 to 2.1 cm/yr fault-parallel (right-lateral) displacement across the San Andreas fault (BLAC-PINY) and 3.0 to 3.5 cm/yr across the valley (BLAC-MONU). The GPS measurements suggest 1.4 cm/yr displacement across the fault and 3.2 cm/yr across the valley (Table 5.3 rates are different since they represent averages over the entire network). While the BLAC-MONU velocities roughly

Table 5.4 Displacement Rates Across San Andreas Fault

Baseline	Method	Interval	North (cm/yr)	East (cm/yr)	Fault Parallel (cm/yr)
BLAC-PINY	VLBI[1]	1982-1987	1.8	-1.1	2.1
	VLBI[2]	1979-1988	1.5	-1.0	1.8
	VLBI[3]	1982-1988	1.2	-0.9	1.5
	GPS	1986-1988	1.1		1.4
BLAC-MONU	VLBI[1]	1982-1987	2.3	-2.7	3.2
	VLBI[2]	1979-1988	2.5	-2.5	3.5
	VLBI[3]	1982-1988	2.4	-1.8	3.0
	GPS	1986-1989	2.5		3.2

[1] *Clark et al.* [1987]
[2] *Ma* [1988]
[3] *Sauber* [1989]

agree with the conventional geodetic measurements (3.4-4.3 cm/yr), the fault-crossing displacements are somewhat surprising as they are lower than geologic evidence. The long-term geomorphological slip rate along the southern San Andreas fault over the last 10,000-30,000 years is estimated between 2.3 and 3.5 cm/yr [*Keller et al.*, 1982; *Weldon and Sieh*, 1985], with 2.5 cm/yr a commonly accepted average [e.g., *Sieh and Williams*, 1990]. The geologic slip rate and radiocarbon dating of Holocene offsets along the fault suggest a recurrence interval of about 300 years with the last major event in 1680 [*Sieh*, 1986]. This logic leads to the conclusion that the potential for a major earthquake along the southern San Andreas is high. However, the geodetic evidence reported here indicates a smaller strain accumulation rate during the last decade, suggesting decreased earthquake potential assuming these measurements are indicative of the last few hundred years. This will be observed either as a longer recurrence interval or less slip per event. The geodetic data are supported by geologic trenching studies which suggest a decreasing southern San Andreas slip rate during the past 1000 years *Sieh* [1986]. If this is true, the San Jacinto fault should play a more active role in regional tectonics. In fact, the shear strain along the fault determined from EDM observations between 1973 and 1984 is nearly the same as that for networks which lie on the San Andreas fault *Savage et al.* [1986]. The two fault systems may alternately assume dominant roles in absorbing plate motions, as is suggested by variable Quaternary slip rates along the San Jacinto fault [*Sharp*, 1981].

Future analyses

The 1986, 1988, and 1989 Imperial Valley GPS observations are not

Figure 5.9: VLBI (solid arrows) and GPS (dashed arrows) velocities at stations PINY and MONU relative to station BLAC (Table 5.4). The GPS vectors contain large uncertainty in the east-west direction. The fault-parallel geodetic velocities across the San Andreas fault are less than geologic estimates.

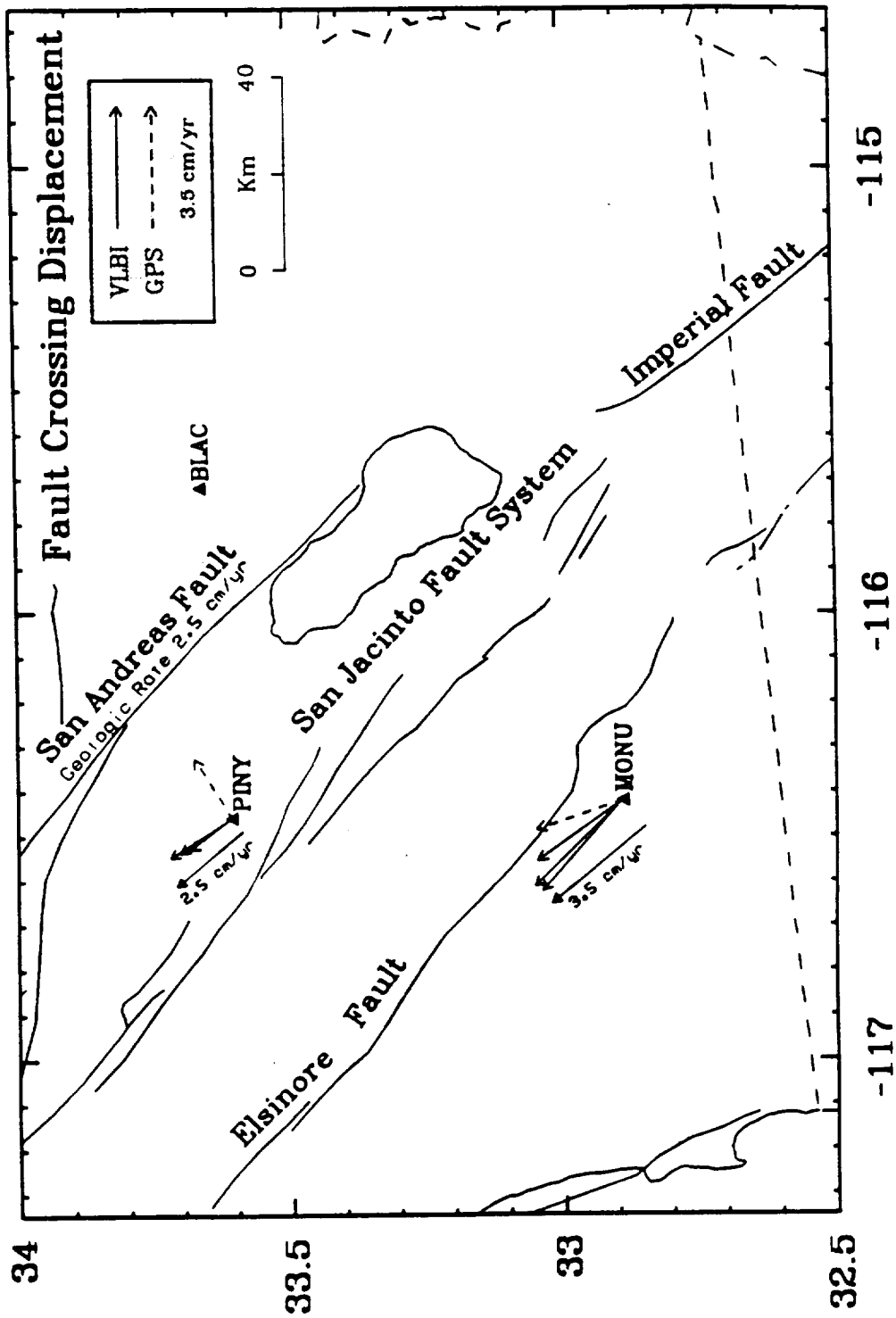
Fault Crossing Displacement
VLBI
GPS
3.5 cm/yr
0
Km
40
BLAC
San Andreas Fault
Geologic Rate 2.5 cm/yr
San Jacinto Fault System
Imperial Fault
Elsinore Fault
PINY
2.5 cm/yr
MONU
3.5 cm/yr
34
33.5
33
32.5
-115
-116
-117

sufficiently resolved to accurately map details of the strain distribution in this portion of southern California. This is due to poor data quality from the 1986 measurements, complications due to the 1987 Superstition Hills earthquake sequence, the inability to incorporate L2 phase data from several sites during 1989, and the short interval spanned by the observations (1 year of nonseismic displacement). However, additional GPS data have been collected in southern California in March/April 1988 and again in February/March 1990 (Figure 5.10). The 1988 measurements were made in conjunction with the Riverside County (California) Flood Control District and the Riverside County Survey Department. In a network of 62 stations spanning an entire cross section of southern California, a maximum of 8 TI-4100 GPS receivers were deployed each day over the two week survey. The daily observation period was about 4.5 hours. Although the instruments collected data every 3 seconds, during the download from receiver to floppy disk only every 10th measurement was recorded (30 second epochs). Unfortunately, the receivers were not synchronized and the recorded time-tags were randomly distributed at 30-second intervals. These data have been subsequently processed with the Bernese software. The day to day baseline repeatability on the 18 lines with multiple observations is 1.1 cm, suggesting that the receiver time-tag offsets are not a serious source of solution error considering the 3 to 5 cm tectonic movements expected in southern California.

During 1990, a high precision GPS network was established along a 400 km segment of the Pacific-North American plate-boundary from the Gulf of California in northern Mexico to just south of the junction of the San Andreas and San Jacinto faults ($\sim 34^\circ$N) [*Reilinger et al.*, 1990]. Twenty-

three receivers were used for approximately two weeks including the TI-4100, Trimble 4000SD, and Trimble 4000SDT models. A total of 134 stations were occupied during the campaign. Data collection at 103 sites lasted 6 to 7 hours each day, while the daily observation interval at 31 stations was 3 to 4 hours (half-sessions). The following month (April 1990), 3 additional monuments near Upland, California, were established and surveyed by the Riverside County Flood Control District in support of university research associated with the February 28 (1990) M_L 5.5 Upland earthquake. The 1990 observations are in the process of being analyzed, although obtaining geodetic coordinates for the entire survey will be time consuming due to the enormity of the data set and the uncertainty in correlating GPS measurements from different receivers.

The 1986-1990 GPS occupation summary for the Imperial Valley, Riverside County, and Baja California is listed in Table 5.5. A total of 183 stations have been occupied at least once (Figure 5.10), and of these 85 have been occupied at least twice with most dating back to 1986 or 1988. The station coverage does not include kinematic GPS measurements made on relatively short transects (few kilometer) crossing the southern San Andreas fault [K. Hudnut, personal communication, 1990]. In addition to the dense distribution within the Imperial Valley and Baja California, the established network north of the Salton Sea provides station coverage extending from the California-Arizona border to near the Pacific Ocean. This network will be used to constrain the slip distribution along the major fault systems in southern California. When combined with geologic data of fault activity, the strain estimates will better define the earthquake potential in this region. The

Figure 5.10: GPS stations occupied from 1986 to 1990 in Riverside County, the Imperial Valley, and northern Baja California. Triangles inside circles indicate stations with multiple occupations. The network is composed of 183 stations, of which 85 have repeated observations.

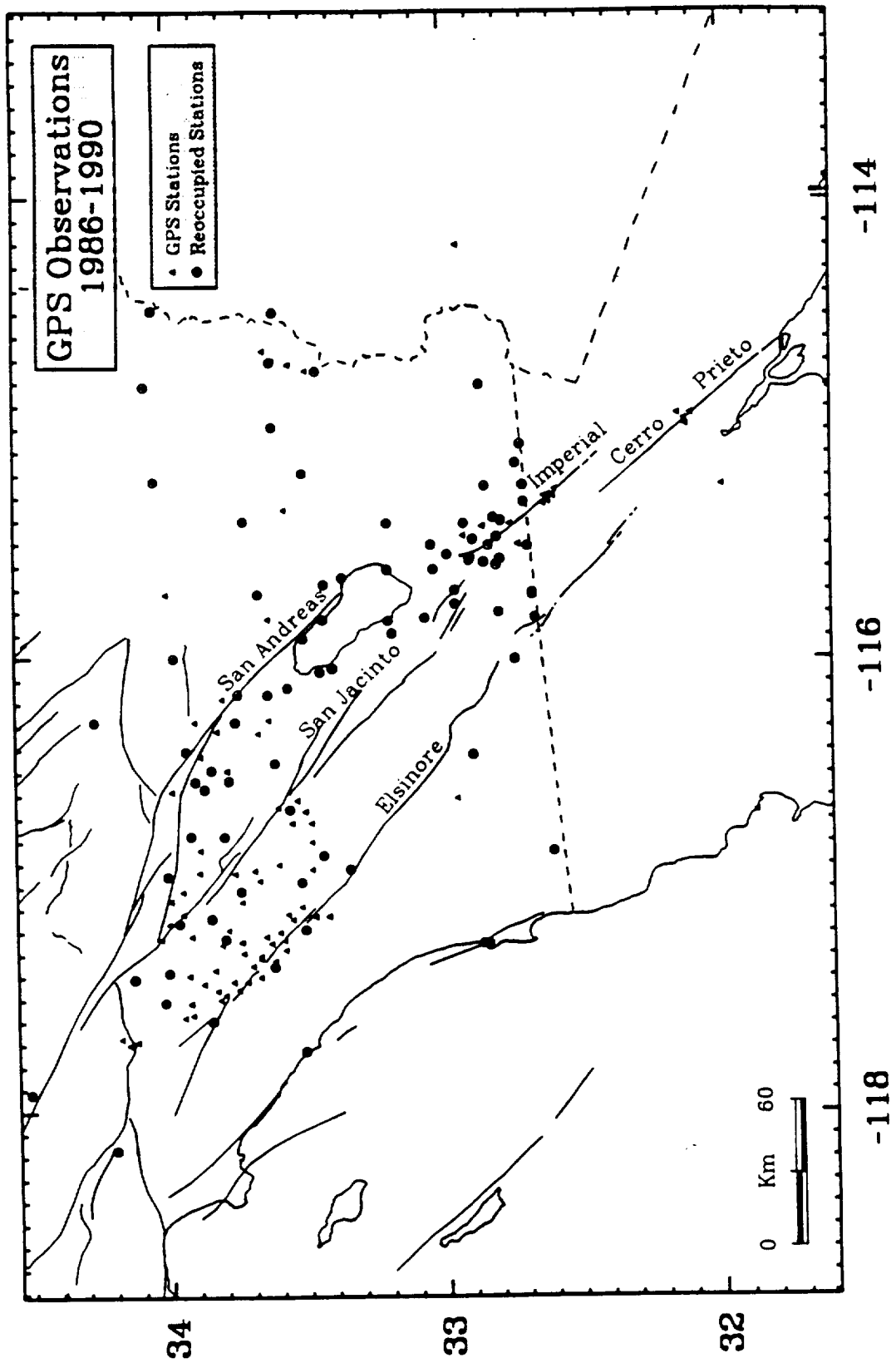
GPS Observations
1986-1990
GPS Stations
Reoccupied Stations
San Andreas
San Jacinto
Elsinore
Imperial
Cerro Prieto
0 Km 60
34
33
32
-114
-116
-118

Table 5.5 GPS Campaign Summary

Year	Stations	Region	Organization
1986	42	Imperial Valley	NGS
1988	15	Imperial Valley	UNAVCO
1988	62	Riverside County	RCFC/RCSD
1988	21	Imperial Valley	NGS
1989	28	Imperial Valley	UNAVCO
1990	134	Imperial Valley/Riverside County	UNAVCO/RCFC/RCSD/NGS

NGS - National Geodetic Survey
UNAVCO - University Navstar Consortium
RCFC - Riverside County Flood Control
RCSD - Riverside County Survey District

best GPS estimate of secular strain to date is provided by the 11 displacement vectors obtain from the 1988 and 1989 surveys. Once the 1990 data are fully analyzed, the increased station density (85 stations) and longer measurement interval (at least 2 years) will yield an order of magnitude increase in deformation extent and resolution. It should be possible to assess the present-day strain accumulation rates on the major fault systems in southern California to within a few millimeters per year. The network also provides good coverage along the southern San Andreas fault, which will be used to constrain fault rupture parameters in the likely event of a large earthquake within the next several decades [*Larsen*, 1990].

5.6 Conclusions

GPS measurements from southern California indicate 5.9 $\pm$ 1.0 and 5.2 $\pm$ 0.9 cm/yr right-lateral southeast trending displacement across the Imperial Valley for the intervals 1986-1988 and 1988-1989, respectively. These rates are significantly larger than those obtained from conventional geodetic surveys (3.4-4.3 cm/yr), suggesting the GPS observations may overestimate the true deformation. The earlier measurements contain relatively large errors, and are influenced by the 1987 Superstition Hills earthquake sequence. The 1988-1989 data are modeled nearly as well by 3.4 cm/yr of valley crossing movement. Regardless, a significant secular deformation component is clearly observed in the GPS displacements, which is attributed to the relative movement between the Pacific and North American plates. There is evidence from VLBI and GPS measurements that the strain accumulation rate along the southern-most San Andreas fault is smaller than the calculated long-term

geologic estimate. This indicates a lower earthquake potential for this segment of the fault than is presently assumed, and suggests that the San Jacinto system plays a more dominant role for relieving the strain accumulation in this region. The measurements discussed here are part of a larger 183 station GPS network which spans an entire cross section of southern California. A total of 134 stations were observed during a recent 1990 campaign; many of these sites were previously occupied in 1986 and/or 1988. An order of magnitude increase in resolution and detail regarding the strain accumulation rates along the San Andreas, San Jacinto, and Elsinore faults is expected once the 1990 GPS data are integrated with the previous surveys.

Acknowledgements

This research is a collaborative effort conducted jointly with Robert Reilinger at MIT. Helen Neugebauer and Bill Strange provided coordinate solutions from the 1986 NGS GPS survey. This research could not have taken place without the invaluable field support provided by many people. I thank my advisor Hiroo Kanamori for his support. This work is supported by U.S. Geological Survey contracts 14-08-0001-61679 (MIT) and 14-08-001-61354 (Caltech), and by NASA grant NAG-5-814 (MIT).

References

Anderson, J. G., and P. Bodin, Earthquake recurrence models and historical seismicity in the Mexicali-Imperial Valley, *Bull. Seismol. Soc. Am.*, *77*, 562-578, 1987.

Archuleta, R. J., A faulting model for the 1979 Imperial Valley earthquake, *J. Geophys. Res.*, *89*, 4559-4585, 1984.

Chin, M., CIGNET report, *GPS Bull.*, Global Positioning System Subcomm. of Comm. VIII, Int. Coord. of Space Tech. for Geod. and Geodyn., Natl. Geod. Surv., Rockville, Md., 1988.

Clark, T. A., D. Gordon, W. E. Himwich, C. Ma, A. Mallama, and J. W. Ryan, Determination of relative site motions in the western United States using Mark III very long baseline interferometry, *J. Geophys. Res.*, *92*, 12,741-12,750, 1987.

Davis, J. L., W. H. Prescott, J. L. Svarc, and K. J. Wendt, Assessment of global positioning system measurements for studies of crustal deformation, *J. Geophys. Res.*, *94*, 13,635-13,650, 1989.

DeMets, C., R. G. Gordon, S. Stein, and D. F. Argus, A revised estimate of Pacific-North America motion and implications for western North America plate boundary zone tectonics, *Geophys. Res. Letts.*, *14*, 911-914, 1987.

DeMets, C., R. G. Gordon, D. F. Argus, and S. Stein, Current plate motions, *Geophys. J. Inter.*, *101*, 425-478, 1990.

Dong, D., and Y. Bock, Global Positioning System network analysis with phase ambiguity resolution applied to crustal deformation studies in California, *J. Geophys. Res.*, *94*, 3949-3966, 1989.

Drew, A. R., and R. A. Snay, DYNAP: software for estimating crustal deformation from geodetic data, *Tectonophysics*, *162*, 331-343, 1989.

Elders, W. A., R. W. Rex, T. Meidav, P. T. Robinson, and S. Biehler, Crustal spreading in southern California, *Science*, *178*, 15-24, 1972.

Fuis, G. S., W. D. Mooney, J. H. Healey, G. A. McMechan, and W. J. Lutter, Crustal structure of the Imperial Valley region, *U.S. Geol. Surv. Prof. Pap.*, *1254*, 25-50, 1982.

Hartzell, S. H., and T. H. Heaton, Inversion of strong ground motion and teleseismic waveform data for the fault rupture history of the 1979 Imperial Valley, California, earthquake, *Bull. Seis. Soc. Am.*, *73*, 1553-1583, 1983.

Jackson, M., R. Reilinger, M. Bevis, B. Perin, C. Rocken, B. Stephens, and J. Stowell, Impact of ionospheric effects on GPS campaigns in southern California and the South Pacific, *EOS Trans.*, *70*, p. 1049, 1989.

Johnson, C. E., and D. P. Hill, Seismicity of the Imperial Valley, *U.S. Geol. Surv. Prof. Pap.*, *1254*, 14-24, 1982.

Keller, E. A., M. S. Bonkowski, R. J. Korsch, and R. J. Shiemon, Tectonic geomorphology of the San Andreas fault zone in the southern Indio Hills, Coachella Valley, California, *Geol. Soc. Am. Bull.*, *93*, 46-56, 1982.

King, R. W., E. G. Masters, C. Rizos, A. Stolz, and J. Collins, *Surveying with GPS, Monograph 9*, School of Surveying, The University of New South Wales, Kensington, Australia, 1985.

Kroger, P. M., G. A. Lyzenga, K. S. Wallace, and J. M. Davidson, Tectonic motion in the western United States inferred from very long baseline interferometry measurements, 1980-1986, *J. Geophys. Res.*, *92*, 14,151-14163, 1987.

Larsen, S. C., Inverting GPS displacement vectors for seismic slip distribution: Implications for network geometry along the southern San Andreas fault, paper presented at NSF/USGS joint workshop: crustal deformation measurement and earthquake mechanics, Morro Bay, California, 1990.

Larsen, S. C., R. E. Reilinger, H. Neugebauer, W. Strange, GPS measurements of deformation associated with the 1987 Superstition Hills earthquake, Imperial Valley, California: Evidence for conjugate faulting, *J. Geophys. Res.*, in preparation, 1990.

Lomnitz, C., F. Mooser, C. R. Allen, J. N. Brune, and W. Thatcher, Seismicity and tectonics of northern Gulf of California region, Mexico: Preliminary results, *Geofis. Int.*, *10*, 34-48, 1970.

Ma, C., J. W. Ryan, D. Caprette, Crustal dynamics project data analysis – 1988, VLBI geodetic results 1979-1988, *NASA Technical Memorandum, 100723*, 1989.

Magistrale, H., L. Jones, and H. Kanamori, The Superstition Hills, California, earthquakes of 24 November, 1987, *Bull. Seismol. Soc. Am.*, *79*, 239-251,

1989.

Mansinha, L., and D. E. Smylie, The displacement fields of inclined faults, *Bull. Seismol. Soc. Am.*, *61*, 1433-1440, 1971.

Neugebauer, H. C., The 1986 Salton trough GPS survey and data processing results, National Geodetic Survey (unpublished report), 1988.

Prescott, W. H., J. C. Savage, and M. Lisowski, Crustal strain, in National Earthquake Hazards Reduction Program, Summaries of Technical Reports, *U.S. Geol. Surv. Open-File Rep.*, *87-374*, 272-280, 1987a.

Prescott, W. H., M. Lisowski, and J. C. Savage, Velocity field along the San Andreas fault in southern California, *EOS Trans.*, *68*, p. 1506, 1987b.

Reilinger, R., Coseismic and postseismic vertical movements associated with the 1940 M7.1 Imperial Valley, California, earthquake, *J. Geophys. Res.*, *89*, 4531-4537, 1984.

Reilinger, R. E., and S. C. Larsen, Vertical crustal deformation associated with the 1979 M = 6.6 Imperial Valley, California earthquake: Implications for fault behavior, *J. Geophys. Res.*, *91*, 14,044-14,056, 1986.

Reilinger, R., J. Beavan, L. Gilbert, S. Larsen, K. Hudnut, C. Aiken, D. Ziegler, B. Strange, M. F. de la Fuente, J. G. Garcia, J. Stowell, W. Young, G. Doyle, and G. Stayner, 1990 Salton Trough-Riverside County GPS Network, *EOS Trans. abst.*, *71*, p. 447, 1990.

Sauber, J., Geodetic measurement of deformation in California, Ph.D. Thesis, Massachusetts Institute of Technology, 1989.

Savage, J. C., W. H. Prescott, M. Lisowski, and N. King, Deformation across the Salton Trough, California, 1973-1977, *J. Geophys. Res.*, *84*, 3069-3079, 1979.

Savage, J. C., W. H. Prescott, M. Lisowski, and N. E. King, Strain accumulation in Southern California, 1973-1980, *J. Geophys. Res.*, *86*, 6991-7001, 1981.

Savage, J. C., W. H. Prescott, and G. Gu, Strain accumulation in southern California, 1973-1984, *J. Geophys. Res.*, *91*, 7455-7473, 1986.

Sharp, R. V., Variable rates of late Quaternary strike slip on the San Jacinto fault zone, southern California, *J. Geophys. Res.*, *86*, 1754-1762, 1981.

Sharp, R. V., Comparison of 1979 surface faulting with earlier displacements in the Imperial Valley, *U.S. Geol. Surv. Prof. Pap.*, *1254*, 213-221, 1982.

Sieh, K. E., Slip rate across the San Andreas fault and prehistoric earthquakes at Indio, California, *Eos Trans. abst.*, *67*, p. 1200, 1986.

Sieh, K. E., and P. L. Williams, Behavior of the southernmost San Andreas fault during the past 300 years, *J. Geophys. Res.*, *95*, 6629-6645, 1990.

Snay, R. A., and A. R. Drew, Supplementing geodetic data with prior information for crustal deformation in the Imperial Valley, California, Technical Report Series, University of Stuttgart, 30 p., 1988.

Sykes, L. R., and S. P. Nishenko, Probabilities of occurrence of large plate rupturing earthquakes for the San Andreas, San Jacinto, and Imperial faults, California, 1983-2003, *J. Geophys. Res.*, *89*, 5905-5927, 1984.

Thatcher, W., Horizontal crustal deformation from historic geodetic measurements in southern California, *J. Geophys. Res.*, *84*, 2351-2370, 1979.

Trifunac, M. D., and J. N. Brune, Complexity of energy release during the Imperial Valley, California, earthquake of 1940, *Bull. Seismol. Soc. Am.*, *60*, 137-160, 1970.

Weldon, R. J., and K. E. Sieh, Holocene rate of slip and tentative recurrence interval for large earthquakes on the San Andreas fault, Cajon Pass, southern California, *Geol. Soc. Am. Bull.*, *96*, 793-812, 1985.

U. S. G. S., The Imperial Valley, California, earthquake of October 15, 1979, *U.S. Geol. Surv. Prof. Pap.*, *1254*, 451 p., 1982.

APPENDIX 2

GPS measurements of deformation associated with the 1987 Superstition Hills earthquake: Evidence for conjugate faulting

by S. Larsen, R. Reilinger, H. Neugebauer, and W. Strange

Submitted to *Journal of Geophysical. Research*, 1991

GPS Measurements of Deformation Associated with the 1987 Superstition Hills Earthquake: Evidence for Conjugate Faulting

Abstract

Large station displacements observed from Imperial Valley GPS campaigns are attributed to the November 24, 1987 Superstition Hills earthquake sequence. Thirty sites from a 42 station GPS network established in 1986 have been reoccupied during 1988 and/or 1990. Displacements at three sites within 3 kilometers of the surface rupture approach 0.5 m. Eight additional stations within 20 km of the seismic zone are displaced at least 10 cm. This is the first occurrence of a large earthquake (M_S 6.6) within a preexisting GPS network. Best-fitting uniform slip models of rectangular dislocations in an elastic half-space indicate 130 cm right-lateral displacement along the northwest trending Superstition Hills fault and 30 cm left-lateral offset along the conjugate northeast trending Elmore Ranch fault. The geodetic moments are 9.4 x 10^{25} dyne-cm and 2.3 x 10^{25} dyne-cm for the Superstition Hills and Elmore Ranch faults, respectively. Distributed slip solutions using Singular Value Decomposition suggest near uniform displacement along the Elmore Ranch fault and concentrated slip to the northwest and southeast along the Superstition Hills fault. A significant component of non-seismic secular displacement is observed across the Imperial Valley, which is attributed to interseismic plate-boundary elastic deformation.

4.1 Introduction

The Global Positioning System (GPS) is rapidly becoming one of the most important tools to study tectonic deformation. By recording signals from earth orbiting satellites it is possible to determine 3-dimensional coordinates of geodetic monuments with high accuracy. With repeated observations the station displacement or deformation between surveys is measured. GPS can be used to monitor secular deformation such as that associated with plate motion, or to record rapid strain fluctuations such as those due to seismic and volcanic activity. In its final configuration scheduled for the mid 1990's, 18 satellites will be deployed in 6 orbital planes (with 3 additional satellites used as active spares). When GPS becomes fully operational it will be possible to continuously determine 3-dimensional positions anywhere on or near the earth. The available satellite constellation existing for the last several years, was optimized for North America making geodetic studies in California practical. The observation window in which enough satellites have been visible to obtain the high accuracies necessary to measure tectonic motion has been about 6 to 8 hours each day.

On November 24, 1987, two large earthquakes separated by 12 hours occurred in the northwest portion of the Imperial Valley region of southern California. The first event was located on a northeast trending seismic lineament and was followed 12 hours later by rupture along the northwest trending Superstition hills fault. What makes this earthquake sequence so significant from a GPS standpoint, is that it occurred spatially and temporally within a preexisting GPS network. This network was established in the Imperial Valley in 1986, with partial resurveys in 1988 and 1990.

Fifteen stations are located within 20 km of the rupture zone; three stations are within 3 km. This is the first occurrence of a large earthquake within a preexisting GPS network.

We compute GPS displacements in the Imperial Valley between 1986 and 1990. Observed movements of near 0.5 meters are attributed to the Superstition Hills earthquake sequence. The earthquake-induced displacements are inverted to estimate seismic slip and the corresponding geodetic moment along the rupture planes. In addition, there is a large component of deformation which can not be explained by the seismic disturbance; we assume this to be a manifestation of continuous strain accumulation across the Imperial Valley due to the relative motion of the Pacific and North American plates.

4.2 Imperial Valley Seismicity and Tectonics

The Imperial Valley region of southern California is a complex transition zone between crustal spreading in the Gulf of California and right-lateral transform motion along the San Andreas fault (Figure 4.1) [*Lomnitz et al.*, 1970; *Elders et al.*, 1972]. The valley is 4-5 million years old and has been filled by up to 5 km of late Cenozoic sediments [*Fuis et al.*, 1982]. The major fault systems and structural grain of the valley trend to the northwest, roughly parallel to the direction of plate motion. A significant fraction of the North American and Pacific relative motion may be accommodated across this region.

The valley is one of the most seismically active regions of California

(Figure 4.1) with much of the activity occurring along the Imperial fault and within the Brawley Seismic Zone [*Johnson and Hill*, 1982]. Several large earthquakes have occurred in and near the Imperial Valley since 1940 (Figure 4.1). The Imperial fault ruptured with a M_S 7.1 event in 1940 and a M_L 6.6 event in 1979 [*U.S. Geol. Surv.*, 1982]. Segments of the San Jacinto fault system broke with a M_L 6.2 earthquake in 1954 (Clark segment) and the 1968 M_L 6.5 Borrego Mountain event (Coyote Creek segment). The most GPS relevant episode of seismic activity occurred in 1987 along the Superstition Hills segment of the San Jacinto fault system, with a M_S 6.2 earthquake on a northeast trending seismic lineament followed 12 hours later by a M_S 6.6 event on the Superstition Hills fault.

Conventional geodetic measurements suggest considerable deformation across the Imperial Valley. In fact, a significant fraction of the Pacific-North American relative plate motion may be accommodated here. New global plate model estimates (NUVEL-1) [*DeMets et al.*, 1987; *DeMets et al.*, 1990] predict the rate of relative motion between the North American and Pacific plates (at Imperial Valley coordinates: 33.0°N, 115.5°W) is 4.7 cm/yr oriented N39.6°W. Triangulation measurements spanning this region have been modeled as 4.3 cm/yr of plate-boundary deformation averaged between 1941 and 1986 [*Snay and Drew*, 1988]. Trilateration measurements made by the U.S.G.S. between 1972 and 1987 indicate 3.45 cm/yr relative movement between stations on opposite sides of the valley [*Prescott et al.*, 1987b]. The orientations of the conventional geodetic displacements are approximately N40°W, although to some extent the direction is non-unique and depends upon a priori assumptions [e.g., *Prescott*, 1981]. In addition, the conventional

Figure 4.1: Seismicity and major fault systems of the Imperial Valley. The Brawley Seismic Zone is the region of anomalously high activity between the Imperial and southern San Andreas faults. The valley represents a transition zone between crustal spreading in the Gulf of California to the and right-lateral transform motion along the San Andreas system.

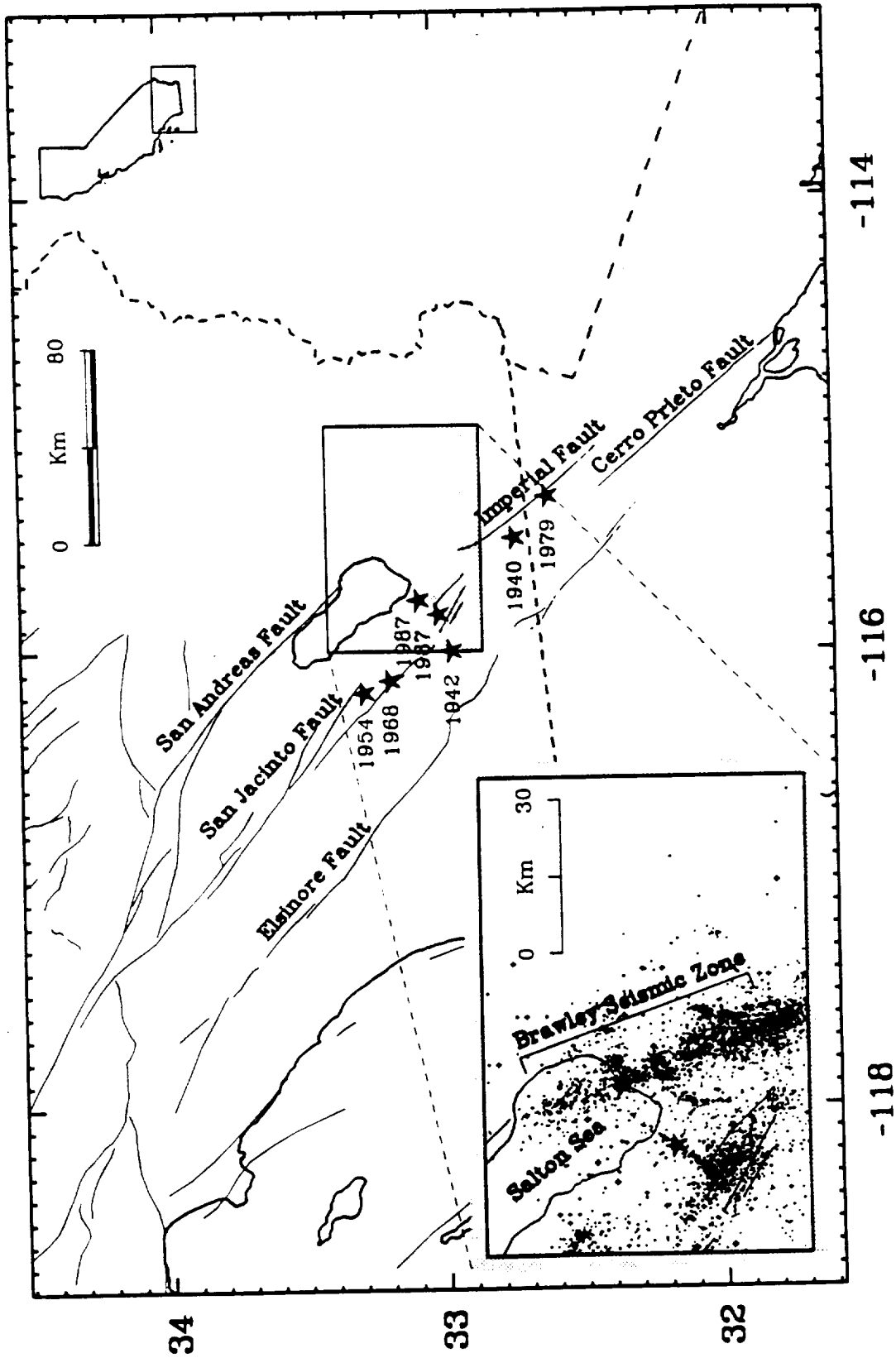
0
Km
80
San Andreas Fault
San Jacinto Fault
Elsinore Fault
Imperial Fault
Cerro Prieto Fault
1940
1979
1942
1954
1968
1987
1987
0
Km
30
Brawley Seismic Zone
Salton Sea
-114
-116
-118
34
33
32

geodetic measurements indicate that deformation is concentrated in a narrow 20 km wide zone along the Imperial fault, while to the north it is distributed over a region at least 50 km wide. Presumably, deformation is transferred from the Imperial fault, which acts as the primary strain release mechanism near the border, to distributed shear along the San Andreas, San Jacinto, and Elsinore faults.

4.3 Superstition Hills Earthquake Sequence

On November 24, 1987 (1:54 GMT), a large M_S 6.2 earthquake occurred along a northeast trending seismic lineament northeast of the Superstition Hills fault (Figure 4.2) [*Magistrale et al.*, 1988]. The focal mechanism and aftershock sequence, which extended for 26 km to the northeast and into the Brawley Seismic Zone, are consistent with left-lateral strike slip motion on a vertical fault. Seven foreshocks were recorded in the 22 minutes prior to the main event, including two with $M_L > 4.0$. Surface rupture consisted of a complex pattern of left-lateral northeast-trending offsets ranging in length from 1.5 to 10 km, and with maximum displacements between 3 and 13 cm [*Budding and Sharp*, 1988; *Hudnut et al.*, 1989a]. We refer to this northeast trending lineament as the Elmore Ranch fault, although more precisely this name refers only to the longest of the surface fractures.

Twelve hours after the Elmore Ranch event (13:15 GMT), a M_S 6.6 earthquake occurred along the northwest trending Superstition Hills fault. The epicenter was near the intersection of the Elmore Ranch and Superstition Hills faults. Strong ground motion and teleseismic data suggest the rupture process for this second event was somewhat complicated, consisting of

multiple sub-events [*Bent et al.*, 1989; *Frankel and Wennerberg*, 1989; *Hwang et al.*, 1990; *Wald et al.*, 1990]. Surface rupture extended 24 km along the previously mapped trace of the fault [*Williams and Magistrale*, 1989]. Up to 50 cm right-lateral displacement were measured immediately following the earthquake. The aftershock pattern was concentrated slightly to the west of the fault and did not extend the length of the surface rupture. *Magistrale et al.* [1989] suggested the aftershock sequence was highly correlated with basement structure. Both the Superstition Hills and Elmore Ranch events triggered sympathetic surface offsets along the Imperial, San Andreas, and Coyote Creek faults [*McGill et al.*, 1989; *Hudnut and Clark*, 1989].

Significant afterslip was recorded along the Superstition Hills fault following the second mainshock. No afterslip was measured along any of the surface ruptures associated with the Elmore Ranch event. In fact, all seismic activity essentially stopped along this segment after the initiation of the 2nd mainshock.

One of the most interesting aspects of this earthquake sequence is the conjugate nature of faulting. That is, two surface ruptures oriented nearly perpendicular to each other. As discussed below, this type of fault interaction may be typical of Imperial Valley tectonics and may dictate the mode of stress/strain transfer from one fault system to another.

What makes the Superstition Hills earthquake sequence unique from a GPS perspective is that it occurred within a preexisting GPS network. Stations located near the seismic rupture zone were displaced nearly 0.5 meters. These movements, as well as smaller displacements observed at

Figure 4.2: Seismicity and surface faulting associated with the November 24, 1987 Superstition Hills earthquake sequence. A M_S 6.2 event occurred along a northeast trending structure (referred to here as the Elmore Ranch fault) and was followed by 12 hours with a M_S 6.6 event along the northwest trending Superstition Hills fault. The focal mechanisms, aftershock distribution, and surface offset measurements are consistent with left-lateral strike-slip motion along the Elmore Ranch fault and right-lateral strike-slip motion along the Superstition Hills fault. A significant amount of postseismic slip was observed along the surface trace of the Superstition Hills fault, while activity essentially ceased on the Elmore Ranch fault after the M_S 6.6 event. The shaded strips along each fault indicate the geometrical extent of the dislocations used to model the geodetic displacements.

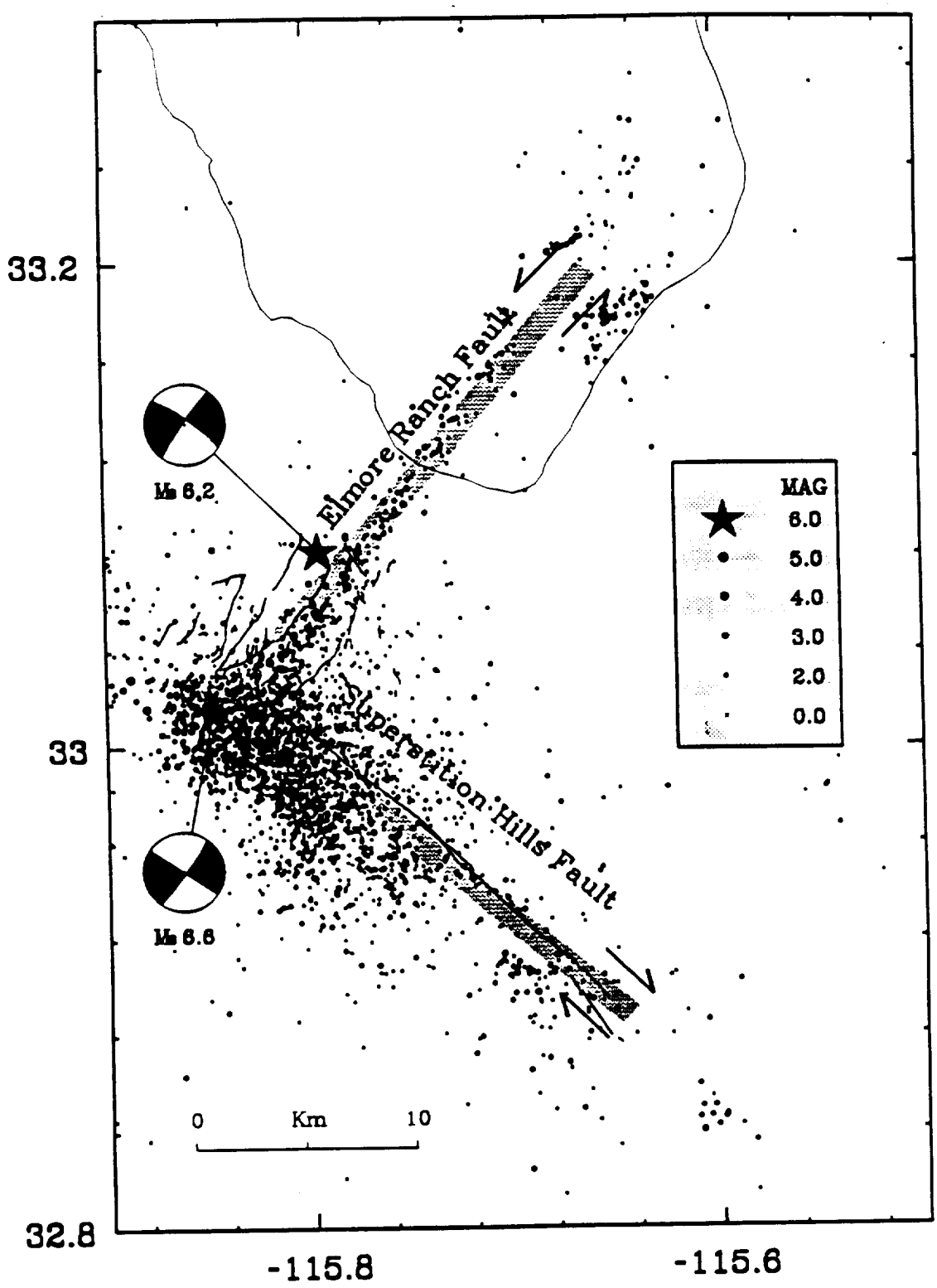
33.2
33
32.8
-115.8
-115.6
Elmore Ranch Fault
Superstition Hills Fault
Ms 6.2
Ms 6.6
MAG
6.0
5.0
4.0
3.0
2.0
0.0
0
Km
10

nearby stations can be inverted to infer properties of the rupture process. This is the first time GPS measurements have recorded the deformation from a large earthquake.

4.4 GPS Observations

After a brief introduction to the Global Positioning System, in this section we report how the GPS data were obtained from field campaigns in 1986, 1988, and 1990, as well as the processing methods used to obtain station coordinates. The GPS displacement vectors between surveys are presented and we discuss how measurement errors are handled for this study. More complete details about the Global Positioning System, including theoretical aspects and processing methods, are found in *King et al.* [1985], *Wells et al.* [1987], and *Rocken* [1988].

The signal structure broadcast from each GPS satellite consists of two carrier phase signals modulated by a navigational message as well as pseudo-random codes. The two carrier frequencies, known as the L1 and L2 phases, are broadcast at 1575.42 Mhz (L1) and 1227.60 Mhz (L2). This is equivalent to wavelengths of about 19 cm for the L1 and 24 cm for the L2. The navigational message contains the satellite coordinates (broadcast ephemeris), clock parameters, satellite health, and general system status. The pseudo-random codes are accurate time marks which allow a GPS receiver to determine the transmission time of the signal. When scaled by the speed of light, the pseudorange, or the satellite-receiver distance is computed. If measurements to at least 4 GPS satellites are available, and if satellite coordinates are known (usually with the broadcast ephemeris), the 3-

dimensional receiver position as well as the satellite-receiver time offset can be determined. The positioning accuracy with the pseudorange is 1 to 100 m, depending on whether the P or C/A code is used, the receiver type, length of observation, and the static or kinematic behavior of the instrument. It is the pseudorange which will be used for civilian and military navigation. For highly accurate geodetic positioning, however, it is necessary to use the carrier phase measurements in a post-processing mode. That is, the data collected in the field are brought back to the office or laboratory for analysis, usually with a fairly robust computer software system.

GPS Surveys -- Data Collection

The GPS data for this study were collected during 4 Imperial Valley field campaigns from 1986 to 1990 (Table 4.1). A total of 46 stations in or near the valley have been occupied at least once during this interval (Figure 4.3), while 30 sites have been reoccupied since 1986 (Figure 4.3, Table 4.2). TI-4100 GPS receivers supporting GESAR software were used during 1986 and 1988, while Trimble 4000SDT instruments were used during the 1990 survey As one of the first commercially available instruments, the TI-4100 is a code correlating receiver which allows the simultaneous tracking of up to 4 satellites at a time. This instrument records the L1 and L2 carrier signals, the P and C/A pseudo-codes, and the broadcast message. The Trimble 4000SDT is able to record the L1 and L2 phase components for up to 8 satellites at once, as well as the C/A code and the broadcast message

The National Geodetic Survey (NGS) occupied 54 sites in southern California in May/June 1986; 42 stations were located in or near the Imperial

Figure 4.3a: Imperial Valley and related GPS stations surveyed in 1986, 1988, and/or 1990. Station names for sites indicated in the shaded box are given in Figure 4.3b.

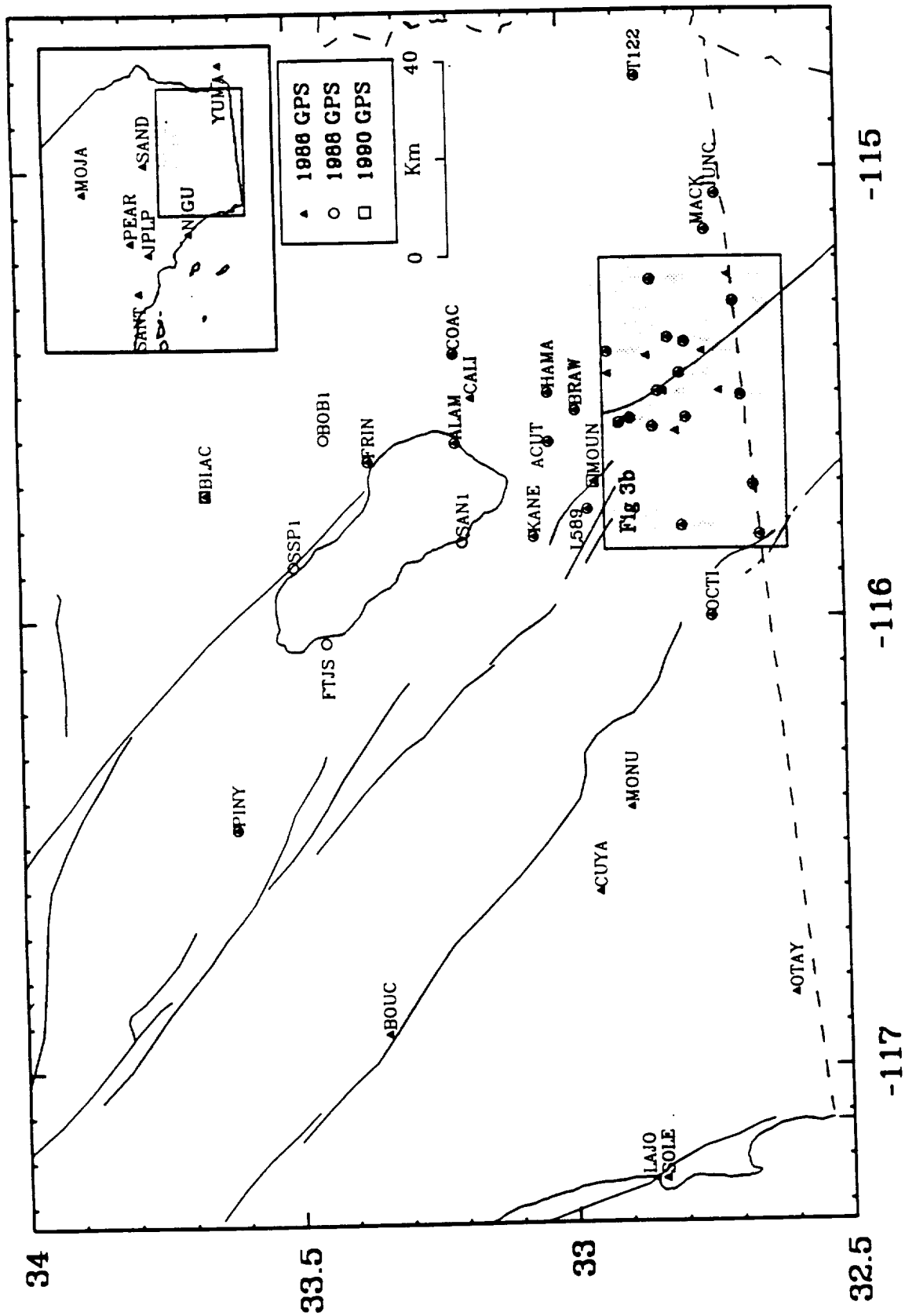
1986 GPS
1988 GPS
1990 GPS
0
40
Km
MOJA
SAND
PEAR
JPLP
YUMA
NGU
SANT
BLAC
OBOB1
FRIN
OSSP1
FTJS
PINY
SAN1
CALI
COAC
ALAM
HAMA
BRAW
ACUT
KANE
1589
MOUN
Fig 3b
T122
MACK
UNC
OCTI
MONU
CUYA
BOUC
OTAY
LAJO
SOLE
34
33.5
33
32.5
-115
-116
-117

Figure 4.3b: Central-southern Imperial Valley and related GPS stations surveyed in 1986, 1988, and/or 1990.

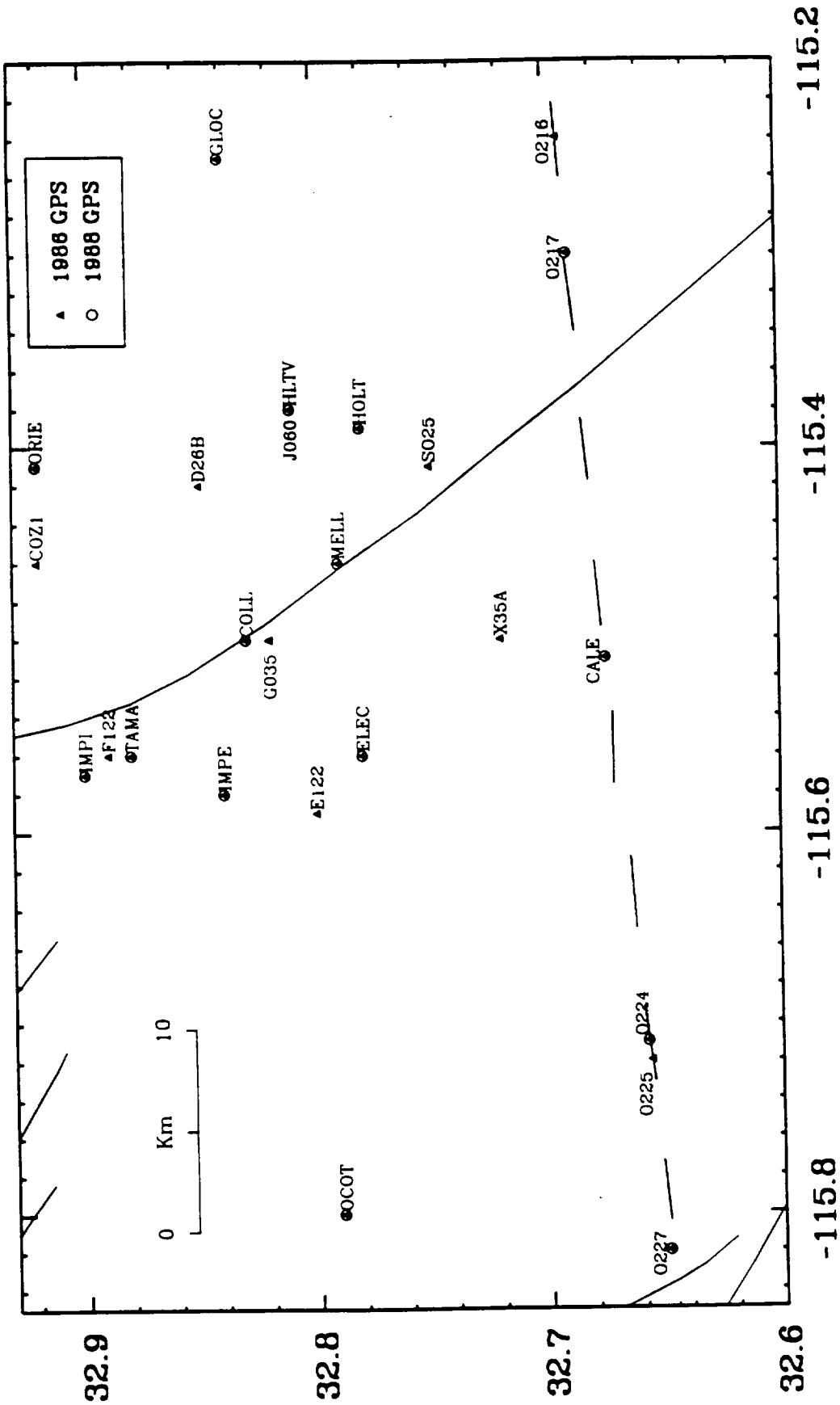
1988 GPS
1988 GPS
GLOC
0216
0217
ORIE
D26B
J060
HLTV
HOLT
S025
COZ1
MELL
COLL
X35A
G035
CALE
MPI
F122
TAMA
MPE
E122
ELEC
0224
0225
OCOT
0227
0
Km
10
-115.2
-115.4
-115.6
-115.8
32.9
32.8
32.7
32.6

Table 4.1 Imperial Valley GPS Campaign Summary

Year	Month	Days	Stations	Organization
1986	May e	20	42	NGS
1988	Febr farch	9	19	UNAVCO
1988	March/April	6	21	NGS
1990	April	1	3	UNAVCO/RCFC

NGS - National Geodetic Survey
UNAVCO - University Navstar Consortium
RCFC - Riverside County Flood Control

Table 4.2 Reoccupied GPS Stations

Station Name	Abbr.	Occupation				Longitude	Latitude	Elevation
		1986	1988[1]	1988[2]	1990	°	°	(m)
Acute 1934	ACUT	•	•	•		-115.6093	33.0300	-80.91
Alamo	ALAM	•	•	•		-115.6111	33.1964	-72.91
Black Butte NCMN 1982	BLAC	•	•		•	-115.7198	33.6638	490.01
Brawley 2 rm 5	BRAW	•		•		-115.5434	32.9773	-66.78
Calexico 1954	CALE	•	•			-115.5064	32.6645	-34.07
Coach	COAC	•	•			-115.4070	33.1962	-8.40
College 1967	COLL	•	•			-115.5024	32.8269	-54.63
El Centro 2 1959	ELEC	•		•		-115.5622	32.7846	-45.76
Frink 1934	FRIN	•	•	•		-115.6470	33.3603	-85.39
GLO Cornew 1934	GLOC	•	•			-115.2465	32.8396	-15.46
Hamar 2 1967	HAMA	•	•	•		-115.5007	33.0375	-79.80
Holt 1924	HOLT	•		•		-115.3963	32.7814	-36.79
Holtville (Alt) 1934	HLTV	•		•		-115.3821	32.8084	-38.77
Imp 1934	IMPI	•		•		-115.5698	32.8982	-59.27
Imperial 1934	IMPE	•		•		-115.5788	32.8439	-51.85
Junction	JUNC	•		•		-115.0619	32.7092	8.35
Kane 1939	KANE	•	•	•		-115.8237	33.0614	10.05
L 589 1967	L589	•	•	•		-115.7611	32.9506	13.62
Mack 2 1967 bm reset	MACK	•		•		-115.1441	32.7288	1.20
Mello 3 1967	MELL	•		•		-115.4653	32.7961	-47.00
Mound 1934	MOUN	•			•	-115.6998	32.9502	3.40
Ocotillo NCMN 1982	OCOT	•	•	•		-115.7962	32.7901	-36.43
Ocotillo 1935	OCTI	•	•	•		-116.0017	32.7338	111.33
Offset 217	O217	•	•	•		-115.3131	32.6782	-17.16
Offset 224	O224	•		•		-115.7055	32.6493	50.00
Offset 227	O227	•		•		-115.8173	32.6414	70.64
Orient 1939	ORIE	•	•			-115.4064	32.9168	-61.36
Pinyon Flat	PINY	•		•		-116.4588	33.6093	1235.88
T 1226	T122	•		•		-114.8050	32.8583	141.19
Tamarisk 3 1967	TAMA	•	•			-115.4783	32.8829	-68.19

[1] UNAVCO
[2] NGS

Valley. Most marks were observed at least two days (Table 4.3), although redundant baselines were relatively uncommon (i.e., simultaneous occupation of the same station-station pair for two or more days). Unfortunately, the quality of the observations were very poor. The scheduled 4.5 hour daily occupations were somewhat less than the 6-8 hour sessions typical of other southern California campaigns. In addition, due to a variety of equipment and logistical problems, less than 2 hours of data were collected at several sites. In the observation scenario, there was less than a 2 hour period in which more than 3 satellites were simultaneously tracked. In fact, there was a scheduled 1 hour gap in Satellite 6 during the middle of the measurement session. The data were generally noisy and the final double difference phase observables may contain uncorrected cycle slips.

In February/March 1988 university field crews (UNAVCO) observing for 9 days reoccupied 15 of the Imperial Valley marks, as well as establishing 4 new stations along the Salton Sea. These new sites were installed at tide gauge monitoring facilities and will be used to constrain vertical GPS baseline components and for monitoring tectonic tilting in the Salton Trough. Most monuments were occupied for 2 days (Table 4.3) (1 was observed 3 days, 1 for 4 days, and 2 for 1 day). The scheduled nightly observation scenario lasted 7.5 hours, with a total of 7 satellites tracked.

In March/April 1988 the NGS reoccupied 21 of the 1986 stations (7 of which were observed by the university crews a month earlier). Most sites were occupied only 1 day (Table 4.3). The daily observation period of 6.0 hours was slightly shorter than the February/March survey, although 7 satellites were tracked each day.

Table 4.3 Imperial Valley GPS Occupation History

Year	Day	Stations							
1986	141	COLL	CALE	L589					
	142	O217	O216	MELL	E122	HOLT	ELEC	O227	
	143	COLL	CALE	TAMA	HLTV	MACK	O224	IMPE	O225
	144	OCTI	IMPI	F122	OCOT		O224	O227	O225
	145	HAMA	IMPI	ALAM			ACUT	MOUN	
	146	HAMA	CALE	TAMA	ORIE		GLOC	CO12	BRAW
	147	COAC	CALI	ALAM	ORIE	FRIN	BLAC	KANE	
	148	OCTI	MONU	L589	OCOT	FRIN	ACUT	KANE	BRAW
	149	O217	O216	J060	T122	MACK	GLOC	MOUN	YUMA
	150	COAC	MONU	MELL	T122	HOLT	BLAC	CO12	YUMA
	151	G035	S025	L589	D26B	HOLT	ACUT	X35A	JUNC
	153	G035	S025	J060	D26B			X35A	BRAW
	161	PINY		SAND	OCOT	PEAR	BLAC		
	162	PINY		SAND	OCOT	PEAR	BLAC		YUMA
	163	PINY		SAND	OCOT	SANT	BLAC		YUMA
	164	PINY		JPLP	OCOT		BLAC		YUMA
	167	PINY	MONU	MOJA	NIGU	SOLE			YUMA
	168	PINY	MONU	MOJA	NIGU	SOLE	OTAY		YUMA
	169	LAJO	MONU	MOJA	BOUC		OTAY		YUMA
	170	LAJO	MONU	MOJA	BOUC	CUYA			YUMA
1988[1]	55	L589	BLAC	FTJS	COAC	SAN1			
	56	ALAM	GLOC	OCOT	SSP1	SAN1			
	57	ALAM	GLOC	OCOT	SSP1	ORIE			
	58	L589	GLOC	BOB1	COAC	ORIE			
	59	L589	BLAC	FTJS	KANE	FRIN			
	60	L589	CALE	TAMA	KANE	FRIN			
	62	O217	CALE	TAMA					
	63	O217	COLL	OCTI					
	64	HAMA	COLL	OCTI					
1988[2]	88	PINY	OCOT	BRAW	HOLT	MELL			
	89	PINY	OCOT	IMPE	IMPI	O217			
	90	PINY	OCOT	ACUT	HAMA	KANE			
	91	PINY	OCOT	ELEC	HLTV	OCTI			
	92	PINY	OCOT	MACK	O227	T122			
	93	PINY	FRIN	JUNC	L589	O224			
1990	100	BLAC	MOUN	BC01					

Day is Julian day of year

[1] UNAVCO

[2] NGS

In addition to the UNAVCO and NGS campaigns, GPS observations in 1988 were made at Mojave (California), Westford (Massachusetts), and Richmond (Florida). These sites are continuously monitored as part of the Cooperative International GPS Network (CIGNET) [*Chin*, 1988]. Data from CIGNET stations are used to improve satellite orbits in the GPS processing. Unfortunately, these observations are frequently of poor quality and contain abundant cycle slips. During the 1988 campaign, observations were not always available or usable at all CIGNET sites on all days (Table 4.4).

Station MOUN (Mound), which was surveyed in 1986, was destroyed from the 1987 earthquake sequence. The site is located less than 1 km from the surface rupture of the Superstition Hills fault. Field investigation during early 1988 reveiled that the monument and supporting concrete base had been completely uprooted from the ground. Destroyed monuments usually can not be tied to previous surveys because of the high accuracy required for crustal motion research. If the suspected deformation is significantly large, however, some information may be recovered if the monument (or a substitute) is reset in approximately the same location. Site inspection at MOUN clearly showed where the old monument had been and in early April, 1990 a rebar rod acting as a temporary benchmark was set at approximately the same position. We estimate the temporary mark was set within 0.15 m of the previous monument. Because of its proximity to the 1987 rupture zone, the calculated seismic displacement at MOUN is about 0.5 m. Therefore, reoccupation of this site should retrieve a tectonic component larger than the expected uncertainty.

The 1990 survey was conducted to establish the displacement of MOUN

relative to its 1986 position. This "mini-campaign" (Table 4.3), which included stationary GPS receivers at only three sites (MOUN, BLAC, and BC01) was performed interactively with kinematic GPS transects along the southern San Andreas fault (K. Hudnut, personal communication, 1990). Data were collected for only one night; a total of 9 satellites were visible during the scheduled 7.0 hour experiment.

GPS Processing

The 1986 GPS observations were processed with the GPS22 software developed at the National Geodetic Survey. Satellite orbital information was provided by the NSWC (Naval Surface Weapons Center). A tropospheric delay parameter was solved at each station, constrained by surface meteorological measurements. Ambiguities were fixed to the nearest integer. Each of the 20 days of observation was processed separately, and the daily solutions were combined to form one set of station coordinates with the geodetic adjustment program DYNAP (DYNamic Adjustment Program) [*Drew and Snay*, 1989]. All coordinates were computed in the WGS-84 reference frame [*Defense Mapping Agency*, 1987]. Due to poor data quality and observation constraints, the accuracy of these measurements is believed to be on the order of 1 ppm (parts per million) [*Neugebauer*, 1988].

Data from both 1988 campaigns were processed with the Bernese GPS analysis software (version 3.0), from the University of Bern in Switzerland. (Preliminary processing such as data translation and cycle slip fixing were performed with an earlier version of the software.) The Bernese GPS analysis package allows 3-dimensional station coordinates to be determined from the

integration of carrier phase, pseudo-range, and orbital data [e.g., *Gurtner et al.*, 1985; *Beutler et al.*, 1985; *Rocken*, 1988]. In addition to measuring station coordinates, the double difference estimation algorithm can solve for adjustments to six Keplerian elements and two radiation pressure coefficients for each satellite, an atmospheric zenith delay parameter at each station, a clock error term at each site, ionospheric model coefficients, and cycle ambiguity terms [e.g., *Rocken*, 1988].

For each of the 1988 surveys, all data were combined into a simultaneous multi-day solution. Surface meteorologic data (temperature, pressure, relative humidity) were used to constrain a Saasmotonian atmospheric model, and independent tropospheric zenith delay parameters were estimated at each station. We experimented with fixing ambiguities but found mixed results, therefore, ambiguities were left unresolved in the final solutions.

In addition to station coordinates, satellite orbital parameters were estimated for both solutions. GPS observations from the CIGNET tracking sites were used to constrain the orbits. The Bernese software is able to combine ephemeris information from several days into a single multi-day arc. It has been suggested that multi-day satellite arcs significantly improve GPS precision [e.g., *Lichten*, 1987]. Typically, 6 Keplerian elements and 2 radiation pressure coefficients are estimated for each satellite. *Davis et al.* [1989] utilized 4-day arcs (72 hours plus the length of the daily observation session) to analyze GPS data from North America. A 5-day satellite arc was used to process GPS data off the southern California coast near Santa Barbara [*Larsen et al.*, 1990].

There comes a point, however, when the force model describing the satellite orbits begins to break down. It is unlikely that the 10-day interval of the February/March 1988 survey (9 observation days plus one day of no measurements) could be modeled from a 10-day satellite arc. For purposes of orbit determination, therefore, this campaign is divided into multiple 3-day arc segments (days 55-57, 58-60, and 62-64), each defined by its own initial conditions. The data are still processed simultaneously, except that independent satellite parameters are estimated for each 3-day arc. For the entire campaign, 18 Keplerian orbital elements and six radiation pressure terms are estimated for each satellite. A similar technique is used for the March/April survey. The satellite orbits for this campaign are defined by two 3-day arcs (days 88-90 and 91-93).

Orbits are improved by holding the coordinates of at least 3 CIGNET stations fixed, to values well determined from VLBI and satellite laser ranging [Murray and King, MIT interoffice memorandum, 1988]. The GPS phase observables from these fiducial sites constrain the orbits, which in turn improve the solution accuracy of the unfixed stations estimated as free parameters. Notice in Table 4.4 that there are several gaps in the fiducial coverage. Although it would be better to have complete data, in general, this is not a problem since there is always at least one day in each 3-day arc interval where observations from 3 fiducial sites are available.

After each 1988 campaign was processed separately, the Cartesian coordinate differences from the two solutions were adjusted by least squares to obtain one set of coordinates for that year.

Table 4.4 CIGNET Data Availability 1988

Day	MOJA	WEST	RICH
55	●	●	
56	●	●	
57	●	●	●
58	●	●	●
59	●	●	●
60	●	●	
62	●	●	●
63	●	●	●
64	●	●	●
88	□	●	●
89	●	●	●
90	●	●	●
91	●	●	●
92	□	●	●
93	●	●	●

Day is Julian day of year
● Good quality data
□ Poor quality data

The 1990 "mini-campaign" was processed with the Trimvec software, made available from the receiver manufacturer (Trimble Navigation, Sunnyvale, California). Recall that the purpose of this survey was to establish the displacement at station MOUN, presumed large because of its proximity to the 1987 seismic rupture. Since this mark had been reset between the 1986 and 1990 occupations, the error in the displacement estimate will be fairly large ($\sim$ 15 cm). Therefore, high accuracy from a GPS perspective is not required. Only stations BLAC and MOUN were included in the processing since BC01 was not occupied in 1986. The orbits were given by the broadcast ephemeris, and surface meteorological data were used to constrain a tropospheric delay model. (This line was processed by K. Hudnut.)

Station Displacements 1986-1988

GPS station displacements for the interval 1986 to 1988 are shown in Figure 4.4. All movements are made relative to station OCTI. Only horizontal components are shown. The method in which errors are formulated and utilized is disussed below. Generally, the observed displacements can be decomposed into 3 components: 1) seismic deformation due to the Superstition Hills earthquake sequence, 2) secular deformation due to the Pacific-North American relative plate motion, and 3) measurement error attributed to poor data quality from the 1986 survey, most notable in the east-west direction.

The GPS displacement vectors suggest considerable deformation between the 1986 and 1988 campaigns, of which a significant fraction is attributed to

Figure 4.4: Imperial Valley GPS station displacements between 1986 and 1988. All movements are relative to station OCTI. The observed displacements are attributed to the 1987 earthquake sequence, secular plate-boundary deformation across the Imperial Valley, and measurement error. Movements near the 1987 rupture zone approach 0.5 m. Error ellipses are determined by multiplying the formal errors by a variance factor, determined so the average error scales as 1 ppm (parts per million). The uncertainty in the east-west direction is about 4 time larger than that in the north-south direction. The anomalous southwest trending apparent movements for those stations to the southeast are attributed to measurement error.

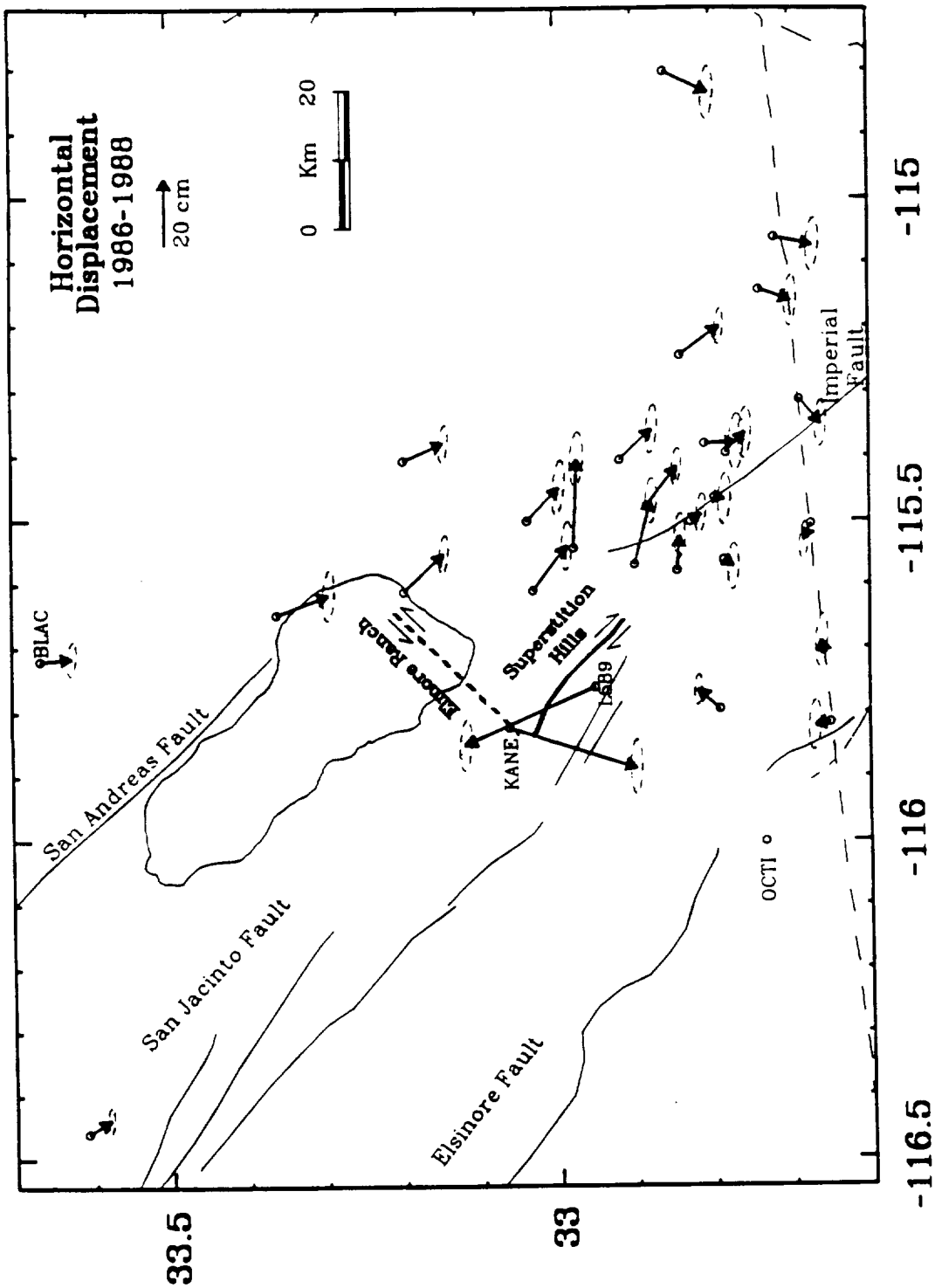
Horizontal
Displacement
1986-1988
20 cm
0 Km 20
BLAC
San Andreas Fault
San Jacinto Fault
Elsinore Fault
Superstition
Hills
KANE
OCTI
Imperial
Fault
33.5
33
-116.5
-116
-115.5
-115

the 1987 Superstition Hills earthquake sequence. Stations nearest the seismic rupture zone (KANE and L589) show movements on the order of 40 cm. In fact, the 13 km KANE-L589 baseline was shortened by 70 cm. The orientations of the displacements are consistent with the conjugate fault pattern indicated by the mapped surface offsets (i.e., right-lateral rupture on the Superstition Hills fault and left-lateral rupture along the Elmore Ranch fault). Other stations near the active fault system appear to have been affected by the 1987 event as well.

There is an additional component of displacement not readily explained by the seismic deformation. Stations east of the Imperial fault tend to be moving south or southeast relative to sites on the other side of the valley. This secular displacement is attributed to the relative motion between the North American and Pacific plates. Unfortunately, it is difficult to ascertain the magnitude of this deformation since station coverage west of the Imperial fault is somewhat lacking and many of these sites have rather large seismically induced displacements (recall that all GPS vectors are relative to OCTI). However, the plate-boundary deformation does appear to be considerable, which is not too surprising considering conventional geodesy indicates a significant fraction of relative plate motion is occurring across the Imperial Valley.

Also evident in Figure 4.4 are unusual movements which do not appear to be tectonically related. Most notable are the southwest trending vectors (as opposed to southeast) for those sites near the border east of the Imperial fault. It appears as if the entire network has undergone a systematic clockwise rotation. We have investigated this possibility by assuming the

network could be rotated (and translated) in terms of an outer coordinate solution by minimizing the displacement component perpendicular to the structural axis of the valley (N40°W) [e.g., *Prescott*, 1981]. Stations KANE and L589 were not included in the solution. However, the applied adjustment did not correct for the anomalous displacements, and in fact, made the apparent deformation less uniform. Although these unusual movements can not be attributed to a simple coordinate rotation, they can be explained by large east-west trending systematic measurement errors in the 1986 survey. This is consistent with the longitudinal orientation of the computed error ellipses (see below) and suggests the north-south displacement components may be a more reliable indicator of tectonic deformation.

Station Displacements 1986-1990

The 1986-1990 displacement of MOUN relative to BLAC is shown in Figure 4.5 (dashed arrow). Although the errors are large because MOUN was reset between surveys, the GPS data indicate significant movement attributed to the Superstition Hills events (recall MOUN is less than 1 km from the 1987 surface rupture). However, based on conventional geodesy as well as the 1986-1988 GPS movements, a non-seismic plate-boundary displacement component is suspected in the measurements. We attempt to remove this component by estimating the MOUN-BLAC secular displacement based on EDM observations. This is discussed in more detail below. We remove 2 years of the accumulated MOUN-BLAC secular movement, and then compute the displacement relative to station OCTI. Although the measurements still contain 2 years of non-seismic deformation, it places the displacements into the same reference frame as the 1986-1988 movements. The adjusted MOUN

Figure 4.5: Imperial Valley GPS station displacements between 1986 and 1990. The displacement at MOUN relative to BLAC is shown by the dashed arrow. For consistency with the 1986-1988 observations the estimated displacement at MOUN relative to OCTI is calculated by subtracting the estimated secular velocity of BLAC relative to OCTI obtained from conventional geodetic measurements (see Figure 4.9). Station MOUN was reset between surveys and site inspection during 1990 revealed a positioning error of about 15 cm.

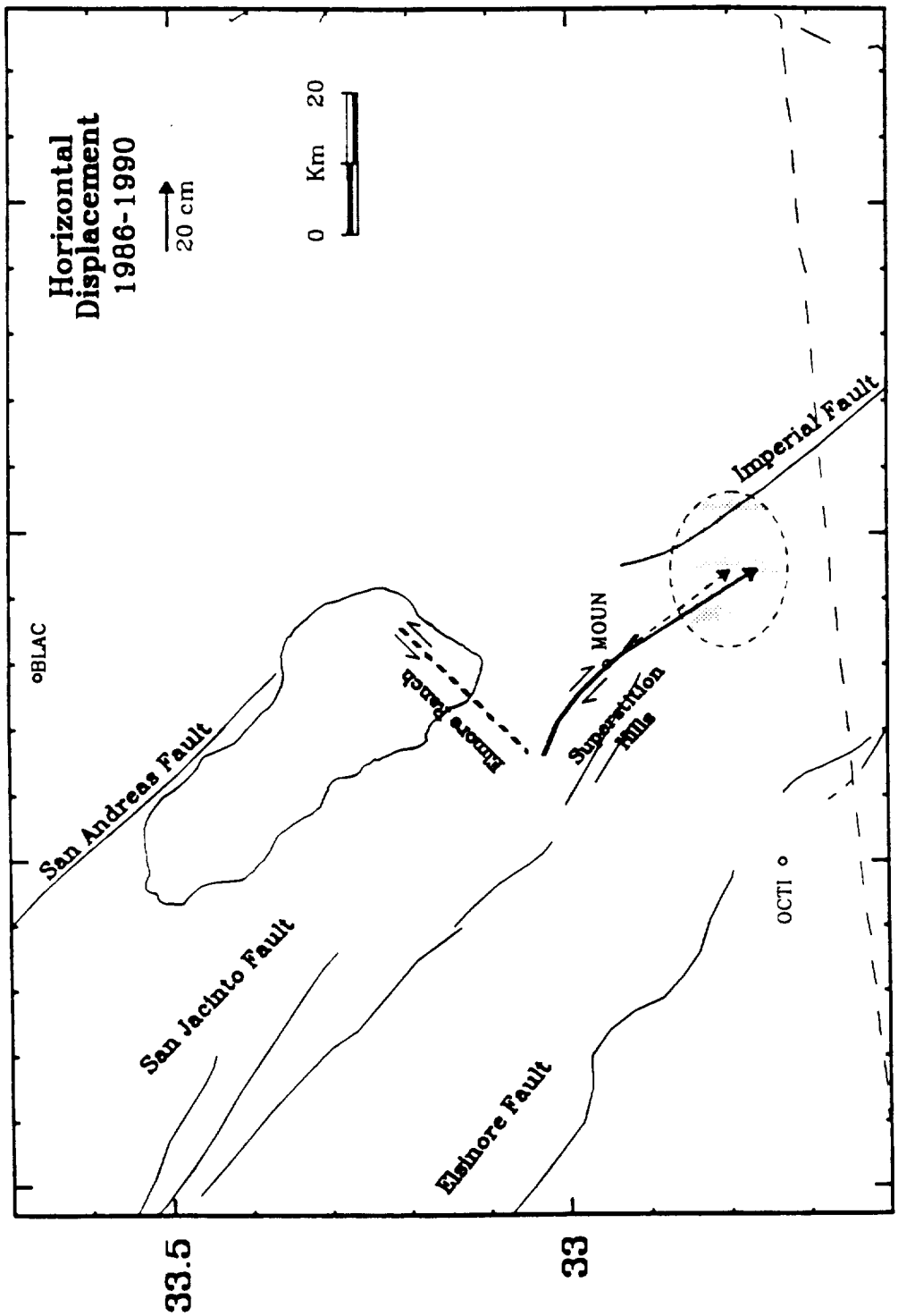
Horizontal
Displacement
1986-1990
20 cm
0 Km 20
BLAC
MOUN
OCTI
San Andreas Fault
San Jacinto Fault
Elsinore Fault
Imperial Fault
Superstition
Hills
33.5
33
-116.5
-116
-115.5
-115

displacement is shown in Figure 4.5 (solid arrow).

Station Displacements 1988-1988 (February-April)

Seven GPS sites were occupied during both 1988 campaigns (Table 4.2). Calculated site displacements for this 1 month interval are shown in Figure 4.6. An adjustment (simple translation) was applied to all movements so that the sum of the vector displacements is zero. The magnitude of the apparent movements range from 0.9 to 2.9 cm, averaging 1.6 cm. It is interesting that the 2.9 cm displacement at KANE is to the west-southwest, more or less expected if left-lateral afterslip occurred along the Elmore Ranch fault. However, while postseismic offsets were significant along the Superstition Hills fault, almost all Elmore Ranch activity ceased after the initiation of the 2nd main event [*Williams and Magistrale*, 1989; *Magistrale*, 1989; *Hudnut et al.*, 1989a]. The observed displacements probably represent measurement error as opposed to real deformation. Note that the largest vector components are oriented in the east-west direction. Station O217 also exhibits a fairly large apparent east-west directed movement, although this is almost certainly not tectonically related.

Even if the displacements shown in Figure 4.6 are entirely measurement error, they do illustrate two points: 1) the accuracy with GPS is easily sufficient to monitor tectonic motions, and 2) the anomalous displacements for the 1986-1988 interval (Figure 4.4) are probably due to the poor quality of the 1986 data. Typical crustal deformation rates across major tectonic structures in southern California are between 1 and 5 cm/yr. At 1 to 2 cm GPS accuracy, such deformation would be resolvable in time scales as short as 1

year. Although the short baseline ($\sim$ 50 km) horizontal precisions computed from GPS repeatability studies are generally at the sub-centimeter level [e.g., *Dong and Bock*, 1989], these tests usually involve multiple occupations of the same network over a consecutive 4 to 5 day interval. Because the 7 stations shown in Figure 4.6 were not all observed simultaneously (Table 4.3), the repeatability is somewhat degraded since errors will tend to propagate through the solutions. However, the relatively good consistency suggested with the 1988 results suggest that some of the unusual movements observed with the 1986-1988 displacement vectors are probably due to poor data quality from the 1986 campaign.

GPS Errors

Formal estimates of GPS uncertainty almost always underestimate variances derived from repeatability studies. We attempt to determine more realistic and illustrative errors by multiplying the structure of the formal covariance matrix calculated with the GPS solution by an estimated variance factor, which scales as average baseline length. For the 1986-1988 displacements, the primary error source is presumably due to the 1986 survey, where the estimated accuracies are on the order of 1 ppm. We have chosen a variance factor so that the average baseline error scales as 1 ppm. Since the 1988 data were processed robustly utilizing orbit improvement techniques (not available with the 1986 data), we assume these errors are negligible. Although this method is somewhat ad hoc, it does illustrate an important fundamental. Notably, the error in the east-west component is about 4 times larger than the north-south uncertainty. This is attributed to the north-south ground-track of the satellite orbits.

Figure 4.6: Imperial Valley GPS station displacements between February/March 1988 and March/April 1988. The observed movements indicate the magnitude of errors due to the 1988 survey. The vector scale is twice that of Figures 4.4 and 4.5. The displacement at KANE could represent postseismic deformation from the 1987 earthquake sequence.

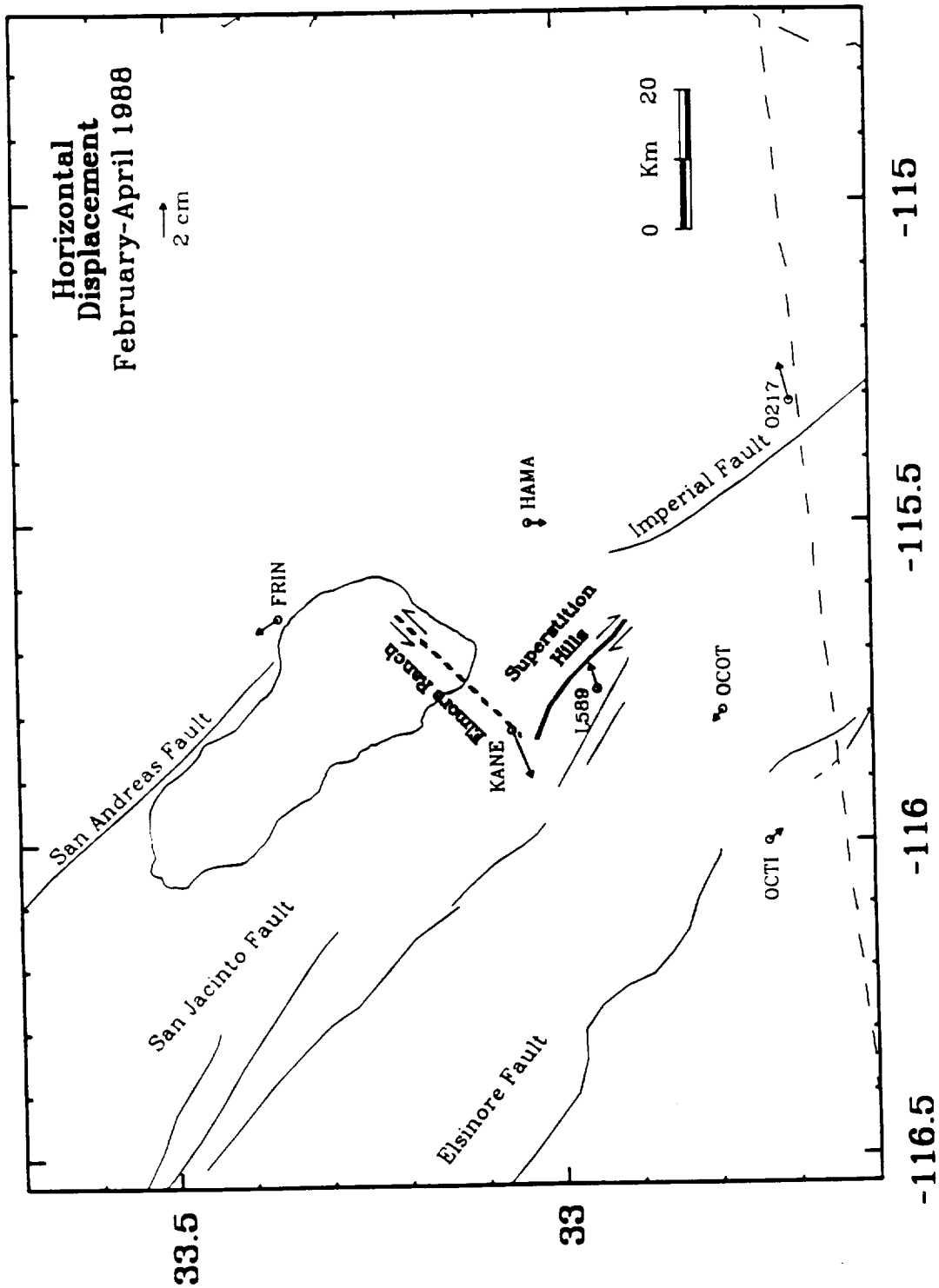
Horizontal
Displacement
February-April 1988
2 cm
0 Km 20
Imperial Fault
0217
HAMA
FRIN
Superstition
Hills
Elmore Ranch
KANE
1588
OCOT
OCTI
San Andreas Fault
San Jacinto Fault
Elsinore Fault
33.5
33
-116.5
-116
-115.5
-115

Because station MOUN was reset between the 1986 and 1990 surveys, the largest error source is due to the difficulty in establishing the new mark at the previous location. From field inspection, this uncertainty is estimated at 15 cm (in all directions) and is additive to the GPS measurement error.

4.5 Modeling

Theory

Simple dislocation theory is often used to model seismically induced geodetic deformation. The earth is considered a homogeneous isotropic elastic half-space with no stress applied to the free surface. The displacement field u_k for a dislocation Σ in the medium is given by

$$u_k = \frac{1}{8\pi\mu}\int\int_{\Sigma}\nabla u_i w_{ij}^k v_j d\Sigma \qquad (4.1)$$

where ∇u_i is the discontinuity, w_{ij}^k are the displacement Green's functions due to a set of strain nuclei, and v_j are the direction cosines of the normal to the surface element $d\Sigma$ [*Steketee*, 1958; *Chinnery*, 1961]. Analytical solutions to this integral are rather complex, but have been simplified for special cases of dislocation or fault geometry [e.g., *Chinnery*, 1961; *Savage and Hastie*, 1966; *Mansinha and Smylie*, 1967]. General expressions of the displacement field for rectangular strike and dip-slip faults of arbitrary inclination have been computed by *Mansinha and Smylie* [1971] and *Okada* [1985]. Arbitrary slip directions can be designed by the superposition of strike and dip-slip dislocations.

The strain/stress within a medium is computed by differentiating the displacement field. For the displacement u_k where u is a function of the

geometrical coordinates x_i, the components of the strain tensor **E** are given by

$$\epsilon_{ij} = \frac{1}{2}\left(\frac{\partial u_i}{\partial x_j} + \frac{\partial u_j}{\partial x_i}\right) \tag{4.2}$$

In an isotropic medium the stress tensor σ is given by

$$\sigma_{ij} = \lambda\theta\delta_{ij} + 2\mu\epsilon_{ij} \tag{4.3}$$

where θ is the dilatation ($\theta = \sum_{i=1}^{3}\epsilon_{ii}$). We consider the medium as a Poisson solid with $\lambda = \mu = 2.8\text{x}10^{11}$ dyne-cm^{-2}.

A rectangular dislocation within an elastic half-space will create a spatially dependent stress tensor σ throughout the volume. The force acting at a point along an arbitrarily oriented plane in the medium is computed by multiplying σ by the outward normal vector to the plane ($\vec{N}_n$). That is, the traction vector $\vec{T}$ is given by

$$\vec{T} = \sigma\vec{N}_n \tag{4.4}$$

If we assume the plane is coincident with a fault, then the forces generated on this secondary structure due to the initial dislocation are determined by calculating the traction vectors at selected points along the fault. The normal (σ_n), strike-slip (σ_s), and dip-slip (σ_d) stresses on the fault plane are computed by

$$\sigma_n = \vec{T}\cdot\vec{N}_n \tag{4.5a}$$

$$\sigma_s = \vec{T}\cdot\vec{N}_s \tag{4.5b}$$

$$\sigma_d = \vec{T}\cdot\vec{N}_d \tag{4.5c}$$

where $\vec{N}_n$, $\vec{N}_s$, and $\vec{N}_d$ are the normalized vectors perpendicular to, along strike, and along dip to the fault plane. Analytic solutions for the dislocation generated stress and strain fields within a medium are given by *Iwasaki and Sato* [1979] and *Alewine* [1974].

Inverse Methods

Inversion of seismically generated geodetic displacements can yield fault-rupture parameters, such as the slip distribution along a fault plane [e.g., *Ward and Barrientos*, 1986; *Harris and Segall*, 1987; *Segall and Harris*, 1987; *Snay*, 1989]. We use a method similar to that outlined in *Segall and Harris* [1987]. Singular Value Decomposition (SVD) [e.g., *Lanczos*, 1961; *Jackson*, 1972; *Menke*, 1984] and elastic dislocation theory are used to invert the Imperial Valley GPS measurements for seismic slip along the Superstition Hills and Elmore Ranch faults.

The relationship between surface deformation and slip along a rectangular dislocation is defined by Equation (4.1). The rupture plane is modeled as a set of non-overlapping rectangular dislocations. That is, the fault plane is partitioned into multiple sub-elements or sub-faults. The slip distribution along the seismically active fault is given as the discreate approximation of slip along each sub-element. The normal equations which govern surface displacement resulting from such slip is given by

$$\mathbf{A}^g \mathbf{m}^f = \mathbf{d}^g \tag{4.6}$$

where the superscripts g and f refer to geodetic observation and fault slip, respectively. Each row of $\mathbf{A}^g$ is determined from (4.1), and is a function of sub-fault geometry and geodetic position. The slip distribution $\mathbf{m}^f$ is defined by $\mathbf{m}^f = [m_1, m_2, \cdots, m_n]^T$, where m_i is the slip along the ith sub-fault. The data vector $\mathbf{d}^g$ contains the geodetic observables. Each GPS station displacement will add 3 rows to $\mathbf{A}^g$ and 3 elements to $\mathbf{d}^g$, corresponding to the vertical and two horizontal components. In practice, we may choose to ignore the less accurate vertical observation. This is especially true in strike-slip

environments where the predominant displacement direction is horizontal.

Surface rupture is easily included into (4.6) by considering measurements of surface displacement as geodetic observation. The offsets are modeled as a priori slip information on the surface intersecting sub-faults. Equation (4.6) becomes

$$\mathbf{A}\mathbf{m}^f = \begin{bmatrix} \mathbf{A}^g \\ \mathbf{A}^s \end{bmatrix} \mathbf{m}^f = \begin{bmatrix} \mathbf{d}^g \\ \mathbf{d}^s \end{bmatrix} = \mathbf{d} \tag{4.7}$$

where d_i^s are the discreate approximations of surface slip along the fault trace and $A_{ij}^s = 1$ if sub-fault element j corresponds to surface slip offset i; otherwise $A_{ij}^s = 0$.

The GPS displacements shown in Figures 4.4 and 4.5 are not connected to an external reference but are defined relative to station OCTI. (Some geodetic measurements such as line-length change recorded by EDM observations are independent of an absolute reference.) The displacement at OCTI is assumed to be 0, which in fact may be true from a seismic standpoint since this site is far from the Superstition Hills rupture zone. However, any attempt to use the GPS displacements as a criteria for evaluating the effect of the earthquake sequence will be distorted by measurement error at OCTI and/or non-seismic deformation between this site and the other stations. This ambiguity is largely circumvented if displacement-offset terms are estimated in addition to the fault slip parameters. Equation (4.7) is then rewritten

$$\mathbf{A}\mathbf{m} = \mathbf{A} \begin{bmatrix} \mathbf{m}^f \\ \mathbf{m}^\circ \end{bmatrix} = \mathbf{d} \tag{4.8}$$

where m_i° is the ith non-seismic component (i.e., north-south, east-west, vertical) uniformly added to all station displacements.

The Singular Value Decomposition of **A** is given by

$$\mathbf{A} = \mathbf{U}\lambda\mathbf{V}^{\mathrm{T}} \tag{4.9}$$

where U is a matrix of eigenvectors spanning the data space, V is a matrix of eigenvectors spanning the parameter space, and λ is a diagonal matrix of singular values. Without loss of generality this is written

$$\mathbf{A} = \mathbf{U}_p\lambda_p\mathbf{V}_p^{\mathrm{T}} \tag{4.10}$$

where p refers to the non-zero singular values. If the normal equations of (4.8) are normalized to have unit variance [e.g., *Segall and Harris*, 1987], the generalized inverse of (4.8) and (4.10) is given by

$$\mathbf{A}^{-1} = \mathbf{V}_p\lambda_p^{-1}\mathbf{U}_p^{\mathrm{T}} \tag{4.11}$$

[*Lanczos*, 1961; *Menke*, 1984]. In practice it is often necessary to restrict the volume of the parameter space by considering only the k largest singular values, setting all others to 0.

The generalized solution to (4.8) for the k largest singular values is given by

$$\mathbf{m} = \mathbf{A}_k^{-1}\mathbf{d} + \mathbf{V}_0\alpha_0 \tag{4.12}$$

where $\mathbf{V}_0$ are eigenvectors spanning the null space of the model and α_0 is a vector of arbitrary coefficients. The volume of the model space not constrained by observation is defined by $\mathbf{V}_0\alpha_0$. This term is not influenced by the geodetic data and is thus arbitrary. Often it is the minimum-length solution $\mathbf{m} = \mathbf{A}_k^{-1}\mathbf{d}$ which is of interest (the coefficients of α_0 are 0). However, some other solution criteria can be satisfied by carefully designating the coefficients of α_0.

For high resolution fault models where the rupture plane is partitioned into numerous sub-faults, it is necessary to apply some type of smoothing

C-2

constraint over the dislocation surface to prevent the slip distribution from taking on an oscillatory pattern. *Segall and Harris* [1987] showed that the "roughness" of fault slip could be minimized by considering smoothness as an a priori constraint utilized from the model null space through the coefficients of α_0 (Equation 4.12). They considered a smoothing matrix T, with coefficients determined from the discreate approximation of the Laplacian operator $\nabla^2 = \partial^2/\partial x^2 + \partial^2/\partial y^2$, where x and y are the fault distances along strike and dip, respectively. The boundary conditions around the lower and lateral edges of the dislocation are assumed to be null slip, so that the applied smoothing operator causes the calculated fault offset to tend toward zero along these boundarys. Because the Superstition Hills and Elmore Ranch faults ruptured the surface, the upper boundary is considered an unconstrained dislocation. The estimated fault slip is then given by

$$\mathbf{m} = [\mathbf{I} - \mathbf{V}_0(\mathbf{V}_0^T\mathbf{T}^T\mathbf{T}\mathbf{V}_0)^{-1}\mathbf{V}_0^T\mathbf{T}^T\mathbf{T}]\mathbf{A}_k^{-1}\mathbf{d} \qquad (4.13)$$

(Equation 13, [*Segall and Harris*, 1987]). A similar formulation for utilizing fault smoothness over the model null space is given by *Harris and Segall* [1987]; an alternate method considering fault smoothness as quasi-data is provided by *Snay* [1989].

For over-constrained solutions, where there are more independent data than parameters, if $k = p$ then SVD is equivalent to simple least-squares. This is advantageous since the solution provided by (4.12) can be utilized for either uniform dislocations or for detailed parameterizations where the fault plane is partitioned into multiple sub-elements.

Simple dislocation theory has the advantage that the displacement and stress/strain fields for simple fault ruptures can be computed almost

instantaneously. The inverse problem of using geodetic data to calculate the slip distribution along a fault plane is also straightforward. However, we have assumed the earth can be modeled as a homogeneous half-space. Crustal layering or inhomogeneities in the earth can introduce non-existent structure into half-space models [*Savage*, 1987]. While low-resolution schemes such as the average slip over the fault plane will not be seriously affected, attempts to resolve detailed properties may be badly contaminated by artifacts of earth structure.

Seismic Displacement

We model rupture along the Superstition Hills and Elmore Ranch faults as strike-slip dislocations along vertical planes extending from the surface to 10 km depth. Each dislocation approximately coincides with the mapped surface rupture and/or aftershock distribution. The geometrical parameters for the modeled faults are listed in Table 4.5. Initially, the Superstition Hills and Elmore Ranch faults are considered uniform dislocations, with no slip variation allowed on the rupture planes. The dislocations are then partitioned into multiple sub-elements and the slip distribution along the two faults is calculated from the discrete offset for each sub-fault.

For an initial estimate of slip along the two faults, we consider only the displacements at KANE, MOUN, and L589; the three GPS sites nearest the seismic rupture zone (Figure 4.7). Because the observed movements at these stations are relative to OCTI, we also solve for a uniform north-south and east-west offset in the displacements. This will remove any systematic distortion due to measurement error at OCTI. Both faults are regarded as

Table 4.5 Parameters for Modeled Dislocations

	Superstition Hills	Elmore Ranch
Length (km)	25	25
Width (km)	10	10
Strike	N50°W	N40°E
Dip	90	90
Depth (km)	0	0
Latitude (°N)	32.9569	33.1078
Longitude (°E)	-115.7431	-115.7505

Latitude and Longitude are coordinates
at top center of dislocation
Depth is depth to top of fault

Figure 4.7: The best-fit solution to Model 1 (3-station inversion). The solid arrows indicate the observed displacements, while the dashed arrows represent the computed displacement based on Model 1. The shaded region indicates where horizontal displacements are greater than 4 cm.

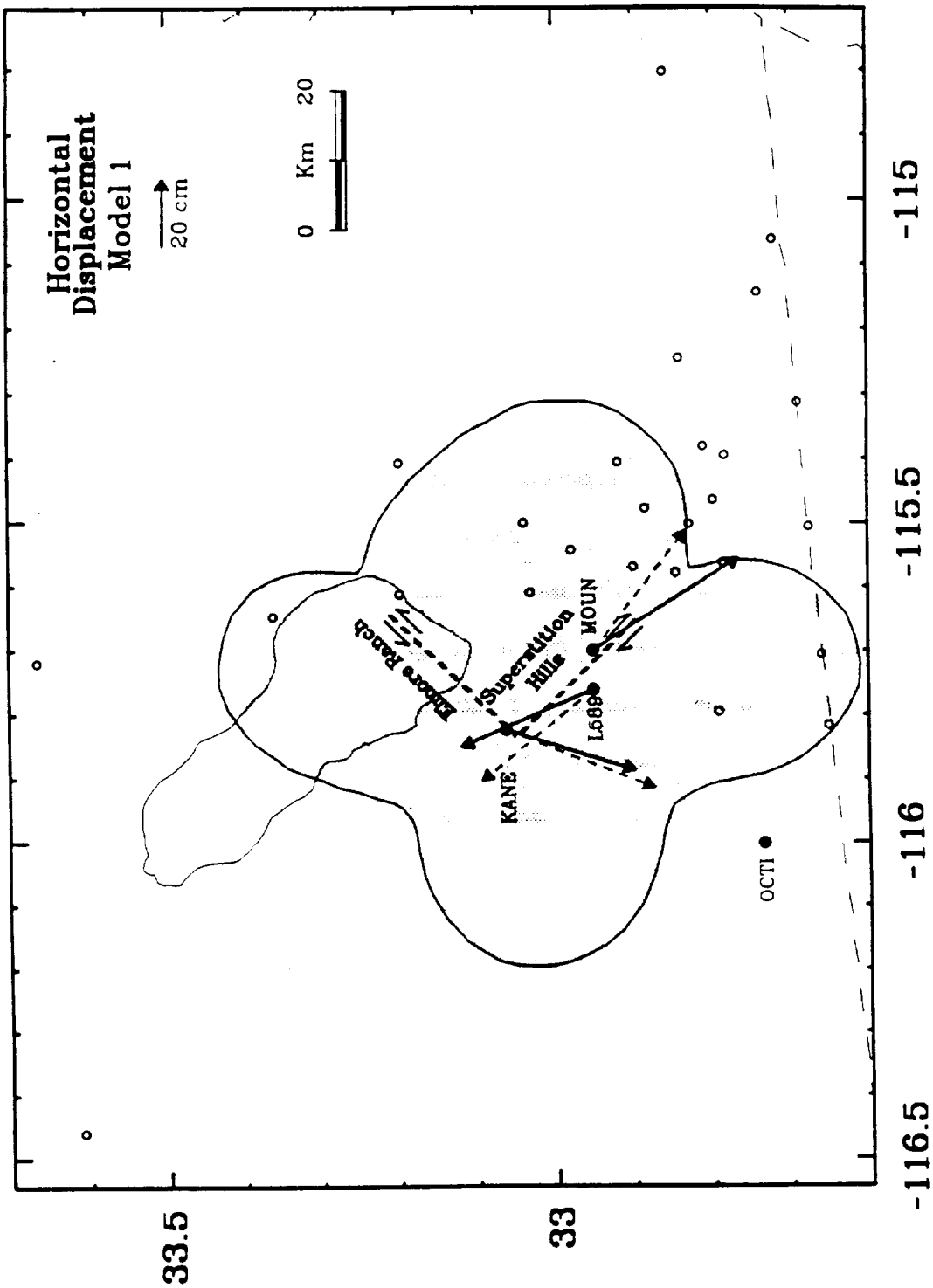
Horizontal
Displacement
Model 1
20 cm
0 Km 20
Superstition
Hills
MOUN
L689
KANE
OCTI
33.5
33
-116.5
-116
-115.5
-115

simple dislocations not segmented into sub-regions. The solution to this simple model is given in Table 4.6 (Model 1) and the observed vs. calculated displacements are shown in Figure 4.7. Generally, there is good agreement between model and observation. This is not altogether unexpected since we are solving for 4 parameters with 6 data. The large discrepancy at MOUN is presumably due to the uncertainty in relocating the 1990 reset monument at the 1986 position (recall the estimated error is 15 cm in each direction). The surface deformation pattern computed from Model I is fairly extensive; the 4 cm horizontal displacement contour is shown in Figure 4.7.

The north-south and east-west displacement components at each Imperial Valley site, plotted as a function of distance from a N40°W trending line through OCTI are shown in Figure 4.8. Shown are the non-seismic movements; that is, the seismic component computed from Model 1 is subtracted from the observed displacements (Figure 4.4). Stations where the seismic correction is greater than 4 cm (in the component plotted) are shown as open circles, other sites as filled circles. The displacements represent a cross-section of non-seismic deformation perpendicular to the plate motion direction.

A fairly consistent pattern is observed in the north-south components (Figure 4.8). Stations to the northeast have moved south (or southeast) about 8.1 cm relative to sites on the other side of the valley. Stations which display the largest deviation are for the most part those sites where the applied seismic correction is greater than 4 cm (open circles). This may indicate additional fault complexity not accounted for by the simple dislocation model used to remove the effects of the 1987 earthquake. The

Table 4.6 Inverse Models of Seismic Slip

Model	Fault	Sub-faults		Slip	Moment
		Strike	Dip	(cm)	($x10^{25}$ dyne-cm)
Model 1	SH	1	1	109. ± 13.	7.8
Model 1	ER	1	1	-45. ± 19.	3.4
Model 2	SH	1	1	130. ± 8.	9.4
Model 2	ER	1	1	-30. ± 10.	2.3
Model 3a	SH	10	5		9.9
Model 3a	ER	10	5		5.9
Model 3b	SH	10	5		8.4
Model 3b	ER	10	5		7.0
Model 3c	SH	10	5		6.2
Model 3c	ER	10	5		3.9
Model 3d	SH	10	5		9.2
Model 3d	ER	10	5		4.9

SH - Superstition Hills fault
ER - Elmore Ranch fault

Figure 4.8: The north-south and east-west GPS displacement components for the 1986-1988 interval. All distances are computed relative to OCTI on a cross section trending N50°E, perpendicular to the plate motion direction. The effects of the 1987 Superstition Hills earthquake sequence based on Model 1 are removed. Open circles indicate stations where the seismic correction is greater than 4 cm (for that component). The 8.1 cm north-south offset between stations on opposite sides of the valley is equivalent to 5.9 cm/yr displacement oriented N40°W. The large scatter for the east-west component is presumably due to large measurement errors in the 1986 survey.

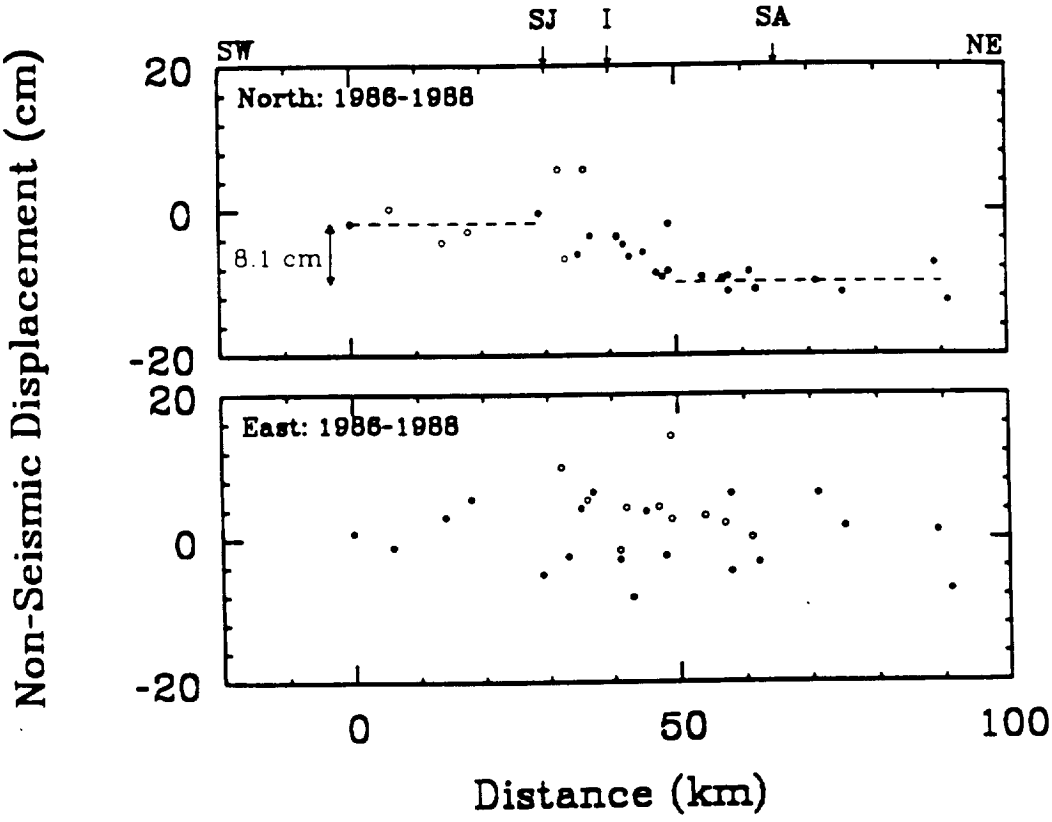
SJ
I
SA
SW
NE
20
0
-20
North: 1986-1988
8.1 cm
20
0
-20
East: 1986-1988
0
50
100
Distance (km)
Non-Seismic Displacement (cm)

east-west oriented displacements, however, show large data scatter; no distinguishable pattern is readily visible across the valley. The scatter is not a function of the magnitude of the applied seismic correction, so presumably it represents the large measurement errors inherent in the east-west direction.

We assume the 8.1 cm north-south offset (Figure 4.8) is attributed to plate-boundary deformation between the North American and Pacific plates. Taking into account the orientation of the suspected deformation (N40°W), as well as the time interval between the 1986 and 1988 surveys (2 years), the north-south movements are consistent with 5.9 cm/yr displacement across the valley. This is significantly larger than the 3.45-4.3 cm/yr rates obtained from conventional surveys. Although accelerated deformation between the GPS campaigns can not be ruled out, there is relatively poor station coverage in the southwest portion of the valley so it is difficult to estimate the valley crossing displacement precisely. This is even more true considering most of the southwestern sites suffered large seismic displacements during 1987. If Model 1 (Table 4.6) does not adequately reflect the rupture process during the Superstition Hills earthquake, the unmodeled effects will propagate into the non-seismic estimate.

The fault rupture calculated from Model 1 depends heavily on shallow slip since the three stations used are all within close proximity to the dislocation planes. While the observed surface offsets indicate rupture extends to the surface, greater slip at depth may go undetected. Therefore, it is necessary to examine the displacement at stations away from the fault to ascertain the depth extent of faulting.

To incorporate more GPS data into the fault-plane inversion, it is necessary to remove the non-seismic deformation from the displacement field. Perhaps the best example of secular deformation across the Imperial Valley is provided by U.S.G.S. trilateration measurements between 1972 and 1987 [e.g., *Prescott et al.*, 1987a; *Prescott et al.*, 1987b]. Computed station velocities for the Salton Trough EDM network (Figure 4.9) are roughly parallel to the direction of plate motion (N40°W), although to some degree the geodetic orientation is dictated by the outer coordinate solution imposed to transform EDM line-length changes into station displacements [*Prescott*, 1981]. The total differential velocity across the network is 3.45 cm/yr and is accommodated in a 50 km wide zone [*Prescott et al.*, 1987b]. Triangulation measurements suggest a larger rate between 1941-1986 (4.3 cm/yr) but these observations are not as accurate as the EDM measurements [*Snay and Drew*, 1988]. However, along the Imperial fault where EDM sites are sparse, the triangulation data suggest concentrated deformation in a narrow 20 km wide zone. The conventional geodetic data are modeled using the following empirical approach. The differential velocity across the valley is taken to be 3.45 cm/yr. Running along the axis of the valley is a transition zone(s) (Figure 4.9), where the strain gradient is defined by simple shear with the displacements oriented N40°W. The transition zone north of the Imperial fault is 50 km wide; to the south it is 20 km wide. The modeled station movements shown by the dashed arrows in Figure 4.9 fit the observed EDM displacements extremely well.

The secular deformation derived from the conventional measurements is removed from the observed GPS displacements (Figures 4.4 and 4.5) leaving

Figure 4.9: Imperial Valley EDM station velocities computed between 1972 and 1987 (solid arrows). The movements are largely attributed to secular deformation due to the relative motion between the North American and Pacific plates. The displacements are modeled (dashed arrows) by 3.45 cm/yr displacement across the valley, with right-lateral simple shear oriented N40°W occurring in a transition zones 50 km wide north of the Imperial Fault and 20 km wide to the south (shaded). The secular deformation is subtracted from the GPS displacements shown in Figures 4.4 and 4.5.

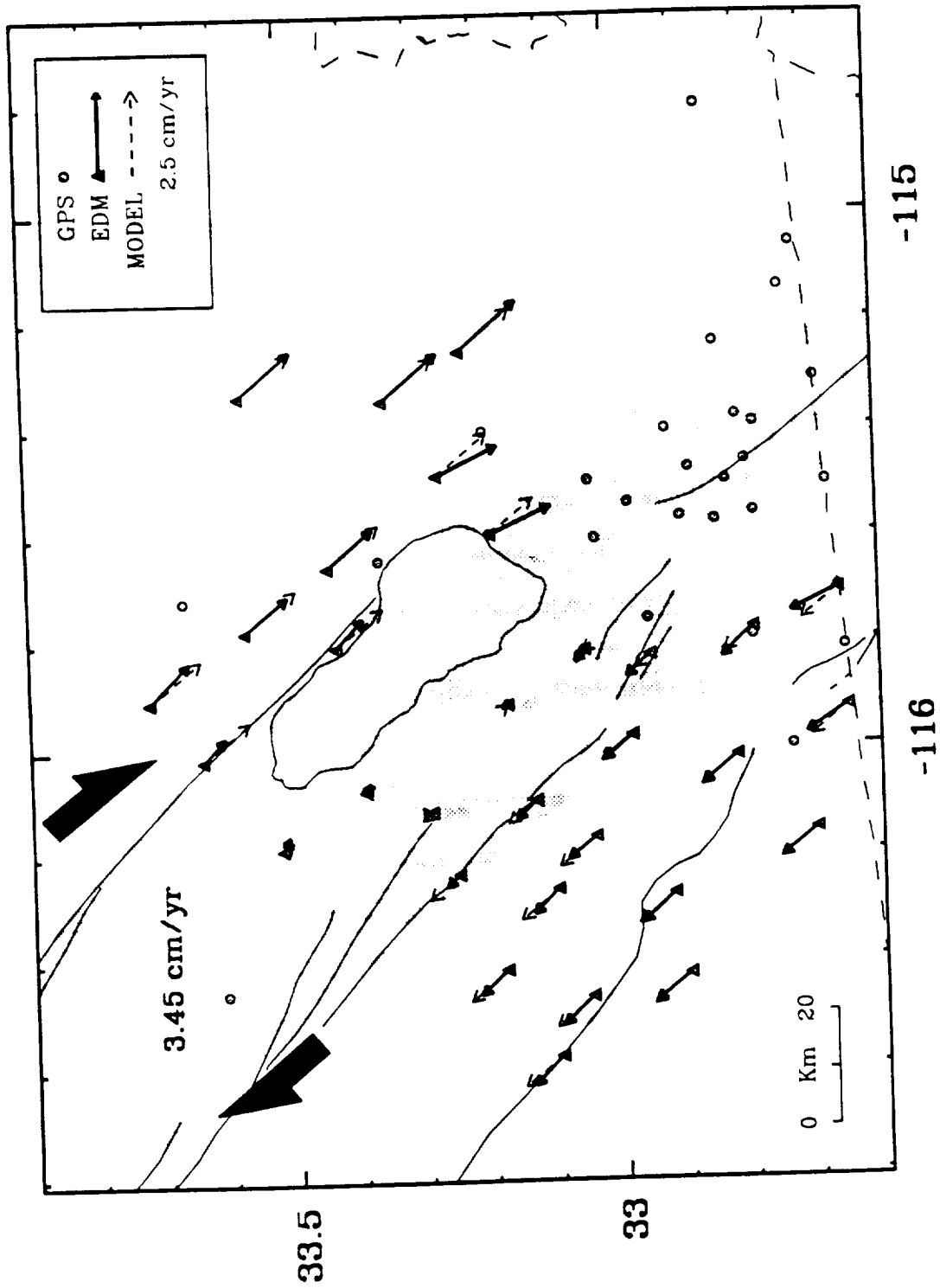
GPS
EDM
MODEL ----->
2.5 cm/yr
3.45 cm/yr
0 Km 20
33.5
33
-116
-115

the seismic component (and measurement error). For Model 2 (Table 4.6) the uniform slip along the Superstition Hills and Elmore Ranch faults is recomputed using all GPS data (without the secular deformation). The residuals (observed minus calculated) for this model are shown in Figure 4.10. The largest station discrepancies between model and observation trend in the longitudinal direction and are especially noticeable for those sites in the southeast. This simply reconfirms our speculation for large east-west trending errors. However, the residuals at the three stations nearest the seismogenic zone are unusually large. The large vector at MOUN is easily explained since this station was reset between surveys. The residuals at L589 and KANE, however, are significantly larger than the average discrepancy computed for the other stations. Because both sites are located in close proximity to the earthquake rupture zone, this suggests additional seismic slip not accounted for by the simple dislocation parameters used for Model 2.

Although the inversion results (Table 4.6) between Model 1 and 2 are marginally different (less slip on the Elmore Ranch fault; more on the Superstition Hills fault), this is not significant considering the estimated uncertainties. In fact, because the near-field (Model 1) and far-field (Model 2) solutions are similar, this suggests that to first order there is not significant slip dependence with depth (within a factor of 2 or 3). It is also noteworthy that the uncertainties improve by only $\sim$ 50 % with the additional data supplied with Model 2. This illustrates the necessity of measurements near the seismic rupture. For simple fault models, where uniform slip is constrained to a single dislocation plane (or two planes in the case of the Superstition Hills sequence), it is as important to have at least minimal

station coverage within a few kilometers of the seismogenic zone as it is to have many sites located away from the fault(s).

Seismic Slip Distribution

Uniform dislocations along the Superstition Hills and Elmore Ranch faults were utilized for Models 1 and 2. To estimate the seismic slip distribution, it is necessary to partition the rupture planes into multiple regions or sub-faults (Model 3). The divisions must be sufficiently dense as to provide reasonable slip resolution. We choose 10 sub-fault elements in the horizontal and 5 in the vertical, so that each fault is partitioned into 50 sub-regions. The dimensions of each dislocation element is 2.0 km in width (vertical) and 2.4-2.6 km in length (2.4 km for Superstition Hills and 2.6 km for the Elmore Ranch fault). The slip distribution along the two rupture planes is constrained to be sufficiently smooth (Equation 4.13). The GPS displacements are adjusted according the the estimated north-south and east-west offsets from Model 2.

In addition to the GPS data, a priori surface-slip information is added to the solution. Surface slip along the Superstition Hills fault (Figure 4.11) [*Williams and Magistrale*, 1989] extends (nearly) the entire length of the modeled fault plane. The surface rupture has been incremented into 2.4 km segments corresponding to the horizontal dimension of each sub-fault. The average slip over each segment is assigned as an a priori slip estimate for the surface fault element which it corresponds. Surface rupture along the Elmore Ranch fault is confined to the southwestern segment (Figure 4.11). Recall for this event that the mapped surface breaks occurred along several nearly

Figure 4.10: The residuals (observed minus calculated) for the best-fit solution to Model 2. The large residual components in the east-west direction are suggestive of measurement error. The residual at MOUN is likely attributed to the reset benchmark between surveys. The unusually large discrepancy at L589 (and KANE) suggest additional seismic deformation not accounted for by the simple uniform slip parameterization considered for Model 2.

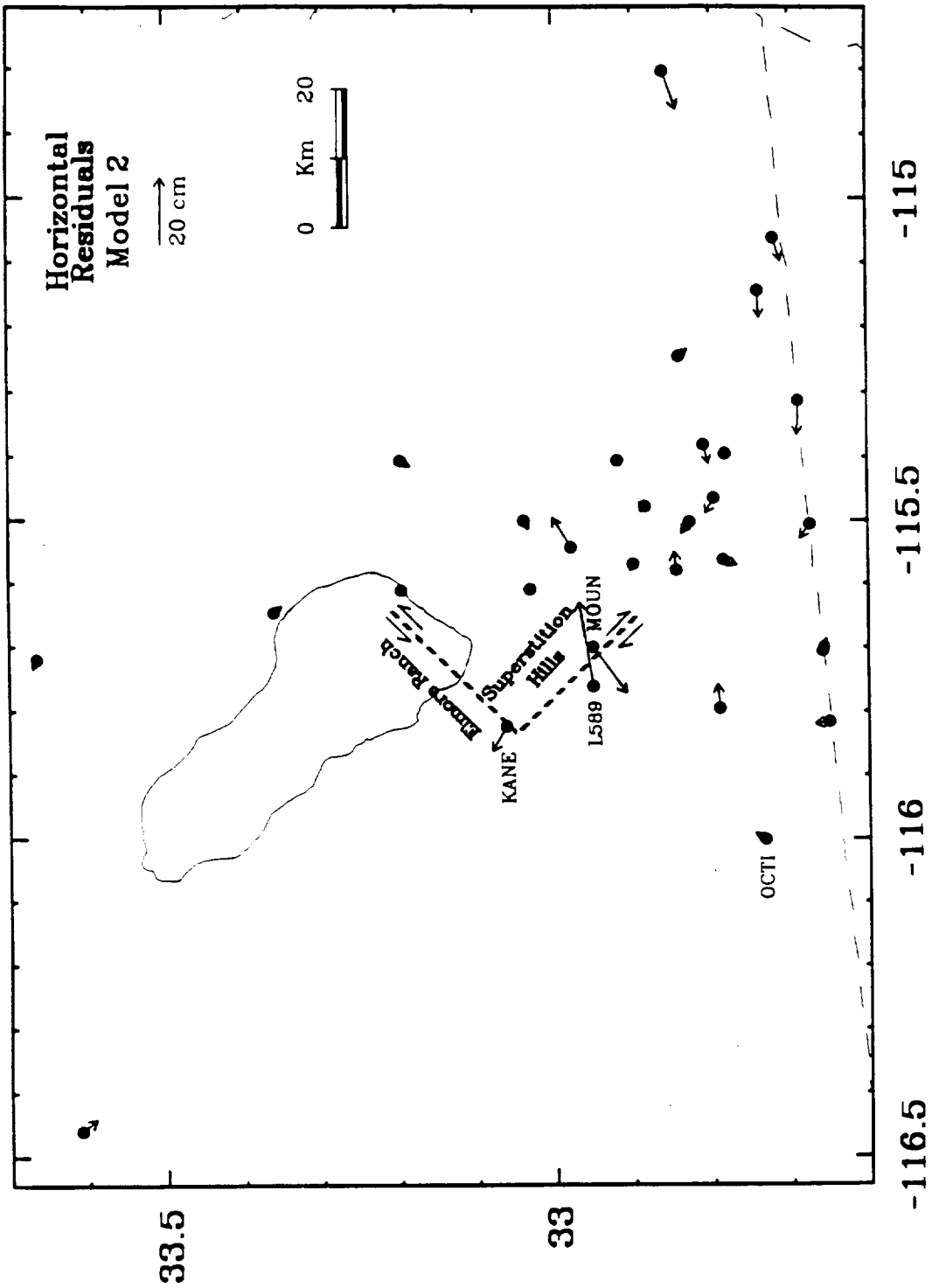
Horizontal
Residuals
Model 2
20 cm
0 Km 20
Superstition
Hills
Elmore Ranch
KANE
L589
MOUN
OCTI
33.5
33
-116.5
-116
-115.5
-115

Figure 4.11: Observed surface slip along the Superstition Hills and Elmore Ranch faults (dashed lines). The Superstition Hills offsets were measured on January 25 and 26, 1988 about 1 month before the GPS observations. Decaying afterslip is recorded up to nearly 1 year after the earthquake sequence. The Elmore Ranch measurements are the cumulative slip from multiple surface breaks across a 10 km wide zone, with no recorded postseismic offset after the earthquake. The discrete approximation to the surface slip used to constrain the uppermost subfault elements in Models 3a and 3b is shown by the solid lines.

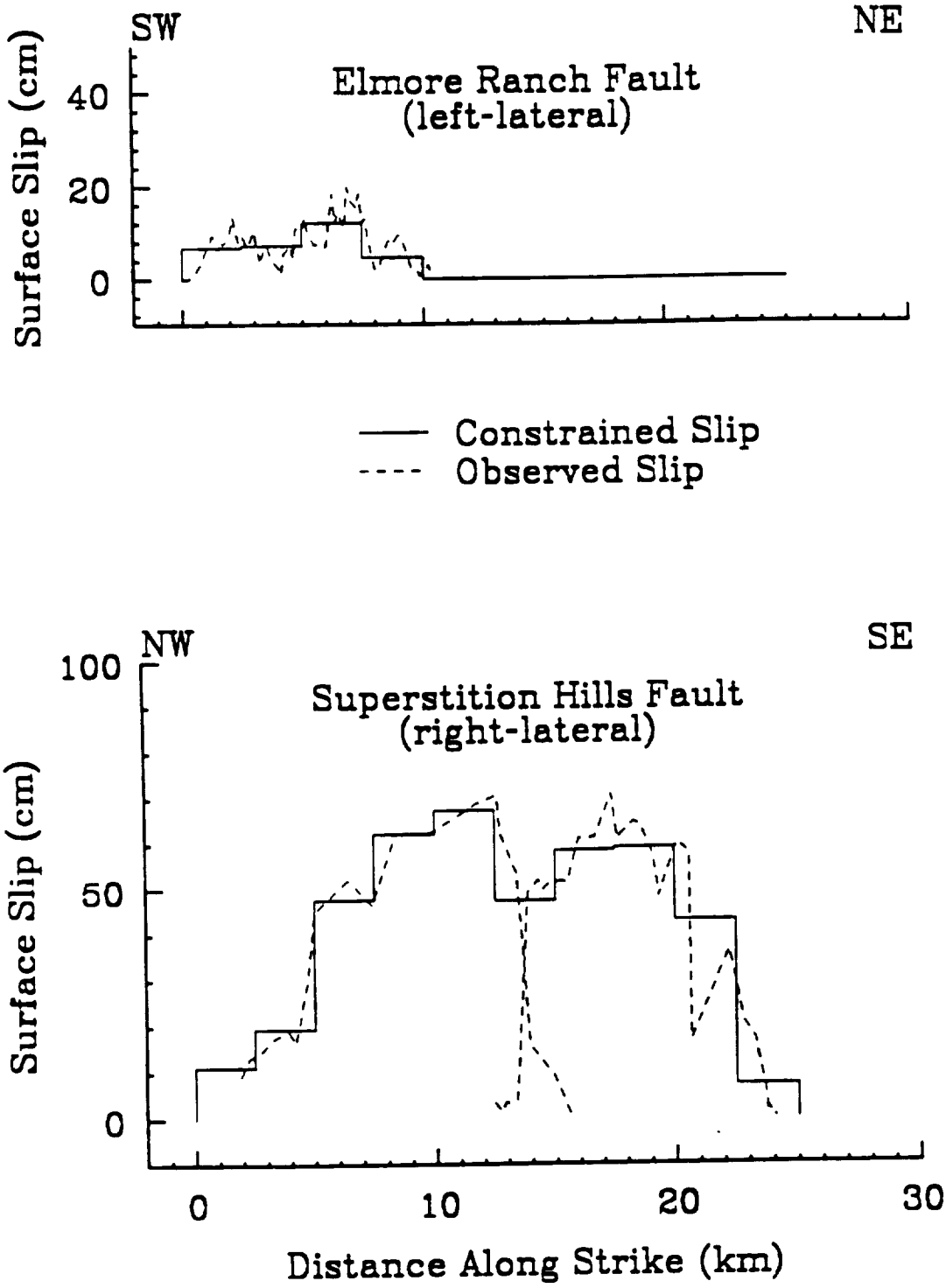
SW
NE
Elmore Ranch Fault
(left-lateral)
Surface Slip (cm)
40
20
0
Constrained Slip
Observed Slip
NW
SE
Superstition Hills Fault
(right-lateral)
Surface Slip (cm)
100
50
0
0
10
20
30
Distance Along Strike (km)

parallel strands (Figure 4.2). We take the cumulative surface offset for all strands [*Hudnut et al.*, 1989a] averaged over 2.6 km segments along the fault, and apply this as a priori slip information for the surface sub-fault elements. Where no rupture is mapped (to the northeast), the surface intersecting fault partitions are assigned 0 slip. The a priori uncertainty for each surface-slip estimate is assumed to be 10 cm.

The number of independent parameters estimated through singular value decomposition depends on the number of singular values k utilized in Equation (4.12). A trade-off exists between solution variance and resolution [e.g., *Menke*, 1984]. While large k produces highly resolved models, this is at the expense of increasing solution uncertainty. Correspondingly, small k yields low variance solutions but does not provide detailed resolution. A total of 100 sub-fault elements are incorporated into Model 3 (50 for each fault). If $k = 100$ then slip along each sub-fault will be determined uniquely. Because of limited geodetic coverage, however, it is practical to consider only the first few eigenvectors of the parameter space defined by the geodetic observations. Therefore, each solved parameter is a function of some average slip over multiple sub-fault elements. This is fundamental property of singular value decomposition when used to solve under-determined or poorly-determined problems [e.g., *Jackson*, 1972]. It is necessary to determine the k which maximizes the resolution without allowing the solution to become too oscillatory or unstable.

The geodetic moment, solution instability, and model residual calculated for different values of k are shown in Figure 4.12. The moment is a function of the average slip along the fault planes, while solution instability is

determined from the standard deviation of slip for each sub-fault element. An instability of 0 (stable) indicates uniform slip along the fault planes, while high values indicate an oscillatory or unstable solution. The RMS indicates the agreement between model and observation and is calculated by $RMS = \sum(o_i - c_i)^2/\sigma_i^2$ where o_i is the observed, c_i is the calculated, and σ_i is the uncertainty assigned to the ith observation.

With surface slip incorporated into the solution (Figure 4.12a), the first 20 singular values are well constrained by the measured offset along the fault, and are influenced little by the geodetic observations. The surface measurements reflect the dislocation on the uppermost fault elements, with little depth resolution. This is illustrated by the solution for $k = 20$. The calculated moments are significantly less than that for Model 2, presumably because the surface offset is not representative of the larger displacement along the rest of the fault plane(s). Consequently, in order to estimate the slip distribution with depth it is necessary to consider solutions where $k > 20$. After $k = 30$ the solution becomes very oscillatory as is indicated by the increasing instability value. The RMS is significantly reduced beyond $k = 20$ but only improves marginally with increasing k. The solution fit for $k > 20$ is slightly better than that for Model 2.

Also evident in Figure 4.12a are the large moment estimates for the Elmore Ranch fault, which are almost equal to the computed moments for the Superstition Hills fault. This is unexpected considering the latter event yielded a significantly greater surface wave magnitude, as well as a larger moment estimated from Model 2. It is difficult to distinguish slip between the two faults using SVD as is illustrated by Figure 4.13. The displacement

Figure 4.12a: The geodetic moment, standard deviation of sub-fault slip (instability), and solution RMS calculated for different singular values (k). Shown here are solutions constrained by surface slip measurements ($20 \leq k \leq 30$).

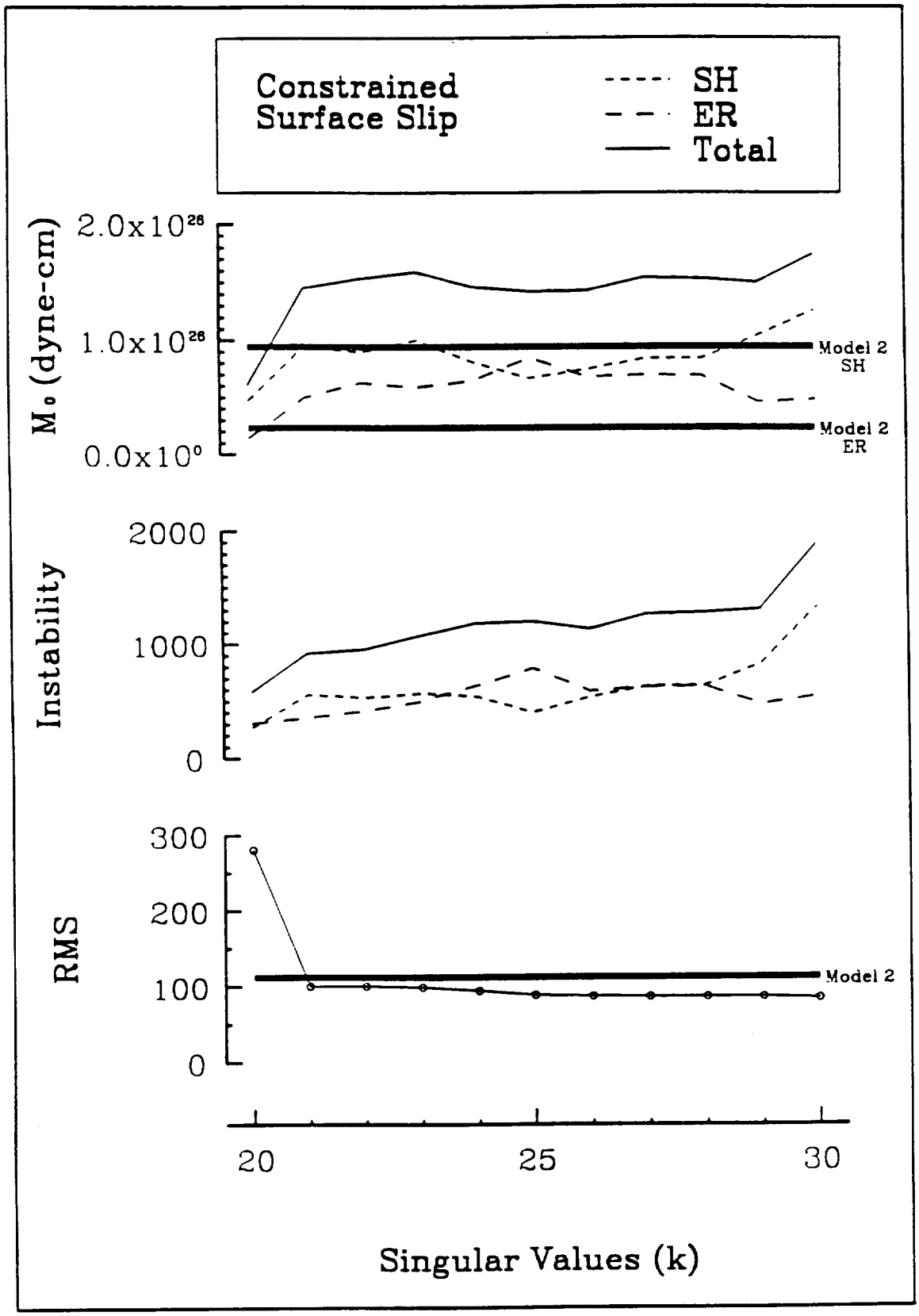
Constrained
Surface Slip
SH
ER
Total
M_o (dyne-cm)
2.0x10²⁶
1.0x10²⁶
0.0x10⁰
Model 2
SH
Model 2
ER
Instability
2000
1000
0
RMS
300
200
100
0
Model 2
20
25
30
Singular Values (k)

Figure 4.12b: The geodetic moment, standard deviation of sub-fault slip (instability), and sol[illegible]S calculated for different singular values (k). Shown here are solutic[illegible]onstrained by surface slip measurements ($1 \leq k \leq 10$).

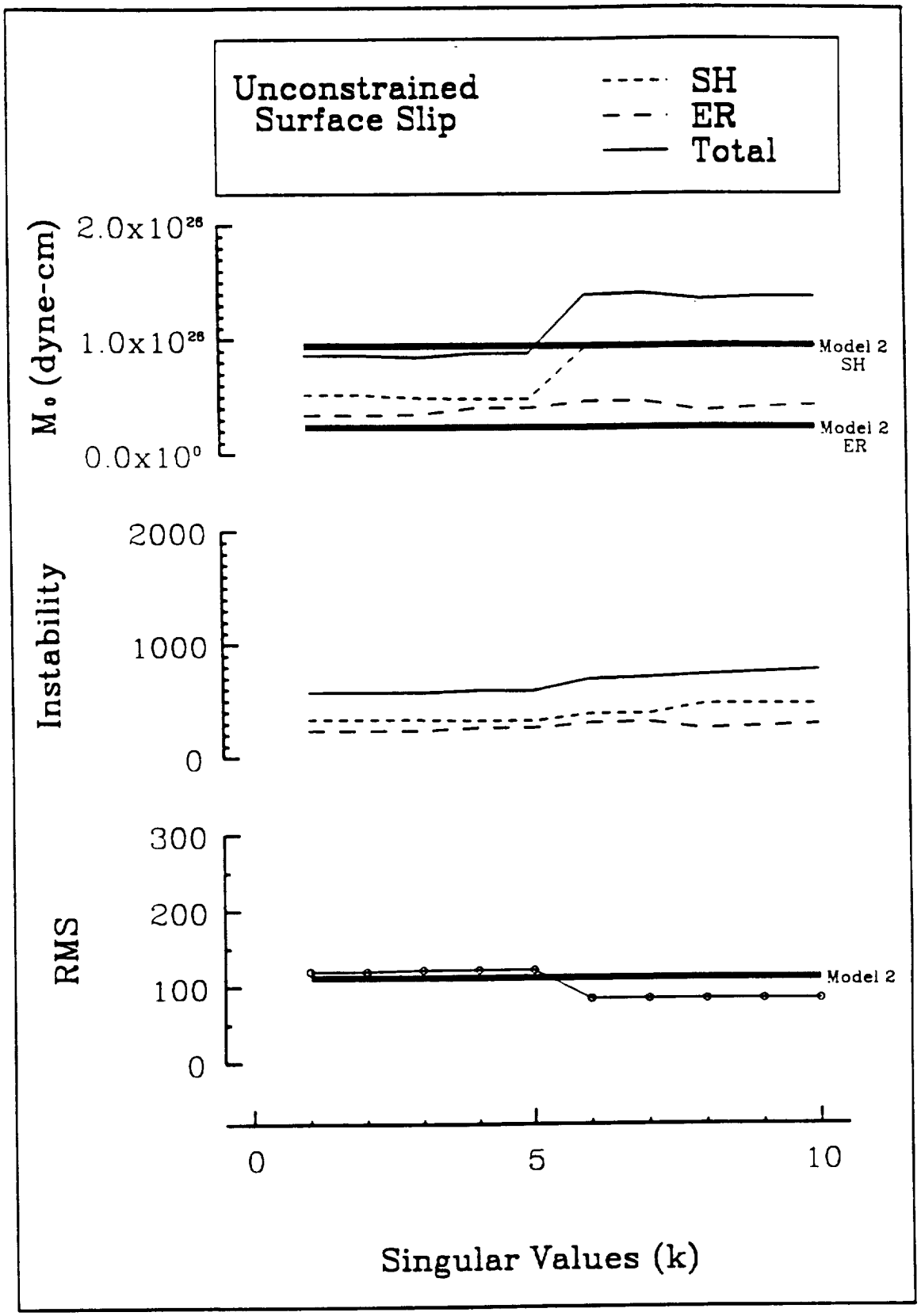
Unconstrained
Surface Slip
SH
ER
Total
M_o (dyne-cm)
2.0x10²⁶
1.0x10²⁶
0.0x10⁰
Model 2
SH
Model 2
ER
Instability
2000
1000
0
RMS
300
200
100
0
Model 2
0
5
10
Singular Values (k)

Figure 4.13: The horizontal slip distribution calculated independently for the Superstition Hills and Elmore Ranch faults based on Model 2. The shaded region indicates where the horizontal deformation is greater than 2 cm for the Superstition Hills fault and 0.5 cm for the Elmore Ranch fault. The scale for the Elmore Ranch event is altered to account for the smaller dislocation. The deformation pattern is almost identical between the two faults, although the displacement magnitudes are larger for the Superstition Hills event. This illustrates the difficulty in using the GPS measurements to resolve slip between the two faults.

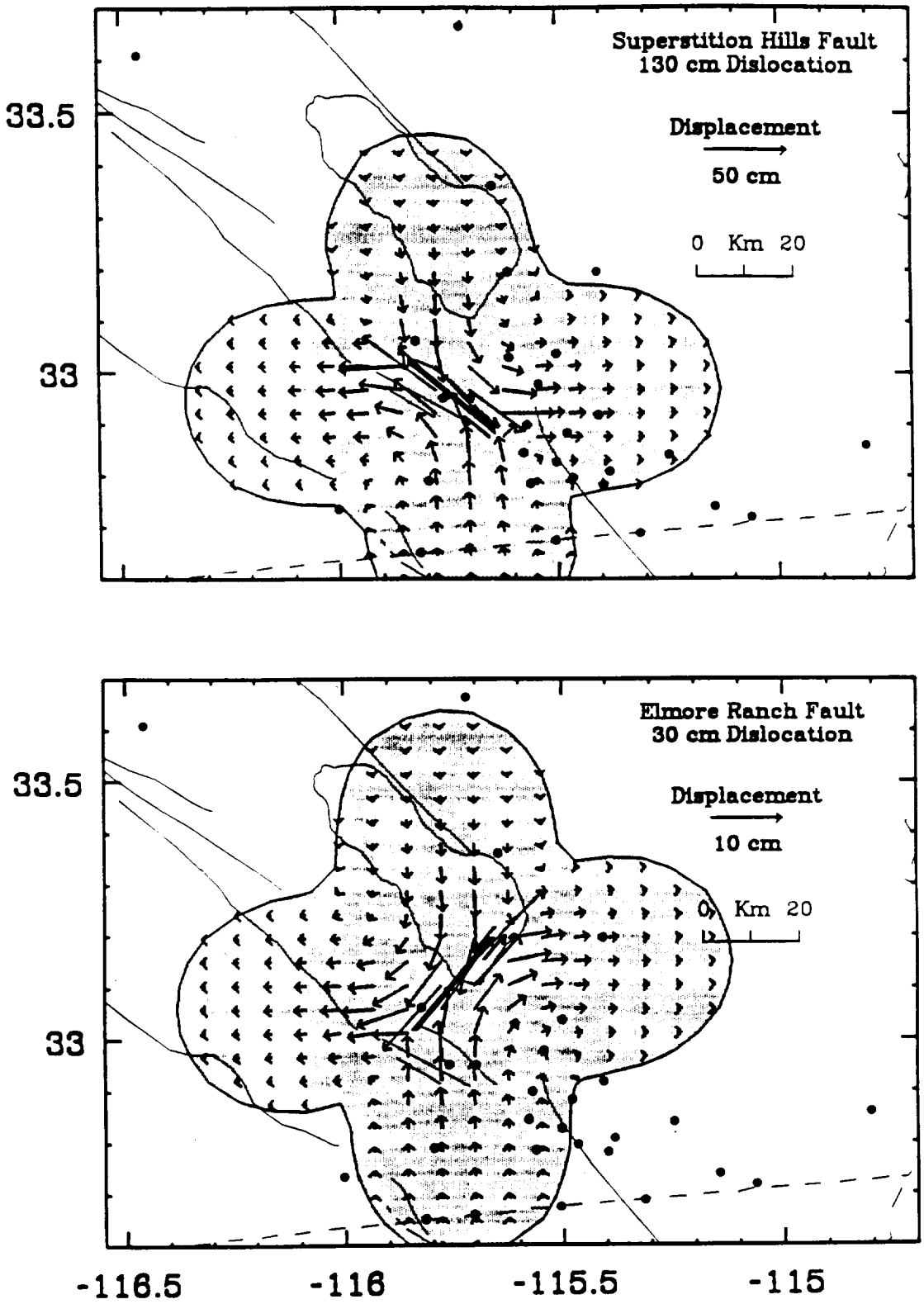
Superstition Hills Fault
130 cm Dislocation
Displacement
50 cm
0 Km 20
Elmore Ranch Fault
30 cm Dislocation
Displacement
10 cm
0 Km 20
33.5
33
-116.5
-116
-115.5
-115

pattern for a 130 cm rupture on the northwest trending right-lateral Superstition Hills fault is compared with a 30 cm rupture on the northeast trending left-lateral Elmore Ranch fault. Although the magnitude is different, the deformation pattern between the two dislocations is almost identical. As a result, the larger slip estimate along the Superstition Hills fault is being mapped onto the Elmore Ranch fault plane producing the higher moment. This is all the more true considering only the first few model-space eigenvectors are utilized, as is necessary since Model 3 is very underdetermined (more model parameters than data). Therefore, only linear combinations of model parameters are uniquely defined. The similar moments indicated by Figure 4.12a suggest slip between the two faults is strongly correlated in the solution.

The estimated seismic slip distribution along the Superstition Hills and Elmore Ranch faults for $k=23$ and $k=27$ are shown in Figure 4.14a. We refer to these solutions as Models 3a and 3b, respectively (Table 4.6). Although both faults are partitioned into 50 elements, the fault-rupture is not as resolved as the contours suggest since only the first few (non-surface) model-space eigenvectors are independently solved. For $k=23$ the solution suggests fairly uniform rupture along both fault planes. The dislocation may be slightly concentrated to the southwest along the Elmore Ranch fault. The apparent "bullseye" pattern is due to the smoothness constraints requiring the slip to tend towards 0 along the lateral edges and lower boundaries (the upper boundaries are constrained by the surface slip information). There is little difference in the slip distribution for $k=21$ through $k=26$. However, there is a noticeable change in the dislocation pattern starting with $k=27$. While slip

along the Elmore Ranch fault still appears fairly uniform, displacement along the Superstition Hills fault is concentrated to the northwest and to the southeast. This change is significant and is caused by the GPS displacement at one station. Recall the large residual for L589 in Model 2 (Figure 4.10). This discrepancy is nearly eliminated beginning with $k = 27$. Therefore, in order to satisfy the observed displacement at L589, it is necessary to concentrate rupture at each end of the Superstition Hills fault. Of course this analysis assumes the observed GPS displacement at L589 is seismically generated, and not contaminated by unusually large measurement error. The dislocation null near the center of the fault roughly corresponds to the drop in fault offset measured at the surface (Figure 4.11).

Independent solutions are made without constraining the upper sub-fault elements by measurements of surface offset (Figure 4.12b). The unconstrained moments are generally smaller than when surface slip is incorporated into the model. This is because the surface measurements are less than the average slip estimate along the fault plane. Without surface constraint, the geodetic data are satisfied to a greater degree by slip near the surface; otherwise, it is necessary to compensate the small shallow offsets by increased slip at greater depths. The seismic slip distribution estimated without surface constraint along the Superstition Hills and Elmore Ranch faults for $k = 3$ and $k = 7$ are shown in Figure 4.14b. We refer to these solutions as Models 3c and 3d, respectively (Table 4.6). For these unconstrained solutions the slip distribution is confined to shallower depths. Slip concentration at each end of the Superstition Hills fault is suggested for $k = 7$, although this division is not as pronounced as in Model 3b. We conclude that incorporating measurements

Figure 4.14a: Slip distribution along the Superstition Hills and Elmore Ranch faults computed from Singular Value Decomposition. Each fault is partitioned into the 50 sub-elements indicated by the grid spacing. Shown here are solutions for $k = 23$ and $k = 27$ constrained by measurements of surface offset.

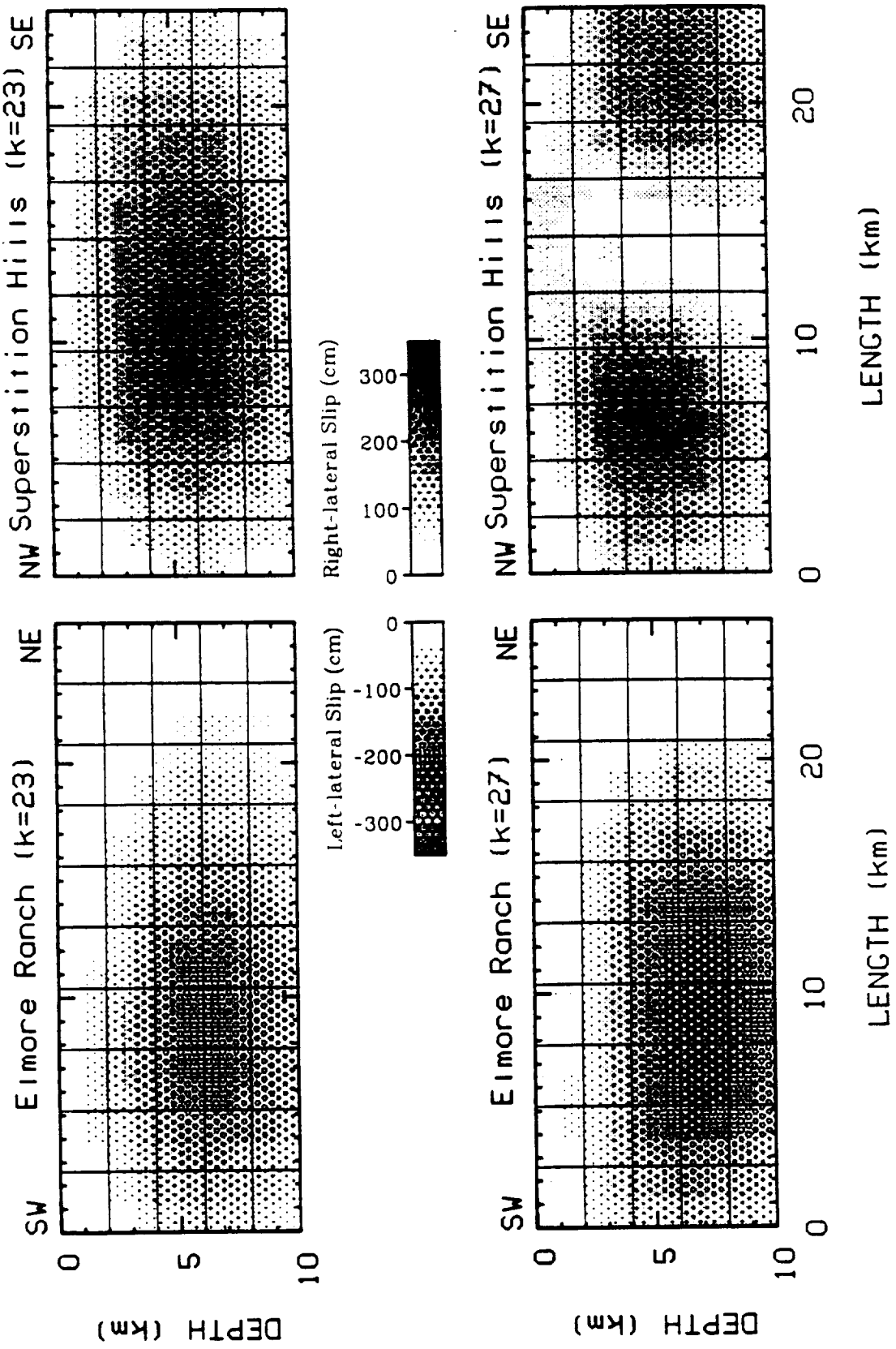
NW Superstition Hills (k=23) SE
SW Elmore Ranch (k=23) NE
NW Superstition Hills (k=27) SE
SW Elmore Ranch (k=27) NE
Right-lateral Slip (cm)
300
200
100
0
Left-lateral Slip (cm)
0
-100
-200
-300
DEPTH (km)
0
5
10
LENGTH (km)
0
10
20

Figure 4.14b: Slip distribution along the Superstition Hills and Elmore Ranch faults computed from Singular Value Decomposition. Each fault is partitioned into the 50 sub-elements indicated by the grid spacing. Shown here are solutions for $k = 3$ and $k = 7$ unconstrained by surface slip measurements.

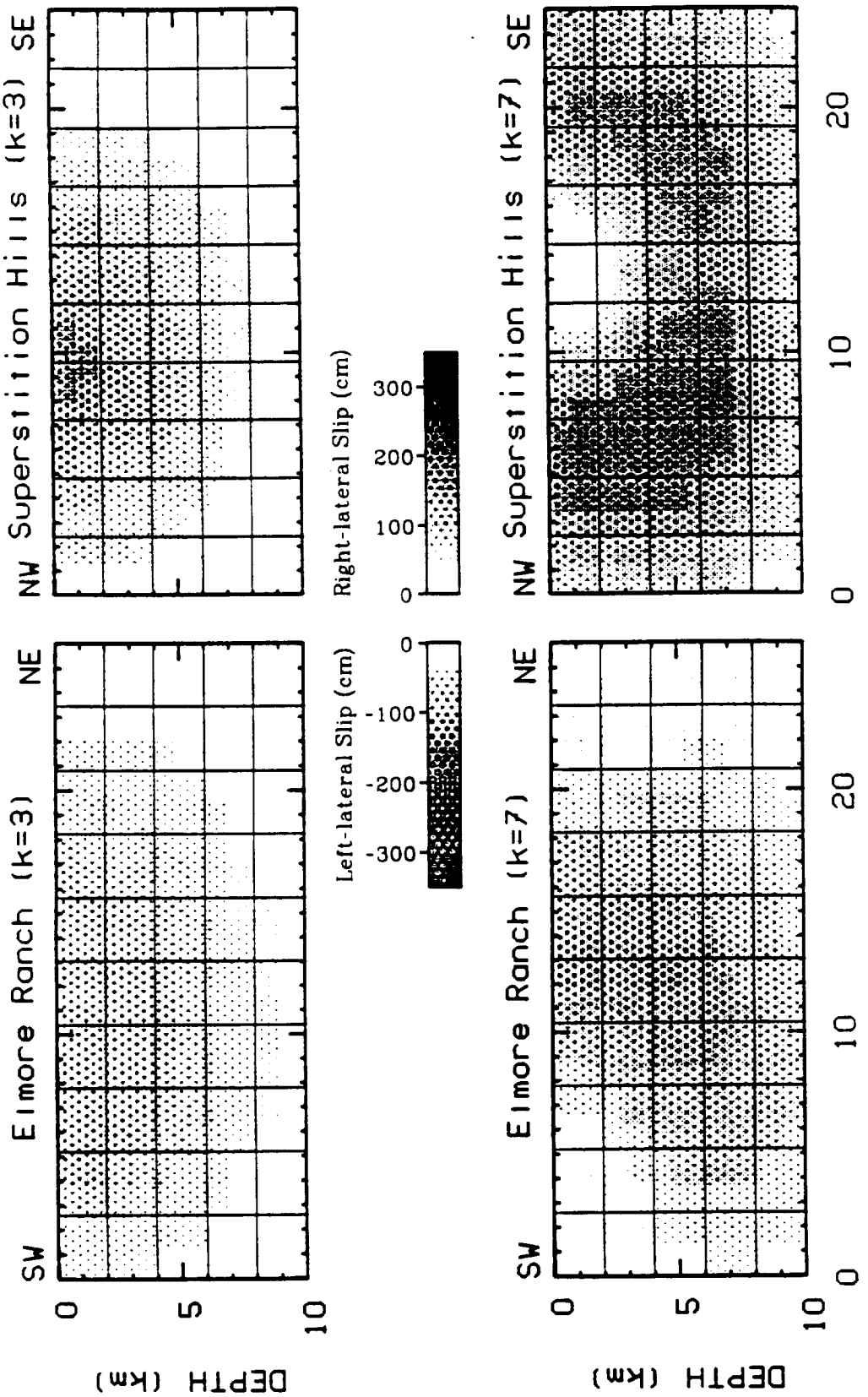
SW
Elmore Ranch (k=3)
NE
NW
Superstition Hills (k=3)
SE
SW
Elmore Ranch (k=7)
NE
NW
Superstition Hills (k=7)
SE
DEPTH (km)
0
5
10
LENGTH (km)
0
10
20
Right-lateral Slip (cm)
300
200
100
0
Left-lateral Slip (cm)
0
-100
-200
-300

of surface offset tends to change displacement magnitude by requiring slip at greater depths, however, it does not significantly alter estimates of slip distribution.

4.6 Geophysical Implications

Conjugate Faulting

The most prominent feature of the Superstition Hills earthquake sequence is the conjugate relationship exhibited by near-simultaneous ruptures along right-lateral northwest and left-lateral northeast trending faults. In the context of the Imperial Valley, the northeast trending structures are termed "cross-faults" [e.g., *Hudnut et al.*, 1989a]. Conjugate and cross-fault seismicity seems to be a fairly typical phenomenon for this region (Figure 4.15), and may dictate the strain transfer mechanism between faults. The 1981 Westmorland earthquake (M_L 4.1) is a prime example of cross-fault tectonics. The mainshock and aftershock sequence is clearly mapped onto a northeast trending lineament. Other examples are associated with the Imperial fault. The largest aftershock (M_L 5.8) following the 1979 Imperial Valley earthquake (M_L 6.6) was located near the town of Brawley [*Johnson and Hutton*, 1982]. The focal mechanism and following seismicity suggested left-lateral slip along a vertical northeast trending fault. *Reilinger and Larsen* [1986] found that rupture along an identical conjugate structure successfully modeled geodetic observations within the Brawley Seismic Zone. A large (M_L 5.5) aftershock was also recorded near Brawley following the 1940 earthquake [*Neumann*, 1942]. Due to the sparsity of seismic data, neither the mechanism nor location are precisely determined, although we speculate this event occurred

along the same northeast trending feature as the large 1979 aftershock. Of historical interest are Imperial Valley earthquake pairs during 1915 (M_L 6.3, M_L 6.3) and 1927 (M_L 5.8, M_L 5.5) [*Beal*, 1915; *Toppozada et al.*, 1978]. In each case the 2nd shock followed the first by about 1 hour, contrasting with the 12 hour interval between the 1987 events. It is not known which fault(s) ruptured during these earthquake sequences, but conjugate fault interaction is highly probable.

Rupture on the Superstition Hills fault was almost certainly triggered by the Elmore Ranch event (occurring 12 hours earlier) suggesting some mechanism of stress transfer between the two faults. Figure 4.16 shows the normal (σ_n) and strike-shear (σ_S) stress components instantaneously applied to the Superstition Hills fault due to a 30 cm left-lateral Elmore Ranch dislocation (Model 2). Tension and right-lateral shear are considered positive, both tending to induce failure on the rupture plane. Also shown is the Coulomb failure stress (σ_c), here given by $\sigma_c = \sigma_s + \mu\sigma_n$, where $\mu = 0.75$. Positive values indicate stress-loading leading toward shear failure.

The stress regime necessary for left-lateral rupture along a northeast trending fault is identical to that required for right-lateral failure along a northwest trending fault. Hence, we can assume that the Superstition Hills rupture plane was at or near failure at the time of the Elmore Ranch event. The initial shock generated an increase in the Coulomb failure potential along the Superstition Hills fault (Figure 4.16), possibly advancing it past its failure threshold. This is seen mostly as a combination of reduced compressive normal stress (earthquake inducing) countered by left-lateral shear (earthquake inhibiting). The increase is maximized along the northwest

Figure 4.15: Known and/or potential conjugate/cross-fault seismic episodes in the Imperial Valley since 1900. Seismic release on (left-lateral) northeast trending structures was observed in 1979, 1981, and 1987. Earthquake pairs or mainshock/aftershock sequences suggestive of conjugate faulting were observed in 1915, 1927, 1940. This suggests conjugate/cross-fault interaction is typical for the Imperial Valley.

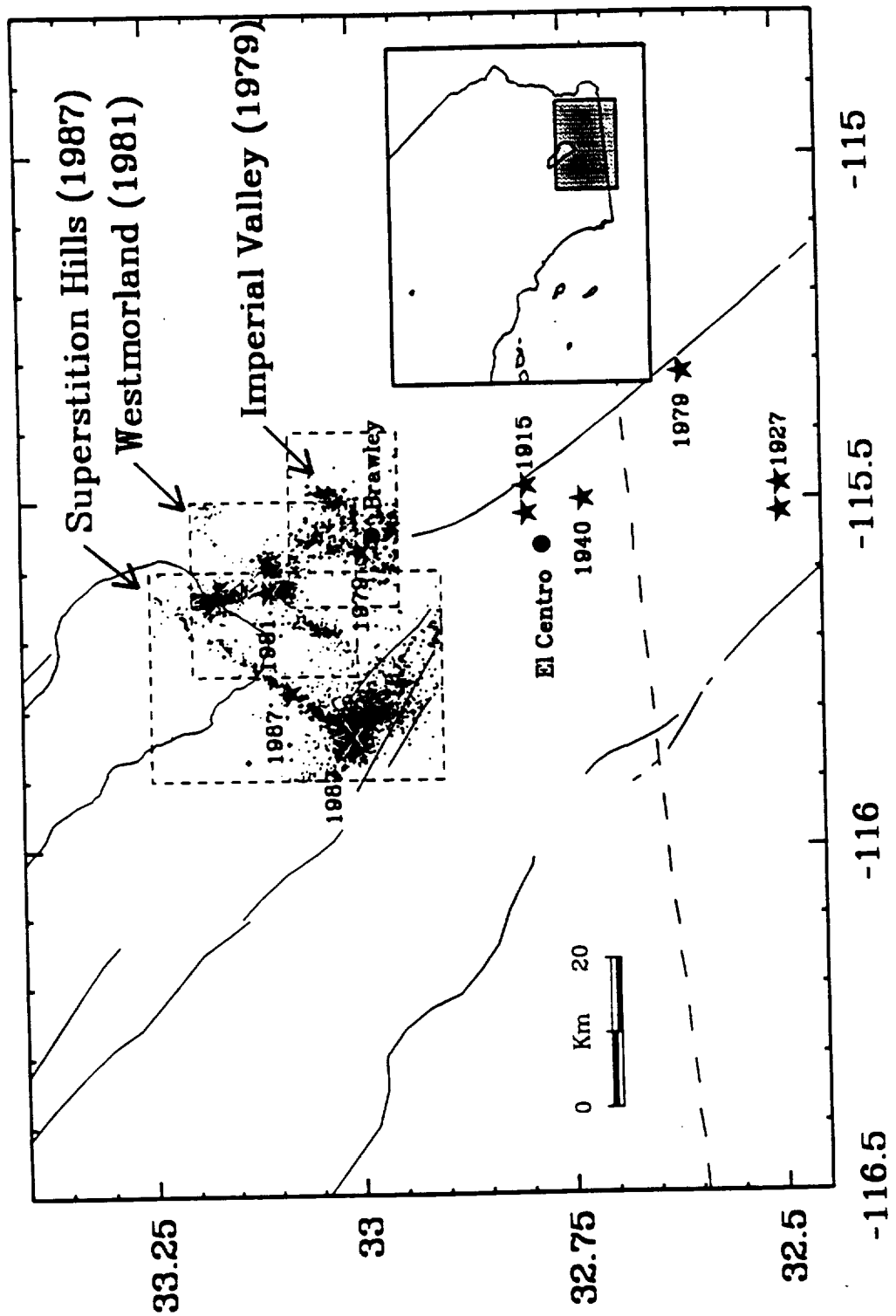
Superstition Hills (1987)
Westmorland (1981)
Imperial Valley (1979)
Brawley
El Centro
1915
1940
1979
1927
1981
1987
1979
0 Km 20
33.25
33
32.75
32.5
-116.5
-116
-115.5
-115

Figure 4.16: Strike-shear (right-lateral positive) and normal stress change (dilatation positive) induced on the Superstition Hills fault due to a 30 cm left-lateral Elmore Ranch dislocation (Model 2). Also shown is the Coulomb failure stress change, where positive values indicate an increased potential for rupture (earthquake inducing stress). The northwest third of the 1987 Superstition Hills rupture plane underwent a stress change tending it toward failure with the maximum change calculated in the epicentral region near the intersection with the Elmore Ranch fault. There was no rupture to the northwest where the Coulomb failure stress was negative (reduced earthquake potential). The magnitude of the stress change (in bars) is in the range of typical earthquake stress drops.

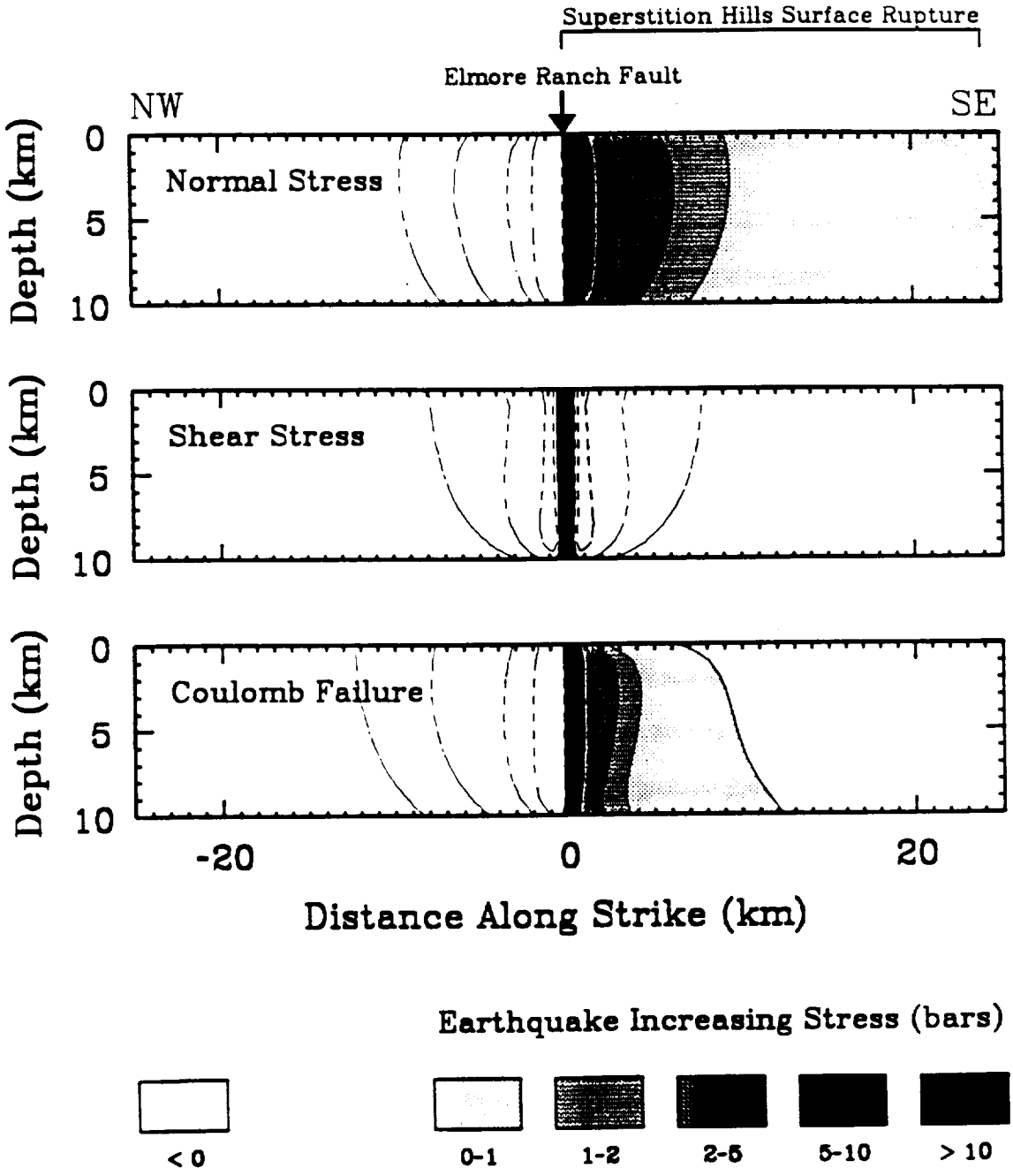
Superstition Hills Surface Rupture
Elmore Ranch Fault
NW
SE
Depth (km)
0
5
10
Normal Stress
Shear Stress
Coulomb Failure
-20
0
20
Distance Along Strike (km)
Earthquake Increasing Stress (bars)
< 0
0-1
1-2
2-5
5-10
> 10

boundary of the rupture plane, near the nucleation point of the second event. Presumably rupture began where the applied stress was greatest and then propagated to the southeast. Northwestward rupture is prohibited because the increase in compressive forces tends to inhibit shear failure along this segment of the fault. The magnitude of the Coulomb stress increase near the Superstition Hills epicentral zone ($\sim$ 10 bars) is comparable to typical earthquake stress drops.

The one to several hour delay recorded between events during observed and suspected conjugate episodes in the Imperial Valley is significant from an earthquake failure perspective. Shown in Figure 4.17 are potential scenario's for earthquake ruptures involving conjugate-mainshock interaction, such as that observed for the Superstition Hills events. We assume faults fail by an undefined mechanism when they are at or above some critical stress level. The regional strain acting over several years brings a given fault near this critical failure point. A stress increase is induced along part of the fault plane due to rupture on a conjugate structure (e.g., Figure 4.16), which may or may not be sufficient to push the stress state past its critical threshold. In the case of Earthquake 1 (Figure 4.17a), the stress change caused by the conjugate event is not enough to induce failure. Some form of time dependent stress transfer onto the fault is active and eventually the critical level is reached. Such a mechanism involving postseismic viscous creep along the Elmore Ranch fault has been suggested for the 1987 Superstition Hills sequence [*Given and Stuart*, 1988]. If this scenario is valid we would equally expect failure modes such as that indicated by Earthquake 2. Here the instantaneous stress applied to the fault from the conjugate event pushes the stress state past the

critical level and rupture is immediate. In this case failure along the two perpendicular fault planes will occur simultaneously. However, this behavior is not observed in the Imperial Valley. Conjugate episodes characteristically have been separated by one to several hours. This suggests that the critical stress level can be exceeded without immediate failure. Therefore, some time dependent mechanism must be active on the fault plane, as opposed to additional stress transfer through the crust. We loosely refer to this as "stress corrosion" (Figure 4.17b) [e.g., *Das and Scholz*, 1981]. In the case of Earthquakes 3 and 4, it is suggested that the critical stress level must be exceeded for a period of one to several hours before failure occurs. *Hudnut et al.* [1989b] proposed fluid diffusion as an alternate mechanism, whereby the effective normal stress was reduced (made more positive) due to pore-fluid infiltration into the rupture plane, thus increasing the Coulomb failure stress. This process still involves action on the fault plane rather than stress transfer. Regardless of cause, the temporal and geometric relationship exhibited by the conjugate fault interaction is seemingly typical of Imperial Valley tectonics and is thus an important factor for the potential prediction of large earthquakes and aftershocks.

Moment and slip distribution

The geodetic (GPS) source parameters for the Superstition Hills and Elmore Ranch earthquakes are listed in Table 4.6 and Figure 4.14. The seismic moment is best defined by Model 2, while the slip distribution is best expressed by Models 3a and 3b. Model 1 is constrained with minimal station coverage and Models 3c and 3d do not include the additional information supplied from surface slip measurements. The GPS observations are directly

Figure 4.17: Schematic of potential earthquake failure processes in the Imperial Valley. a) Earthquake failure occurs after some critical stress is reached. b) Earthquake failure occurs following a time dependent delay after critical stress is exceeded.

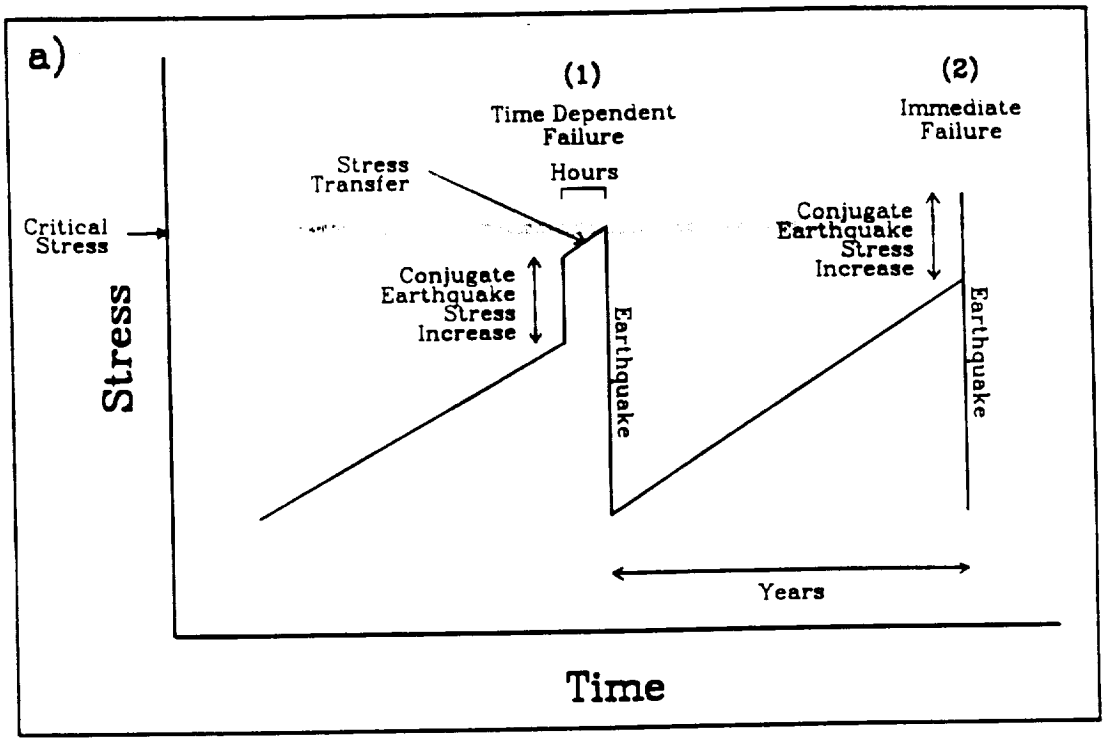
a)
(1)
Time Dependent Failure
Hours
(2)
Immediate Failure
Stress Transfer
Critical Stress
Conjugate Earthquake Stress Increase
Earthquake
Conjugate Earthquake Stress Increase
Earthquake
Stress
Years
Time

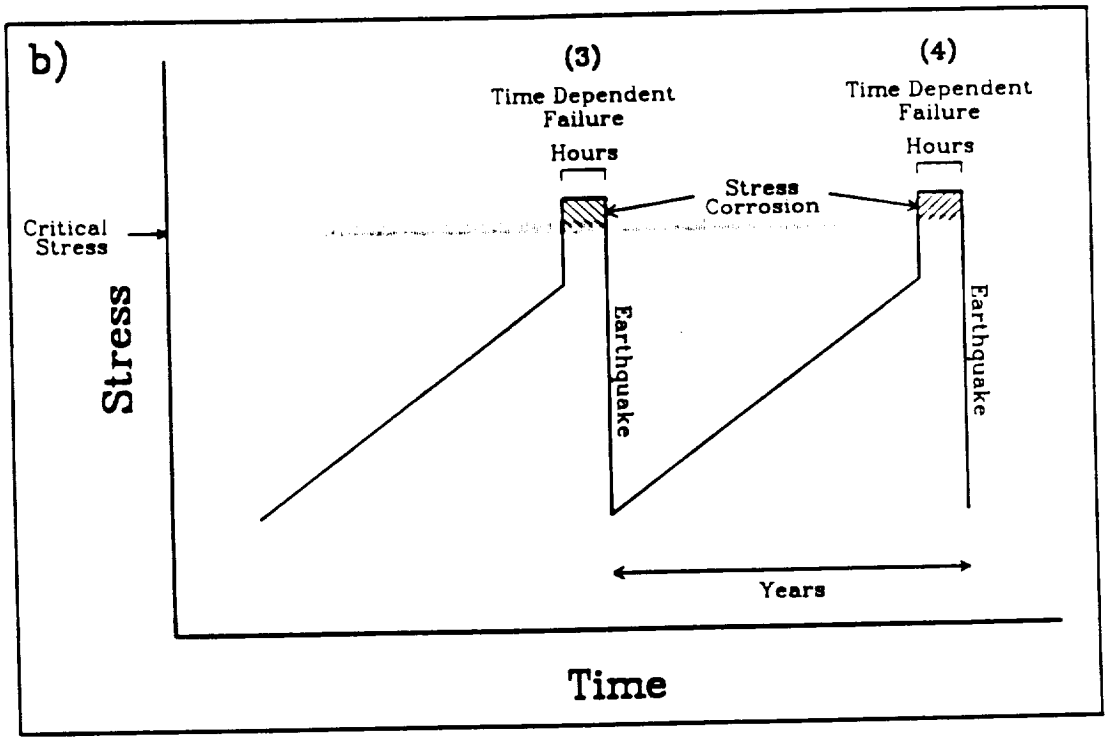
b)
(3)
Time Dependent Failure
Hours
(4)
Time Dependent Failure
Hours
Stress Corrosion
Critical Stress
Earthquake
Earthquake
Stress
Years
Time

proportional to the combined effect of the Elmore Ranch and Superstition Hills events, although we have attempted to resolve slip between each fault plane. The calculated parameters are a function of the coseismic offset, as well as 3-4 months of postseismic slip (plus 1.5 years of preseismic movement, if any). The average Elmore Ranch dislocation is about 30 cm (left-lateral) with fairly uniform distribution along the fault plane. In the case of the Superstition Hills fault, the average slip is estimated at 130 cm with concentrated deformation along the northwest and southeast sections of the fault. Because the GPS sampling frequency is so low (years), the calculated source parameters should contain the total coseismic moment release, which includes several months of postseismic slip.

In Table 4.7 the GPS moments are compared with estimates made through seismic and other geodetic studies. Forward and inverse models using teleseismic [*Dziewonski et al.*, 1989; *Bent et al.*, 1989; *Sipkin*, 1989; *Hwang et al.*, 1990] and strong-motion recordings [*Frankel and Wennerberg*, 1989; *Wald et al.*, 1990] are used to constrain source parameters, as well as investigate complexities of the Superstition Hills rupture process. The teleseismic moments agree fairly well with the GPS estimates, while the strong ground motion data yield significantly lower results. The high-frequency strong-motion measurements are dominated by energy around 1 second and conceivably miss a sizable portion of the long-period energy release recorded with the teleseismic and GPS data. Hence, the near field seismic solutions may underestimate the total moment release.

Geodetic measurements from Pinyon Flat observatory are used to constrain planer and curved dislocation models for the Superstition Hills and

Table 4.7 Moment Comparison

Method	Moment ($x10^{26}$ dyne-cm)				Reference
	SH	ER	Total	Ratio	
GPS (Model 2)	9.4	2.3	11.7	4.1	This Study
Teleseismic	7.2	1.4	8.6	5.1	*Dziewonski et al.* [1988]
Teleseismic	10.	2.3	12.	4.3	*Sipkin* [1989]
Teleseismic	10.8	2.7	13.5	4.0	*Bent et al.* [1989]
Teleseismic	8.				*Hwang et al.* [1990]
Strong Motion	5.2				*Wald et al.* [1989]
Strong Motion	1.8				*Frankell and Wennerberg* [1989]
Pinyon Flat (Planar-A)	3.7	0.8	4.3	4.6	*Agnew and Wyatt* [1989]
EDM	9.3				*Lisowski and Savage* [1988]

SH - Superstition Hills fault
ER - Elmore Ranch fault

Elmore Ranch faults [*Agnew and Wyatt*, 1989]. The data are obtained from long-base strain and tilt-meters, as well as a borehole dilatometer. The best-fit planer models to all observations (Table 4.7) are significantly lower than those calculated with the GPS and teleseismic data, although a 70 % moment increase for the Superstition Hills fault is obtained when the strainmeter data are excluded. The low moment estimate may be due to a number of factors [*Agnew and Wyatt*, 1989]: 1) measurement quality, particular with the strainmeter, 2) rheologic differences between Superstition Hills and Pinyon Flat, and 3) strainmeter-dilatometer sensitivity to the nodal deformation plane roughly on azimuth with the observatory.

Geodolite observations of the Salton Trough EDM network were made in early December (1987), several days after the two large earthquakes [*Lisowski and Savage*, 1988]; the last previous occupation was in January, 1987. Simple dislocation models with 40 cm left-lateral slip along the Elmore Ranch fault and 120 cm right-lateral slip along the Superstition Hills fault best-fit the observations. The estimated moment for the Superstition Hills event (Table 4.7) is comparable to that obtained with the GPS displacements.

The discrepancies in Table 4.7 are largely attributed to the alternate methodologies, observations, and parameters used to constrain each model. However, for those calculations which include moment estimates for both the Superstition Hills and Elmore Ranch events, the ratio between the two ruptures is fairly constant. This illustrates an internal consistency with each method. More importantly, it suggests that postseismic slip along the Superstition Hills fault is probably confined to the shallow segment of the rupture plane. Since seismic activity on the Elmore Ranch fault essentially

ceased after the 2nd main event, if postseismic slip were occurring in mass along a large fraction of the Superstition Hills rupture plane, the GPS moment ratio would be considerably larger.

While the epicenter and aftershock sequence for the Superstition Hills event were concentrated along the northwestern portion of the fault, strong ground motion, teleseismic, and surface offset data suggest significant moment release on the southern section of the Superstition Hills fault [*Wald et al.*, 1989; *Bent et al.*, 1989; *Hwang et al.*, 1990; *Williams and Magistrale*, 1989]. An exception is the strong ground motion study of *Frankel and Wennerberg* [1989] where slip is confined to the northwest. However, their low Superstition Hills moment (Table 4.7) suggests this analysis may be strongly susceptible to the high-frequency content of the data, indicating rupture along the southeast segment was dictated primarily by low-frequency energy release. The GPS data also reveal dislocation along the southeastern segment of the fault, and further suggests a displacement null near the faults mid-section. This slip deficiency may be related to the surface offset drop observed along the center of the fault (Figure 4.10).

Deformation across the Imperial Valley

The 1986-1988 GPS station displacements indicate a significant component of deformation across the Imperial Valley not associated with the 1987 Superstition Hills earthquake sequence (Figures 4.4 and 4.8). This motion is attributed to plate-boundary deformation due to the relative velocity between the Pacific and North American plates. From empirical evidence provided by Salton Trough EDM observations between 1972 and

1987, these non-seismic movements were modeled as 3.45 cm/yr differential velocity across the valley. However, after removing the seismic deformation predicted with a preliminary model (Model 1, Table 4.6) the calculated GPS displacements average 5.9 cm/yr (Figure 4.8), significantly larger than that obtained with the trilateration measurements over the last two decades. This GPS velocity is also larger than the 4.7 cm/yr plate motion predicted from global models (for Imperial Valley coordinates) [*DeMets et al.*, 1990]. Most likely the GPS rate is an overestimate, especially considering it contains large measurement uncertainty due to poor 1986 data quality, and is heavily influenced by seismic effects from the 1987 earthquake sequence. It is possible, however, that the 1986-1988 GPS rate could represent accelerated deformation. In fact, GPS observations between 1988 and 1989 indicate 5.2 $\pm$ 0.9 cm/yr displacement across the Imperial Valley [*Larsen and Reilinger*, 1990]. Accelerated deformation is not without precedence. Triangulation observations suggest a rate of 6.2 cm/yr between 1941 and 1954, although this is attributed to postseismic deformation following the 1940 Imperial Valley earthquake. Increased deformation following the 1979 earthquake is not observed in the EDM observations [*Savage et al.*, 1986]. Additional GPS measurements are necessary in the Imperial Valley in order to ascertain the current deformation rate.

4.7 Conclusions

Station movements computed from 4 Imperial Valley GPS campaigns indicate large crustal displacements during the periods 1986-1988 and 1986-1990. Much of the deformation is attributed to the 1987 Superstition Hills

earthquake sequence. Ten sites near the seismic rupture zone are displaced at least 10 cm, although the GPS observations contain large uncertainties due to poor data quality from the initial (1986) survey. This is the first occurrence of a large earthquake within a preexisting GPS network.

The 1987 earthquake sequence is initially modeled as uniform offsets along rectangular dislocations in an elastic half-space. The best-fit model to the GPS observations requires 130 cm right-lateral slip along the northwest trending Superstition Hills fault and 30 cm left-lateral motion along the conjugate northeast trending Elmore Ranch fault. The slip distribution along each fault is investigated by partitioning the rupture planes into 50 sub-elements and utilizing Singular Value Decomposition to estimate the slip along each sub-fault. Measurements of surface offset are used to constrain the shallow elements of the fault plane. The estimated slip distribution along the Elmore Ranch fault is fairly uniform. Slip along the Superstition Hills fault appears to be concentrated to the northwest and the southeast with a displacement drop indicated near the faults midsection. There is some evidence that postseismic slip along the Superstition Hills fault was concentrated near the surface. The estimated moments are 9.4×10^{25} dyne-cm and 2.3×10^{25} dyne-cm for the Superstition Hills and Elmore Ranch faults, respectively, which are consistent with moments obtained from teleseismic data.

In addition, the 1986-1988 GPS observations suggest non-seismic movements across the Imperial Valley of up to 5.9 cm/yr. These secular displacements are attributed to plate-boundary deformation due to the relative motion between the North American and Pacific plates. The observed

rate is probably an overestimate, however, as it is heavily influenced by unmodeled seismic effects and measurement error. Regardless, the observed seismic and secular deformations clearly emphasize the importance of future GPS study in the Imperial Valley.

Acknowledgements

This research was a collaborative effort conducted under the auspices of Robert Reilinger (MIT). The field support provided by so many people has proven invaluable. William Young and Gerald Dole at the Riverside County Flood Control District and Gerald Stayner at the Riverside County Survey Department provided support for the 1990 mini-campaign. I am especially grateful to the support provided by Hiroo Kanamori. This work is supported by U.S.G.S. grants 14-08-0001-61679 (MIT) and 14-08-001-61354 (Caltech), and by NASA contracts NAG-5-842 (Caltech) and NAG-5-814 (MIT).

References

Agnew, D. C., and F. K. Wyatt, The 1987 Superstition Hills earthquake sequence: Strains and tilts at Pinon Flat observatory, *Bull. Seismol. Soc. Am.*, *79*, 480-492, 1989.

Alewine, R. W., Application of linear inversion theory toward the estimation of seismic source parameters, Ph.D. Thesis, California Institute of Technology, Pasadena, 303 pp., 1974.

Beal, C. H., The earthquake in the Imperial Valley, California, June 22, 1915, *Bull. Seismol. Soc. Am.*, *5*, 130-149, 1915.

Bent, A. L., D. V. Helmberger, R. J. Stead, and P. Ho-Liu, Waveform modeling of the November 1987 Superstition Hills earthquakes, *Bull. Seismol. Soc. Am.*, *79*, 500-514, 1989.

Beutler, G., W. Gurtner, I. Bauersima, and R. Langley, Modeling and estimating the orbits of GPS satellites, paper presented at First International Symposium on Precise Positioning with the Global Positioning System, Int. Assoc. of Geod., Rockville, Md., April 15-19, 1985.

Budding, K. E., and R. V. Sharp, Surface faulting associated with the Elmore Ranch and Superstition Hills, California, earthquake of 24 November 1987, *Seismol. Res. Letts.*, *59*, p. 49, 1988.

Chinnery, M. A., The deformation of the ground around surface faults, *Bull. Seismol. Soc. Am.*, *51*, 355-372, 1961.

Chinnery, M. A., The stress changes that accompany strike-slip faulting, *Bull. Seismol. Soc. Am.*, *53*, 921-932, 1963.

Das, S., and C. H. Scholz, Off-fault aftershock clusters caused by shear stress increase?, *Bull. Seismol. Soc. Am.*, *71*, 1669-1675, 1981.

Davis, J. L., W. H. Prescott, J. L. Svarc, and K. J. Wendt, Assessment of global positioning system measurements for studies of crustal deformation, *J. Geophys. Res.*, *94*, 13,635-13,650, 1989.

Defense Mapping Agency, Department of Defense world geodetic system 1984, *DMA TR 8350.2*, D.M.A. Washington, D. C., 122 pp., 1987.

DeMets, C., R. G. Gordon, S. Stein, and D. F. Argus, A revised estimate of Pacific-North America motion and implications for western North America plate boundary zone tectonics, *Geophys. Res. Letts.*, *14*, 911-914, 1987.

DeMets, C., R. G. Gordon, D. F. Argus, and S. Stein, Current plate motions, *Geophys. J. Inter.*, *101*, 425-478, 1990.

Dong, D., and Y. Bock, Global positioning system network analysis with phase ambiguity resolution applied to crustal deformation studies in California, *J. Geophys. Res.*, *94*, 3949-3966, 1989.

Drew, A. R., and R. A. Snay, DYNAP: software for estimating crustal deformation from geodetic data, *Tectonophysics*, *162*, 331-343, 1989.

Dziewonski, A. M., G. Ekstrom, J. H. Woodhouse, and G. Zwart, Centroid-moment tensor solutions for October-December 1987, *Phys. Earth Planet.*

Inter., *54*, 10-21, 1989.

Elders, W. A., R. W. Rex, T. Meidav, P. T. Robinson, and S. Biehler, Crustal spreading in southern California, *Science*, *178*, 15-24, 1972.

Frankel, A., and L. Wennerberg, Rupture process of the M_S 6.6 Superstition Hills earthquake determined from strong-motion recordings: Application of tomographic source inversion, *Bull. Seismol. Soc. Am.*, *79*, 515-541, 1989.

Fuis, G. S., W. D. Mooney, J. H. Healey, G. A. McMechan, and W. J. Lutter, Crustal structure of the Imperial Valley region, *U.S. Geol. Surv. Prof. Pap.*, *1254*, 25-50, 1982.

Given, D. D., and W. D. Stuart, A fault interaction model for triggering of the Superstition Hills earthquake of November 24, 1987, *Seismol. Res. Letts.*, *59*, p. 48, 1988.

Gurtner, W., G. Beutler, I. Bauersima, and T. Schildknecht, Evaluation of GPS carrier difference observations: The Bernese second generation software package, paper presented at First International Symposium on Precise Positioning With the Global Positioning System, Int. Assoc. of Geod., Rockville, Md., April 15-19, 1985.

Harris, R. A., and P. Segall, Detection of a locked zone at depth on the Parkfield segment of the San Andreas fault, *J. Geophys. Res.*, *92*, 7945-7962, 1987.

Hudnut, K. W., L. Seeber, T. Rockwell, J. Goddmacher, R. Klinger, S.

Lindvall, and R. McElwain, Surface ruptures on cross-faults in the 24 November 1987 Superstition Hills, California, earthquake sequence, *Bull. Seismol. Soc. Am.*, *79*, 282-296, 1989a.

Hudnut, K. W., L. Seeber, and J. Pacheco, Cross-fault triggering in the November 1987 Superstition Hills earthquake sequence, southern California, *Geophys. Res. Letts.*, *16*, 199-202, 1989b.

Hudnut, K., and M. Clark, New slip along parts of the 1968 Coyote Creek fault rupture, California, *Bull. Seismol. Soc. Am.*, *79*, 451-465, 1989.

Hwang, L. J., H. Magistrale, and H. Kanamori, Teleseismic source parameters and rupture characteristics of the 24 November 1987, Superstition Hills earthquake, *Bull. Seismol. Soc. Am.*, *80*, 43-56, 1990.

Iwasaki, T., and R. Sato, Strain field in a semi-infinite medium due to an inclined rectangular fault, *J. Phys. Earth*, *27*, 285-314, 1979.

Jackson, D. D., Interpretation of inaccurate, insufficient and inconsistent data, *Geophys. J. R. Astron. Soc.*, *28*, 97-107, 1972.

Johnson, C. E., and D. P. Hill, Seismicity of the Imperial Valley, *U.S. Geol. Surv. Prof. Pap.*, *1254*, 14-24, 1982.

Johnson, C. E., and L. K. Hutton, Tectonic implications of the November 24, 1987, Superstition Hills earthquakes, Imperial Valley, CA, *Seismol. Res. Letts.*, *59*, p. 48, 1988.

King, R. W., E. G. Masters, C. Rizos, A. Stolz, and J. Collins, *Surveying with GPS, Monograph 9*, School of Surveying, The University of New South

Wales, Kensington, Australia, 128 pp., 1985.

Lanczos, C., *Linear Differential Operators*, D. Van Nostrand, New York, 1961.

Larsen, S. C., R. E. Reilinger, GPS measurements of strain accumulation across the Imperial Valley, California: 1986-1989, in preparation, 1990.

Larsen, S. C., D. C. Agnew, B. H. Hager, Strain accumulation in the Santa Barbara channel: 1971-1987, in preparation, 1990.

Lichten, S. M., and J. S. Border, Strategies for high-precision Global Positioning Systems orbit determination, *J. Geophys. Res.*, *92*, 12,751-12,762, 1987.

Lisowski, M., and J. C. Savage, Deformation associated with the Superstition Hills, California, earthquakes of November 1987, *Seismol. Res. Letts.*, *59*, p. 35, 1988.

Lomnitz, C., F. Mooser, C. R. Allen, J. N. Brune, and W. Thatcher, Seismicity and tectonics of northern Gulf of California region, Mexico: Preliminary results, *Geofis. Int.*, *10*, 34-48, 1970.

Magistrale, H., L. Jones, and H. Kanamori, The Superstition Hills, California, earthquakes of 24 November, 1987, *Bull. Seismol. Soc. Am.*, *79*, 239-251, 1989.

Mansinha, L., and D. E. Smylie, Effect of earthquakes on the Chandler wobble and the secular polar shift, *J. Geophys. Res.*, *72*, 4731-4743, 1967.

Mansinha, L., and D. E. Smylie, The displacement fields of inclined faults,

Bull. Seismol. Soc. Am., *61*, 1433-1440, 1971.

McGill, S. F., C. R. Allen, K. W. Hudnut, D. C. Johnson, W. F. Miller, and K. E. Sieh, Slip on the Superstition Hills fault and on nearby faults associated with the 24 November 1987 Elmore Desert Ranch and Superstition Hills earthquakes, southern California, *Bull. Seismol. Soc. Am.*, *79*, 362-375, 1989.

Menke, W., *Geophysical Data Analysis: Discrete Inverse Theory*, Academic, Orlando, Fla., 1984.

Neugebauer, H. C., The 1986 Salton trough GPS survey and data processing results, National Geodetic Survey (unpublished report), 1988.

Neumann, F., United States earthquakes, 1940, *U.S. Coast and Geod. Sur. Serial*, *647*, 74 pp., 1942.

Okada, Y., Surface deformation due to shear and tensile faults in a half-space, *Bull. Seismol. Soc. Am.*, *75*, 1135-1134, 1985.

Prescott, W. H., The determination of displacement fields from geodetic data along a strike slip fault, *J. Geophys. Res.*, *86*, 6067-6072, 1981.

Prescott, W. H., J. C. Savage, and M. Lisowski, Crustal strain, in National Earthquake Hazards Reduction Program, Summaries of Technical Reports, *U.S. Geological Survey Open-File Report*, *87-374*, 272-280, 1987a.

Prescott, W. H., M. Lisowski, and J. C. Savage, Velocity field along the San Andreas fault in southern California, *EOS Trans.*, *68*, p. 1506, 1987b.

Reilinger, R. E., and S. C. Larsen, Vertical crustal deformation associated with the 1979 M=6.6 Imperial Valley, California earthquake: Implications for fault behavior, *J. Geophys. Res.*, *91*, 14,044-14,056, 1986.

Rocken, C., The global positioning system: A new tool for tectonic studies, Ph.D. Thesis, University of Colorado, Boulder, 365 pp., 1988.

Savage, J. C., and L. M. Hastie, Surface deformation associated with dip-slip faulting, *J. Geophys. Res.*, 71, 4897-4904, 1966.

Savage, J. C., W. H. Prescott, and G. Gu, Strain accumulation in southern California, 1973-1984, *J. Geophys. Res.*, *91*, 7455-7473, 1986.

Savage, J. C., Effect of crustal layering upon dislocation modeling, *J. Geophys. Res.*, *92*, 10,595-10,600, 1987.

Segall, P., and R. Harris, Earthquake deformation cycle on the San Andreas fault near Parkfield, California, *J. Geophys. Res.*, *92*, 10,511-10,525, 1987.

Sipkin, S. A., Moment-tensor solutions for the 24 November 1987 Superstition Hills, California earthquake, *Bull. Seismol. Soc. Am.*, *79*, 493-499, 1989.

Snay, R. A., Enhancing the geodetic resolution of fault slip by introducing prior information, *Manuscripta Geodaetica*, *14*, 391-403, 1989.

Snay, R. A., and A. R. Drew, Supplementing geodetic data with prior information for crustal deformation in the Imperial Valley, California, Technical Report Series, University of Stuttgart, 30 pp., 1988.

Steketee, J. A., On Volterra's dislocations in a semi-infinite medium, *Can.*

Jour. Phys., *96*, 192-205, 1958.

Toppozada, T. R., D. L. Parke, and C. T. Higgins, Seismicity of California 1900-1931, *Calif. Div. of Mines and Geol Spec. Rep.*, *135*, 39 pp., 1978.

U.S. Geological Survey, The Imperial Valley, California, earthquake of October 15, 1979, *U.S. Geol. Surv. Prof. Pap.*, *1254*, 451 pp., 1982.

Wald, D. J., D. V. Helmberger, S. H. Hartzell, Rupture process of the 1987 Superstition Hills earthquake from the inversion of strong motion data, *Bull. Seismol. Soc. Am.*, in press, 1990.

Ward, S. N., and S. E. Barrientos, An inversion for slip distribution and fault shape from geodetic data observations of the 1983, Borah Peak, Idaho, earthquake, *J. Geophys. Res.*, *91*, 4909-4919, 1986.

Wells, D., N. Beck, D. Delikaraoglou, A. Kleusberg, E. J. Krakiwsky, G. Lachapelle, R. B. Langley, M. Nakiboglu, K. Schwarz, J. M. Tranquilla, and P. Vanicek, *Guide to GPS Positioning*, Canadian GPS Associates, Fredericton, N. B., Canada, 1987.

Williams, P. L., and H. W. Magistrale, Slip along the Superstition Hills fault associated with the 24 November 1987 Superstition Hills, California, earthquake, *Bull. Seismol. Soc. Am.*, *79*, 390-410, 1989.

APPENDIX 3

Lateral variation in upper mantle temperature and composition beneath mid-ocean ridges inferred from shear-wave propagation, geoid, and bathymetry

by Anne F. Sheehan

Abstract from Ph.D. thesis, Massachusetts Institute of Technology, Cambridge, 258 pp., 1991

ABSTRACT

Resolution of both the extent and mechanism of lateral heterogeneity in the upper mantle constrains the nature and scales of mantle convection. Oceanic regions are of particular interest as they are likely to provide our closest glimpse at the patterns of temperature anomalies and convective flow in the upper mantle because of their young age and simple crustal structure relative to continental regions. Our objectives in this thesis are to determine lateral variations in the seismic velocity and attenuation structure of the lithosphere and asthenosphere beneath the oceans, and to combine these seismological observations with the data and theory of geoid and bathymetry anomalies in order to test and improve current models for seafloor spreading and mantle convection. We concentrate on determining variations in mantle properties on a scale of about 1000 km, comparable to the thickness of the upper mantle. Seismic velocity, geoid, and bathymetry anomalies are all sensitive to variations in upper mantle density, and we formulate inversions to combine quantitatively these different data and search for a common origin. Variations in mantle density can be either of thermal or compositional origin and are presumably related to mantle convection and differentiation.

By means of a large data base of digital seismograms and waveform cross-correlation and spectral ratio techniques, we have measured SS-S differential travel time residuals and differential attenuation in order to determine lateral variations in upper mantle structure beneath the Mid-Atlantic Ridge and East Pacific Rise. Differential travel times of such phases as SS and S with identical source and receiver have the advantage that residuals are likely to be dominated by contributions from the upper mantle near the surface bounce point of the reflected phase (SS). Under this assumption, differential SS-S travel time residuals are mapped at the SS bounce points as a means of delineating lateral variations in mantle structure. After removing the signature of lithosphere age, we find evidence for long-wavelength variations in SS-S residuals along the Mid-Atlantic Ridge. The dominant wavelength of these variations is 1000 to 2000 km. These travel time anomalies correlate qualitatively with along-axis variations in bathymetry and geoid height. We formulate a joint inversion of travel time residual, geoid height, and bathymetry under the assumption that all arise from variations in upper mantle temperature or bulk composition (parameterized in terms of Mg#). The inversion employs geoid and topography kernels which depend on the mantle viscosity structure. Inversion for temperature perturbations alone provides good fits to travel time and geoid data. The fit to topography, which is likely dominated by unmodeled crustal thickness variations, is not as good. The inversions for temperature favor the presence of a thin low viscosity layer in the upper mantle and temperature perturbations concentrated at depths less than 300 km. Compositional variations alone are unable to match the travel time and geoid or bathymetry data simultaneously. A joint inversion for temperature and composition provides good fits to both geoid and travel time anomalies. Temperature variations are $\pm$ 50 K and compositional variations are $\pm$ 0.5-3 % Mg# for models with the temperature variations uniformly distributed over the uppermost 300 km and the compositional variations either distributed uniformly over the same interval or concentrated at shallower depths. The magnitudes of these variations are consistent with the chemistry and geothermometry of dredged peridotites along the Mid-Atlantic Ridge.

Differential travel times of SS-S pairs in the east central Pacific show several differences from the north Atlantic. The most obvious difference is that the travel time residuals are significantly larger than in the Atlantic, even at a fixed age. The travel time - age relation is weaker in the Pacific, although this may be partially attributable to the fact that we have not sampled a large range of plate ages in the eastern Pacific. In the Atlantic

our results are not consistent with the presence of a simple pattern of azimuthal anisotropy, while in the Pacific the data are consistent with the presence of weak anisotropy in the upper mantle. It has been suggested that anisotropy may be more pronounced at fast spreading rates than at slow spreading rates both in the lithosphere (due to a rate dependence of the mechanism for orienting olivine crystals in the lithosphere) and the asthenosphere (because the asthenospheric flow beneath fast moving plates is likely to take the form of a progressive simple shear which can produce a lattice preferred orientation of olivine crystals), and our results are consistent with this suggestion. There is substantial ambiguity in our anisotropy measurements for the Pacific, however, due to a poor sampling of azimuths, so that it is also possible that lateral heterogeneity rather than azimuthal anisotropy is producing the observed azimuthal pattern. Sampling at a more uniform distribution of azimuths should make this result less ambiguous, and as more seismic stations are deployed at new geographic locations our chances of resolving this issue will improve.

Inversion of travel time residuals, geoid, and bathymetry data for the eastern Pacific indicates that compositional variations alone are inadequate to match all of the data simultaneously, similar to our results for the north Atlantic. Temperature variations alone, however, produce significant variance reduction. The inversion solutions indicate excess temperature in the vicinity of the Galapagos hotspot in the range 50 - 150 K. Further analysis is needed to determine the effects of subduction zone structure and possible crustal thickening in the eastern Cocos plate region.

As a complement to the study of travel times, we have measured SS-S differential attenuation in the north Atlantic region. Mapping seismic Q in the upper mantle is an important tool for assessing mechanisms of lateral heterogeneity because the attenuation of seismic waves is sensitive to variations in temperature and to partial melting. Differential attenuation is positively correlated with SS-S travel time residual. Both differential attenuation and travel time residual decrease with increasing seafloor age. The age dependence of SS-S travel time residual can be explained entirely by the cooling of the oceanic lithosphere, i.e., contributions from the asthenosphere or from a mantle melt fraction are not required. On the assumption that plate cooling also dominates the variation of differential attenuation with age, we derive an empirical Q^{-1}-temperature relation for the oceanic lithosphere. The variation of Q^{-1} with temperature that we derive is not as strongly dependent on temperature as that observed in laboratory studies. Systematic long-wavelength (1000-6000 km) variations in upper mantle differential attenuation are evident along the axis of the Mid-Atlantic Ridge. These variations correlate approximately with long-wavelength variations in shear wave travel time residuals and are attributed to along-axis differences in upper mantle temperature.

APPENDIX 4

Joint inversion of shear wave travel time residuals, geoid, and depth anomalies along the Mid-Atlantic Ridge for long-wavelength variations in upper mantle temperature and composition

by Anne. F. Sheehan and Sean C. Solomon

Submitted to *Journal of Geophysical Research*, March 1991

ABSTRACT

Utilizing a digital data base of over 500 seismograms and a waveform cross-correlation technique, we have measured SS-S differential travel time residuals as a means to examine the shear wave velocity structure in the vicinity of the Mid-Atlantic Ridge. Differential travel times of such phases as SS and S with identical source and receiver have the advantage that residuals are likely to be dominated by contributions from the upper mantle near the surface bounce point of the reflected phase (SS). Under this assumption, differential SS-S travel time residuals are mapped at the SS bounce points as a means of delineating lateral variations in mantle structure. After removing the signature of lithosphere age, we find evidence for long-wavelength variations in SS-S residuals along the ridge. The dominant wavelength of these variations is 1000 to 2000 km. These travel time anomalies correlate qualitatively with along-axis variations in bathymetry and geoid height. We formulate a joint inversion of travel time residual, geoid height, and bathymetry under the assumption that all arise from variations in upper mantle temperature or bulk composition (parameterized in terms of Mg#). The inversion employs geoid and topography kernels which depend upon the mantle viscosity structure. Inversion for thermal perturbations alone provides good fits to travel time and geoid data. The fit to topography, which is likely dominated by unmodeled crustal thickness variations, is not as good. The inversions for temperature favor the presence of a thin low viscosity layer in the upper mantle and temperature perturbations concentrated at depths less than 300 km. Compositional variations alone are unable to match the travel time and geoid or bathymetry data simultaneously. A joint inversion for temperature and composition provides good fits to both geoid and travel time anomalies. Temperature variations are $\pm$ 50 K and compositional variations are $\pm$ 0.5-3 % Mg# for models with the temperature variations uniformly distributed over the uppermost 300 km and the compositional variations either distributed uniformly over the same interval or concentrated at shallower depths. The magnitudes of these variations are consistent with the chemistry and geothermometry of dredged peridotites along the Mid-Atlantic Ridge.

INTRODUCTION

Seismic velocity and density of upper mantle material are expected to be functions of temperature and composition. The delineation of long wavelength variations in these physical properties thus provide important constraints on mantle convection, crust-mantle differentiation, and mantle chemical heterogeneity. In this study we determine lateral variations in upper mantle temperature and composition along the Mid-Atlantic Ridge through the combined inversion of shear wave differential travel times, geoid height, and bathymetric depth anomalies.

The advent of seismic tomography has led to a number of three-dimensional maps of lateral variations in seismic velocity in the upper mantle, and several such models of the north Atlantic region have been developed, both as parts of global studies [e.g., *Woodhouse and Dziewonski* , 1984; *Nakanishi and Anderson*, 1984; *Tanimoto*, 1990] and through regional investigations of long-period surface waves [e.g., *Honda and Tanimoto*, 1987; *Mocquet et al.*, 1989; *Mocquet and Romanowicz*, 1990]. With surface wave methods each wave samples the average vertical variation in upper mantle structure along its path, but because of the long wavelengths involved the inversion of phase or group velocity from many paths tends to smooth out lateral variations. Body wave travel times can provide independent information about upper mantle heterogeneity at potentially shorter horizontal scales than surface waves can resolve, and progress has been made in the determination of lateral heterogeneity in the North Atlantic through the use of both differential and absolute travel times of body waves [*Kuo et al.*, 1987; *Grand*, 1987, 1989].

The travel times used in this study are differential times of the body wave phase pair SS-S. Differential travel times of shear wave pairs are well suited to the study of upper mantle heterogeneity [*Sipkin and Jordan*, 1976, 1980; *Stark and Forsyth*, 1983; *Butler*, 1979; *Kuo et al.*, 1987; *Woodward and Masters*, 1991] and have the advantage that source and receiver effects are approximately common to both phases and are thus largely eliminated by differencing. Under the assumption that the lower mantle is relatively homogeneous and that the portions of the ray paths in

the upper mantle are steep, the differential travel time anomaly is associated with upper mantle heterogeneity in a small volume centered beneath the surface bounce point of the reflected (SS) phase. This technique is thus well suited to the investigation of horizontal variations in structure, but the resolution of variations with depth is poor.

Oceanic bathymetry and geoid height data are sensitive to variations in mantle density at depth. Such variations can be either thermal or compositional in origin and, like seismic velocity, are presumably related to mantle convection and differentiation. Geoid (or gravity) and topography have become the most commonly used tools for mapping out and constraining models of upper mantle convection [e.g., *Anderson et al.*, 1973, *McKenzie and Bowin*, 1976; *McKenzie*, 1977; *McKenzie et al.*, 1980, *Parsons and Daly*, 1983; *Buck and Parmentier*, 1986; *Craig and McKenzie*, 1986]. In addition, measurement of the admittance (the spectral ratio of geoid to topography) has been widely utilized to estimate the depth and mode of compensation of oceanic swells and plateaus [e.g., *Watts et al.*, 1985, *Cazenave et al.*, 1988; *Sandwell and MacKenzie*, 1989; *Sheehan and McNutt*, 1989]. Several workers [*Dziewonski et al.*, 1977; *Nakanishi and Anderson*, 1984; *Tanimoto and Anderson*, 1984; *Stark and Forsyth*, 1983; *Dziewonski*, 1984; *Kuo et al.*, 1987] have noted correlations of geoid and travel time (or velocity structure) at a number of different wavelengths, although only a few [*Richards and Hager*, 1984; *Hager and Clayton*, 1989] have combined observational seismology with geoid anomalies in a quantitative and dynamically consistent manner.

In this study we present the first formal inversion of geoid, depth, and travel time anomaly data for lateral variations in upper mantle temperature and composition along the Mid-Atlantic Ridge. Given a distribution of temperature or density perturbations in the upper mantle, the forward problem of calculating differential travel time, geoid, and depth anomalies is straightforward. This forward problem forms the basis for a joint linear inversion of these three types of observations under the assumption that all arise from parameterized long-wavelength variations in upper mantle temperature or composition. Results of a set of inversions carried out

under different assumptions regarding the depth extent of lateral heterogeneity and the mantle viscosity structure are compared with other constraints on variations in mantle temperature and degree of melt removal.

MEASUREMENT OF DIFFERENTIAL TRAVEL TIMES

The seismic data used in this study consist of long-period S and SS phases obtained from the Global Digital Seismic Network (GDSN) [*Peterson et al.*, 1976; *Peterson and Hutt*, 1982]; the Network of Autonomously Recording Seismographs (NARS), a linear broadband array in western Europe [*Nolet and Vlaar*, 1982]; and several broadband stations from the global GEOSCOPE network [*Romanowicz et al.*, 1984]. A list of stations used in this study is presented in Table 1. We use only transversely polarized (SH) seismograms (rotated from N-S and E-W components) to avoid interference from the SKS phase and contamination from P-SV conversions at the base of the crust and other near-surface discontinuities. Recent work by *Gee and Jordan* [1989] suggests that travel times depend on the frequency band used in the analysis. In order to maintain a self-consistent data set for our study, additional processing is applied to data from the NARS and GEOSCOPE arrays in order to mimic the instrument response of the longer period GDSN stations. This processing allows us to measure travel times from a set of seismograms that all have essentially the same frequency response. Data from the NARS and GEOSCOPE arrays are decimated (with a low-pass antialiasing filter) to a common sampling interval of 1 s. The data are further filtered using a noncausal 3-point Butterworth filter [*Rader and Gold*, 1967] with a frequency bandpass of 0.01 - 0.20 Hz. This additional filtering greatly improves the signal-to-noise ratio of the SS phase.

A waveform cross-correlation method is utilized to determine the differential travel time between the phases S and SS [*Butler*, 1979; *Stark and Forsyth*, 1983; *Kuo et al.*, 1987]. The procedure involves the construction of a "synthetic" SS pulse from S and the evaluation of the

cross-correlation function between the real and synthetic windowed SS phases (Figure 1). The synthetic SS pulse is created from S in the following manner. The S pulse is windowed and attenuated (with attenuation parameter t*= 3 s) [*Grand and Helmberger*, 1984; *Kuo et al.*, 1987] to account for the additional time SS travels in the mantle, and then a $\pi/2$ phase shift (Hilbert transform) is applied to the attenuated S pulse to simulate the frequency-dependent phase shift which the SS wave undergoes at an internal caustic [*Choy and Richards*, 1975]. The differential time is obtained from the peak of the cross correlation between the synthetic SS constructed from the S wave and the real SS. The residual SS-S times are obtained by subtracting the observed differential time from that predicted by the PREM Earth model [*Dziewonski and Anderson*, 1981] and correcting for Earth ellipticity [*Dziewonski and Gilbert*, 1976] and SS bounce point bathymetry. Our convention is that negative residuals are indicative of either early SS or late S.

Constant window lengths of 120 s are used for both the S and SS phases. In general, the observed differential travel times vary by as much as 1 s depending on how S and SS are windowed. Our modelling with synthetic seismograms indicates that emphasizing the onset of the SS waveform can lead to bias for bounce points in areas of oceanic sediments. The effect of sediments at long periods is to produce precursory arrivals from reflections at the base of the sediments and late arrivals from waves which travel through the low-velocity sediments and are reflected at the crust-water interface. The net affect, after convolving the crustal response with the long-period GDSN instrument response, is that the time center of the SS phase is effectively unchanged but the pulse is broadened both at the front and at the back. In our procedure the use of a constant window containing the entire SS pulse should yield differential travel times that are little affected by the presence of sediments.

DATA

The north Atlantic is an ideal area for conducting a differential travel time study in terms of

the geographic distribution of available events and stations at suitable distances. The range in source-receiver separation was taken to be 55° to 86° to ensure separation of S and ScS at the longer distances and to avoid triplication in SS at shorter distances. The SS and S phases bottom from about 670 km to 2300 km depth. We performed a search over all earthquakes in the Harvard centroid moment tensor (CMT) catalog for the years 1977-1987 [*Dziewonski et al.*, 1981; *Dziewonski and Woodhouse*, 1983] and over all GDSN, NARS, and GEOSCOPE digital seismic stations in order to find event-station pairs of the proper epicentral distance which provide SS bounce points in the North Atlantic region. Epicenters were obtained from the Bulletin of the International Seismological Centre (ISC) for events occurring before 1987 and from the "Preliminary Determination of Epicenters" of the U.S. National Earthquake Information Service (NEIS) for events occurring in 1987. The final distribution of sources and stations used to measure SS-S differential travel times is shown in Figure 2. The majority of data in this study comes from records of equatorial fracture zone earthquakes at North American and European stations, north and central Atlantic events at North American stations, Central American events at European stations, and Mediterranean and European earthquakes at North American stations.

This search yielded over 2000 event-station pairs with the proper epicentral separation. After winnowing the list because of station inoperation, poor signal to noise ratio for the phases of interest, and interfering events, the final data set consists of nearly 500 SS-S differential travel time residuals with bounce points in the north Atlantic (Figure 3). Uncertainties are determined for each measurement following the procedure outlined in Appendix A.

RESULTS

We interpret the variations in SS-S differential travel times in terms of lateral velocity variations within the crust and upper mantle beneath the surface reflection points of the SS wave path. *Kuo et al.* [1987] and *Woodward and Masters* [1991] tested the validity of this assumption

by plotting absolute S and SS residuals against SS-S residuals. They found that S and SS-S residuals are uncorrelated while SS and SS-S residuals are strongly correlated, indicating that the assumption is justified. The validity of this assumption is further supported by the strong correlation of SS-S times with surface tectonic features in the vicinity of the SS bounce point. The residuals are further interpreted in terms of such upper mantle processes as lithospheric aging, flow-induced anisotropy, and along-axis heterogeneity in mantle structure.

Lithospheric Aging

Cooling and thickening of the lithosphere should yield a tendency toward an increase in seismic velocity with increasing lithospheric age. A linear regression experiment was performed to examine the correlation of the SS-S residuals with seafloor age. A gridded map of seafloor ages was constructed for the north Atlantic from the magnetic anomalies of *Klitgord and Schouten* [1986] and ages assigned according to *Kent and Gradstein* [1986] and *Klitgord and Schouten* [1986]. The isochrons of *Sclater et al.* [1981] were used in a few regions which were not covered by the *Klitgord and Schouten* [1986] data set. To obtain a representative age value for the region spanning approximately one horizontal wavelength of the incident (SS) wave, an average seafloor age was estimated for a 1° x 1° box centered on each SS bounce point. To reduce scatter, measurements whose bounce point depths differed by more than 2500 m from the depth predicted by the *Parsons and Sclater* [1977] plate cooling model were excluded from the final age regression. Although each SS wave samples the upper mantle at a finite range of lithosphere ages, we expect that the different travel time anomalies contributed by the SS path segments on the younger and older sides of the bounce point approximately cancel so that the age at the SS bounce point is appropriate to the associated SS-S residual.

The SS-S residuals for the north Atlantic are consistent with the expectation of an increase in seismic velocity with seafloor age. For bounce points between 0° and 60°N latitude, the coefficient derived by linear regression of residual with square root of age is -0.68 ± 0.08 s $My^{-1/2}$ from 0 to

100 My, with a linear correlation coefficient of -0.85 (Figure 4). However, residuals from 60 - 90°N do not seem to be strongly correlated with lithospheric age. This may be due to the fact that this area is more tectonically complicated than 'normal' oceanic lithosphere [e.g., *White*, 1988; *Zehnder and Mutter*, 1990], includes several ridge jumps, is in close proximity to continental regions, and does not closely follow the age-depth relation of *Parsons and Sclater* [1977]. Compared with the residuals for 0-60°N, those from 60-90°N are anomalously negative at young ages and anomalously positive at older ages. The slope of SS-S residual vs. square root of age for data from 0 to 60°N is smaller than that inferred from S delays of intraplate earthquakes in the Atlantic by *Duschenes and Solomon* [1977] (two-way S delay = -1.2 s $My^{-1/2}$) and that reported by *Kuo et al.* [1987] (-1 s $My^{-1/2}$). It is larger, however, than the global average obtained by *Woodward and Masters* [1991] (-0.51 s $My^{-1/2}$). We find that the residual-age relation is not constant over the entire north Atlantic, so that some of these variations in slope may reflect real geographic differences.

We may compare the variation of SS-S residual versus age with that due only to lithospheric cooling. For a lithospheric structure given by the plate cooling model of *Parsons and Sclater* [1977], we may convert temperature variations to differences in shear velocity v_S by adopting a value for $\partial v_S/\partial T$, which we take to be uniform and equal to -0.6 m/s K^{-1} [*McNutt and Judge*, 1990]. For a horizontal slowness typical of the teleseismic S and SS waves of this study (0.1375 s/km), the slope of the line best fitting the SS-S travel time delay versus age given by the plate cooling model over 0-100 My is then -0.73 ± 0.07 s $My^{-1/2}$, a result indistinguishable from the observed slope. This agreement indicates that the dependence of travel time residual on plate age can be explained entirely by lithospheric cooling.

The trend of the travel time residual versus lithospheric age relation changes at about 100 My. After 100 My, the residuals appear to flatten out (Figure 4), in the same sense as the plate cooling model of *Parsons and Sclater* [1977]. Such a pattern may reflect the unmodeled effect of increased sediment or crustal thickness, or, as suggested by *Parsons and Sclater* [1977] may be partially the

result of secondary convection which supplies heat to the base of the plate at older ages. To avoid possible biases associated with any of these effects we shall restrict our analysis to data with bounce points on lithosphere less than 100 My. To look for other systematic variations in the residuals, we correct for age by removing the linear relation shown by the solid line in Figure 4. This correction is effectively a normalization of residuals to 22-My-old lithosphere (the zero crossing of the regression line).

Anisotropy

Another systematic velocity variation that has been suggested as a possible contributor to residual SS-S travel times is azimuthal anisotropy. *Kuo et al.* [1987] examined this phenomenon in detail and concluded that alignment of olivine cystals in the asthenosphere created a significant pattern of azimuthal anisotropy in SS-S residuals measured in the Atlantic region. We have also searched for evidence of azimuthal anisotropy with our data set.

Backus [1965] and *Crampin* [1977] demonstrated, from the general form of body wave anisotropy in a weakly anisotropic medium, that the linear form of the azimuthal variation of velocity is given by

$$V^2 = A_0 + A_1 \cos 2\theta + A_2 \sin 2\theta + A_3 \cos 4\theta + A_4 \sin 4\theta \qquad (1)$$

where V is the body wave velocity, the A_n are linear functions of the elastic moduli, and θ is an azimuth, defined for our problem by the angle between the great circle path and the direction to geographic north measured at the SS bounce point. Equation (1) was further simplified by *Kuo et al.* [1987] and parameterized in terms of travel time residuals:

$$R = R_0 + R_1 \cos 2\theta + R_2 \sin 2\theta + R_3 \cos 4\theta + R_4 \sin 4\theta \qquad (2)$$

where R is the travel time residual and the R_n are constants. By fitting a function of this form to our age-corrected measurements we can determine if our data are consistent with the presence of anisotropy.

We have conducted several tests of azimuthal anisotropy with our travel time data. We performed least squares inversions to determine 2θ and 4θ patterns which provide best fits to the age-corrected SS-S residuals. The anisotropy indicated by our regression experiments differs significantly from the preferred model of *Kuo et al.* [1987] both in magnitude and in phase (Figure 5). Our results indicate that for the 2θ model the slow direction for SS-S is N4°W and the peak-to-peak magnitude of the effect is less than 1 s; for the 4θ model the slow directions are N32°W and N58°E and the magnitude is 2.5 s; for the joint 2θ and 4θ model the slow direction is N32°W and the magnitude is just under 3 s. *Kuo et al.* [1987] obtained a peak-to-peak variation with azimuth of 5-7 s and a slow direction at N13°W. The slowest residuals in the *Kuo et al.* [1987] study were from north-south paths, i.e., nearly along the ridge, and the fastest residuals were from northeast-southwest-trending paths with bounce points north of the Azores-Gibraltar plate boundary (an area noted to be anomalously fast in their study), so their reported anisotropy may have been at least partly the result of unmodelled upper mantle heterogeneity. Our inversion for a 2θ pattern of anisotropy provided a variance reduction of only 2%, compared with 20% for a 4θ pattern, and 22% for a combined 2θ and 4θ pattern. On the basis of these values of variance reduction and the number of free parameters involved, our results suggest that there is no single coherent pattern of upper mantle anisotropy in the north Atlantic. The latest anisotropic upper mantle models obtained from surface wave tomography [*Montagner and Tanimoto*, 1990] also show a complex pattern of anisotropy in the region. Any azimuthal anisotropy in the asthenosphere induced by plate motions in the north Atlantic may be heterogeneous because the three plates in the region are slow-moving and the return flow is not closely related to plate divergence [*Hager and O'Connell*, 1979, 1981; *Parmentier and Oliver*, 1979].

Spatial Patterns of Age-corrected Residuals

After removal of the dependence on seafloor age, a plot of SS-S travel time residuals at the SS surface reflection point (Figure 6) shows several interesting features. Perhaps the most striking is that residuals in the western Atlantic north of about 35° N are on average nearly 4 s more negative than those to the south. This feature is also noticeable in Figure 3 but is more obvious after age-dependence is removed. A similar change at approximately this latitude was noted for SS-S residuals with bounce positions on the eastern side of the Mid-Atlantic Ridge by *Kuo et al.* [1987] and was attributed to a change in upper mantle structure across the Azores-Gibraltar plate boundary. The signal we observe is predominantly from data with bounce points on the western side of the ridge. A map view of the azimuthal distribution is shown in Figure 7 and serves as an aid to assess qualitively the geometry of wave paths to the south and north of 35°N. We examined the possibility that this signal may be from the Caribbean anomaly, a region of anomalously high velocity in the mantle between 600 and 1400 km depth beneath the Caribbean originally reported by *Jordan and Lynn* [1974] and further confirmed by *Grand* [1987]. If the first leg of the SS rays propagating to western Europe were to bottom in the high velocity Caribbean region, the result would be early SS-S residuals. This would produce a feature of opposite sign from that observed, so we discount it as an influence here. Another possible explanation for the long-wavelength signal could be azimuthal anisotropy, but the examination above of possible patterns of azimuthal anisotropy does not support this suggestion.

Another distinctive feature of the residuals in Figure 6 is a row of negative values which trends northwest to southeast along the trend of the New England Seamounts and across the ridge to the vicinity of the Great Meteor Seamount. This feature comes from event-station pairs at a number of different azimuths and distances so cannot be attributed to a source or receiver effect. We do not observe distinctive anomalies in the vicinity of the Bermuda, Azores, Iceland or Canary Islands hotspots. The data density is poor for the Bermuda region and Iceland, however, and any signal associated with the Canary Islands may be obscured by the ocean-continent transition.

Recently active hotspot islands might be expected to display strong positive (late) residuals, such as *Stewart and Keen* [1978] observed for PP-P residuals at the Fogo Seamounts. In contrast, *Woodward and Masters* [1991] found mostly negative (early) SS-S residuals in the vicinity of the Hawaiin hotspot, and *Jordan* [1979] and *Sipkin and Jordan* [1980] have suggested that the net effect of hotspots may be to produce early arrivals because of the presence of high velocities in a depleted mantle residuum.

There is a systematic variation of SS-S residual with latitude, i.e., effectively along the direction of the Mid-Atlantic Ridge axis. Age-corrected SS-S residuals with SS bounce points on lithosphere younger than 100 My are shown versus latitude in Figure 8. The along-axis variations show a variety of scales, notably at wavelengths of about 1000 - 2000 km in the region from 15° to 35°N, and at about 6000 km wavelength from late (positive residuals) in the south (20-35°) to early (negative residuals) farther north (45-55°N). The largest of these variations are robust with respect to selective removal of portions of the data. The Iceland region appears as a local maximum (positive SS-S delay) on the profile, but the Azores hot spot does not have a distinct seismic signal.

JOINT INVERSION OF TRAVEL TIME RESIDUALS AND GEOID AND DEPTH ANOMALIES

Long-wavelength variations in shear wave velocity of the sort depicted in Figure 8 presumably are a consequence of some combination of variations in temperature and composition of the upper mantle. Such lateral variations should also have signatures in other physical quantities measurable at these wavelengths, notably gravity (or geoid height) and topography (or residual bathymetry), because of the dependence of these quantities on bulk density. Travel time residuals, geoid anomalies, and residual depth anomalies are independent quantities dependent in different ways on temperature, bulk composition, and their variation with depth. We therefore seek a quantitative procedure for treating travel time residuals jointly with geoid and bathymetry data and in particular for a combined inversion of all three quantities for horizontal variations in upper mantle

temperature and composition.

To ensure complentarity of data sets, bathymetry and geoid height values are obtained at each SS bounce point, and both are corrected for subsidence with seafloor age by means of the plate cooling model [*Parsons and Sclater*, 1977; *Parsons and Richter*, 1980]. In this manner we effectively normalize all observations to zero age. Bathymetric data are obtained from the corrected Digital Bathymetric Data Base (5' grid) [*U.S. Naval Oceanographic Office*, 1985]. Geoid data are taken from a combined set of Seasat and GEOS3 altimeter data [*Marsh et al.*, 1986]. Data north of 70° N were not included in the *Marsh et al.* [1986] data set due to the high probability of being over sea ice, so our analysis below is confined to latitudes less than 70°N. We find that the correlation of SS-S residuals with the low order geoid is negative, but that at high order the correlation is positive (Figure 9). This relationship may indicate a depth dependence of contributions to geoid and travel time (e.g., the long wavelength signal may be a lower mantle effect). Low degree harmonics are likely linked to deep-seated density heterogeneities and subducting slabs [*Hager*, 1984; *Hager et al.*, 1985]. Since we are interested in upper mantle processes, we filter out the long-wavelength component of the geoid by subtracting a reference field [*Lerch et al.*, 1979] expanded in spherical harmonics to degree and order 7 and tapered to degree and order 11. To provide a comparable bathymetric data set, bathymetry is high-pass filtered (corner at 4000 km, cutoff at 6000 km) to remove long-wavelength trends. Along-axis profiles are constructed from the age-corrected and filtered geoid and bathymetry data.

Profiles of age-corrected travel time residuals, geoid, and bathymetry are compared in Figure 10. While qualitative correlations among profiles are apparent, we seek to quantify possible models of temperature and compositional variations that can match these observations. Oceanic bathymetry and geoid height are both sensitive to variations in mantle density at depth. Such variations can be either thermal or compositional in origin and, like seismic velocity, are presumably related to mantle convection and differentiation. For a given density change, the seismic signature of thermal and compositional heterogeneity are of opposite sign, so travel time residuals constitute key information

for distinguishing between mechanisms of heterogeneity.

Inversion for Thermal Structure

We seek to formulate an inversion for the distribution of temperature anomalies T(x,z) (where x is along-axis and z is depth) that can produce the along-axis geoid, bathymetry, and travel-time anomalies shown in Figure 10. Topography and geoid kernels were calculated for prescribed models of viscosity for an incompressible, self-gravitating, Newtonian mantle with free slip at the surface and the core-mantle boundary. The convecting region is assumed to be overlain by a high-viscosity layer 40 km thick. We performed calculations both for a mantle of constant viscosity and for a mantle with a shallow low-viscosity layer. Topography and geoid anomalies depend on the viscosity structure, but the predicted travel times do not. Kernels were calculated using a method similar to that of *Richards and Hager* [1984] except that the solution was directly integrated across the layers instead of being obtained via propagator matrices [*McNutt and Judge*, 1990].

The inversion is best conducted in the horizontal wavenumber domain. The thermal anomalies $\Delta T(k,z)$ at depth are related to the predicted dynamic topography h(k) for wavenumber k via an integral of the form

$$\Delta h\,(k) = \frac{\rho_0 \alpha}{\rho_0 - \rho_w} \int_{Z_{min}}^{Z_{max}} H\,(k,z)\,\Delta T\,(k,z)\,dz \qquad (3)$$

[*Parsons and Daly*, 1983] where α is the volumetric coefficient of thermal expansion, ρ_0 and ρ_w are the densities of the mantle and of water at standard temperature and pressure, and z_{min} and z_{max} are the upper and lower boundaries of the layer in which temperatures are allowed to vary. Table 2 contains a summary of the constants adopted here. The depth and wavenumber-dependent topography kernel H(k,z) is calculated from the equations of continuity and motion given a set of boundary conditions, a viscosity model, and a constitutive relation between stress and strain

[*Parsons and Daly*, 1983]. Similarly, the kernel G(k,z) for the geoid relates the thermal anomalies to the geoid N(k) via

$$\Delta N(k) = \frac{2\pi\Gamma\rho_0\alpha}{gk} \int_{z_{min}}^{z_{max}} G(k,z)\, \Delta T(k,z)\, dz \qquad (4)$$

[*Parsons and Daly*, 1983] where Γ is the gravitational constant, and g is the surface gravitational acceleration.

Sample geoid and topography kernels calculated for different wavenumbers and viscosity structures are shown in Figures 11 and 12. Cartesian kernels are used throughout this study because of their computational efficiency and straightforward application to Fourier transform techniques. We have compared extrema of the upper mantle portions of the geoid and topography kernels for a layered cartesian Earth and a spherical Earth for a number of wavelengths and different viscosity structures (Figure 12), and we note good agreement even at very long wavelengths (spherical harmonic order $\ell = 6$). This agreement suggests that the results presented here should be applicable to the spherical Earth without introducing unreasonably large errors.

Temperature perturbations at depth can be converted to a seismic velocity perturbation by assuming a value for the partial derivative of shear wave velocity with respect to temperature, $\partial v_s/\partial T$. The resulting two-wave travel time perturbation is given by

$$\Delta t\,(k) = 2\,\frac{\partial v_s}{\partial T} \int_{z_{min}}^{z_{max}} \frac{\Delta T\,(k,\,z)\,dz}{v_s(z)^2\,(1 - p^2 v_s(z)^2)^{1/2}} \qquad (5)$$

where $v_s(z)$ is from the reference shear velocity model [*Dziewonski and Anderson*, 1981] and p is the ray parameter, generally taken to be a representative value for the range of epicentral distances considered here. We use a value of -0.6 m/s K^{-1} for $\partial v_s/\partial T$. This value is higher than the values of *Anderson et al.* [1968] and *Kumazawa and Anderson* [1969] at standard temperature and

pressure but is similar to the value of -0.62 m/s K^{-1} determined by *McNutt and Judge* [1990] by a least squares fit of Love-wave phase velocities to predicted temperature of the lithosphere. Such a value is consistent with the change in P-wave velocity with temperature, $\partial v_p/\partial T$ = -0.5 m/s K^{-1}, found from modeling wave propagation along subducting slabs [*Creager and Jordan*, 1986; *Fischer et al.*, 1988] if we assume that $\partial v_s/\partial T = 1.1\ \partial v_p/\partial T$ [*Woodhouse and Dziewonski*, 1984]. Partial melt would increase the value of $\partial v_s/\partial T$ [*Sleep*, 1974; *Sato and Sacks*, 1989], but simultaneous analysis of both shear and compressional differential travel times by *Woodward and Masters* [1991] indicates that significant partial melting is not required to explain the differential travel time residuals in the north Atlantic region.

The forward problem consists of calculating geoid, topography, and travel time residual profiles given a starting two-dimensional temperature structure T(x,z). The inverse problem consists of finding a temperature structure that predicts (via equations 3 - 5) geoid, topography, and travel time profiles which best fit those observed. The familiar matrix equation $\mathbf{d} = \mathbf{A}\,\mathbf{m}$ is formed from discrete versions of equations 3 - 5. The data vector **d** consists of the topography, geoid, and travel time residuals, the model vector **m** contains the temperature variations for which we are solving, and the matrix **A** contains the coefficients and kernels which relate the data to the model. As a check on our procedure, we constructed a forward problem for geoid and topography and found good agreement with the modelling results of *McKenzie et al.* [1980].

The bathymetry, geoid, and travel time profiles of Figure 10 are interpolated to a constant spacing, demeaned, tapered at both ends with a 10% sine squared taper, and Fourier transformed. Since our profile extends from 10 to 72°N, the first and last 10% of the profile (10 - 16°N and 66 - 72°N) will be affected by the taper. The 3n x 1 data vector **d** is then constructed, using the complex (to retain both amplitude and phase) bathymetry, geoid, and travel time data sampled at n discrete wavenumbers:

$$\mathbf{d} = [\ \Delta h(k_1),\ldots,\Delta h(k_n),\Delta N(k_1),\ldots,\Delta N(k_n),\Delta t(k_1),\ldots,\ \Delta t(k_n)\ ]^T \qquad (6)$$

where T denotes transpose. For the case where temperature perturbations are constrained to be in a single layer, the n x 1 model vector **m** is given by

$$\mathbf{m} = [\,\Delta T(k_1),\ldots,\Delta T(k_n)]^T \tag{7}$$

For the more general case of a multi-layer system, the nj x 1 model vector **m** is given by

$$\mathbf{m} = [\,\Delta T(k_1, z_1),\ldots,\Delta T(k_1, z_j),\ \Delta T(k_2,z_1),\ldots,\Delta T(k_2,z_j),\Delta T(k_n,z_1)\ldots,\Delta T(k_n,z_j)]^T \tag{8}$$

where z_i is the layer index and j is the total number of layers. In this paper we perform inversions for single-layer models only. The "layers" of temperature variations are independent of the "layering" system of lid, low viscosity zone, and mantle which we use for the calculation of kernels, although major changes in viscosity would tend to segment ΔT as well. The temperature layering simply refers to that region bounded by z_{min} and z_{max} in the integrals of equations 1 - 3.

The 3n x n matrix **A** contains the coefficients and kernels that relate the temperature perturbations to the observations, which for the single-layer case is given by

$$
\mathbf{A} = \begin{pmatrix}
\frac{\rho_0 \alpha}{\rho_0 - \rho_w} \sum_{z_{min}}^{z_{max}} H(k_1,z)\ \Delta z & 0 & \cdots & 0 \\
0 & \frac{\rho_0 \alpha}{\rho_0 - \rho_w} \sum_{z_{min}}^{z_{max}} H(k_2,z)\ \Delta z & \cdots & 0 \\
0 & 0 & \cdots & 0 \\
0 & 0 & \cdots & \frac{\rho_0 \alpha}{\rho_0 - \rho_w} \sum_{z_{min}}^{z_{max}} H(k_n,z)\ \Delta z \\
\frac{2\pi\Gamma\rho_0\alpha}{g k_1} \sum_{z_{min}}^{z_{max}} G(k_1,z)\Delta z & 0 & \cdots & 0 \\
0 & \frac{2\pi\Gamma\rho_0\alpha}{g k_2} \sum_{z_{min}}^{z_{max}} G(k_2,z)\Delta z & \cdots & 0 \\
0 & 0 & \cdots & 0 \\
0 & 0 & \cdots & \frac{2\pi\Gamma\rho_0\alpha}{g k_n} \sum_{z_{min}}^{z_{max}} G(k_n,z)\Delta z \\
2\frac{\partial v_s}{\partial T} \sum_{z_{min}}^{z_{max}} \frac{v_s(z)^{-2}}{(1-p^2 v_s(z)^2)^{\frac{1}{2}}} \Delta z & 0 & \cdots & 0 \\
0 & 2\frac{\partial v_s}{\partial T} \sum_{z_{min}}^{z_{max}} \frac{v_s(z)^{-2}}{(1-p^2 v_s(z)^2)^{\frac{1}{2}}} \Delta z & \cdots & 0 \\
0 & 0 & \cdots & 0 \\
0 & 0 & \cdots & 2\frac{\partial v_s}{\partial T} \sum_{z_{min}}^{z_{max}} \frac{v_s(z)^{-2}}{(1-p^2 v_s(z)^2)^{\frac{1}{2}}} \Delta z
\end{pmatrix} \tag{9}
$$

The matrix **A** contains both bathymetry and topography kernels and is thus viscosity dependent; i.e., a viscosity structure must be assumed. We solve the equation $\mathbf{d} = \mathbf{A}\,\mathbf{m}$ by least squares

$$\mathbf{m} = (\tilde{\mathbf{A}}\, \mathbf{R}_{dd}^{-1}\, \mathbf{A})^{-1}\, \tilde{\mathbf{A}}\, \mathbf{R}_{dd}^{-1}\, \mathbf{d} \tag{10}$$

where $\tilde{\mathbf{A}}$ is the complex conjugate transpose of the matrix **A**. Construction of the data covariance matrix $\mathbf{R}_{dd}$ is discussed in Appendix B. Equation (10) is solved for the solution vector **m**, and variance reduction is calculated via

$$\text{variance reduction} = 1 - \frac{\widetilde{(\mathbf{d}-\mathbf{Am})}\,\mathbf{R}_{\mathbf{dd}}^{-1}\,(\mathbf{d}-\mathbf{Am})}{\widetilde{\mathbf{d}}\,\mathbf{R}_{\mathbf{dd}}^{-1}\,\mathbf{d}} \qquad (11)$$

The resulting model vector **m** is inverse Fourier transformed back to the spatial domain to produce an along-axis temperature profile. The solution **m** is also substituted into equations 3 - 5 to compare predicted geoid, bathymetry, and travel time residuals with those observed.

Six inversion experiments for temperature structure were performed (Table 3). Inversions were carried out for two different viscosity models and for three different thicknesses of the layer in which lateral temperature variations were assumed to occur. Because topography and geoid anomalies depend only on the ratios of viscosity in different layers [*Robinson et al.*, 1987; *Hong et al.*, 1990], we set the dimensionless viscosity of the layer representing the bulk of the mantle to unity. In one viscosity model, termed the "constant viscosity mantle," a 40-km-thick high-viscosity lid overlies a unit viscosity mantle. We set the viscosity in the lid to 10^4, which effectively mimics rigid behavior. In a second model, a 160-km-thick low-viscosity zone is present beneath a 40-km-thick lid; the viscosity in the low-viscosity zone is a factor of 100 less than in the underlying mantle. The thickness of the layer of temperature perturbations was taken variously to extend from 0-150 km depth, 0-300 km depth, and 0-650 km depth. The matrix **A** is different for each of these cases, as it involves viscosity-dependent geoid and topography kernels and also a summation over depth.

Inversion results for the constant-viscosity-mantle cases are shown in Figure 13. The "observed" profile is actually a filtered version of the observations, containing only the wavelengths used in the inversion (1400 to 7100 km). Predicted profiles were calculated from equation 5. For these solutions, the long-wavelength fit to geoid is better than at short wavelengths. The fit to bathymetry is poor. The predicted magnitude of the SS-S residuals range from a factor of 5 too small for the 650-km-thick layer to a factor of about 1.5 too small for the 150-km-thick layer. Increasing the temperature variations to improve the fit to the SS-S residuals leads to predicted geoid variations that are too large. The highest total variance reduction and best fit for the constant-viscosity cases come when lateral variations are constrained to shallow (0-150 km) depth. The

variance reduction is 25% for bathymetry, 79% for geoid, and 58% for travel times. The total variance reduction is 53%. The variation in temperature is 180 K for the 150-km-thick layer, and only 60 K for the 300-km-thick layer.

Figure 14 shows inversion results for the models with a thin low-viscosity zone. A good fit to both geoid and travel time is found, although the alignment in phase of predicted and observed geoid is not as good as for the constant-viscosity case. The fit to bathymetry is again poor. The total variance reduction for the 150-km-thick and 300-km-thick layers are both 57%, although the shallow model provides slightly higher variance reduction for bathymetry (27% for 0-150 km deep layer, 24% for 0-300 km deep layer) and the 300-km-thick-layer model provides higher variance reduction for geoid (79% for 0-150 km deep layer, 85% for 0-300 km deep layer). The variation in temperature for the 150-km-thick layer is 230 K and in the 300-km-thick layer is 110 K.

We have explored the hypothesis that the lack of correlation of predicted and observed topography is an indication that the source of variations in the geoid and travel time anomalies is deep. To test this hypothesis, we performed inversions with temperature variations restricted to deeper layers and found that fits to topography were still poor. It is possible that the bathymetric signal is dominated by crustal thickness variations which are not included in our calculation of dynamic topography. An assessment of such thickness variations is discussed further in Appendix B.

Inversion for Compositional Variations

A possible alternative to along-axis variation in mantle temperature is lateral variation in bulk mantle composition, due perhaps to a variable extent of melt extraction or different degrees of mixing of compositionally distinct volumes of mantle material. The dynamical effects of compositionally induced density variations can be large [*O'Hara*, 1975; *Boyd and McCallister*, 1976; *Oxburgh and Parmentier*, 1977; *Sotin and Parmentier*, 1989]. The fraction of mantle potentially extractable as basaltic melt is thought to be 15-25% [e.g., *Green and Liebermann*, 1976]. Thus, for every volume of basalt removed from the mantle, a volume of residuum several

times larger is left behind. The effect of basalt depletion is to increase the molar ratio Mg/(Mg + Fe) (or Mg#) in the residuum, which reduces the density and increases the seismic velocities [e.g., *Liebermann*, 1970; *Akimoto*, 1972]. For example, subtraction of 20 mole % olivine basalt from pyrolite can decrease the density of the residuum by nearly 2%, equivalent to a thermal perturbation of nearly 500 K [*Jordan*, 1979]. Thus compositional changes need only be slight to produce effects on the order of 100 K, comparable to values obtained from the inversions for temperature variations. In this section we explore the effects of compositional variations parameterized in terms of the variation in the Mg# in the upper mantle along the ridge. Our motivation for parameterizing compositional variations simply in terms of Mg# is that differences in this quantity yield significant variations in seismic velocity and density, in contrast to most other measures of degree of melt extraction.

Partial derivatives of density and seismic velocity with respect to Mg# are obtained from *Akimoto* [1972]. These values were measured on a suite of samples ranging from pure forsterite (Mg_2SiO_4) to pure fayalite (Fe_2SiO_4). While these partial derivatives are at standard temperature and pressure, it is expected that a change to elevated temperature and pressure will have only a second order effect, since temperature and pressure corrections work in opposite directions [*Jordan*, 1979]. Above the solidus temperature, however, the amount and distribution of partial melt, which may depend strongly on composition and particularly volatile content, is important. The presence of melt is likely to have a larger effect on shear wave velocities than on bulk density. Calculations of melt migration, however, suggest that once created, melt segregates rapidly by a percolation mechanism [e.g. *Scott and Stevenson*, 1989], so that the melt fraction present in the mantle at any given time is probably small. Studies of mantle peridotites [*Johnson et al.*, 1990] also support the importance of fractional melting.

It is straightforward to convert equations (3) and (4) to relations between geoid or topography and a compositionally induced density perturbation by means of the relation

$$\Delta\rho = - \rho_0 \alpha \Delta T \tag{12}$$

Compositional anomalies at depth yield a dynamic topography h(k) given by

$$\Delta h(k) = \frac{1}{\rho_0 - \rho_w} \frac{\partial \rho}{\partial Mg} \int_{z_{min}}^{z_{max}} H(k,z)\, \Delta Mg(k,z)\, dz \tag{13}$$

where ΔMg represents the fractional change in the Mg#. Compositional anomalies yield a geoid anomaly

$$\Delta N(k) = \frac{2\pi\Gamma}{gk} \frac{\partial \rho}{\partial Mg} \int_{z_{min}}^{z_{max}} G(k,z)\, \Delta Mg(k,z)\, dz \tag{14}$$

For a compositional perturbation at depth the resulting two-wave travel time perturbation is given by

$$\Delta t(k) = 2 \frac{\partial v_s}{\partial Mg} \int_{z_{min}}^{z_{max}} \frac{\Delta Mg(k,z)\, dz}{v_s(z)^2 \left(1 - p^2 v_s(z)^2\right)^{1/2}} \tag{15}$$

Using equations (13) - (15), an inversion scheme similar to that used for thermal perturbations is formed. The solution vector now has the form

$$\mathbf{m} = [\Delta Mg(k_1), \ldots, \Delta Mg(k_n)]^T \tag{16}$$

The data vector remains the same as in equation (6), while the matrix of coefficients, **A**, changes to reflect the relation between the data and mantle composition, rather than temperature, as outlined in equations (13) - (15).

The results of the inversions for compositional variations are summarized in Table 3 and in Figures 15 and 16. We are unable to match simultaneously both SS-S travel time residuals and

geoid and bathymetric anomalies with solely mantle compositional variations for either a constant viscosity mantle or one with a low viscosity zone. This is not surprising, as the travel times are for the most part positively correlated with geoid and bathymetry, but compositional variations (at least for the Mg_2SiO_4 - Fe_2SiO_4 system examined here) have an opposite effect on travel time and geoid-bathymetry.

For the constant viscosity case, the fit to the geoid is excellent, and the fit to bathymetry is slightly better than in the inversion for temperature. The fit to SS-S residuals is so poor that the variance reduction is negative for travel time. Large compositional changes would be required to affect travel times, whereas only small compositional changes are needed to produce significant density contrasts to match the geoid signal. The total variance reduction for the constant viscosity case does not vary greatly (from 32-33%) for compositional changes constrained to be over different depth intervals, though the variance reductions for individual data sets (bathymetry, geoid, travel time) vary significantly from model to model (see Table 3). The range in Mg# is about 1% if the variation is constrained to the depth range 0-150 km and only 0.1% for the 0-650 km depth range.

Figure 16 shows inversion results for the model with a low viscosity zone. A good fit to both geoid and bathymetry is found, although the alignment of predicted and observed geoid is not as good as in the constant viscosity case. The fit to bathymetry is the best of any models so far. The total variance reduction is still low (43 to 49%), due to the poor fit to travel times (negative variance reduction in all cases except the 0-650 km model). The range in Mg# is 2.4% if constrained to 0-150 km depth, 1.3% over 0-300 km depth, and 0.5% over 0-650 km depth.

Joint Inversion for Temperature and Composition

We next explore whether a combination of temperature and compositional variations can provide a good match to the observed geoid, travel time, and bathymetry. Joint inversions provide improved fits to all data at the expense of introducing additional free parameters. For these

inversions the data vector remains the same as in equation (6), the solution vector is modified to include both temperature and composition, and the matrix of coefficients, **A**, includes the effects of both temperature and composition. The matrix-building equations become, for example, for topography,

$$\Delta h(k) = \frac{\rho_0 \alpha}{\rho_0 - \rho_w} \int_{z_{min}}^{z_{max}} H(k,z)\, \Delta T(k,z)\, dz + \frac{1}{\rho_0 - \rho_w} \frac{\partial \rho}{\partial Mg} \int_{z_{min}}^{z_{max}} H(k,z)\, \Delta Mg(k,z)\, dz \qquad (17)$$

which is simply a combination of equations (3) and (13). The new geoid equation comes from a combination of equations (4) and (14) and the travel time equation from a combination of equations (5) and (15). Cross terms, such as compositional changes induced by increases or decreases in temperature, are neglected.

The results for the joint inversion for temperature and composition are summarized in Table 3 and Figures 16 and 17. The travel time residuals are well-modeled in all cases, as are the geoid data. The topography is best fit for the case with a low viscosity zone. Resolution of the depth interval of the most important lateral variations is rather poor. The topography is fit marginally better for the case where temperature and compositional anomalies are constrained to be shallower than 300 km. For the constant viscosity mantle, the temperature variations range from 210 K, if constrained to 0-150 km depth, to 55 K if over 0-650 km depth; variations in Mg# range from 1.5% if over 0-150 km depth to 0.4% for 0-650 km depth. For the case with an upper mantle low viscosity zone, the temperature variations are similar to those in the constant viscosity case, but the variations in Mg# are larger, from over 2% for 0-150 km depth to nearly 1% for 0-650 km depth.

The travel time residuals are perfectly fit in the joint inversions for temperature and composition (Table 3). This occurs because of the way the model parameters act in a similar manner on both geoid and bathymetry, producing a singular matrix if only geoid and bathymetry data are inverted for both temperature and composition. Undamped least squares always provides perfect solutions when the number of equations is equal to the number of unknowns unless the

matrix to be inverted is singular. If we perform an inversion including only travel time and geoid data, we have the same number of equations as unknowns, the matrix is nonsingular, and we obtain perfect fits to both travel time and geoid. Similarly, if we perform an inversion of travel time and bathymetry data, we again obtain perfect fits to both data sets. If we perform an inversion of geoid and bathymetry data, however, we are unable to obtain solutions without applying damping. In the joint inversion of travel time, geoid, and bathymetry, we have more equations than unknowns and the inversion is overdetermined. However, the travel times are perfectly determined in this case because of the nonuniqueness inherent with geoid and bathymetry. We have performed undamped inversions with various weightings on the geoid, bathymetry, and travel time data, and in all cases the travel times remain perfectly fit.

We have also performed joint inversion for temperature and composition with Mg# variations constrained to be in the upper 50 km of the lithosphere so as to mimic compositional variations due solely to variable melt extraction at the ridge. Temperature perturbations were allowed to remain within the depth ranges adopted earlier. The results for this inversion are summarized in Table 3 and Figures 19 and 20. The variance reduction was similar for the constant viscosity case and for the model with a low viscosity zone. In general, the geoid is fit very well, the predicted amplitudes are a bit low for travel time residuals, and the topography fit is slightly out of phase. For the constant viscosity mantle, the range in temperature is 210 K over 0-150 km depth and 25 K over 0-650 km, while Mg# variations constrained to be confined to 0-50 km depth were over 5%. For the case with a low viscosity zone, the temperature variations were not dramatically different from those in the constant viscosity case, and variations in Mg# were about 4.5%. The inversion solution shows high temperatures near 30°N and low temperatures in the region from 50-60°N. Iceland also appears to be underlain by high-temperature mantle. Going from south to north along the ridge, compositional variations indicate low Mg# in the vicinity of 20-30°N, high Mg# in the Azores region (40°N), low values near 50°N, and high values near 60°N.

DISCUSSION

The temperature and compositional variations in Figures 13-20 are broadly consistent with observed travel time, geoid, and bathymetry anomalies in the north Atlantic region. Temperature variations alone can account for most of the observed anomalies. In contrast, compositional variations alone cannot match all anomalies simultaneously. We infer that a component of the observed anomalies is due to long-wavelength variations in upper mantle temperature. Joint inversions for temperature and composition provide better fits than single-variable models, but at the expense of introducing additional free parameters.

It is difficult to select a 'best' model from the suite of inversions presented. The variance reductions in Table 3 serve as a guide, but independent criteria may allow us to reject some of the models, even those with high variance reductions. In particular, those models with large temperature variations (well in excess of 100 K) can be seriously questioned. Lateral temperature variations at upper mantle levels beneath oceanic ridges are thought to be no more than about 300 K globally [*Klein and Langmuir*, 1987; *Johnson et al.*, 1990], so a variation in temperature of 230 K (as in the inversion with a low-viscosity zone and a 150-km-thick layer of temperature perturbations) solely within a section of the north Atlantic is probably unreasonably large. Further, as *White and McKenzie* [1989] have noted, relatively small increases in mantle temperature above values typical for the mid-ocean ridge are sufficient to cause large increases in melt production. Their models indicate that, for fixed bulk composition, an increase of 100 K above normal doubles the amount of melt while a 200 K increase can quadruple it. Such increased melt production should lead to approximately corresponding increases in crustal thickness. Variations in oceanic crustal thickness away from fracture zones, however, are generally thought to be small, with thicknesses typically 6-7 km and ranging from 4.5 to 8.5 km [*Spudich and Orcutt*, 1980; *White*, 1984; *Purdy and Detrick*, 1986]. In the joint inversion for temperature and composition, temperature variations if confined to 150 km depth are excessive (over 200 K) and if the variations extend over 0-650 km

the fit to topography is poor, especially for the constant-viscosity mantle. On the basis of these results we prefer the models with temperature variations occurring over 0-300 km depth. For the constant viscosity mantle, the temperature variation is 110 K, and the variation in Mg# is 0.75%. For the case with an upper mantle low viscosity zone, the predicted temperature variation is 125 K, and the variation in Mg# is 1.1 %. The total variance reduction is greater in the model with a low viscosity zone.

Even a temperature variation of about 100 K is high for a mantle of constant composition, since we do not observe increased crustal thickness in regions that our models indicate have high temperatures. The assumption of approximately constant upper mantle composition warrants discussion. In particular, lateral variation in trace amounts of mantle volatiles may have a large effect on seismic velocity at a given temperature. The presence of even a slight amount of water, for instance, is sufficient to cause a significant decrease in the initial melting temperature of peridotite [*Wyllie*, 1971]. Estimates of volatile contents and their lateral variations in the north Atlantic region have been made from measurements of abundances of halogens, SiO_2, K_2O, and H_2O in basalts and from the volumes of vesicles in basalts [*Schilling et al.*, 1980, 1983; *Schilling*, 1986; *Michael*, 1988]. These studies indicate that Cl, Br, F, and H_2O contents increase toward the Azores and Iceland and that H_2O is two to three times more abundant in Mid-Atlantic Ridge basalts erupted over the Azores platform than at adjacent normal ridge segments. The effect of volatiles on density and shear wave velocity will be slight at subsolidus temperatures but can be major over the melting interval [*Goetze*, 1977]. The presence of melt will act to decrease significantly the seismic velocity [*Duschenes and Solomon*, 1973] and, to a lesser extent, lower the density of the mantle. To the extent that seismic velocity depends on proximity of the temperature to the solidus temperature [*Sato et al.*, 1988, 1989], volatile content can trade off with temperature in its effect on velocity at subsolidus conditions. Thus, variation in volatile content could lessen the variations in melt production implied by the inversion solutions.

Even without significant variations in volatile content, it is clearly an oversimplification to

parameterize mantle composition in terms of only a single quantity. Further we have assumed that the partial derivatives of bulk density and seismic velocity with respect to Mg# that are those for olivine [*Akimoto*, 1972]. The work of *Jordan* [1979] indicates that these derivatives remain nearly constant for many different mantle compositions (i.e., pyrolite-type compositions with various amounts of olivine, orthopyroxene, clinopyroxene, spinel, and garnet), so the latter assumption is sound. However, at any given Mg#, orthopyroxene and clinopyroxene have lower velocities and are less dense than olivine, while garnet and spinel are seismically faster and denser than olivine [*Jordan*, 1979], so an increase in the weight percent of orthopyroxene and clinopyroxene or a decrease in the weight percent of garnet and spinel with respect to olivine in the mantle could counteract some of the temperature variations obtained under the assumption of effectively uniform mineralogy. Several studies [*Wood*, 1979; *Jacques and Green*, 1980; *Dick et al.*, 1984] have suggested that compositional variations in the mantle are plausible. Indeed a number of workers [e.g., *Davies*, 1984; *Allegre et al.*, 1984] favor dynamic models for the mantle in which dispersed heterogeneities of various sizes and shapes are passively embedded in a continually mixed, convecting mantle. Variations in modal fractions of olivine, orthopyroxene, and clinopyroxene in peridotites recovered along the Mid-Atlantic Ridge have been reported in several studies [*Dick et al.*, 1984; *Michael and Bonatti*, 1985]. These variations are typically attributed to different degrees of melt extraction but could also be partially due to intrinsic upper mantle heterogeneity. For example, the relative fractions of olivine, clinopyroxene, and orthopyroxene indicated by *Michael and Bonatti* [1985] at 26°N and 30°N, if extended to depth, could counteract a portion of the temperature differences indicated by the inversion solutions for these regions.

Chemical analysis of dredged peridotites in the north Atlantic indicate a range of about 2.5% variation in Mg# [*Michael and Bonatti*, 1985]. This value is intermediate between what we find for models with compositional variations constrained to be shallow (4.5 to 6% variation) and those models with compositional variations in the same depth ranges as the thermal variations (1-2%). This suggests that compositional variations may be concentrated slightly shallower than the

temperature variations. *Michael and Bonatti* [1985] present an along-axis profile of Mg# variations from dredged peridotites which can be compared with our calculated profile. The main feature in their profile is a zone of high values of Mg# in the Azores region, from 34-45°N, relative to the rest of the ridge, consistent with our modelling results. Their data sampling is too sparse to delineate other long-wavelength features. Their average value for 26°N also has a high Mg# relative to adjacent data. This is consistent with our observation of early SS-S travel times and low geoid in this region. This anomaly is of too short a wavelength (< 1000 km), however, to resolve in our inversions. We should note that comparisons merit caution, as small scale features, such as those due to ridge segmentation, can produce large differences in composition between peridotites over scales of tens of kilometers. In addition, dredged peridotites are mostly from fracture zone environments, which may not be representative of typical ridge mantle [*Dick*, 1989].

On the SS-S residual profile the Iceland region appears as a local maximum (late SS) but the Azores hotspot does not show a distinct seismic signal. The inversion results for these two regions are also markedly different. The results of the joint inversion for temperature and composition predict a high Mg# in the Azores region while indicated temperatures are not anomalously high. At Iceland, in contrast, high temperatures dominate. Work by *Schilling* [1986] and *Bonatti* [1990] outlines the differences in geochemical signatures between the Azores and Iceland hot spots. These workers suggest that Iceland is a "traditional" plume hot spot, with a predominantly thermal origin, but that the Azores might be more aptly named a "wet spot" because of the presence of excess hydrous phases and the lack of a thermal anomaly. *Bonatti* [1990] suggests that because the Azores hotspot is rich in volatiles, enhanced melt production could occur with little or no increase in temperature. The high Mg# indicated in our inversions allows the region to be seismically fast (as we observe) but of low density (as geoid and bathymetry require). The results are consistent with the hypothesis that the Azores hot spot is not associated with a plume-like thermal anomaly. Inversion of surface wave dispersion data can potentially provide further tests of these ideas, but studies to date have yielded apparently conflicting results. Results of several such investigations

[*Nakanishi and Anderson*, 1984; *Tanimoto*, 1990; *Zhang and Tanimoto*, 1990] suggest that the Azores region is seismically slow at depths less than 300 km but a study utilizing 50-200-s-period Rayleigh waves by *Mocquet et al.* [1989] does not. These differences may be partially attributable to the differences in wave periods employed and mode of analysis from study to study. It may be possible that what appear to be low velocities at the Azores are a result of horizontal smoothing of the low velocities along the ridge and have little to do with the actual structure in the Azores region. None of these long-period surface wave studies resolve a distinctive anomaly at Iceland. Clearly, more work is needed to resolve the upper mantle velocity structure of hot spot regions.

Bonatti [1990] has constructed profiles of the equilibrium temperature of dredged peridotites along the Mid-Atlantic Ridge axis from 0 to 60°N by means of two different geothermometers [*Wells*, 1977; *Lindsley*, 1983]. Comparison of these profiles with the along-axis temperature variations obtained from our inversions reveals a number of qualitative correlations as well as a few discrepancies. The range of temperature variations in the profile based on the *Lindsley* [1983] geothermometer is about 150 K, neglecting high values termed "anomalous." When the high values are included the range increases to 400 K. The profile utilizing the *Wells* [1977] geothermometer has a range of 100 K neglecting the anomalous values and 350 K including them. The highest temperatures in our inversions are near 30°N (Figures 17-18), a region showing a slight peak in Bonatti's temperature profile estimated according to *Lindsley* [1983] and a very weak rise in the profile utilizing the *Wells* [1977] geothermometer. There is a small dip in temperature at 26°N (a region which we find to be seismically fast) in the *Lindsley* [1983] and *Wells* [1977] profiles, but the difference may not be significant considering the error bars. *Bergman and Solomon* [1989] also found the upper mantle near 26°N to be seismically fast from an analysis of teleseismic P-wave travel time residuals from earthquakes in this region recorded by a local ocean-bottom seismic network. The lowest temperatures on the profiles of *Bonatti* [1990] are at 43°N. Temperatures from our inversion solutions are also low in this region, although the *Bonatti* [1990] profiles indicate an increase in temperature proceeding north from 43°N to 53°N, whereas our results favor

continued low temperatures. Part of the difference between our results and the geochemical studies may be attributed to the fact that the depth sampled by basalts and peridotites is likely to be shallower than the layer thicknesses of most of our models. Assuming that the 6-km-thick oceanic crust was formed by 9 to 22 % partial melting of the mantle [*Klein and Langmuir*, 1987], then the volume of residual peridotite will extend from the base of the crust to somewhere between 30 and 70 km depth. The amount of depletion will vary with depth if we assume a fractional melting model. Our models with compositional variations confined to depths less than 50 km are most representative of shallow fractionation and differentiation.

Several improvements in future studies of the type presented here may be envisioned. Our models thus far have been limited to simply parameterized one-dimensional variations in temperature and composition within a single layer. It is likely that these lateral variations are not constant within a given layer and that there are two-dimensional lateral variations independent of lithospheric aging. The techniques outlined in this paper can be generalized to a multilayer system and to two-dimensional wavenumber (see equation 8), but we do not feel that the resolution of our data can justify more complicated models at this time. Kernels for seismic surface waves are strongly peaked in the upper mantle, and such data would provide a useful constraint in future models. The inclusion of surface wave data would help to distinguish between lithospheric and asthenospheric effects and may allow for two or more independently resolved layers. Extension of the modelling to three dimensions would permit an assessment of the degree to which mantle anomalies beneath the ridge extend off axis. Implicit in our age-correction is the assumption that the anomalous properties of the ridge mantle are steady state on a time scale of 100 My. Recent seafloor surveys and theoretical studies [e.g., *Pockalny et al.*, 1988; *Scott and Stevenson*, 1989] bring this assumption into question and suggest that at least on short time scales (< 1 My) and at slow spreading rates (as in the Atlantic) intermittent periods of melting and crustal formation may be separated by periods with little or no melt production. These temporation variations are likely to be averaged out, however, over the typical horizontal wavelength (100 km) of a long-period SS wave.

Another limitation of our models is that they depend on the assumed values of several physical constants. It is straightforward, however, to estimate the effect of choosing different values. The viscosity structures we employ are also quite simple but have been chosen to represent two models widely invoked in other studies - a constant or nearly constant viscosity mantle [e.g., *Peltier*, 1989] and a mantle with a thin low viscosity layer [e.g., *Craig and McKenzie*, 1986; *Robinson et al.*, 1987]. The viscosity structure of the Earth may be temperature and pressure dependent or vary laterally, but we have not considered viscosity structures of this type. Nor have we modelled the effects of partial melting which could accompany the temperature variations we predict. The effect of retained melt on the physical properties of the mantle depends critically on the melt fraction and geometry, characteristics presently poorly known. *Sato et al.* [1988, 1989] downplay the importance of partial melt and suggest that most mantle seismic velocity anomalies can be explained by temperature variations at subsolidus conditions. The combined analysis of both shear and compressional differential travel times also suggest that significant partial melting is not required to explain the travel time residuals in the north Atlantic region [*Woodward and Masters*, 1991].

CONCLUSIONS

We have measured 500 SS-S differential travel times for paths in the north Atlantic region. The SS-S travel time residual decreases linearly with square root of age, in general agreement with the plate cooling model to an age of 80-100 My [*Parsons and Sclater*, 1977]. Azimuthal anisotropy is not clearly resolved, and the azimuthal patterns of our data are not consistent with the preferred upper mantle anisotropy model of *Kuo et al.* [1987] for the north Atlantic. An along-axis profile of age-corrected travel time residuals displays significant long-wavelength variations, notably at wavelengths of 1000-2000 km. The largest of these variations are robust with respect to selective removal of portions of the data.

We have formulated a joint inversion of travel time residuals and geoid and bathymetric anomalies for lateral variation in upper mantle temperature and composition. On the basis of variance reduction, inversion for temperature favors the presence of an upper mantle low viscosity zone and temperature anomalies concentrated at depths less than 300 km. We are unable to match travel time residuals simultaneously with geoid and bathymetry solely with lateral variations in bulk composition (Mg#). Joint inversions for temperature and composition provide good fits to both travel time and and geoid regardless of viscosity structure or layer depth and thickness, but the best fits to bathymetry come from models with a low-viscosity zone and thermal or compositional variations confined to shallow depth. The Mg# variations predicted in the joint inversion for temperature and composition are comparable to those found by *Michael and Bonatti* [1985] in a study of dredged peridotites along the Mid-Atlantic Ridge and may be related to variations in melt production along the ridge.

The preferred inversion solutions have variations in upper mantle temperature along the Mid-Atlantic Ridge of about 100 K. For a constant bulk composition, such a temperature variation would produce about a 7 km variation in crustal thickness [*White and McKenzie*, 1989], larger than is generally observed [*Spudich and Orcutt*, 1980; *White*, 1984; *Purdy and Detrick*, 1986]. Introducing compositional variations as well as temperature variations in the inversions does not change the range of temperature appreciably. The presence of volatiles in the mantle can have a strong effect on temperatures required for melting, and variations in volatile content along the ridge may reduce the large variation in melt production implied by the lateral temperature variations indicated in our models.

APPENDIX A: ESTIMATION OF ERRORS FOR SS-S DIFFERENTIAL TRAVEL TIMES

It is important to quantify the uncertainties in the differential travel time measurements. After cross-correlation, the "quality" of each individual SS-S measurement is rated and a grade is assigned. The cross correlation coefficient, which describes the degree of fit between the synthetic and real SS phases, is used as an objective aid in the assignment of quality. However, our final assignment of quality is largely subjective and based upon visual inspection of the "synthetic" SS, real SS, and cross correlogram, taking into account the sharpness of the arrivals and their alignment, the clarity of the seismogram, and the appearance of a single clear peak in the cross correlation function. An "A" quality grade indicates an excellent fit, "B" quality indicates good phase alignment but only a fair fit, and a "C" quality grade indicates a poor fit or some ambiguity as to phase alignment. In addition to A, B, and C grades, there were data that were rejected due to poor signal to noise ratio for either the S or SS phases.

Assuming that the uncertainty in an individual measurement comes from a combination of measurement error, unmodeled lower mantle structure, and epicentral error, we write, for example, for the measurement variance of an "A" quality datum:

$$\sigma_A^2 = \sigma_{Am}^2 + \sigma_{lm}^2 + \sigma_{epi}^2 \qquad \text{(A1)}$$

where σ_A is the total uncertainty, σ_{Am} is the measurement error, σ_{lm} is the uncertainty due to unmodeled lower mantle structure, and σ_{epi} is the epicentral error. We assume that σ_{lm} and σ_{epi} are the same for A, B, and C quality measurements, but the measurement error is obviously a strong function of data quality.

Effect of Epicentral Error

In general, epicentral errors affect the travel times only slightly. The events used in this

study were well recorded by a large number of stations over a wide range of azimuths, and typical epicentral mislocations are probably less than 10 km (which would yield a differential travel-time error of 0.35 s at 75° distance). The travel times are even less sensitive to errors in focal depth; an error in depth of 25 km contributes only about 0.3 s to the SS-S residual. Using the rule of thumb that one standard deviation is about one half of the estimated extremes, we adopt $\sigma_{epi} = 0.75$ s as a conservative estimate of epicentral error.

Effect of Unmodelled Lower Mantle Heterogeneity

We estimate the likely magnitude of lateral variations in the shear wave velocity of the lower mantle from models of lower mantle heterogeneity in P wave velocity (such as model L02.56 of *Dziewonski* [1984]). The average variation in travel times of direct P waves bottoming in the lower mantle is in the range ± 0.5 s. Global tomographic studies by *Dziewonski and Woodhouse* [1987] indicate that the scaling ratio $(\delta V_s/V_s)/(\delta V_p/V_p) \approx 2$ in the lower mantle. Such a scaling is also suggested by comparison of lower mantle P wave models with the recent lower mantle S model of *Tanimoto* [1990]. Assuming such an S to P velocity anomaly scaling, the resulting variation in S wave arrival time contributed by the lower mantle would likely be about ± 1.5 s, a fraction of the observed range in SS-S residual. While the major features of lower mantle model L02.56 [*Dziewonski*, 1984] and the lower mantle portions of *Tanimoto's* [1990] model are for the most part similar, enough differences exist that the application of a lower mantle "correction" to our data might add more uncertainty than it removes. Further, absolute S-wave travel times do not show enough variance for us to suspect large lower mantle effects [e.g., *Randall*, 1971; *Girardin and Poupinet*, 1974; *Hart and Butler*, 1978; *Uhrhammer*, 1978, 1979], and the work of *Gudmundson et al.* [1990] indicates that most of the variance from the ISC tables is attributable to the shallow mantle, i.e., most of the Earth's heterogeneity is in the upper mantle and the lower mantle is fairly homogeneous. On the basis of the above information, we set $\sigma_{lm} = 0.5$ s for our study.

Measurement error

As an objective means to obtain error estimates, we examine the scatter in A, B, and C quality picks in a small region. We measured the root mean square (rms) difference between travel time residuals of the same grade (A, B, or C) with bounce points separated by less than 80 km and with differences in path azimuth at the bounce point of less than 10°. An 80-km distance is less than the horizontal wavelength of SS (which is about 180 km at 25 s period) so we do not expect much contribution to the rms difference from actual lateral variations in structure. The rms difference for the 16 A quality residual pairs which were within 80 km of each other was 1.15 s.

uality picks, an rms difference of 2.08 s was measured using 20 residual pairs, and for C quality picks 44 residual pairs yielded an rms difference of 2.96 s.

We interpret these estimates of the rms diffences as representing the average overall errors in the A, B, and C grade measurements. (Unmodelled lower mantle structure should be nearly identical for data with bounce points within 80 km and at similar azimuths). Under this interpretation we can write, for A-quality residuals,

$$\sigma_{Arms}^2 = \sigma_{Am}^2 + \sigma_{epi}^2 \qquad \text{(A2)}$$

Substituting values of σ_{Arms} and σ_{epi} into (A2) yields σ_{Am}= 0.87 s. Similarly, for B and C quality measurements, we find σ_{Bm} = 1.94 s and σ_{Cm} = 2.86 s. From (A1), the total uncertainty for A, B, and C quality is, respectively, σ_A = 1.25 s, σ_B = 2.14 s, and σ_C = 3.00 s.

In the weighted regression experiments the A, B, and C quality measurements are weighted inversely by their measurement variance.

APPENDIX B: ERRORS IN THE ALONG-AXIS PROFILES AND CONSTRUCTION OF THE DATA COVARIANCE MATRIX

Errors in Bathymetry, Geoid, and Travel Time Profiles

Uncertainties in the along-axis profiles of geoid, bathymetry, and travel times are important information in the inversion. The gridded bathymetric data [*U.S. Naval Oceanographic Office*, 1985] include corrections for the deviation of water column acoustic velocity from the assumed value of 1500 m s^{-1}. The geoid data, provided in the form of a 0.25° x 0.25° grid [*Marsh et al.*, 1986], include corrections for orbit errors, instrument and atmospheric propagation effects, and solid Earth and ocean tides.

We have averaged the bathymetry and geoid height values within a 1° x 1° box centered at each SS bounce point. The averaging yields a representative value for a region over approximately one horizontal wavelength of the SS wave and acts to smooth out short-wavelength variations. Both bathymetry and geoid are corrected for subsidence with seafloor age, using the plate cooling model [*Parsons and Sclater*, 1977; *Parsons and Richter*, 1980]. Error introduced into depth and geoid anomalies by isochron mislocation is difficult to estimate precisely, but for an error in age of 2 My, depth and geoid errors at 80 My would be about 30 m and 0.2 m, respectively, while at 2 My, an error in age of 2 My would have a much larger affect, giving depth and geoid errors of 350 m and 0.3 m. The magnitude of this error highlights the importance of accurate age determination, especially at young ages.

The presence of oceanic sediments is another source of error. In the Atlantic Ocean, the sediment thickness increases regularly from less than 100 m along the Mid-Atlantic Ridge toward continental margins where it can exceed 1 km [*Ewing et al*, 1973; *Tucholke*, 1986]. A 1-km sediment thickness leads to corrections to residual depth and geoid of about 500 m and 0.3 m, respectively [*Cazenave et al.*, 1988; *Sheehan and McNutt*, 1989]. On Atlantic lithosphere of 100 My age or less the sediment thickness is less than 500 m in most areas. Hence, neglecting the

sediment loading correction should not be crucial in this region.

The along-axis profile of SS-S residual is a weighted moving average of 10 adjacent data points grouped by latitude, using the weights discussed in Appendix A. The same weights and moving average are applied to geoid and bathymetry values at a given SS bounce point, even though bathymetry and geoid data are presumed to be of equal quality, in order that these profiles will be consistent with the SS-S residuals. The standard error of the mean values for SS-S residual ranges from 0.2 s to 1.6 s. For bathymetry the range of standard deviations from the mean value is from 24 to 370 m, and for geoid, 0.08 to 1.0 m. The largest variances in the bathymetry and geoid data come from the Iceland region (north of 60°N), and may be due to the more complicated tectonics of this region [*White*, 1988].

Before Fourier transforming, the along-axis profiles must be interpolated to a constant spacing. We use a simple linear interpolation scheme to estimate values at a 0.5° spacing. We estimate that the typical error in the interpolated data is comparable to that in the along-axis moving averages, which for bathymetry is on the order of 125 m, for geoid 0.4 m, and for travel time 1 s.

Effect of Crustal Thickness Variations

Our poor fit to topography in the inversion experiments can be at least partially attributed to unmodelled effects such as crustal thickness differences. Variations in oceanic crustal thickness about the typical value of 6-7 km [*Spudich and Orcutt*, 1980; *White*, 1984; *Purdy and Detrick*, 1986] are generally thought to be small at horizontal scales of 100 km and greater. However, the crust beneath the Azores plateau is estimated to be between 8 and 9 km thick [*Searle*, 1976; *Whitmarsh et al.*, 1982] and that beneath Iceland is at least 8 to 14 km thick [*Bjornsson*, 1983]. By simple isostatic mass balance, the depth anomaly due to excess crustal thickness in the Azores region would be about 400 m, and at Iceland, 200 m to 1.6 km. In general, simple variations in crustal thickness are insufficient to produce a significant SS-S residual. For crustal and mantle S wave velocities of 3.5 and 4.4 km/s, a 2-km variation in crustal thickness would contribute less

than 0.2 s to an SS-S differential travel time corrected for differences in bathymetry. However, at Iceland, where the crust is estimated to be as much as 14 km thick, the additional SS-S travel time could be up to 0.8 s.

Data Covariance Matrix

The data covariance matrix $\mathbf{R}_{dd}$ is of the form

$$R_{dd} = \begin{pmatrix} \sigma_h(k_1)^2 & 0 & 0 & 0 & 0 & 0 & 0 & 0 & 0 \\ 0 & \dots & 0 & 0 & 0 & 0 & 0 & 0 & 0 \\ 0 & 0 & \sigma_h(k_n)^2 & 0 & 0 & 0 & 0 & 0 & 0 \\ 0 & 0 & 0 & \sigma_N(k_1)^2 & 0 & 0 & 0 & 0 & 0 \\ 0 & 0 & 0 & 0 & \dots & 0 & 0 & 0 & 0 \\ 0 & 0 & 0 & 0 & 0 & \sigma_N(k_n)^2 & 0 & 0 & 0 \\ 0 & 0 & 0 & 0 & 0 & 0 & \sigma_t(k_1)^2 & 0 & 0 \\ 0 & 0 & 0 & 0 & 0 & 0 & 0 & \dots & 0 \\ 0 & 0 & 0 & 0 & 0 & 0 & 0 & 0 & \sigma_t(k_n)^2 \end{pmatrix}$$

where σ_h^2, σ_N^2, and σ_t^2 are the nominal variances of the bathymetry, geoid, and travel time data, respectively. We may choose to construct the data covariance matrix not to reflect the true variance of the data but rather to allow weighting between the different data sets. In this way, the data covariance matrix can be altered to test the relative contributions of different data sets to the inversion results.

In all of our inversions, the covariance matrix is constructed to weight the three data sets approximately equally. For example, examination of Figure 10 indicates that at 3000-km wavelength the amplitude of the geoid signal is approximately 4 m, bathymetry 1 km, and travel time 2 s. Thus if a value of 1 m is chosen for σ_N, then a value of 0.5 s for σ_t and 0.25 km for σ_h should yield approximately equal weighting of data sets. The corresponding $1/\sigma^2$ values are then 1 for geoid, 4 for travel time, and 16 for bathymetry.

Acknowledgements. We thank Marcia McNutt for suggesting the inverse problem, and Anne Judge for providing codes for computing geoid and topography kernels. Bob Woodward and Justin Revenaugh provided advice and subroutines for measuring travel times. We thank John Woodhouse and Adam Dziewonski for allowing us access to the digital data archives at Harvard University and Lind Gee for setting up the data retrieval software at MIT. This research was supported by the National Science Foundation under grant EAR-9004750 and the National Aeronautics and Space Administration under grant NAG 5-814.

REFERENCES

Akimoto, S. I., The system MgO-FeO-SiO_2 at high pressures and temperatures - phase equilibria and elastic properties, *Tectonophysics, 13*, 161-187, 1972.

Allègre, C. J., B. Hamelin, and B. Dupré, Statistical analysis of isotopic ratios in MORB: The mantle blob cluster model and the convective regime of the mantle, *Earth Planet. Sci. Lett., 71*, 71-84, 1984.

Anderson, O. L., E. Schreiber, R. C. Lieberman, and N. Soga, Some elastic constant data on minerals relevant to geophysics, *Rev. Geophys., 6*, 491-524, 1968.

Anderson, R. N., D. McKenzie, and J. G. Sclater, Gravity, bathymetry, and convection in the Earth, *Earth Planet. Sci. Lett., 18*, 391-407, 1973.

Backus, G. E., Possible forms of seismic anisotropy of the upper mantle under oceans, *J. Geophys. Res., 70*, 3429-3439, 1965.

Bergman, E. A., and S. C. Solomon, P wave travel times for Mid-Atlantic Ridge earthquakes and evidence for mantle heterogeneity (abstract), *Eos Trans. AGU, 70*, 1227, 1989.

Bjornsson, S., Crust and upper mantle beneath Iceland, in *Structure and Development of the Greenland-Scotland Ridge*, edited by M.H.P. Bott, S. Saxov, and M. Talwani, NATO Conf. Ser., *4*, pp. 31-61, Plenum Press, New York, 1983.

Bonatti, E., Not so hot "hot spots" in the oceanic mantle, *Science, 250*, 107-111, 1990.

Boyd, F. R., and R. H. McCallister, Densities of fertile and sterile garnet peridotites, *Geophys. Res. Lett., 3*, 509-512, 1976.

Buck, W. R., and E. M. Parmentier, Convection beneath young oceanic lithosphere: Implications for thermal structure and gravity, *J. Geophys. Res., 91*, 1961-1974, 1986.

Butler, R., Shear-wave travel times from SS, *Bull. Seismol. Soc. Am., 69*, 1715-1732, 1979.

Cazenave, A., K. Dominh, M. Rabinowicz, and G. Ceuleneer, Geoid and depth anomalies over ocean swells and troughs: Evidence of an increasing trend of the geoid to depth ratio with age of plate, *J. Geophys. Res.*, *93*, 8064-8077, 1988.

Choy, G. L., and P. G. Richards, Pulse distortion and Hilbert transformation in multiply reflected and refracted body waves, *Bull. Seismol. Soc. Am.*, *65*, 55-70, 1975.

Craig, C. H., and D. P. McKenzie, The existence of a thin low viscosity layer beneath the lithosphere, *Earth Planet. Sci. Lett.*, 78, 420-426, 1986.

Crampin, S., A review of the effects of anisotropic layering on the propagation of seismic waves, *Geophys. J. R. Astron. Soc.*, *49*, 9-27, 1977.

Creager, K. C., and T. H. Jordan, Slab penetration into the lower mantle beneath the Mariana and other island arcs of the Northwest Pacific, *J. Geophys. Res.*, *91*, 3573-3589, 1986.

Davies, G. F., Geophysical and isotopic constraints on mantle convection: An interim synthesis, *J. Geophys. Res.*, *89*, 6017-6040, 1984.

DeMets, C., R. G. Gordon, D. F. Argus, and S. Stein, Current plate motions, *Geophys. J. Int.*, 101, 425-478, 1990.

Dick, H. J. B., Abyssal peridotites, very-slow spreading ridges and ocean ridge magmatism, in *Magmatism in the Ocean Basins*, edited by A. D. Saunders and M. J. Norry, *Spec. Pub. Geol. Soc. London*, *42*, pp. 71-105, 1989.

Dick, H. J. B., R. L. Fisher, and W. B. Bryan, Mineralogic variability of the uppermost mantle along mid-ocean ridges, *Earth Planet. Sci. Lett.*, *69*, 88-106, 1984.

Duffy, T. S., and D. L. Anderson, Seismic velocities in mantle minerals and the mineralogy of the upper mantle, *J. Geophys. Res.*, *94*, 1895-1912, 1989.

Duschenes, J. D., and S. C. Solomon, Shear wave travel time residuals from oceanic earthquakes and the evolution of oceanic lithosphere, *J. Geophys. Res.*, *82*, 1985-2000, 1977.

Dziewonski, A. M., Mapping the lower mantle: Determination of lateral heterogeneity in P

velocity up to degree and order 6, *J. Geophys. Res.*, *89*, 5929-5952, 1984.

Dziewonski, A. M., and D. L. Anderson, Preliminary reference Earth model, *Phys. Earth Planet. Inter.*, *25*, 297-356, 1981.

Dziewonski, A. M., and J. F. Gilbert, The effect of small, aspherical perturbations on travel times and a re-examination of the corrections for ellipticity, *Geophys. J. R. Astron. Soc.*, *44*, 7-17, 1976.

Dziewonski, A. M., and J. H. Woodhouse, An experiment in systematic study of global seismicity: Centroid-moment tensor solutions for 201 moderate and large earthquakes in 1981, *J. Geophys. Res.*, *88*, 3247-3271, 1983.

Dziewonski, A. M., and J. H. Woodhouse, Global images of the Earth's interior, *Science*, *236*, 37-48, 1987.

Dziewonski, A. M., B. H. Hager, and R. J. O'Connell, Large-scale heterogeneities in the lower mantle, *J. Geophys. Res.*, *82*, 239-255, 1977.

Dziewonski, A. M., T. A. Chou, and J. H. Woodhouse, Determination of earthquake source patterns from wave-form data for studies of global and regional seismicity, *J. Geophys. Res.*, *86*, 2825-2852, 1981.

Ewing, M., G. Carpenter, C. C. Windisch, and J. I. Ewing, Sediment distribution in the oceans: The Atlantic, *Geol. Soc. Am. Bull.*, *84*, 71-88, 1973.

Fischer, K. M., T. H. Jordan, and K. C. Creager, Seismic constraints on the morphology of deep slabs, *J. Geophys. Res.*, *93*, 4773-4783, 1988.

Gee, L. S., and T. H. Jordan, Generalized seismological data functionals, I: Theory and observational procedures (abstract), *Eos Trans. AGU*, *70*, 1201, 1989.

Girardin, N., and G. Poupinet, Teleseismic S travel-time delay for Mid-Atlantic Ridge earthquakes, *Phys. Earth Planet. Inter.*, *9*, 306-313, 1974.

Goetze, C., A brief summary of our present day understanding of the effect of volatiles and partial melt on the mechanical properties of the upper mantle, in *High-Pressure Research, Applications in Geophysics*, edited by M. H. Manghnani and S. I. Akimoto,

pp. 3-24, Academic Press, New York, 1977.

Grand, S. P., Tomographic inversion for shear velocity beneath the North American plate, *J. Geophys. Res., 92*, 14,065-14,090, 1987.

Grand, S. P., Mantle shear structure from 30°S to 90°N and 120°W to 60°E (abstract), *Eos Trans. AGU, 70*, 389, 1989.

Grand, S. P., and D. V. Helmberger, Upper mantle shear structure beneath the northwest Atlantic Ocean, *J. Geophys. Res., 89*, 11465-11475, 1984.

Green, D. H., and R. C. Liebermann, Phase equilibria and elastic properties of a pyrolite model for the oceanic upper mantle, *Tectonophysics, 32*, 61-92, 1976.

Gudmundsson, O., J. H. Davies, and R. W. Clayton, Stochastic analysis of global traveltime data: Mantle heterogeneity and random errors in the ISC data, *Geophys. J. Int., 102*, 25-44, 1990.

Hager, B. H., Subducted slabs and the geoid: Constraints on mantle rheology and flow, *J. Geophys. Res., 89*, 6003-6015, 1984.

Hager, B. H., and R. W. Clayton, Constraints on the structure of mantle convection using seismic observation, flow models, and the geoid, in *Mantle Convection*, edited by W.R. Peltier, Gordan and Breach, New York, pp. 657-763, 1989.

Hager, B. H., and R. J. O'Connell, Kinematic models of large-scale flow in the Earth's mantle, *J. Geophys. Res., 84*, 1031-1048, 1979.

Hager, B. H., and R. J. O'Connell, A simple global model of plate dynamics and mantle convection, *J. Geophys. Res., 86*, 1031-1048, 1981.

Hager, B. H., R. W. Clayton, M. A. Richards, R. P. Comer, and A. M. Dziewonski, Lower mantle heterogeneity, dynamic topography and the geoid, *Nature, 313*, 541-545, 1985.

Hart, R. S., and R. Butler, Shear-wave travel times and amplitudes for two well-constrained earthquakes, *Bull. Seismol. Soc. Am., 68*, 973-985, 1978.

Honda, S., and T. Tanimoto, Regional 3-D heterogeneities by waveform inversion -

application to the Atlantic area, *Geophys. J. R. Astron. Soc., 91*, 737-753, 1987.

Hong, H. J., D. A. Yuen, and J. Wu, Dynamical effects of a hard garnet layer in the transition zone on geophysical signatures: Geoid anomalies and postglacial rebound, *Phys. Earth Planet. Inter., 64*, 37-51, 1990.

Jaques, A. L., and D. H. Green, Anhydrous melting of peridotite at 0-15 kb pressure and the genesis of tholeiitic basalts, *Contrib. Mineral. Petrol., 73*, 287-310, 1980.

Johnson, K. T. M., H. J. B. Dick, and N. Shimizu, Melting in the oceanic upper mantle: An ion microprobe study of diopsides in abyssal peridotites, *J. Geophys. Res., 95*, 2661-2678, 1990.

Jordan, T. H., Mineralogies, densities, and seismic velocities of garnet lherzolites and their geophysical implication, in *The Mantle Sample: Inclusions in Kimberlites and Other Volcanics*, edited by F. R. Boyd and H.O.A. Meyer, pp. 1-14, AGU, Washington, D.C., 1979.

Jordan, T. H., and W. S. Lynn, A velocity anomaly in the lower mantle, *J. Geophys. Res., 79*, 2679-2685, 1974.

Kent, D. V., and F. Gradstein, A Jurassic to recent geochronology, in *The Western North Atlantic Region, The Geology of North America, Volume M*, edited by P. R. Vogt and B. E. Tucholke, Geological Society of America, Boulder, Colo., pp. 45-50, 1986.

Klein, E. M., and C. H. Langmuir, Global correlations of ocean ridge basalt chemistry with axial depth and crustal thickness, *J. Geophys. Res., 92*, 8089-8115, 1987.

Klitgord, K. D., and H. Schouten, Plate kinematics of the central Atlantic, in *The Western North Atlantic Region, The Geology of North America, Volume M*, edited by P. R. Vogt and B. E. Tucholke, Geological Society of America, Boulder, Colo., pp. 351-378, 1986.

Kumazawa, M., and O. L. Anderson, Elastic moduli, pressure derivatives, and temperature derivatives of single-crystal olivine and single-crystal forsterite, *J. Geophys. Res., 74*, 5961-5972, 1969.

Kuo, B.-Y., D. W. Forsyth, and M. E. Wysession, Lateral heterogeneity and azimuthal anisotropy in the North Atlantic determined from SS-S differential travel times, *J. Geophys. Res., 92*, 6421-6436, 1987.

Lerch, F. J., S. M. Klosko, R. E. Laubscher, and C. A. Wagner, Gravity model improvement using Geos 3 (GEM 9 and 10), *J. Geophys. Res., 84*, 3897-3916, 1979.

Liebermann, R. C., Velocity-density systematics for the olivine and spinel phases of Mg_2SiO_4-Fe_2SiO_4, *J. Geophys. Res., 75*, 4029-4034, 1970.

Lindsley, D. H., Pyroxene thermometry, *Am. Mineral., 68*, 477-493, 1983.

Marsh, J. G., A. C. Brenner, B. D. Beckley, and T. V. Martin, Global mean sea surface based upon the Seasat altimeter data, *J. Geophys. Res., 91*, 3501-3506, 1986.

McKenzie, D. P., Surface deformation, gravity anomalies and convection, *Geophys. J. R. Astron. Soc., 48*, 211-238, 1977.

McKenzie, D. P., and C. O. Bowin, The relationship between bathymetry and gravity in the Atlantic ocean, *J. Geophys. Res., 81*, 1903-1915, 1976.

McKenzie, D. P., A. B. Watts, B. E. Parsons, and M. Roufosse, Planform of mantle convection beneath the Pacific Ocean, *Nature, 288*, 442-466, 1980.

McNutt, M. K., and A. V. Judge, The superswell and mantle dynamics beneath the South Pacific, *Science, 248*, 969-975, 1990.

Michael, P. J., The concentration, behavior and storage of H_2O in the suboceanic upper mantle: Implications for mantle metasomatism, *Geochim. Cosmochim. Acta, 52*, 555-566, 1988.

Michael, P. J., and E. Bonatti, Periodotite composition from the north Atlantic: Regional and tectonic variations and implications for partial melting, *Earth Planet. Sci. Lett., 73*, 91-104, 1985.

Mocquet, A., and B. A. Romanowicz, Three-dimensional structure of the upper mantle beneath the Atlantic Ocean inferred from long-period Rayleigh waves, 2, Inversion, *J. Geophys. Res., 95*, 6787-6798, 1990.

Mocquet, A., B. A. Romanowicz, and J. P. Montagner, Three-dimensional structure of the upper mantle beneath the Atlantic Ocean inferred from long-period Rayleigh waves, 1, Group and phase velocity distributions, *J. Geophys. Res., 94*, 7449-7468, 1989.

Montagner, J. P., and T. Tanimoto, Global anisotropy in the mantle inferred from the regionalization of phase velocities, *J. Geophys. Res., 95*, 4797-4819, 1990.

Nakanishi, I., and D. L. Anderson, Measurement of mantle wave velocities and inversion for lateral heterogeneity and anisotropy, Part II: Analysis by the single station method, *Geophys. J. R. Astron. Soc., 78*, 573 - 617, 1984.

Nolet, G., and N. J. Vlaar, The NARS project: Probing the Earth's interior with a large seismic antenna, *Terra Cognita, 2*, 17-25, 1982.

O'Hara, M. J., Is there an Icelandic mantle plume? *Nature, 253*, 708-710, 1975.

Oxburgh, E. R., and E. M. Parmentier, Compositional and density stratification in oceanic lithosphere - causes and consequences, *J. Geol. Soc. London, 133*, 343-355, 1977.

Parmentier, E. M., and J. E. Oliver, A study of shallow mantle flow due to the accretion and subduction of lithospheric plates, *Geophys. J. R. Astron. Soc., 57*, 1-22, 1979.

Parsons, B. E. and S. Daly, The relationship between surface topography, gravity anomalies, and temperature structure of convection, *J. Geophys. Res, 88*, 1129-1144, 1983.

Parsons, B. E. and F. M. Richter, A relation between the driving force and geoid anomaly associated with mid-ocean ridges, *Earth. Planet. Sci. Lett., 51*, 445-450, 1980.

Parsons, B. E., and J. G. Sclater, An analysis of the variation of ocean floor bathymetry and heat flow with age, *J. Geophys. Res., 82*, 803-827, 1977.

Peltier, W. R., Mantle viscosity, in *Mantle Convection*, edited by W.R. Peltier, Gordon and Breach, New York, pp. 389-478, 1989.

Peterson, J., and C. R. Hutt, Test and calibration of the digital world-wide standardized seismograph, Open-File Report 82-1087, U.S. Geol. Survey, Albuquerque, N.M., 170 pp., 1982.

Peterson, J., H. M. Butler, L. G. Holcomb, and C. R. Hutt, The seismic research observatory, *Bull. Seismol. Soc. Am.*, *66*, 2049-2068, 1976.

Pockalny, R. A., R. S. Detrick, and P. J. Fox, Morphology and tectonics of the Kane transform from Sea Beam bathymetry data, *J. Geophys. Res.*, *93*, 3179-3193, 1988.

Purdy, G. M., and R. S. Detrick, Crustal structure of the Mid-Atlantic Ridge at 23°N from seismic refraction studies, *J. Geophys. Res.*, *91*, 3739-3762, 1986.

Rader, C. M., and B. Gold, Digital filter design techniques in the frequency domain, *Proc. IEEE*, *55*, 149-171, 1967.

Randall, M. J., A revised travel-time table for S, *Geophys. J. R. Astron. Soc.*, *22*, 229-234, 1971.

Richards, M. A., and B. H. Hager, Geoid anomalies in a dynamic Earth, *J. Geophys. Res.*, *89*, 5987-6002, 1984.

Robinson, E. M., B. E. Parsons, and S. F. Daly, The effect of a shallow low viscosity zone on the apparent compensation of midplate swells, *Earth Planet. Sci. Lett.*, *82*, 335-348, 1987.

Romanowicz, B., M. Cara, F. F. Fels, and D. Rouland, GEOSCOPE: A French initiative in long period, three component, global seismic networks, *Eos Trans. AGU*, *65*, 753-754, 1984.

Sandwell, D. T., and K. R. MacKenzie, Geoid height versus topography for oceanic plateaus and swells, *J. Geophys. Res.*, *94*, 7403-7418, 1989.

Sato, H., and I. S. Sacks, Anelasticity and thermal structure of the oceanic upper mantle: Temperature calibration with heat flow data, *J. Geophys. Res.*, *94*, 5705-5715, 1989.

Sato, H., I. S. Sacks, T. Murase, and C. M. Scarfe, Thermal structure of the low velocity zone derived from laboratory and seismic investigations, *Geophys. Res. Lett.*, *15*, 1227-1230, 1988.

Sato, H., I. S. Sacks, and T. Murase, The use of laboratory velocity data for estimating temperature and partial melt fraction in the low-velocity zone: Comparison with heat

flow and electrical conductivity studies, *J. Geophys. Res.*, *94*, 5689-5704, 1989.

Schilling, J. G., Geochemical and isotopic variation along the Mid-Atlantic Ridge axis from 79°N to 0°N, in *The Western North Atlantic Region, The Geology of North America, Volume M*, edited by P. R. Vogt and B. E. Tucholke, Geological Society of America, Boulder, Colo., pp. 137-156, 1986.

Schilling, J. G., M. B. Bergeron, and R. Evans, Halogens in the mantle beneath the North Atlantic, *Phil. Trans. Roy. Soc. London, Ser. A, 297*, 147-178, 1980.

Schilling, J. G., M. Zajac, R. Evans, T. H. Johnston, W. M. White, J. D. Devine, and R. H. Kingsley, Petrologic and geochemical variations along the Mid-Atlantic ridge from 29°N to 73°N, *Am. J. Sci.*, *283*, 510-586, 1983.

Sclater, J. G., B. Parsons, and C. Jaupart, Oceans and continents: Similarities and differences in the mechanism of heat loss, *J. Geophys. Res.*, *86*, 11535-11552, 1981.

Scott, D. R., and D. J. Stevenson, A self-consistent model of melting, magma migration and buoyancy-driven circulation beneath mid-ocean ridges, *J. Geophys. Res.*, *94*, 2973-2988, 1989.

Searle, R. C., Lithospheric structure of the Azores Plateau from Rayleigh-wave dispersion, *Geophys. J. R. Astron. Sci.*, *44*, 537-546, 1976.

Sheehan, A. F., and M. K. McNutt, Constraints on thermal and mechanical structure of the oceanic lithosphere at the Bermuda Rise from geoid height and depth anomalies, *Earth Planet. Sci. Lett.*, *93*, 377-391, 1989.

Sipkin, S. A., and T. H. Jordan, Lateral heterogeneity of the upper mantle determined from the travel times of multiple ScS, *J. Geophys. Res.*, *81*, 6307-6320, 1976.

Sipkin, S. A., and T. H. Jordan, Multiple ScS travel times in the western Pacific: Implications for mantle heterogeneity, *J. Geophys. Res.*, *85*, 853-861, 1980.

Sleep, N. H., Segregation of magma from a mostly crystalline mush, *Geol. Soc. Am. Bull.*, *85*, 1225-1232, 1974.

Sotin, C., and E. M. Parmentier, Dynamical consequences of compositional and thermal

density stratification beneath spreading centers, *Geophys. Res. Lett., 16*, 835-838, 1989.

Spudich, P. K., and J. A. Orcutt, A new look at the seismic velocity structure of the oceanic crust, *Rev. Geophys., 18*, 627-645, 1980.

Stacey, F. D., A thermal model of the Earth, *Phys. Earth. Planet. Inter., 15*, 341-348, 1977.

Stark, M. A., and D. W. Forsyth, The geoid, small-scale convection, and differential travel time anomalies of shear waves in the central Indian Ocean, *J. Geophys. Res., 88*, 2273-2288, 1983.

Stewart, I. C. F., and C. E. Keen, Anomalous upper mantle structure beneath the Cretaceous Fogo seamounts indicated by P-wave reflection delays, *Nature, 274*, 788-791, 1978.

Tanimoto, T., Long wavelength S-wave velocity structure throughout the mantle, *Geophys. J. Int., 100*, 327-336, 1990.

Tanimoto, T., and D. L. Anderson, Mapping convection in the mantle, *Geophys. Res. Lett., 11*, 287-290, 1984.

Tucholke, B. E., Structure of basement and distribution of sediments in the western North Atlantic, in *The Western North Atlantic Region, The Geology of North America, Volume M*, edited by P. R. Vogt and B. E. Tucholke, Geological Society of America, Boulder, Colo., pp. 331-340, 1986.

Uhrhammer, R. A., S-wave travel times for a spherically averaged earth, *Geophys. J. R. Astron. Soc., 55*, 283-309, 1978.

Uhrhammer, R. A., Shear-wave velocity structure for a spherically averaged Earth, *Geophys. J. R. Astron. Soc., 58*, 749-767, 1979.

U.S. Naval Oceanographic Office, Digital bathymetric database 5 (DBDB5), Nat. Geophys. Data Center, Boulder, Colo., 1985.

Watts, A. B., D. P. McKenzie, B. E.Parsons, and M. Roufosse, The relation between

gravity and bathymetry in the Pacific Ocean, *Geophys. J. R. Astron. Soc.*, *83*, 263-298, 1985.

Wells, P. R. A., Pyroxene thermometry in simple and complex systems, *Contrib. Mineral. Petrol.*, *62*, 129-139, 1977.

White, R. S., Atlantic ocean crust: Seismic structure of a slow spreading ridge, in *Ophiolites and Oceanic Lithosphere*, *Spec. Pub. Geol. Soc. London, 13*, edited by I. G. Glass, S. J. Lippard, and A. W. Shelton, pp. 101-112, Blackwell Scientific, St. Louis, Mo., 1984.

White, R. S., A hot-spot model for early Tertiary volcanism in the N Atlantic, in *Early Tertiary Volcanism and the Opening of the NE Atlantic*, edited by A. C. Morton and L. M. Parson, *Spec. Pub. Geol. Soc. London, 39*, pp. 3-13, 1988.

White, R. S., and D. McKenzie, Magmatism at rift zones: The generation of volcanic continental margins and flood basalts, *J. Geophys. Res.*, *94*, 7685-7729, 1989.

Whitmarsh, R. B., A. Ginzburg, and R. C. Searle, The structure and origin of the Azores-Biscay Rise, north-east Atlantic Ocean, *Geophys. J. R. Astron. Soc.*, *70*, 79-108, 1982.

Wood, D. A., A variably veined suboceanic upper mantle - Genetic significance for mid-ocean ridge basalts from geochemical evidence, *Geology*, *7*, 499-503, 1979.

Woodhouse, J. H., and A. M. Dziewonski, Mapping the upper mantle: Three dimensional modelling of Earth structure by inversion of seismic waveforms, *J. Geophys. Res.*, *89*, 5953-5986, 1984.

Woodward, R. L., and G. Masters, Global upper mantle structure from long-period differential travel times, *J. Geophys. Res.*, in press, 1991.

Wyllie, P. J., Role of water in magma generation and initiation of diapiric uprise in the mantle, *J. Geophys. Res.*, *76*, 1328-1338, 1971.

Zehnder, C. M., and J. C. Mutter, Systematics of thickness variations in ocean crust (abstract), *Eos Trans. AGU*, *71*, 1573, 1990.

Zhang, Y. S., and T. Tanimoto, Investigation of the SV-velocity variation of the upper mantle by using Rayleigh waves (abstract), *Eos Trans. AGU, 71*, 1449, 1990.

Figure Captions

Figure 1. An example of the measurement of SS-S differential travel time for the event of December 24, 1985 (10 km focal depth), at GDH (63° epicentral distance). (a) "Synthetic" SS pulse generated from S. The S pulse is windowed and attenuated to account for the additional time that SS travels in the mantle ($t^* = 3$ s), and a $\pi/2$ phase shift is applied. (b) Windowed SS wave pulse. (c) Cross-correlation of the trace in (b) with that in (a). The differential travel time residual is -5.04 s.

Figure 2. Distribution of earthquakes (triangles) and seismograph stations (circles) used to measure SS-S differential travel times. Stations are from the GDSN, NARS, and GEOSCOPE digital arrays. Earthquakes are from the Harvard CMT catalogue (generally $m_b > 5.0$) from the years 1977-1987. Lambert equal area projection with pole of projection at 45°N, 40°W.

Figure 3. (a) Map view of SS-S residuals relative to PREM [*Dziewonski and Anderson*, 1981], corrected for Earth ellipticity and seafloor bathymetry. Residuals are plotted at the SS bounce point. The size of each symbol scales linearly with magnitude of the residual. Lambert equal area projection with pole of projection at 40°N, 60°W. Negative residuals indicate either early SS or late S. Plate boundaries are from *DeMets et al.* [1990].

(b) Same as (a) but including data only for SS bouncepoints on lithosphere younger than 100 My.

Figure 4. SS-S travel time residual versus square root of seafloor age for data from 0-60°N. Each plotted point represents the weighted mean of 14 adjacent data points. Weights are constructed from variances determined as discussed in Appendix A. Horizontal and vertical bars are standard errors of the means of the travel time residuals and $(age)^{1/2}$. Linear regression yields a slope of -0.68 ± 0.08 s/ $(My)^{1/2}$ for a 0-100 My age range (solid line) or -0.76 ± 0.09 s/ $(My)^{1/2}$ for a 0-80 My range (dashed line).

Figure 5. Age-corrected SS-S residual (see text) versus azimuth θ. Each plotted point represents the weighted mean of 10 adjacent data points. The solid curve shows the best-fitting 4θ variation derived from these data. The dashed curve shows the preferred model of *Kuo et al.* [1987], which corresponds to an alignment of the *a* axis of olivine in the approximate direction N13°W.

Figure 6. (a) Map view of age-corrected SS-S residuals.
(b) Same as (a) but including data only with SS bounce points on lithosphere younger than 100 My.

Figure 7. Map view of the distribution of sampling azimuths. Lines indicate the wave path azimuth at the SS bounce point. Mercator projection.

Figure 8. Age-corrected SS-S residual versus latitude along the Mid-Atlantic Ridge from 10 to 90°N. The residuals shown are moving averages (such that each point is used twice) of 12 adjacent data points. Bounce points on lithosphere of age 0-100 My are used. The approximate locations of several fracture zones (Fifteen-Twenty, Kane, Atlantis, Oceanographer, and Charlie-Gibbs, denoted by abbreviations) and of the Iceland and Azores

hotspots are indicated.

Figure 9. Linear correlation, by highest harmonic degree removed from the geoid, of observed SS-S residual with geoid height measured at the corresponding SS bounce point. Both travel time and geoid residuals are age-corrected. First the raw [*Marsh et al.*, 1986] geoid data are correlated with SS-S residuals and a slope and correlation coefficient determined. Then a geoid reference field [*Lerch et al.*, 1979] up to degree and order 2 (with taper to degree and order 6) is calculated and removed from the geoid data, the slope and correlation coefficient with SS-S calculated, and so on for higher harmonic degrees ℓ removed from the geoid data, with appropriate tapers (up to $\ell + 4$). (a) Linear correlation coefficient between geoid and SS-S residuals vs. highest harmonic degree and order removed from the geoid. (b) Slope of the correlation between geoid and SS-S data, as a function of highest harmonic degree and order removed from the geoid. Extra points at degree and order 10 are obtained by using different tapers (no taper, taper to $\ell = 14$, and taper to $\ell = 15$).

Figure 10. Comparative plots of age-corrected (a) bathymetry, (b) geoid, and (c) SS-S residual along the Mid-Atlantic Ridge, 10-65°N. Bathymetry and geoid have been high-pass filtered (see text). All of the residuals shown are moving averages of 10 adjacent data points. Bounce points from lithosphere of age 0-100 My are used, except that data from the Labrador Sea region are omitted.

Figure 11. Upper mantle portion of the kernels for geoid and topography at two wavelengths $\lambda = 2\pi/k$ for two viscosity models. The convecting region in

both models is overlain by a high-viscosity layer 40 km thick, with viscosity 10^4 that of the underlying mantle.

(a) High-viscosity lid is underlain by a mantle of uniform viscosity and other physical parameters.

(b) High-viscosity lid is underlain by a zone extending to a depth of 200 km having a viscosity equal to 0.01 that of the underlying mantle.

Figure 12. Upper mantle portion of the kernels for geoid and topography at two wavelengths in spherical versus cartesian coordinates. The convecting region is overlain by a high-viscosity layer 40 km thick in each of two models for viscosity structure.

(a) Underlying mantle is of uniform viscosity. Cartesian kernels are for 4000 km wavelength (solid lines) and spherical kernels are for $\ell = 10$ (dashed lines).

(b) High-viscosity lid is underlain by zone extending to 200 km depth having a viscosity equal to 0.01 that of the underlying mantle. Cartesian kernels are for 4000 km wavelength and spherical kernels are for $\ell = 10$.

(c) Same as (a) but with Cartesian kernels for 6667 km wavelength and spherical kernels for $\ell = 6$.

(d) Same as (b) but with Cartesian kernels for 6667 km wavelength and spherical kernels for $\ell = 6$.

Figure 13. Results of combined inversion of geoid, bathymetry, and SS-S travel time residuals for upper mantle temperature variations. The viscosity structure is taken to consist of a thick high-viscosity lid overlying a constant-viscosity halfspace.

(a) Three solutions for along-axis temperature variations: Dotted line:

Temperature perturbations constrained to be uniform over 0-150 km depth. Long-dashed line: Temperature perturbations constrained to be uniform over 0-300 km depth. Short-dashed line: Temperature perturbations constrained to be uniform over 0-650 km depth.

(b) Observed (solid line) and predicted along-axis profiles of SS-S travel time residual. The "observed" profile is actually a filtered version of the observations, containing only the wavelengths used in the inversion (1400 to 7100 km). Predicted profiles were calculated from equation 5. Line types correspond to those of the temperature models.

(c) Observed and predicted along-axis geoid profiles. Same treatment as in (b).

(d) Observed and predicted along-axis bathymetry profiles. Same treatment as in (b).

Figure 14. Same as Figure 13 except for that the viscosity structure includes a zone extending from the base of the lid to a depth of 200 km with a viscosity equal to 0.01 that of the underlying mantle.

Figure 15. Results of combined inversion of geoid, bathymetry, and SS-S travel time residuals for variations in upper mantle composition (Mg#). The viscosity structure is taken to consist of a thick high-viscosity lid overlying a constant-viscosity halfspace.

(a) Three solutions for along-axis composition variations: Dotted line: Composition perturbations constrained to be uniform over 0-150 km depth. Long-dashed line: Composition perturbations constrained to be uniform over 0-300 km depth. Short-dashed line: Composition perturbations constrained to be uniform over 0-650 km depth.

(b) Observed (solid line) and predicted along-axis profiles of SS-S travel time residual.

(c) Observed and predicted along-axis geoid profiles.

(d) Observed and predicted along-axis bathymetry profiles.

Figure 16. Same as Figure 15 except for that the viscosity structure includes a zone extending from the base of the lid to a depth of 200 km with a viscosity equal to 0.01 that of the underlying mantle.

Figure 17. Results of combined inversion of geoid, bathymetry, and SS-S travel time residuals for both upper mantle temperature and composition variations. The viscosity structure is taken to consist of a thick high-viscosity lid overlying a constant-viscosity halfspace.

(a) Three solutions for along-axis temperature variations: Dotted line: Composition perturbations constrained to be uniform over 0-150 km depth. Long-dashed line: Composition perturbations constrained to be uniform over 0-300 km depth. Short-dashed line: Composition perturbations constrained to be uniform over 0-650 km depth.

(b) Three solutions for along-axis composition variations: Dotted line: Composition perturbations constrained to be uniform over 0-150 km depth. Long-dashed line: Composition perturbations constrained to be uniform over 0-300 km depth. Short-dashed line: Composition perturbations constrained to be uniform over 0-650 km depth.

(c) Observed (solid line) and predicted along-axis profiles of SS-S travel time residual.

(d) Observed and predicted along-axis geoid profiles.

(e) Observed and predicted along-axis bathymetry profiles.

Figure 18. Same as Figure 17 except for that the viscosity structure includes zone extending from the base of the lid to a depth of 200 km with a viscosity equal to 0.01 that of the underlying mantle.

Figure 19. Same as Figure 17 but compositional variations constrained to be from 0-50 km depth only.

Figure 20. Same as Figure 18 but compositional variations constrained to be from 0-50 km depth only.

TABLE 1. Digital Seismograph Stations Used

Station Code	Network	Latitude (°N)	Longitude (°E)
ALQ	DWWSSN	34.942	-106.458
ANMO	SRO	34.946	-106.457
ANTO	SRO	39.869	32.794
BCAO	SRO	4.434	18.535
BER	DWWSSN	60.387	5.326
BOCO	SRO	4.587	-74.043
COL	DWWSSN	64.900	-147.793
GAC	CAN	45.70	-75.47
GDH	DWWSSN	69.250	-53.533
GRFO	SRO	49.692	11.222
JAS1	DWWSSN	37.947	-120.438
KBS	DWWSSN	78.917	11.924
KEV	DWWSSN	69.755	27.007
KON	HGLP	59.649	9.598
KONO	ASRO	59.649	9.598
LON	DWWSSN	46.750	-121.810
NEO4	NARS	52.810	6.670
NEO6	NARS	50.100	4.600
NEO9	NARS	44.850	0.980
NE10	NARS	43.090	-0.700
NE11	NARS	41.480	-1.730
NE12	NARS	40.640	-4.160

NE13	NARS	38.690	-4.090
NE14	NARS	37.190	-3.600
NE15	NARS	50.810	5.780
NE16	NARS	45.763	3.103
NE17	NARS	39.881	-4.049
RSCP	RSTN	35.600	-85.569
RSNT	RSTN	62.480	-114.592
RSNY	RSTN	44.548	-74.530
RSON	RSTN	50.859	-93.702
RSSD	RSTN	44.120	-104.036
SCP	DWWSSN	40.795	-77.865
SSB	GEOSCOPE	45.280	4.540
TOL	DWWSSN	39.881	-4.049
WFM	GEOSCOPE	42.610	-71.490
ZOBO	ASRO	-16.270	-68.125

TABLE 2. Adopted Constants

Variable	Description	Value
α	volumetric coefficient of thermal expansion	2.5×10^{-5} K^{-1} (a)
ρ_0	average mantle density	3300 kg m^{-3}
ρ_w	density of seawater	1000 kg m^{-3}
Γ	gravitational constant	6.67×10^{-11} N m^{2}kg^{-2}
g	surface gravitational acceleration	9.8 m s^{-2}
$\partial v_S/\partial T$	thermal coefficient of shear velocity	-6.0×10^{-4} km/s K^{-1}
$\partial v_S/\partial Mg$	variation of shear velocity with Mg#	1.8×10^{-2} km/s/Mg# (b)
$\partial \rho/\partial Mg$	variation of density with Mg#	-12 kg/m^3/Mg# (b)
p	average SS ray parameter at 70°	0.1375 s/km

(a) *Stacey* [1977], *Duffy and Anderson* [1989]

(b) *Akimoto* [1972]

TABLE 3. Inversion Models and Variance Reduction

Model: Temperature variations only

Layer thickness	Viscosity structure	ΔT range	Variance reduction, % total	topo	geoid	SS-S
0-150 km	cvm	180 K	53	25	79	58
0-150 km	lvz	230 K	57	27	79	66
0-300 km	cvm	60 K	47	21	85	41
0-300 km	lvz	110 K	57	24	85	65
0-650 km	cvm	20 K	41	14	91	25
0-650 km	lvz	33 K	49	17	83	51

Model: Compositional variations only

Layer thickness	Viscosity structure	ΔMg# range	Variance reduction, % total	topo	geoid	SS-S
0-150 km	cvm	1.1	33	46	74	-9
0-150 km	lvz	2.4	44	75	76	-9
0-300 km	cvm	0.4	33	29	87	-6
0-300 km	lvz	1.3	43	73	73	-7
0-650 km	cvm	0.1	32	19	93	-3
0-650 km	lvz	0.5	49	65	86	+5

Model: Thermal and compositional variations in same layer

Layer thickness	Viscosity structure	ΔT range	ΔMg# range	Variance reduction, % total	topo	geoid	SS-S
0-150 km	cvm	210 K	1.5	75	44	78	100
0-150 km	lvz	235 K	2.1	86	75	80	100

0-300 km	cvm	110 K	0.7	73	28	89	100
0-300 km	lvz	125 K	1.1	84	74	76	100
0-650 km	cvm	55 K	0.4	71	18	94	100
0-650 km	lvz	60 K	0.8	85	66	88	100

Model: Thermal inversion in layers as noted, compositional variations 0-50 km only

Layer thickness	Viscosity structure	ΔT range	ΔMg# range	Variance reduction, % total	topo	geoid	SS-S
0-150 km	cvm	210 K	5.5	84	83	77	91
0-150 km	lvz	240 K	4.5	85	85	70	96
0-300 km	cvm	80 K	5.9	80	84	86	72
0-300 km	lvz	120 K	4.7	86	90	77	89
0-650 km	cvm	25 K	6.0	73	85	92	47
0-650 km	lvz	35 K	4.6	75	82	73	71

---

cvm = constant viscosity mantle

lvz = mantle with low viscosity zone

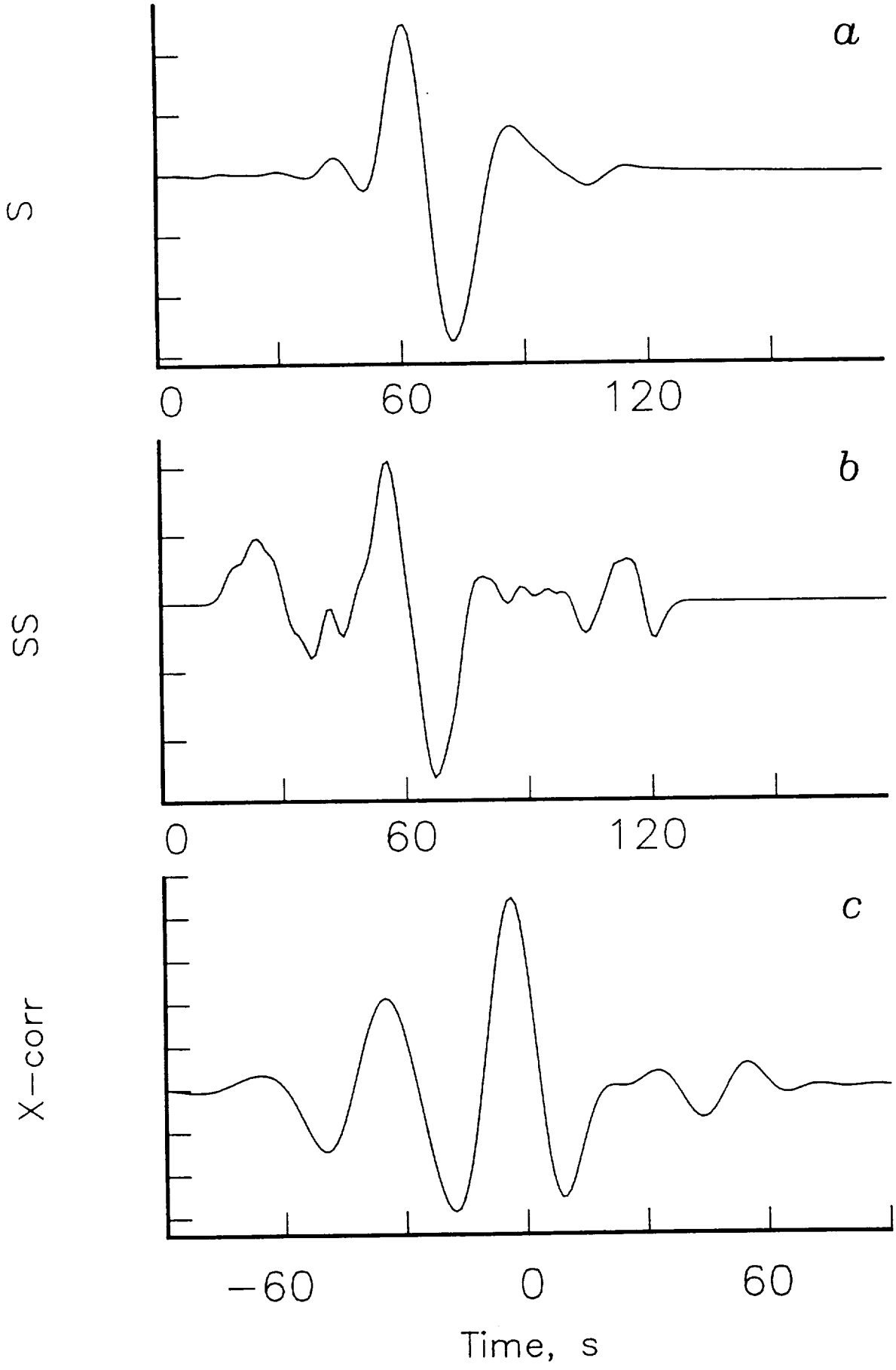

Fig 1

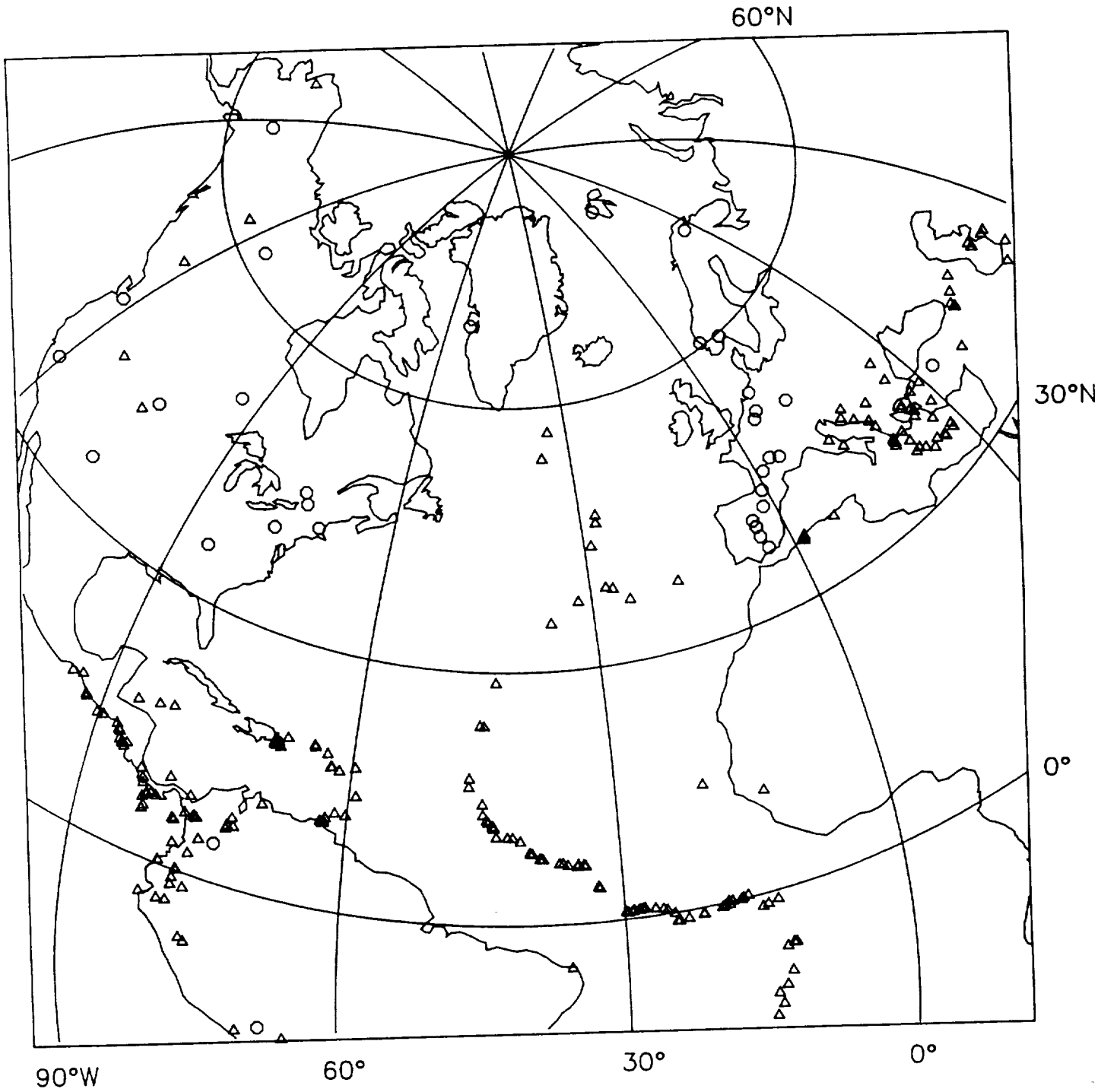

Fig 2

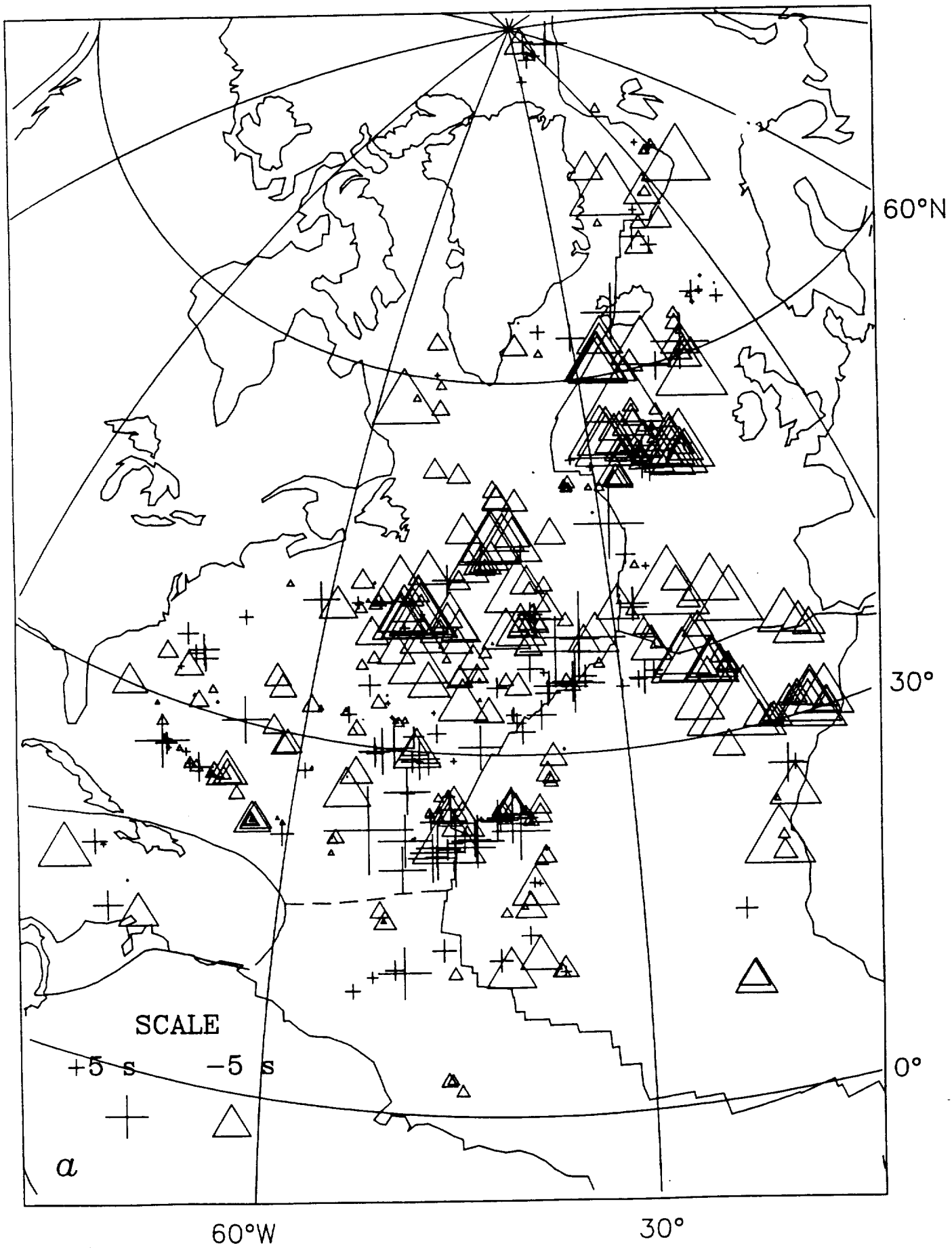

Fig 3a

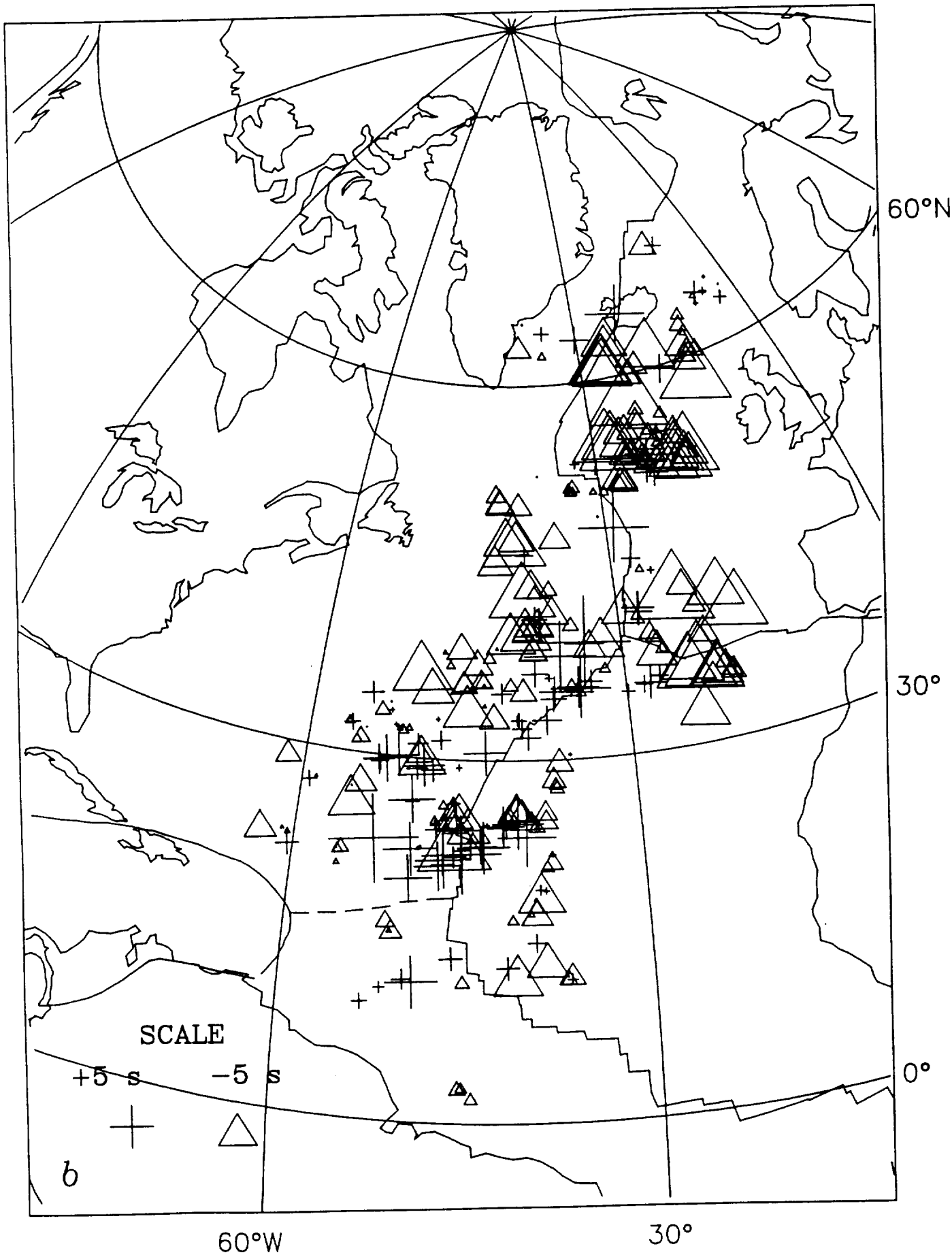

Fig 3b

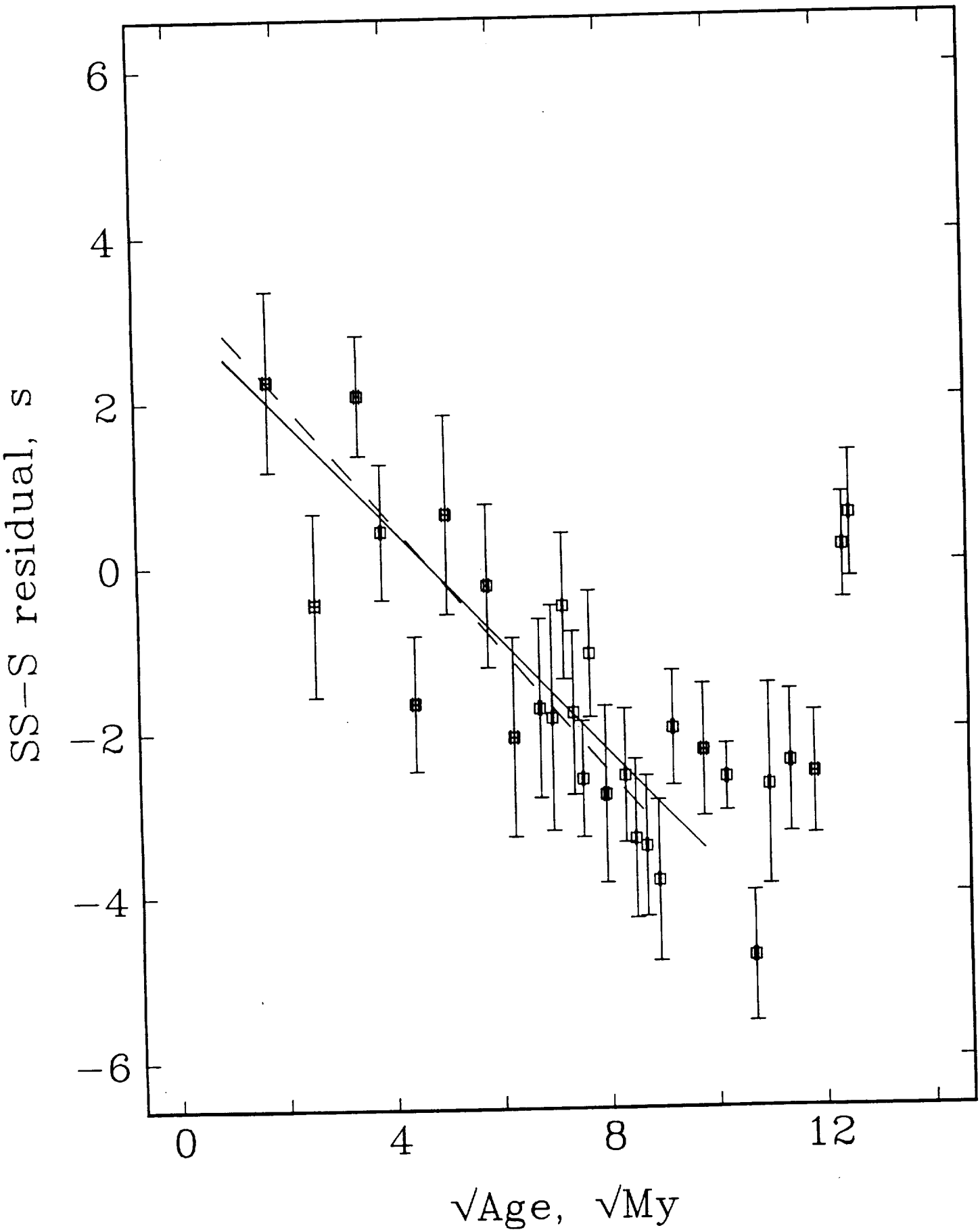

Fig 4

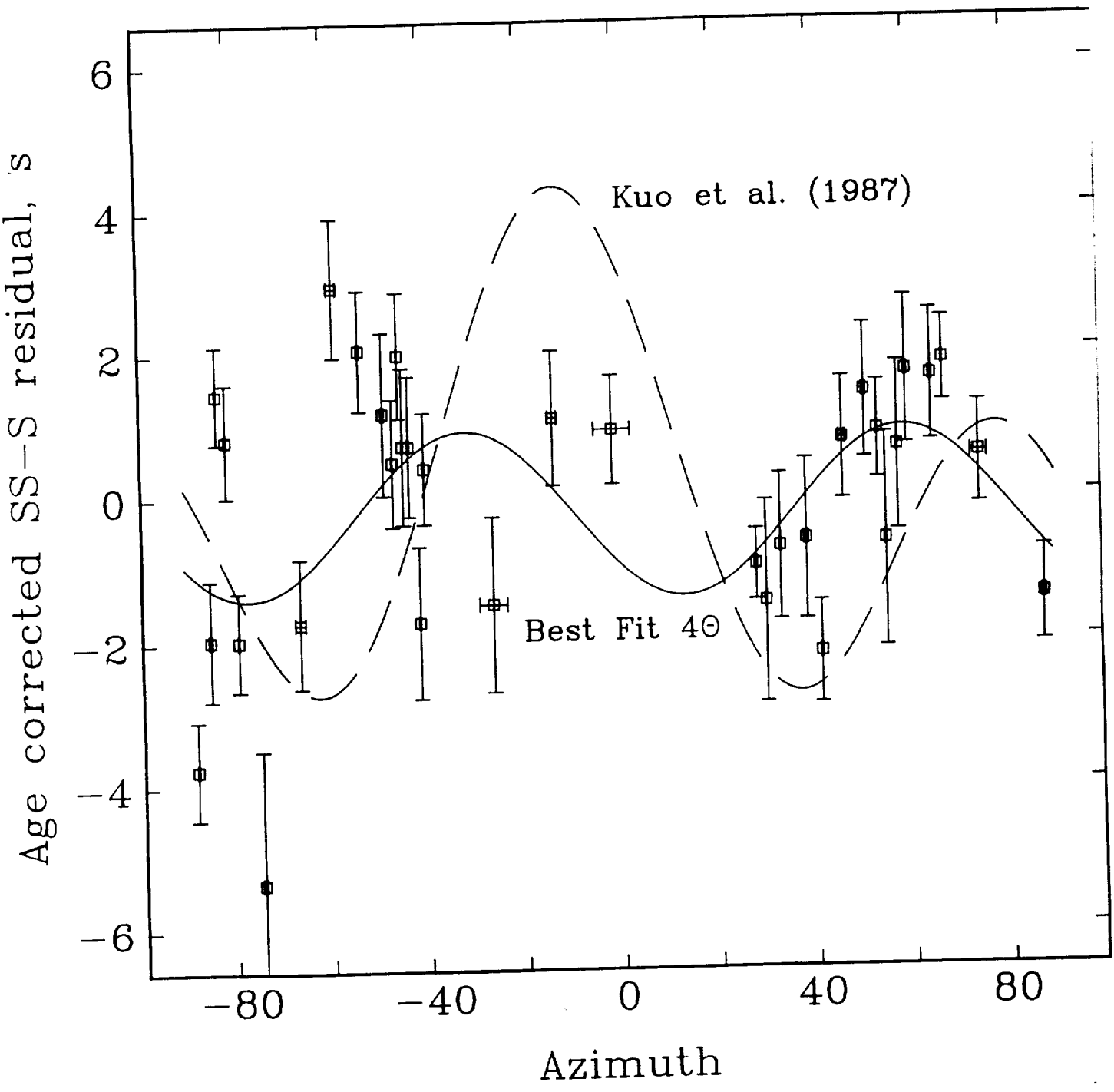
Age corrected SS−S residual, s
6
4
2
0
−2
−4
−6
−80
−40
0
40
80
Azimuth
Kuo et al. (1987)
Best Fit 4Θ

Fig 5

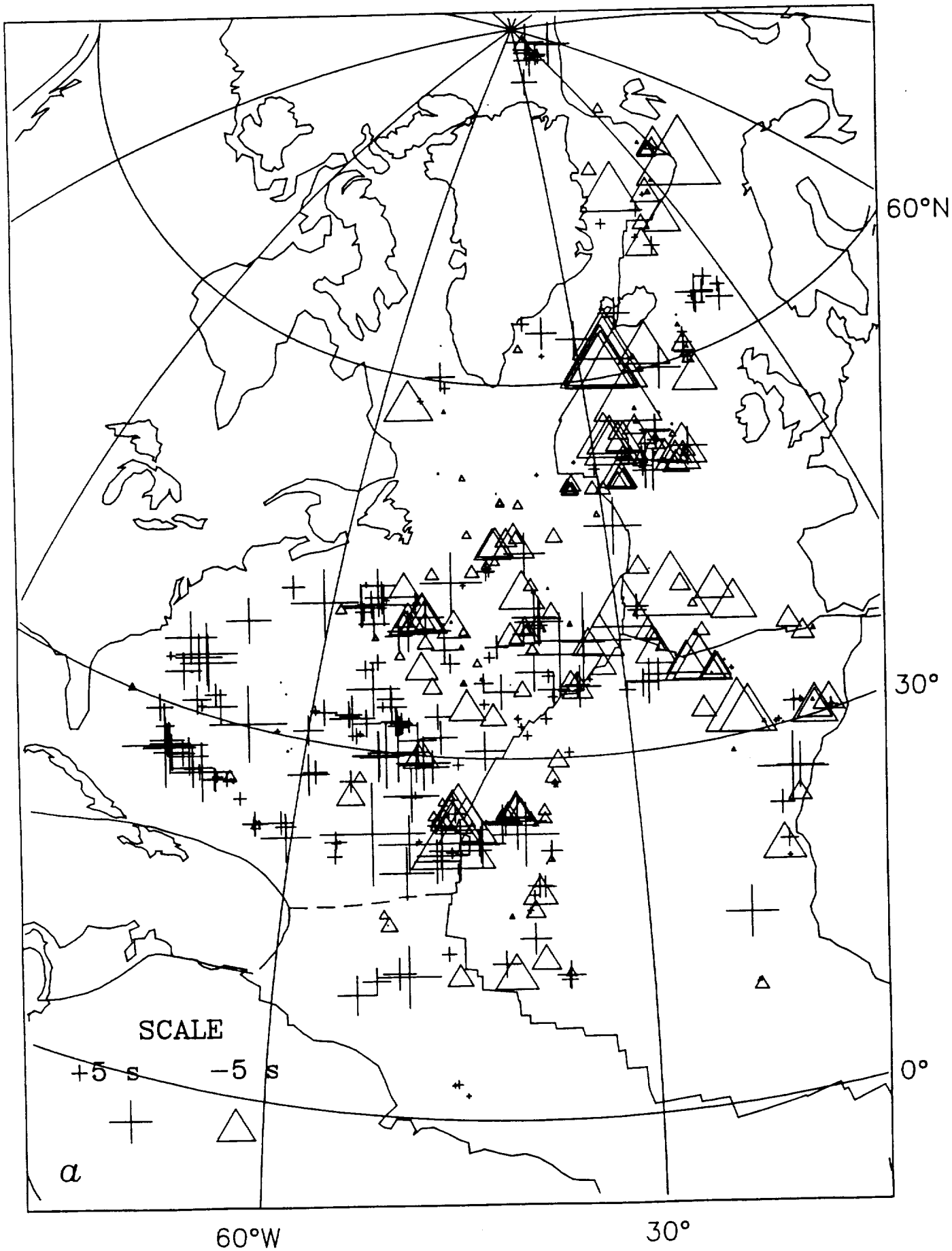

Fig 6a

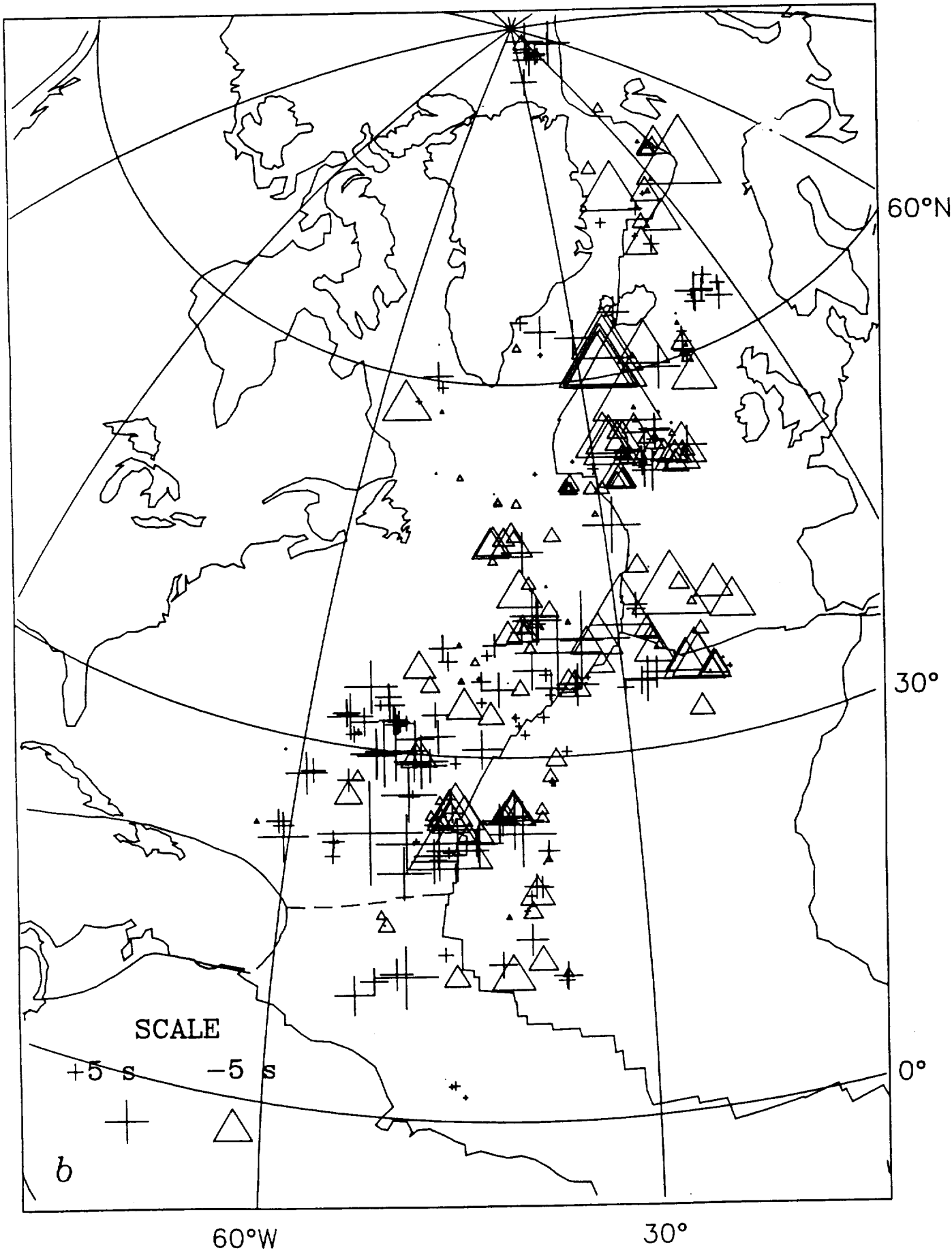

Fig 66

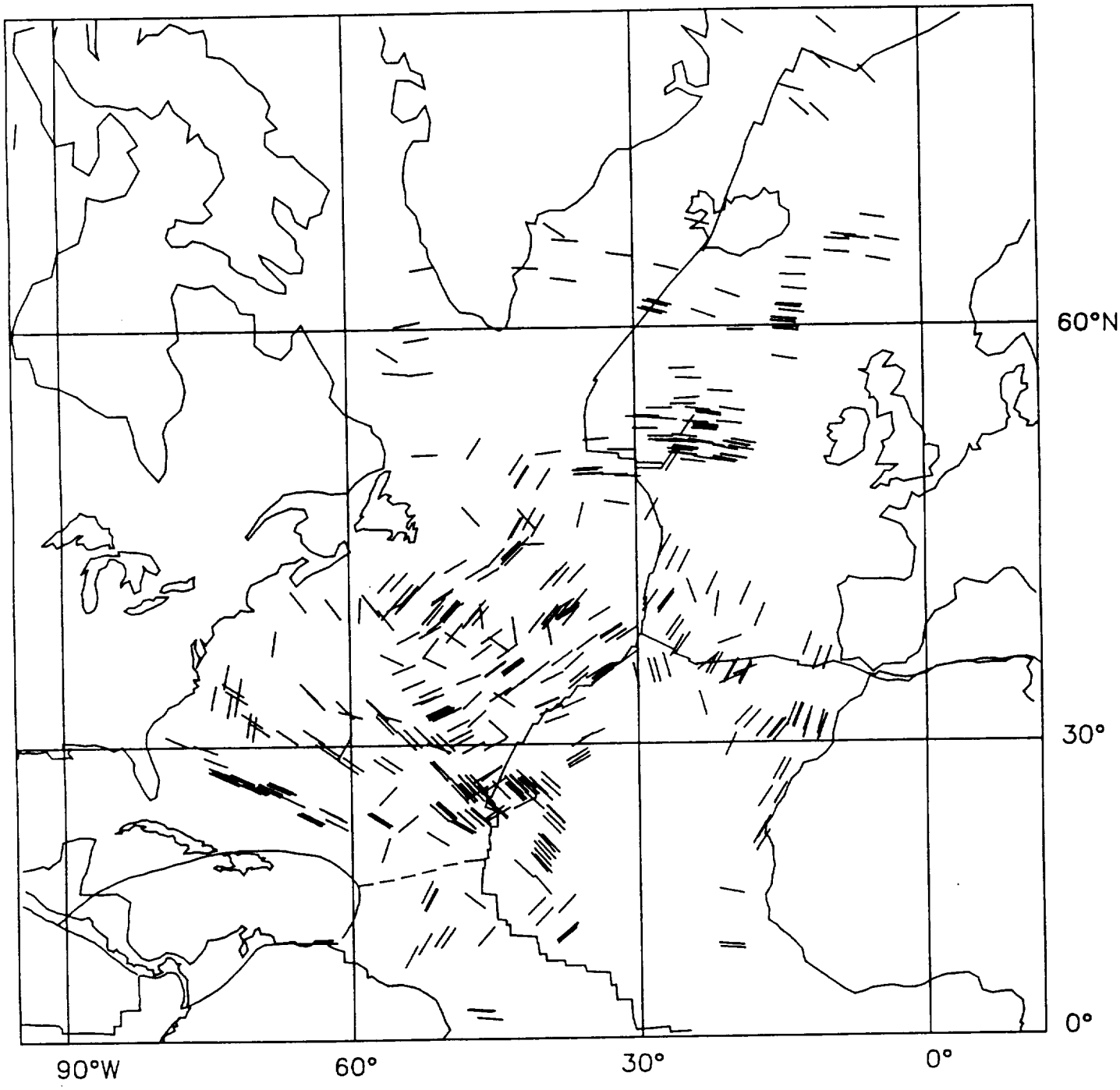

Fig 7

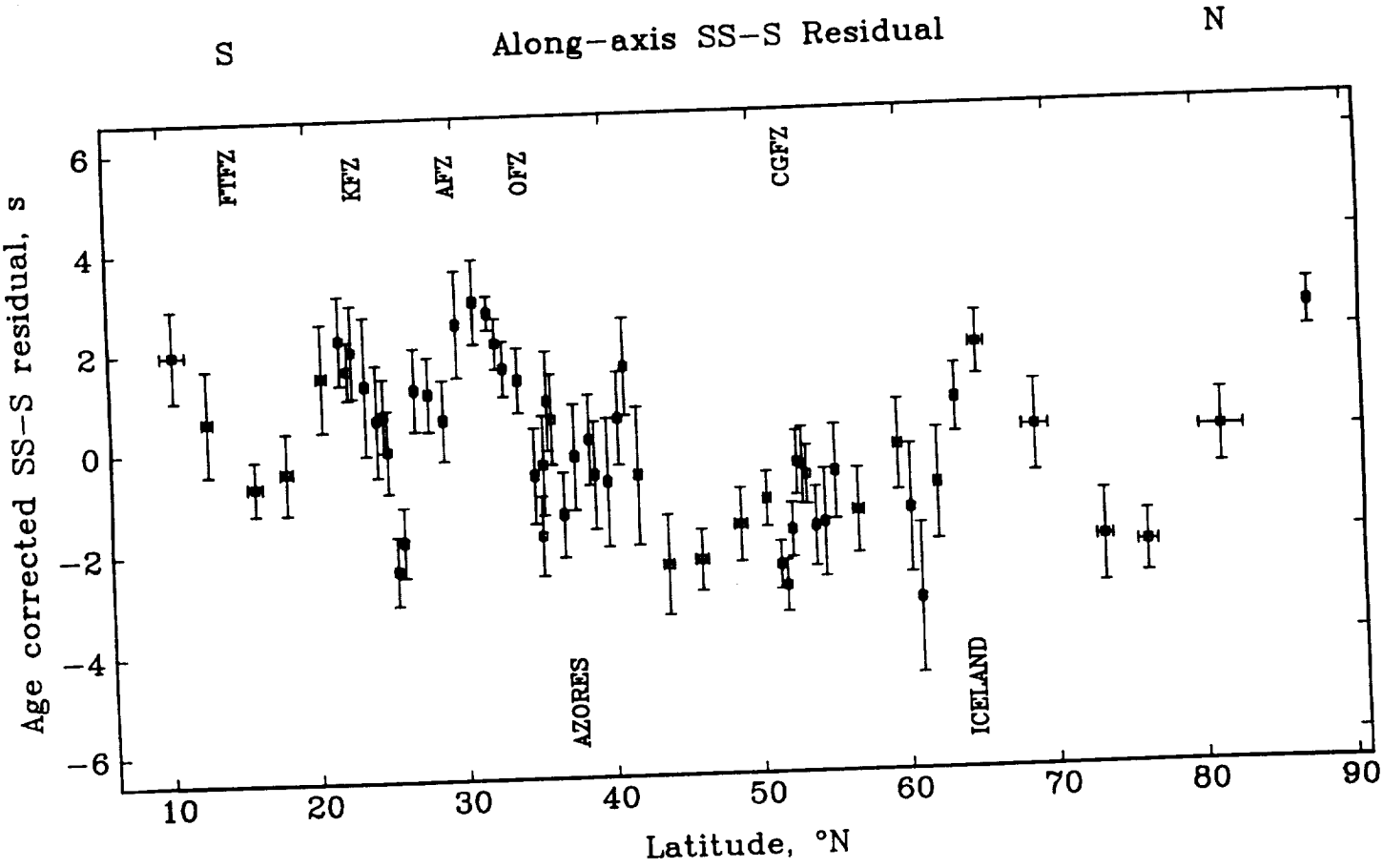
S
Along-axis SS-S Residual
N
FTFZ
KFZ
AFZ
OFZ
CGFZ
AZORES
ICELAND
Age corrected SS-S residual, s
Latitude, °N
6
4
2
0
-2
-4
-6
10
20
30
40
50
60
70
80
90

Fig 8

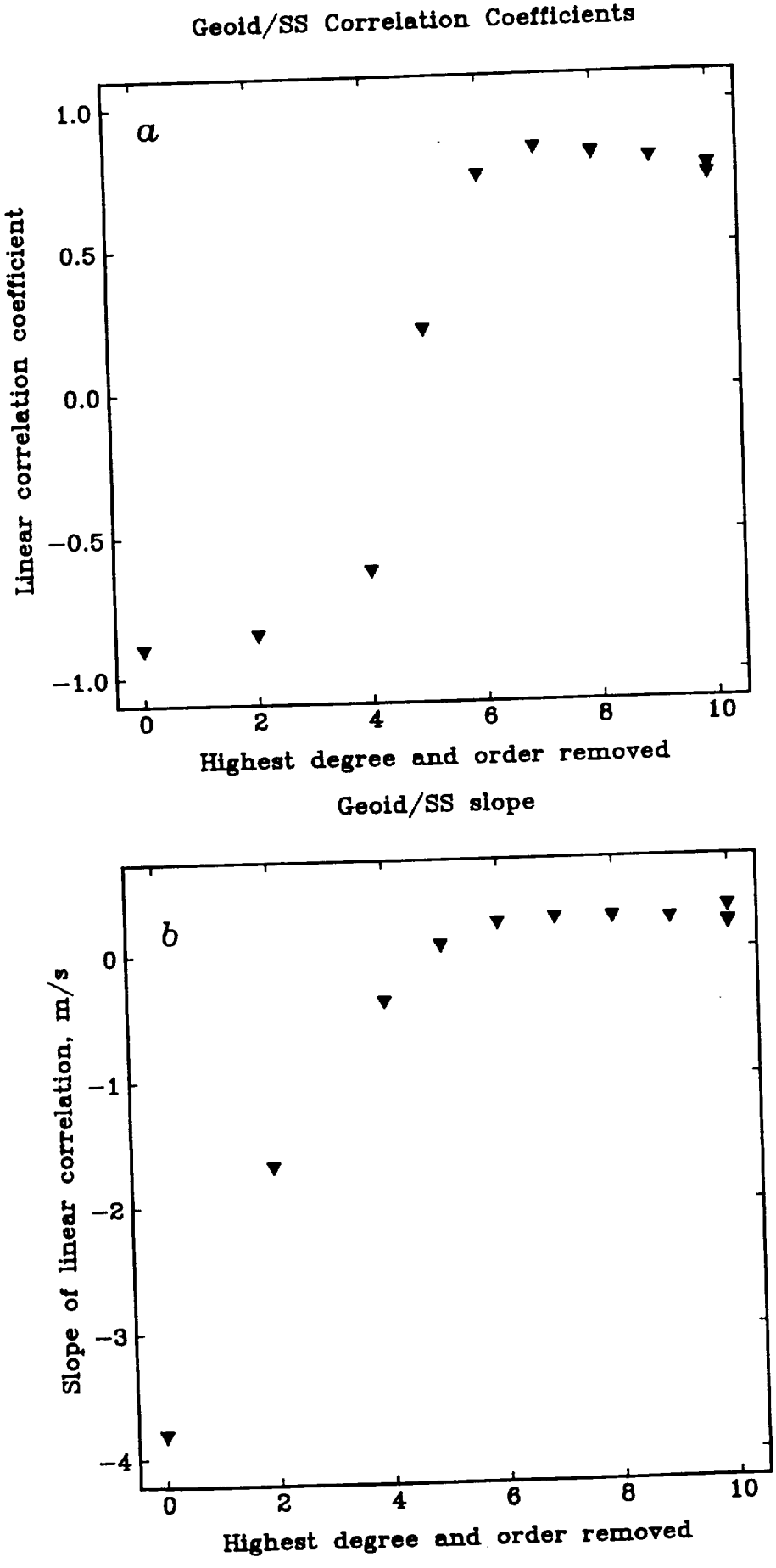
Geoid/SS Correlation Coefficients
a
1.0
0.5
0.0
−0.5
−1.0
Linear correlation coefficient
0
2
4
6
8
10
Highest degree and order removed
Geoid/SS slope
b
0
−1
−2
−3
−4
Slope of linear correlation, m/s
0
2
4
6
8
10
Highest degree and order removed

Fig 9

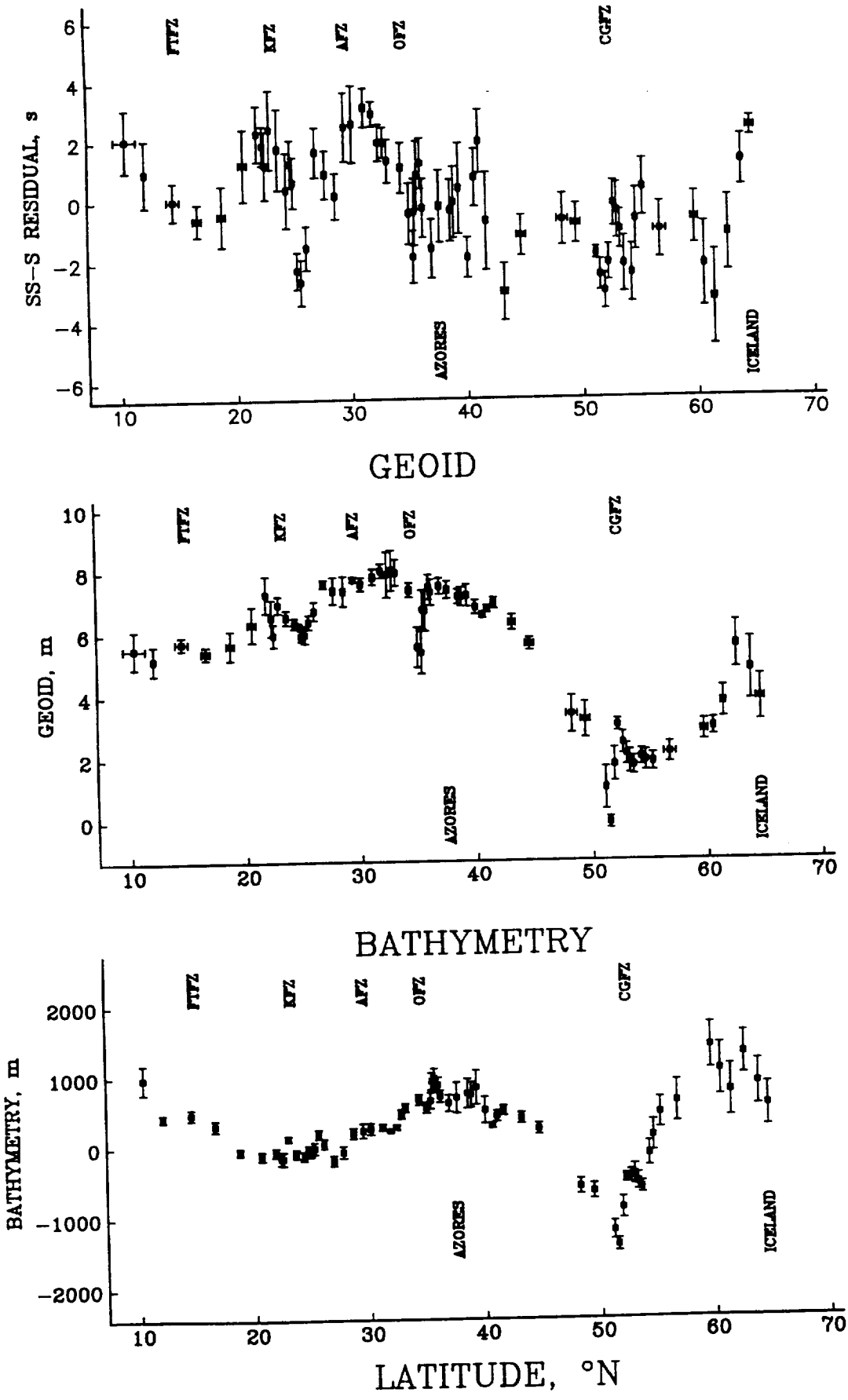
SS−S RESIDUAL
SS−S RESIDUAL, s
FTFZ
KFZ
AFZ
OFZ
CGFZ
AZORES
ICELAND
GEOID
GEOID, m
BATHYMETRY
BATHYMETRY, m
LATITUDE, °N

Fig 10

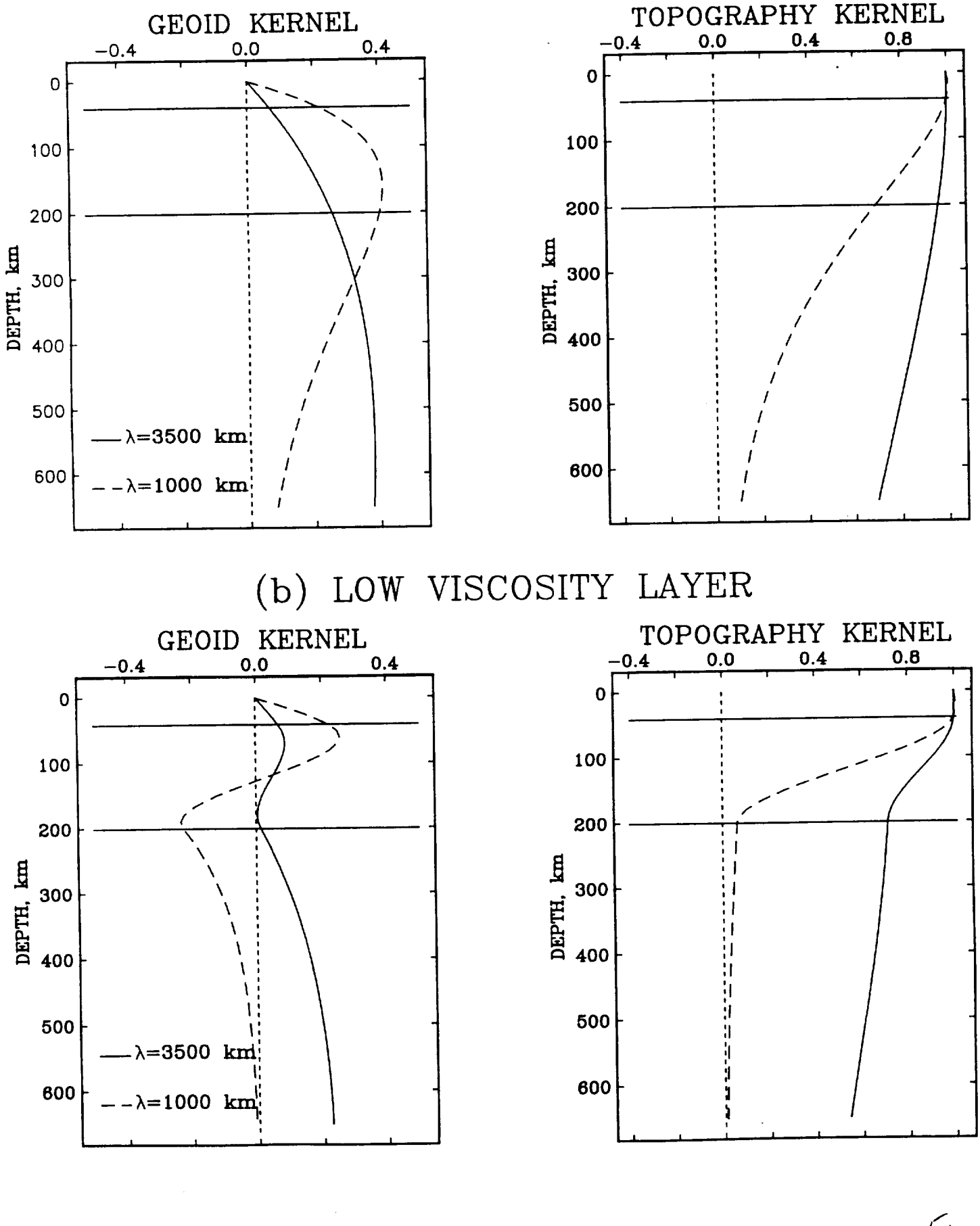
(a) CONSTANT VISCOSITY
GEOID KERNEL
TOPOGRAPHY KERNEL
−0.4
0.0
0.4
0.8
0
100
200
300
400
500
600
DEPTH, km
λ=3500 km
λ=1000 km
(b) LOW VISCOSITY LAYER
GEOID KERNEL
TOPOGRAPHY KERNEL
−0.4
0.0
0.4
0.8
0
100
200
300
400
500
600
DEPTH, km
λ=3500 km
λ=1000 km

Fig 11

SPHERICAL VS. CARTESIAN

(a) CONSTANT VISCOSITY (λ = 4000 km)

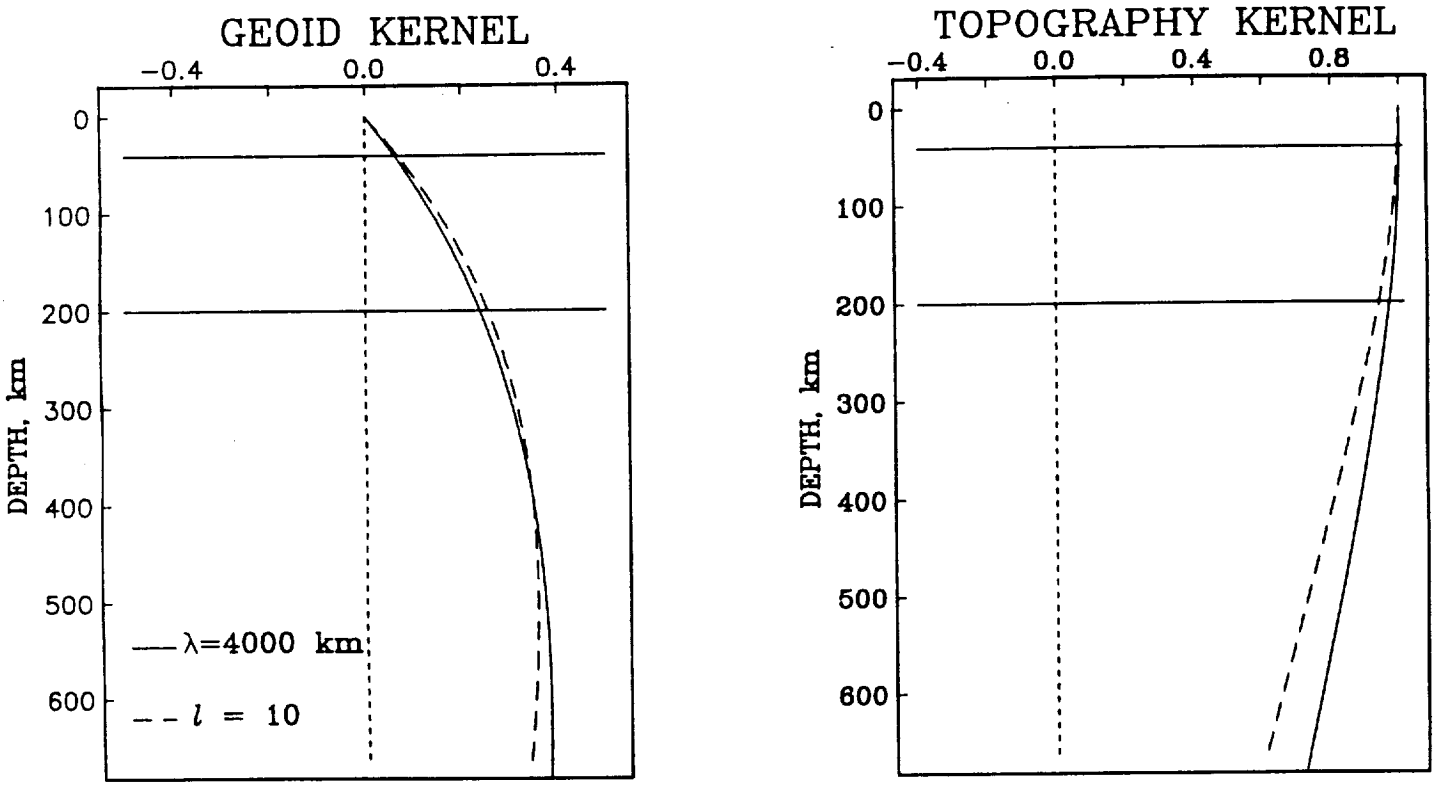

(b) LOW VISCOSITY LAYER (λ = 4000 km)

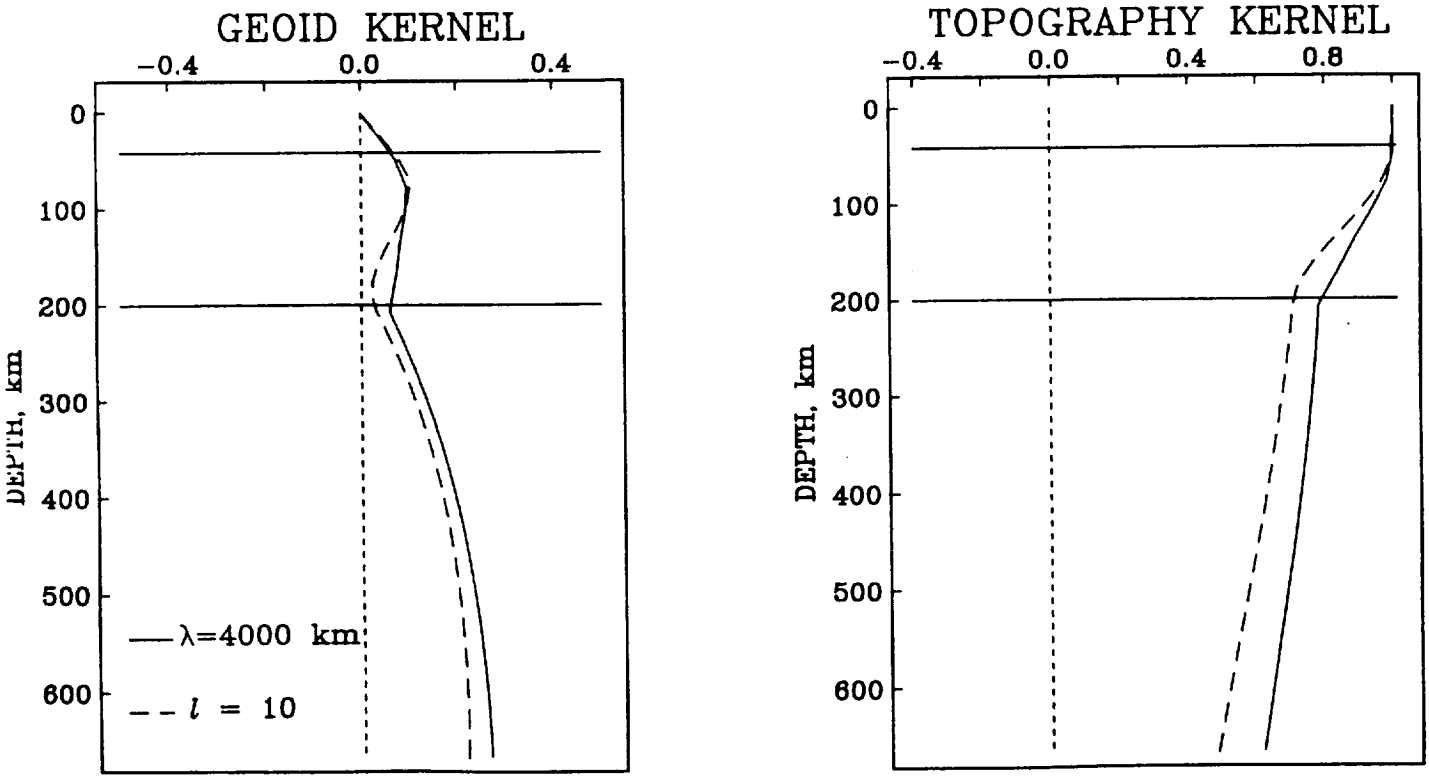

Fig 12 a & b

SPHERICAL VS. CARTESIAN

(c) CONSTANT VISCOSITY (λ = 6667 km)

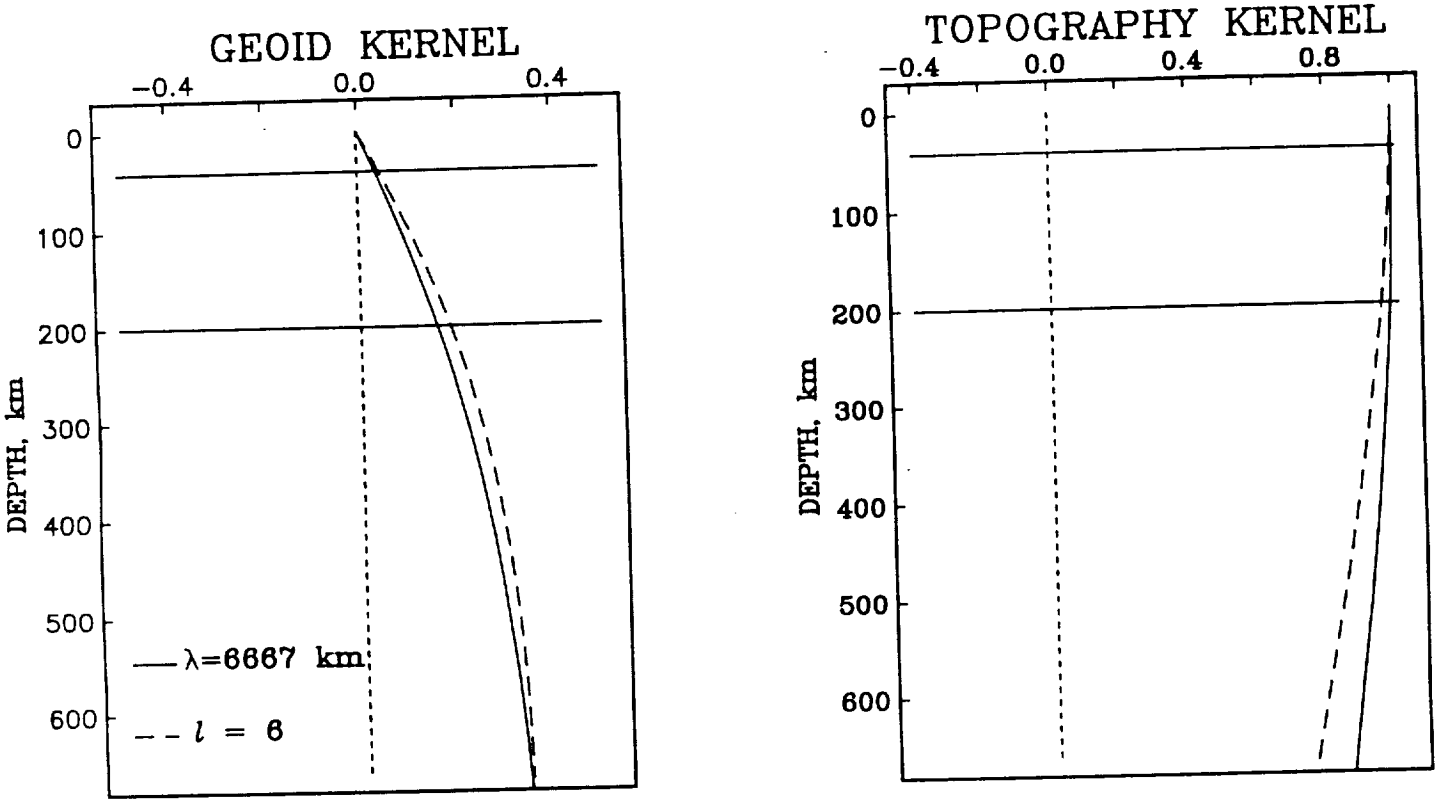

(d) LOW VISCOSITY LAYER (λ = 6667 km)

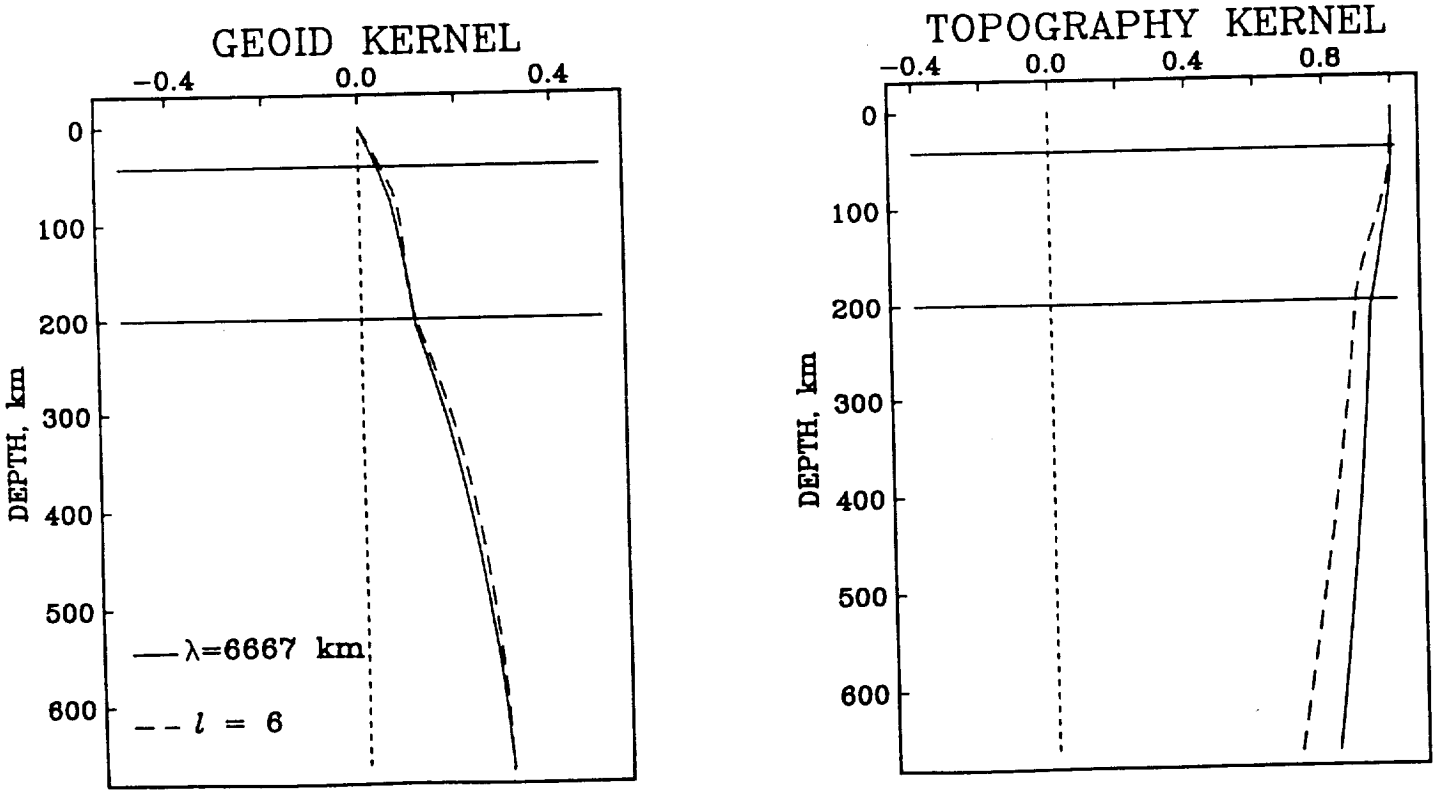

Fig 12 c d

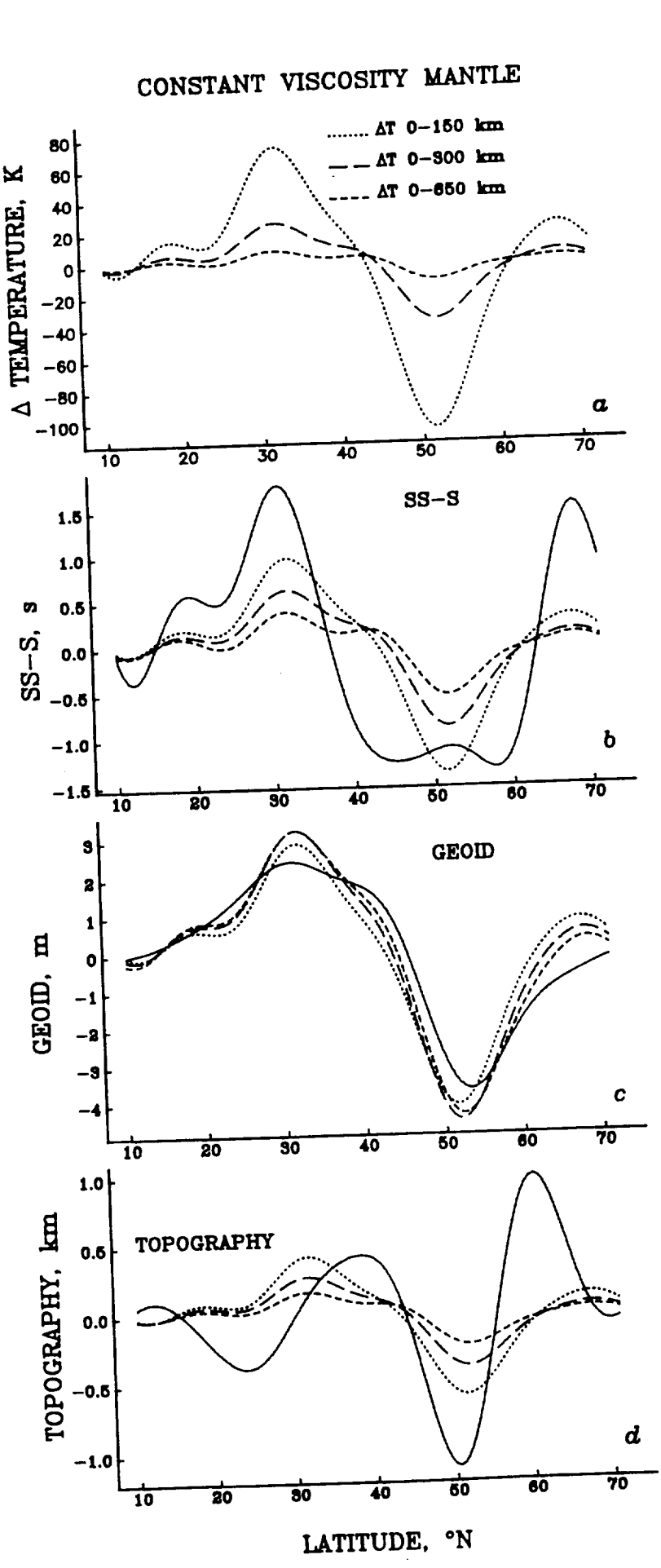
CONSTANT VISCOSITY MANTLE
ΔT 0–150 km
ΔT 0–300 km
ΔT 0–650 km
Δ TEMPERATURE, K
a
SS–S
SS–S, s
b
GEOID
GEOID, m
c
TOPOGRAPHY
TOPOGRAPHY, km
d
LATITUDE, °N

Fig 1.3

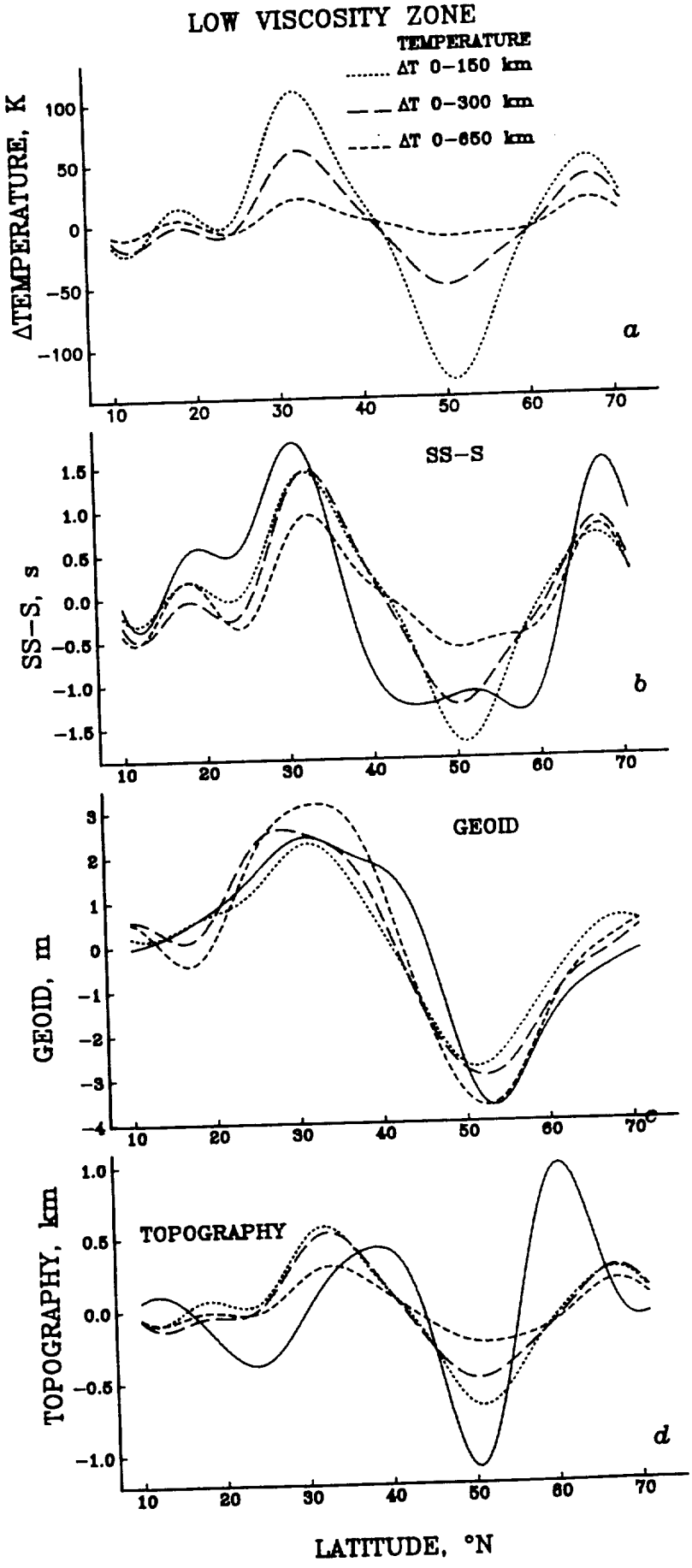
LOW VISCOSITY ZONE
TEMPERATURE
ΔT 0–150 km
ΔT 0–300 km
ΔT 0–650 km
ΔTEMPERATURE, K
a
SS–S
SS–S, s
b
GEOID
GEOID, m
c
TOPOGRAPHY
TOPOGRAPHY, km
d
LATITUDE, °N

Fig 14

CONSTANT VISCOSITY MANTLE

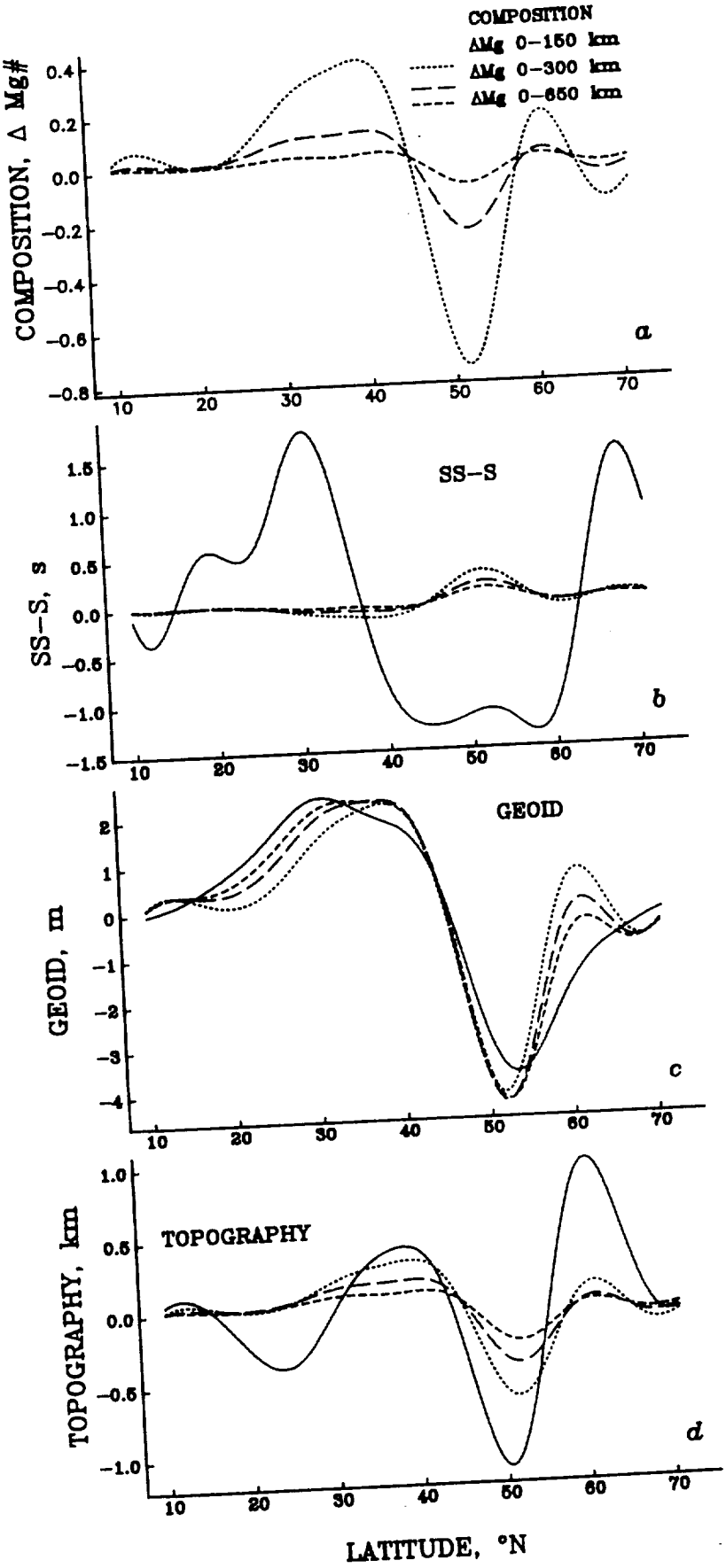

Fig 15

LOW VISCOSITY ZONE

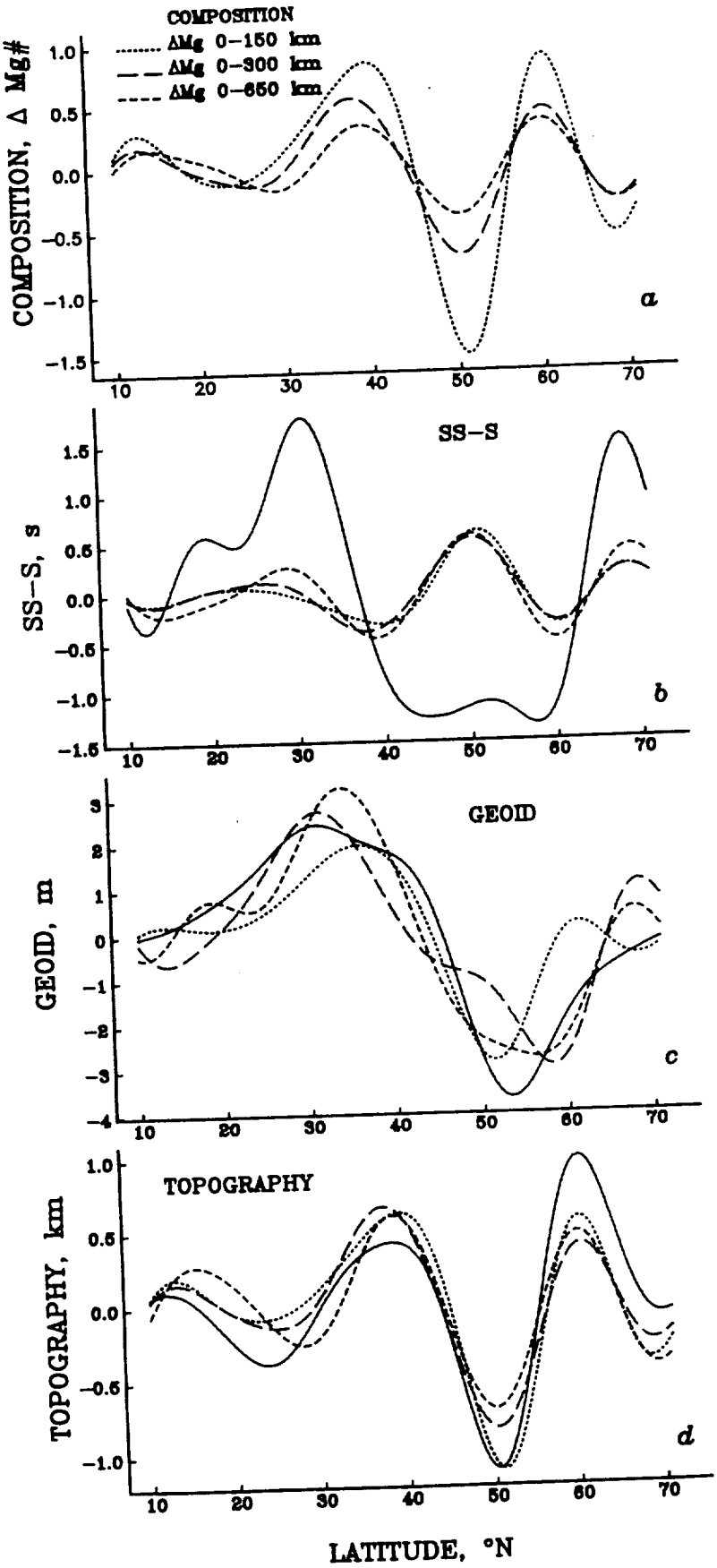

Fig 16

Fig 17

CONSTANT VISCOSITY MANTLE

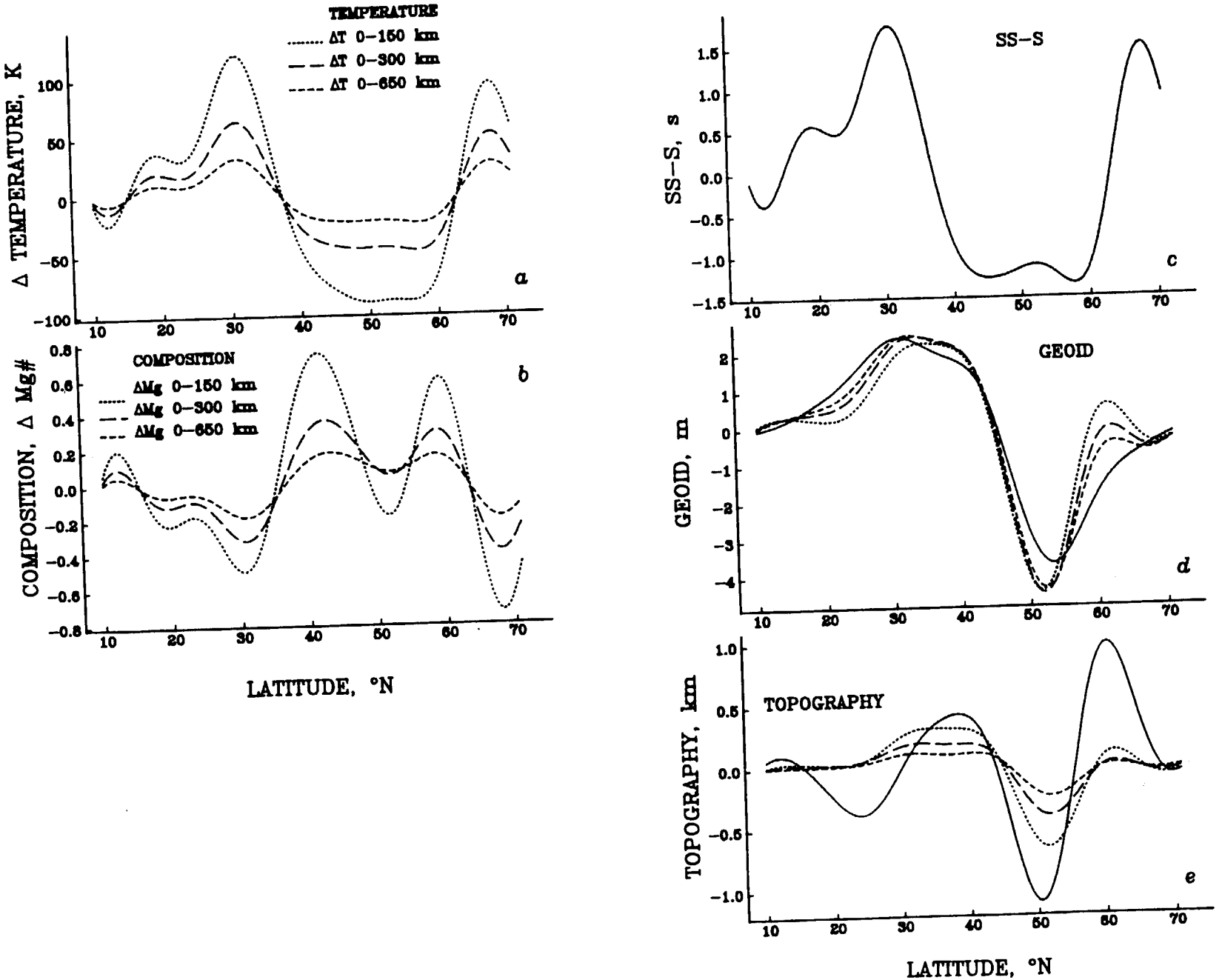

LOW VISCOSITY ZONE

Fig 18

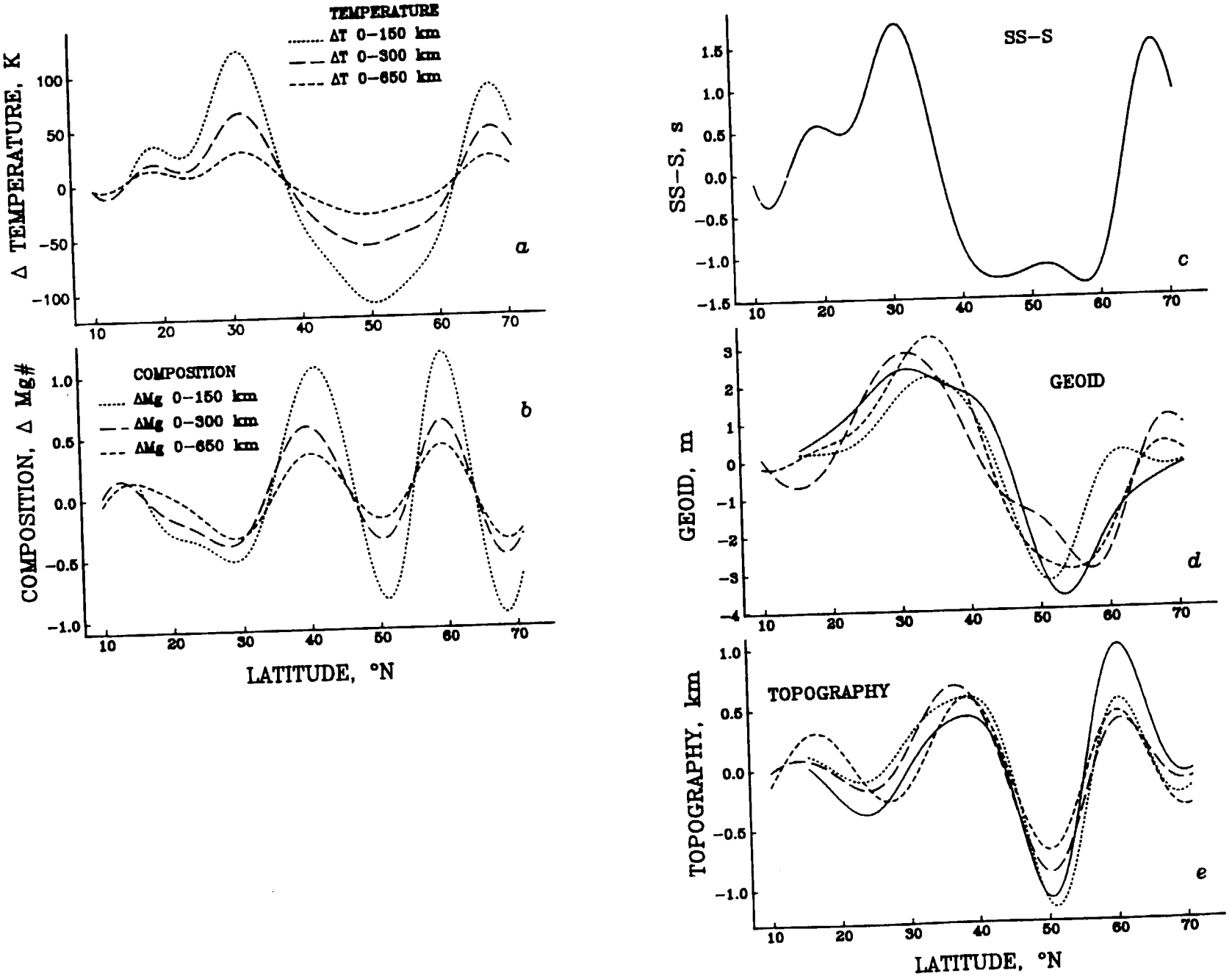

CONSTANT VISCOSITY MANTLE

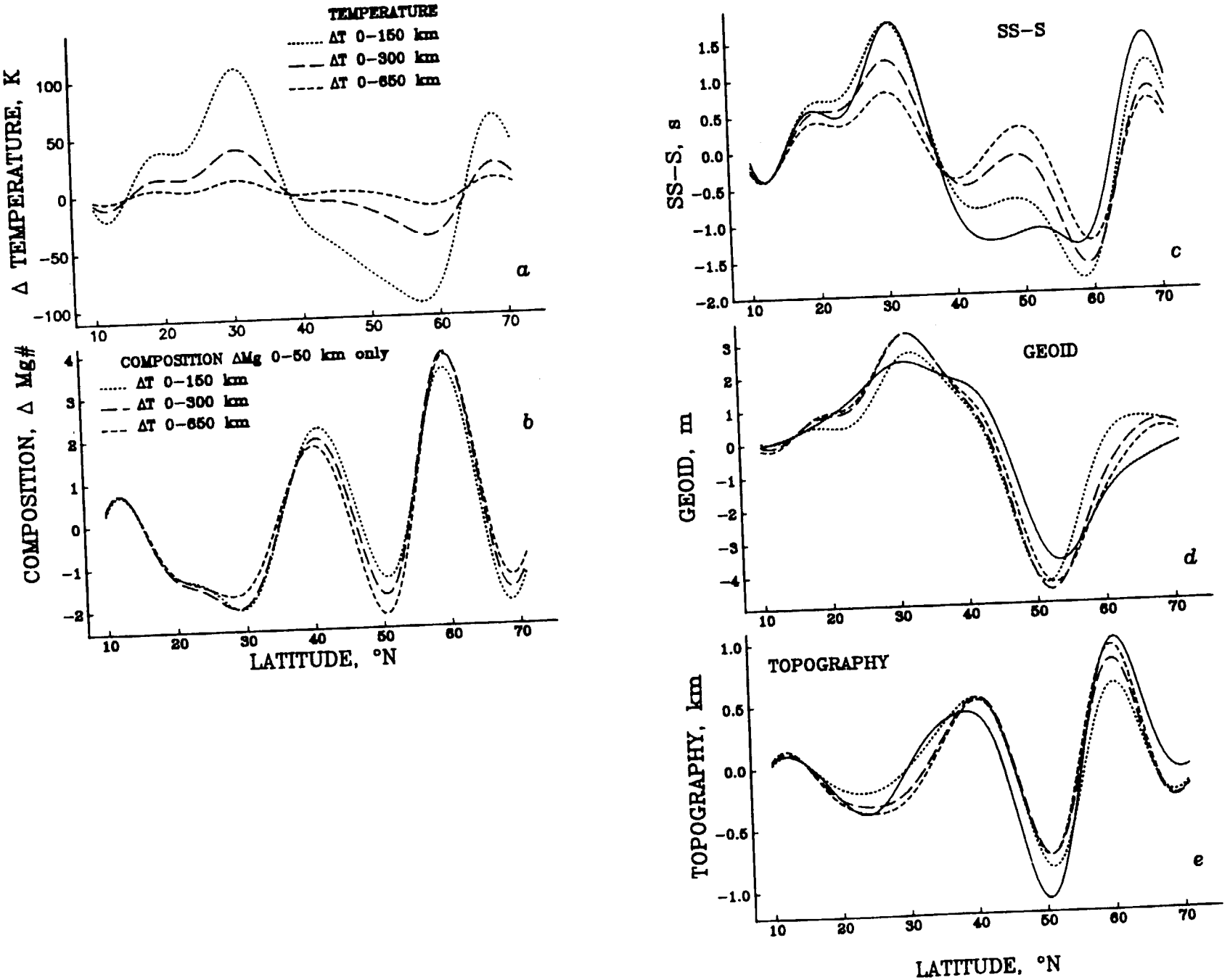

LOW VISCOSITY ZONE